Computational Analysis of the Defect Chemistry of Ceria

Patrick R. L. Keating

Trinity College Dublin

Supervisor: Prof. Graeme W. Watson

A thesis submitted in partial fulfilment of the requirements for the degree of Doctor of Philosophy at the University of Dublin.

2013

Declaration

I hereby declare that:

This thesis has not been submitted as an exercise for a degree at this or any other University.

The work contained herein is entirely my own except where otherwise cited, referenced, or acknowledged in the text.

I agree that the library of the University of Dublin may at their discretion lend or copy this thesis upon request.

Summary

One of the most important issues facing humanity is the impending threat of climate change. In order to combat the rising levels of atmospheric pollutants, many new technologies are being developed to alleviate the strain on the ecosystem. Ceria (CeO_2) is an important material for a variety of applications, from catalysts that remove harmful chemical from the atmosphere, to fuel cells, a highly efficient and environmentally friendly form of energy production. Due to its importance for these technologies, a detailed description of the chemistry CeO_2 would prove highly beneficial for explaining current experimental observations and highlighting new avenues for future research. The main aim of this work is to utilise computational chemistry techniques to gain a detailed understanding on how defects influence and define the chemistry of CeO_2, and to ascertain methods for improving the function of CeO_2 based materials.

This thesis begins with an investigation of intrinsic defects in CeO_2 in order to determine which are most important for defining the properties of CeO_2. It is demonstrated that the most stable defect under oxygen poor conditions will be the oxygen vacancy, while under oxygen rich conditions the most stable defect is an oxygen interstitial, which forms a peroxide ion. Temperature and pressure dependence analyses then assess the relative abundance of intrinsic defects under a range of real–world conditions. It was determined that under the conditions that CeO_2 catalysts and fuel cell electrolytes typically operate at, the oxygen vacancy is the most abundant defect, and also the most important for describing the chemistry of CeO_2.

Next, static structure calculations are employed to investigate a range of trivalent dopants in CeO_2 to determine which are most effective for fuel cell applications. Firstly, the local structure around the dopant ions is assessed to determine the most stable structure. Secondly, the relative attraction between the dopants and oxygen vacancies is calculated. Finally, the effect of the dopants on the reducibility of CeO_2 is investigated. It was found that the defect structure is principally dependent on the ionic radius of the dopant cations, and that dopant–vacancy attraction was lowest for dopants with ionic radii in the range of 0.99–1.13 Å. The reduction energy of CeO_2 was found to be dependent on the structure around the dopants, itself a function of the ionic radius of the dopants, but the reduction energy did not vary significantly between dopants of similar ionic radii. From these results it is possible to suggest which trivalent dopants would be most suitable to enhance ionic conductivity without increasing electronic conductivity in SOFC electrolytes.

To model the dynamical process of oxygen diffusion, *ab intio* molecular dynamics calculations are applied to a series of doped CeO_2 structures. It was found that the movement of anions in these systems is predominantly through a hopping mechanism where anions move along a single direction to fill vacancy sites. However, alternate, high energy conduction mechanisms were also observed at elevated temperatures. It was also found that the defect structure is highly important for improving ionic conductivity and to avoid the vacancies becoming trapped by the dopant cations. The combination of static and dynamical calculations was also shown to be an effective method for assessing new materials for solid oxide fuel cell electrolytes.

An alternate application of CeO_2 as a metal-oxide-semiconductor field-effect transistor is also investigated. Due to its high dielectric constant, large band gap, and very small lattice mismatch with Si, CeO_2 has been proposed as a promising candidate high–κ dielectric material. The performance of CeO_2 as a dielectric material, however, is severely limited due its propensity for facile reduction (oxygen vacancy formation), which causes a high interface state density, and subsequent decreased drain currents. Therefore, a series of trivalent dopants were tested to see which could decrease the concentration of such defects in CeO_2 samples. It was demonstrated that La(III) and Y(III) are the most soluble trivalent dopants in CeO_2, and can reduce the number of the electrons in the system both ionically (formation of dopant–vacancy–dopant clusters) or to a lesser extent electronically (hole formation). La(III) doping also increases the lattice constant of CeO_2, improving the lattice match with Si.

Finally, defects on the pure and doped low index surfaces of CeO_2 are studied. The results reveal the variable nature of the oxygen states on pure surfaces, including the never before modelled intrinsic peroxide surface defects. It is shown that, under O–rich conditions, peroxide defects on the (100) and (110) surfaces are more stable than oxygen vacancies. For the (100), (110) and (111) surfaces of La–doped CeO_2, a series of different charge compensation schemes were tested to determine which was the most stable. For the (100) and (110) surface under O–rich conditions, the charge was compensated by a peroxide ion and not an oxygen vacancy as has been previously reported. The effect of La(III) dopants on the reducibility of CeO_2 was probed by introducing extra oxygen vacancies to the surfaces. The results of the calculations show that La(III) dopants will lead to an increase in the reduction energy for surface oxygen ions. However, an alternate redox mechanism where the surface is reduced by the breakdown of the charge compensating peroxide leaving a surface vacancy is proposed. This mechanism provides a low energy pathway that could explain the enhanced catalytic properties that have been observed for La–doped CeO_2.

Acknowledgements

I would like to thank my supervisor, Prof. Graeme W. Watson for his support, guidance and patience during my time here in Trinity. Thank you for sticking by me, especially during the tough times. I would also like to thank the Heads of the School of Chemistry, formerly Prof. Grayson, and currently Prof. Draper, for the opportunity to pursue this PhD. in such a prestigious institution, and for use of the facilities of the School of Chemistry.

I would like to acknowledge funding from Trinity College Dublin, through the Usher Award, and from SFI. Special thanks also go to ICHEC and TCHPC for access to their computing facilities, without which there would be no thesis today. Special thanks to Dermot, Geoff, Jimmy, Jose, Neil, Paddy and Nicola for the support and help with computer issues over the years. Also, thanks for all the games of Urban Terror!

A massive thank you to Dr David Scanlon, for all the help, advice, suggestions and laughs over the years, although, I could have perhaps done without the nicknames. I would also like to thank Dr Jeremy Allen and Dr Benjamin Morgan in particular for their help. And thank you to all the other members of the Watson group, past and present: Mario, Kalle, Natasha, Aoife K., Aoife L., Souad, Doug, Ni Chaoimh, John, Kate, Berry and Ailbhe. Thanks for making the office such a pleasant place to work, and thanks for putting up with my interminable knock–knock jokes.

I wish to express my love and gratitude for my family; my parents, Geoffrey and Jane, my grandmother Lyndall, my brother John and his wife, Caroline, and all the members of my extended family. Thank you all so much for your love and support over the last few years.

Finally, I would like to dedicate this thesis to the memory of my grandfather, Prof. John Victor Luce. I know how proud you were for a member of the family to pursue a doctorate at Trinity, and I am sorry you cannot be here to see this day.

Publications

Related to Thesis Work

1. P. R. L. Keating, D. O. Scanlon and G. W. Watson, "Intrinsic Ferromagnetism in CeO_2: Dispelling the myth of Vacancy Site localisation Mediated Superexchange", Journal of Physics: Condensed Matter, 21, 405502 (2009)

2. P. R. L. Keating, D. O. Scanlon, B. J. Morgan, N. M. Galea and G. W. Watson, "Analysis of Intrinsic Defects in CeO_2 using a Koopmans-like GGA+U Approach", Journal of Physical Chemistry C, 116, 2443–2452 (2012)

3. P. R. L. Keating, D. O. Scanlon and G. W. Watson, "Computational Testing of Trivalent Dopant in CeO_2 for Improved High–κ Dielectric Behaviour", Journal of Materials Chemistry C, 1, 1093–1098 (2013)

Abbreviations

CB: Conduction band

CBM: Conduction band minimum

CCV: Charge Compensating Vacancy

CSP: Concentrated solar power

DFT: Density Functional Theory

EDOS: Electronic density of states

GDC: Gadolinium doped CeO_2

GGA: Generalised gradient approximation

IR: Infra–red

HF: Hartree–Fock

LDA: Local density approximation

LSC: $La_{0.70}Sr_{0.30}CoO_{3-\delta}$

LSGM: $La_{0.80}Sr_{0.20}Ga_{0.90}Mg_{0.10}O_{2.85}$

LSM: $La_{1-x}Sr_xMnO_3$

NN: Nearest neighbour

NNN: Next–nearest neighbour

PAW: Projector augmented wave

PBE: Perdew Burke Ernzerhof DFT functional

PEDOS: Partial electronic density of states

PW91: Perdew Wang 91 functional

SCF: Self Consistent Field

SIE: Self–interaction error

SOFC: Solid Oxide Fuel Cell

SSZ: Scandium–stabilised zirconia

TEC: Thermal expansion coefficient

TL: Transition level thermodynamic

UPS: Ultraviolet photoelectron spectroscopy

UV: Ultraviolet

VASP: Vienna *Ab–initio* Simulation Package

VB: Valence band

VBM: Valence band maximum

XPS: X–ray photoelectron spectroscopy

YSZ: Yttrium–stabilised zirconia

Contents

1 Introduction **1**

1.1 Climate Change and the Environment 1

1.1.1 Greenhouse Gases and CO_2 1

1.2 Reduction of Green House Gases 3

1.2.1 CO_2 Sequestration 3

1.2.2 Catalysis 4

1.3 Energy Production in the Green Age 5

1.3.1 Wind Energy 5

1.3.2 Hydroelectric Energy 6

1.3.3 Solar Energy 7

1.4 Energy Storage 8

1.4.1 Chemical Storage as Fuels 10

1.4.2 Production and Storage of Hydrogen Fuel 11

1.5 Fuel Cells 12

1.5.1 Solid Oxide Fuel Cells 13

1.5.2 Operation of an SOFC 13

1.5.3 Current Materials used in SOFCs 14

1.5.4 Problems with Current SOFC Materials 16

1.5.5 Development of Intermediate Temperature SOFC 17

1.6 Ceria 19

1.6.1 CeO_2 as a Catalyst 19

1.6.2 CeO_2 as an SOFC Electrolyte 22

1.7 Thesis Outline 26

2 Computational Theory **28**

2.1 Quantum Chemistry Methods 28

2.1.1 Schrödinger Equation 28

2.1.2 The Born-Oppenheimer Approximation 29

2.1.3 The Variational Principle 30

2.1.4 Hartree–Fock Approximation 31

2.1.5 Roothaan–Hall Equations 34

2.1.6 Limitations of the Hartree–Fock Approach 34

2.1.7 Density Functional Theory 35

2.1.8 Exchange–Correlation Functionals 38

2.1.9 The DFT+U Approach 40

2.2 Solid State Simulations 44

2.2.1 Periodic Boundary Conditions 44

2.2.2 Basis Sets and Pseudopotentials 45

2.2.3 Brillouin Zone and k–Points 46

2.2.4 Electronic Optimisation 48

2.2.5 Force Model and Geometry Optimisation 49

2.2.6 Energy Minimisations: From Steepest Descent to Quasi–Newton 50

2.2.7 Molecular Dynamics 52

2.2.8 Molecular–Dynamics Ensembles 54

3 Computational Methodology **57**

3.1 Vienna *ab initio* Simulation Package (VASP) 57

3.2 Structural Optimization and Convergence 57

3.3 Electronic Structure Calculations 58

3.3.1 Band Structures 58

3.3.2 Electronic Density of States 60

3.4 Defect Calculations 61

3.4.1 Formation Energy of a Neutral Defect 61
3.4.2 Chemical Potential Limits 62
3.4.3 Temperature and Pressure Dependence of Defect Formation . . 63
3.4.4 Formation Enthalpy of Charged Defects 64
3.4.5 Thermodynamic Transition Levels 65
3.4.6 Transition Level Diagrams 65
3.5 Mean Square Displacement Plots and the Nernst–Einstein Equation . . 67
3.6 Radial Distribution Function 69

4 Analysis of Intrinsic Defects in CeO_2 71
4.1 Introduction 71
4.2 Computational Methods 72
4.3 Bulk Properties 74
4.4 Defect Structure 75
4.4.1 Oxygen Vacancy 75
4.4.2 Cerium Interstitial 77
4.4.3 Cerium Vacancy 79
4.4.4 Oxygen Interstitial 82
4.4.5 Anion Frenkel and Schottky Defects 83
4.5 Defect Formation Energies 84
4.6 Discussion 87
4.7 Conclusions 91

5 The Structure and Reducibility of CeO_2 Doped with Trivalent Cations 92
5.1 Introduction 92
5.2 Computational Methods 94
5.3 Structure of Doped Ceria 95
5.4 The Effect of Dopants on the Reducibility of CeO_2 103
5.5 Discussion 106
5.6 Conclusions 112

6 Ionic Conductivity in Doped CeO_2 113

6.1 Introduction 113

6.2 Computational Methods 114

6.3 Mean–square Displacement Plots and Diffusion Coefficients. 116

6.4 Conductivity Plots and Activation Energies 124

6.5 RDFs and Structural Analysis 124

6.6 Coordination Analysis 129

6.7 Discussion 132

6.8 Conclusions 135

7 Trivalent Dopants for Improved High–κ Dielectric Behaviour in CeO_2 137

7.1 Introduction 137

7.2 Computational Methods 138

7.3 Intrinsic defects 139

7.4 Trivalent dopants 141

7.5 Discussion 145

7.6 Conclusions 146

8 Defect Chemistry on the Catalytically Active Surfaces of Pure and La–doped CeO_2 147

8.1 Introduction 147

8.2 Computational Methods 150

8.3 The Low Index Surfaces of CeO_2 151

8.4 Intrinsic Defects on the Pure CeO_2 Surfaces 154

8.4.1 Vibrational Frequencies of Surface Peroxide Species 159

8.5 Defect Structures of La–doped CeO_2 161

8.5.1 One La(III) per Surface 161

8.5.2 Two La(III) per Surface 161

8.6 Doping Energies of Doped CeO_2 surfaces 163

8.6.1 Oxygen Core Levels on the Low Index Surfaces 166

8.7 Reduced La–doped surfaces 167
8.7.1 Reduction of surfaces with a peroxide charge compensation mechanism 168
8.7.2 Reduction of surfaces with a vacancy charge compensation mechanism 172
8.8 Alternate reduction mechanism: peroxide–vacancy switching 176
8.9 Conclusions 183

9 Conclusions **185**

9.1 Conclusions 185
9.2 Future Work 189

List of Figures

1.1 A schematic diagram of a SOFC. The red spheres represent oxygen atoms. The fuel, in this case hydrogen, is represented by the green spheres. 15

2.1 The change in energy as a function of the number of electrons, N, in a system for a DFT and an 'exact' calculation. 42

2.2 A diagram that demonstrates how the $+U$ approach counteracts the SIE using three p orbitals as an example. In the top example, a single electron partially occupies three p orbitals, adding a penalty of $\frac{1}{3}U$ to the energy. In the bottom example, one electron fully occupies a p orbital and no energetic penalty is applied. 43

2.3 A 3×3×3 expansion of the a simulation cell (red cube) representing the periodic boundary conditions for a quantum–chemical calculation. . . . 44

2.4 A representative comparison between the pseudopotential, V_{pseudo}, and its resulting pseudowavefunction, Ψ_{pseudo}, (solid red lines) and the all–electron potential, $V_{all-electron}$, and wavefunctions, $\Psi_{all-electron}$ (dashed blue lines). The cut–off radius r_c (black dashed line) is the radius beyond with the pseudo– and all–electron wavefunctions will match each other. 46

2.5 A representation of a band structure within the first Brillouin–zone. The area highlighted in green represents filled states and the blue line represents the Fermi level (E_{Fermi}). 47

2.6 A workflow diagram demonstrating a typical DFT self–consistent calculation. 49

3.1 A flow chart demonstrating the structural optimisation and convergence procedure. 59

3.2 The Brillouin Zone for the $Fm\bar{3}m$ space group (from Bradley and Cracknell[1]). Γ = (0,0,0), X = (0, $\frac{1}{2}$, 0), W = ($\frac{1}{2}$, $\frac{1}{2}$, 0), L = ($\frac{1}{4}$, $\frac{1}{4}$, $\frac{1}{4}$). 60

3.3 A model transition level diagram for a representative material under (a) cation–rich/anion–poor conditions and (b) cation–poor/anion–rich. n–type defects are described by the colour red lines whereas the p–types are denoted by green. The solid circles represent the transition levels ($\epsilon_D(q/q')$). The dashed line shows the Fermi pinning energy. 67

3.4 An example of an MSD for a theoretical oxide material, AO. The red lines show the MSD of the cations while the green lines indicate the MSD of the O anions. 68

3.5 An example of an RDF for a theoretical oxide material, AO. The green line shows the plot of the RDF between A and O. 70

4.1 The variation of the electron addition energy , $E(N+1) - E(N)$ (red line, red circles), and the hole state eigenvalue (relative to the VBM), e_i (blue line, blue squares) of the +1 charge state of CeO_2, as a function of $U\{O_{2p}\}$. For all calculations $U\{Ce_{4f}\}$=5.0 eV. 74

4.2 The band structure and PEDOS of pure CeO_2 for (a) $U_{Ce,O}$={5.0, 0.0} eV and (b) $U_{Ce,O}$={5.0, 5.5} eV. The VBM is set to 0 eV. The blue lines represent Ce $5d$ states, the green lines Ce $4f$ states and the red lines O $2p$ states. All other states are shown in grey. 76

4.3 The structure with spin-density plot when (a) $U_{Ce,O}$={5.0, 0.0} eV and (b) $U_{Ce,O}$={5.0, 5.5} eV and the density of states of an O vacancy in CeO_2 with (c) $U_{Ce,O}$={5.0, 0.0} eV and (d) $U_{Ce,O}$={5.0, 5.5} eV. Ce atoms are represented by white spheres, O atoms are represented by red spheres and the position of the vacancy is represented by the light green sphere. The isosurface is shown in blue and is set to 0.05 e/Å^3. For the EDOS, the Ce 4*f* and O 2*p* states are represented by the green and red lines respectively. All other states are shown in grey. 78

4.4 The full simulation cell when (a) $U_{Ce,O}$={5.0, 0.0} eV and (b) ($U_{Ce,O}$={5.0, 5.5} eV) and the local structure of a Ce interstitial with a partial charge–density plot of the defect peaks for (c) $U_{Ce,O}$={5.0, 0.0} eV and (d) $U_{Ce,O}$={5.0, 5.5} eV and the density of states of a Ce interstitial in CeO_2 when (e) $U_{Ce,O}$={5.0, 0.0} eV and (f) $U_{Ce,O}$={5.0, 5.5} eV. The Ce interstitial is represented by the black sphere and the blue isosurface represents the spin-up electrons and the green isosurface represents the spin-down electrons. The isosurfaces are set to 0.05 e/Å^3. 80

4.5 The local structure around a Ce vacancy in CeO_2 when (a) $U_{Ce,O}$={5.0, 0.0} eV and (b) $U_{Ce,O}$={5.0, 5.5} eV and the density of states for a cerium vacancy with (c) $U_{Ce,O}$={5.0, 0.0} eV and (d) $U_{Ce,O}$={5.0, 5.5} eV. The position of the Ce vacancy is represented by the orange sphere. The isosurfaces are set to 0.05 e/Å^3. In the EDOS, the Ce 4*f* states are the green lines and the O 2*p* states are the red lines. All other states are represented by the grey lines. 81

4.6 The structure when (a) $U_{Ce,O}$={5.0, 0.0} eV and (b) $U_{Ce,O}$={5.0, 5.5} eV and the density of states with $U_{Ce,O}$={5.0, 0.0} eV and $U_{Ce,O}$={5.0, 5.5} eV of a peroxide ion in CeO_2. The peroxide ion is represented by the dark green spheres. In the density of states the Ce $4f$ states are shown in green and the O $2p$ for lattice O ions in red. The purple lines represent the O $2p$ states associated with the peroxide ion and have been magnified by $\times 5$ to aid clarity. 83

4.7 The (a) structure with partial charge-density of the defect peaks and (b) density of states of an anion Frenkel defect in CeO_2 when $U_{Ce,O}$={5.0, 5.5} eV. The O vacancy is represented by the light green sphere and the O interstitial is represented by the purple sphere. The isosurface is set to 0.05 e/Å^3. The green lines in the EDOS show the Ce $4f$ states while the red lines are the O $2p$ states. 85

4.8 The (a) structure and (b) density of states of a Schottky defect in CeO_2 when $U_{Ce,O}$={5.0, 5.5} eV. The Ce vacancy is represented by the orange sphere and the O vacancies are represented by the light green spheres. The Ce $4f$ states and the O $2p$ states are represented by the green an red line respectively in the EDOS. 86

4.9 The temperature dependence of concentration of intrinsic defects in CeO_2 at O partial pressures of (a) $P = 10^{-10}$ atm and (b) $P = 0.2$ atm. 88

5.1 Starting configurations for doped CeO_2 with a CCV placed (a) nearest-neighbour to the dopants (NN–CCV), (b) next nearest-neighbour to the dopants (NNN–CCV), (c) nearest–neighbour to one of the dopants (NN–1–CCV) and (d) far away from the dopants (far–CCV). Ce, O and dopant ions are shown in white, red and brown respectively. The position of the CCV is denoted by the yellow sphere. 96

5.2 Lowest energy structure for Al and Ga-doped CeO_2. The dopant cations are represented by the grey spheres. 99

5.3 Lowest energy structure for Sc, Sb, In, Tl, Lu, Tm, Er, Ho, Y, Dy, Gd, Eu and Bi-doped CeO_2. The dopant cations are represented by the purple spheres. 100

5.4 Lowest energy structure for Nd, Pr and La-doped CeO_2. The dopant cations are represented by the blue spheres. 101

5.5 The charge density around the (a) Y(III) and (b) Bi(III) cations and CCV in doped CeO_2. The charge density plot ranges from 0.0 (blue) to 0.4 (red)e/Å^2. 102

5.6 The electronic density of states for α–Bi_2O_3. The blue lines represent Bi 6s states, the orange lines Bi 6p states and the red lines O 2p states. All other states are shown in grey. The top of the valence band has been is aligned to 0 eV. 103

5.7 The electronic density of states for Bi–doped CeO_2. The blue lines represent Bi 6s states, the orange lines Bi 6p states, the green lines Ce 4f states and the red lines O 2p states. The height of the Bi states have been magnified $\times$80 for clarity. The top of the valence band has been is aligned to 0 eV. 104

5.8 The positions tested for an intrinsic vacancy in doped CeO_2. The positions are (a) vacancy near dopants with a NN-CCV, (b) vacancy far from dopants with a NN-CCV, (c) vacancy near dopants with a NNN-CCV, (d) vacancy far from dopants with a NNN-CCV and (e) an alternate position (Al and Ga–doped CeO_2 only). The position of the intrinsic vacancy is represented by the green sphere. The isosurfaces are shown in blue and are set to 0.05 e/Å^3. 106

5.9 The E_{red} values for doped CeO_2. The blue and red lines represent vacancies formed close to and far from the dopant cations respectively. As the radii of Al(III) and Ga(III) are significantly smaller than the other dopants studied, the results for these two dopants are shown in an inset on the graph, with additional results for removing an under–coordinated O ion (light blue). The green line represents the E_{red} for pure CeO_2 and the black dashed line indicates the ionic radius of Ce(IV). 107

6.1 The starting structures for the *ab initio* MD simulations with a (a) clustered and (b) dispersed arrangement of the dopant cations. The dopants (In(III), Y(III), Bi(III) and La(III)) are represented by the brown spheres, the Ce(IV) ions by the white spheres and the O ions by the red spheres. The yellow spheres indicate the position of the CCVs. 116

6.2 The MSD plot of Y–dispersed at (a) 1073 K and (b) 3073 K. The brown, yellow and red lines represent the movement of the dopant cations, the Ce(IV) cations and the O anions respectively. 117

6.3 The MSD plot of O anions for [I] clustered and [II] dispersed arrangements of (a) In(III), (b) Y(III), (c) Bi(III) and (d) La(III) dopants in CeO_2. The simulations were carried out at 2073 K (red lines), 2323 K (blue lines) and 2573 K (green lines). The black lines show the slopes of the MSD plots. 119

6.4 The structure of the La–clustered system at 2073 K at 15 ps. The Ce(IV), La(III) and O ions are represented by the white, blue and red spheres respectively. The position of the CCVs are shown by the yellow spheres. 120

6.5 The (a) full simulation cell of the In–clustered system at 2573 K with close up views of the structure around (b) the CCV and (c) a vacancy caused by the formation of a Frenkel defect. The picture was taken at 17.50 ps. The In(III) ions are represented by the light purple spheres. The position of the CCVs are shown by the yellow spheres, and the green sphere represents a vacancy formed as a result of a Frenkel defect. The yellow and green boxes designate which section of the structure the close up views are showing. The motion of specific O ions are represented by the arrows. 122

6.6 The (a) full simulation cell of the Bi–clustered system at 2573 K with close up views of the structure around (b) the CCV and (c) a vacancy caused by the formation of a Frenkel defect. The picture was taken at 22.75 ps. The Bi(III) ions are represented by the dark purple spheres. The position of the CCVs are shown by the yellow spheres, and the green sphere represents a vacancy formed as a result of a Frenkel defect. The yellow and green boxes designate which section of the structure the close up views are showing. The motion of specific O ions are represented by the arrows. 123

6.7 The plot of $\ln(\sigma T)$ versus $\frac{1000}{T}$ for the (a) clustered and (b) dispersed arrangement of dopants. The In–doped systems are represented by the red circles/lines, the Y–doped systems by the yellow circles/lines, the Bi–doped systems by the purple circles/lines and the La–doped systems by the blue circles/lines. 125

6.8 The RDF plot of Ce–O (black lines) and La–O (blue lines) for the La–clustered system at (a) 2073 K, (b) 2323 K and (c) 2573 K. 126

6.9 The RDF plots for [I] clustered and [II] dispersed dopant configurations in (a) In(III), (b) Y(III), (c) Bi(III) and (d) La(III) doped CeO_2 at 2323 K. The Ce–O distances are represented by black lines and the M–O distances are represented by the red (In(III)), yellow (Y(III)), purple (Bi(III)) and blue (La(III)) lines. 128

6.10 The local structure around an Y(III) ion (orange sphere) in the Y–dispersed system at 2573 K. The images is taken at a time of 13.80 ps. . 130

7.1 Formation energies for intrinsic defects under O–poor conditions (left panel) and O–rich (right panel) conditions. The coloured regions at the bottom indicate which defect is energetically preferred. 140

7.2 The structure of trivallently doped CeO_2 with electronic charge compensation. Ce ions are represented by the white spheres, O ions by the red spheres and the dopant ions by the brown sphere. The isosurface is shown in light blue and set to 0.05 e/Å^3. 142

7.3 The converged structures of [M'_{Ce}–$V_O^{\bullet\bullet}$–M'_{Ce}] defect clusters in CeO_2 with the CCV (a) nearest neighbour to one dopant (grey spheres; Al, Ga), (b) nearest neighbour to both dopants (purple spheres; Sc, Tl, Y, In) and (c) next–nearest neighbour to both dopants (dark blue sphere, La). The position of the CCV is represented by the yellow sphere. 143

7.4 Formation energies for for trivalent dopants in CeO_2 under O-poor conditions (left panel) and O-rich (right panel) conditions. The full lines indicate the [M'_{Ce}+$O_O^{\bullet}$] defects, with the dashed lines indicating the [M'_{Ce}–$V_O^{\bullet\bullet}$–M'_{Ce}] formation energies. The coloured regions at the bottom indicate which defect is energetically preferred. 143

7.5 The fit of energy/volume data (circles) to the Murnaghan equation of state (solid lines) for La– and Y–doped CeO_2 (black and yellow respectively). The lattice constant is given relative to the lattice constant of CeO_2. The dashed lines indicated the equilibrium lattice volume. . . . 145

8.1 The variation of the surface energies a function of slab thickness. The (100), (110) and the (111) surfaces are represented by the blue, red and green lines respectively. The black circle indicate the slab size that was employed in subsequent calculations. 152

8.2 Plan view of the pure CeO_2 surfaces that were employed in the calculations, (a) (2×2) expansion of (100), (b) (2×3) expansion of (110) and (c) a (4×4) expansion of (111). The Ce cations and O anions are represented by the white and red spheres respectively. 153

8.3 The (a) (100), (b) (110) and (c) (111) surfaces of CeO_2. The vacancies positions that were tested are denoted by the letter V. The Ce ions have been labelled to indicate where the excess electrons associated with vacancy creation localise. Subscript 's' denotes a sub–surface site. . . . 154

8.4 The low index surfaces of CeO_2 displaying the structures and spin density plots of the O vacancy defect on the (a) (100), (b) (110) and (c) (111) surfaces and the peroxide defect on the (d) (100), (e) (110) and (f) (111) surfaces. The Ce and O ions are represented by the white and red spheres respectively. The position of the vacancy is denoted by the letter V. The peroxide ion is represented by the dark green spheres. The isosurfaces, shown in blue, show the spin electrons on the Ce(III) ions and are set to $0.05\,e/Å^3$ 160

8.5 The low index surfaces of La–doped CeO_2 with spin density plots displaying charge compensation through the formation of (a) an O hole (one La(III)), (b) two O holes (two La(III)), (c) a vacancy, an O hole and a Ce(III) ion, (d) a CCV and (e) a peroxide ion on the [I] (100), [II] (110) and [III] (111) surfaces. Where applicable the position of the O vacancy is denoted by the letter V. The La(III) ions and the peroxide ions are represented by the dark blue and green spheres respectively. The isosurfaces, showing the excess spin of the O holes and Ce(III) ions, are shown in light blue and are set to $0.05\,e/Å^3$. 164

8.6 The low index surfaces of CeO_2 displaying the structures and spin density plots of the O vacancy defect on the (a) (100), (b) (110) and (c) (111) surfaces. The Ce and O ions are represented by the white and red spheres respectively. The position of the vacancy is denoted by the letter V. The isosurfaces, shown in blue, show the spin electrons on the Ce(III) ions and are set to $0.05\,e/Å^3$ 167

8.7 The position and formation energy for O vacancies on the La–doped (100) surface of CeO_2 that has been charge compensated with a peroxide ion. The position of the reduction vacancy is denoted by the letter R. The formation energies are given relative the vacancy formation on the pure (100) surface, 0.75 eV. The isosurfaces, shown in light blue, represent the spin density of the excess electrons on the Ce(III) ions and are set to $0.05\,e/Å^3$ 168

8.8 The positions, with spin density plots and formation energy for O vacancies on the La–doped (110) surface of CeO_2 charge compensated with a peroxide ion. The position of the reduction vacancy is represented by the letter R. The formation energies are given relative the vacancy formation on the pure (110) surface, 0.52 eV. The spin of the electrons on the Ce(III) ions are shown with the isosurfaces, coloured light blue, and are set to $0.05\,e/Å^3$ 170

8.9 The position and formation energy for O vacancies on the La–doped (100) surface of CeO_2 where the charge is compensated through a vacancy. The letter V and R show the position of the CCV and the reduction vacancy respectively. The formation energies are given relative the vacancy formation on the pure (100) surface, 0.75 eV. The isosurfaces, representing plots of the spin density of the Ce(III) ions, are shown in light blue and are set to $0.05\,e/Å^3$ 172

8.10 The position with spin density plots and formation energy for O vacancies on the (110) surface of CeO_2 with the O vacancy compensation scheme. V represents the site of the CCV, and R the site of the reduction vacancy. The formation energies are given relative the vacancy formation on the pure (110) surface, 0.52 eV. The isosurfaces, representing the excess spin on the Ce(III) ions, are shown in light blue and are set to 0.05 e/Å^3 174

8.11 The position and formation energy for O vacancies on the (111) surface of CeO_2 with the vacancy charge compensation mechanism. The formation energies are given relative the vacancy formation on the pure (111) surface, 1.04 eV. The letter V denotes the position of the CCV, and R the site of the reduction vacancy. Plots of the spin density of the Ce(III) ions are represented by the light blue isosurfaces and are set to 0.05 e/Å^3 175

8.12 The structures and reduction peroxide/vacancy reduction scheme when the La(III) are positioned according to the lowest energy structure of the (a) vacancy compensation and (b) peroxide compensation for the [I] (100), [II] (110) and [III] (111) surfaces. The letter V shows the position of the CCV 180

List of Tables

3.1 The calculated elemental energies, E_i, for a range of species investigated in this thesis. Two values are given for O_2(g) due to the two values of U that were applied to the O $2p$ states. The first is for U=0.0 eV and the second is for U=5.5 eV. All values are given in eV. 62

4.1 The chemical potential dependent free energies for the formation of the defect clusters, for $U_{Ce,O}$={5.0, 0.0} eV and $U_{Ce,O}$={5.0, 5.5} eV. N.B. O–poor also implies Ce–rich and vice versa. All energies are given in eV. 87

5.1 The values of E_{dop} for trivalent dopants in CeO_2 for different locations of the CCV and the E_{ass} between the dopant and the CCV. The most stable structure (i.e. lowest E_{dop} energy) is highlight in blue. All energies are given in eV. 97

5.2 A summary of the ionic radii, E_{dop}, E_{ass} and E_{red} for the trivalent dopants studied in this report. The ionic radii are given in Å and energies are given in eV. The values of E_{red} given are relative to the E_{red} of pure CeO_2, 2.23 eV. The blue shading indicates the properties which are best suited for SOFC applications according to the previously decided criteria. 111

6.1 The volume of the simulation cells for doped CeO_2. 116

6.2 The diffusion coefficients, D for doped CeO_2. All values for the diffusion coefficients are given in 10^{-6} cm^2/s, and activation energies are given in eV. 120

6.3 The calculated activation energies, E_a, for ionic diffusion in doped CeO_2. 126

6.4 The M–O bond lengths (M=In(III), Y(III), Bi(III), La(III)) and dopant cation coordination numbers for the doped CeO_2 systems. 127

6.5 The coordination numbers of the cations in doped CeO_2. 130

6.6 The ionic conductivities, σ in doped CeO_2. All values are given in S/cm. 133

6.7 The projected ionic conductivities, σ, with the activation energies, E_a, of doped CeO_2 at 1073 K. 134

7.1 The chemical potentials for M(III) cations (M=Al, Ga, Sc, In, Tl, Y and La). All energies are given in eV. 139

7.2 The stability of $[M_{Ce}–V_O–M_{Ce}]$ defect clusters compared to $[M_{Ce}–O_O^{\bullet}]$. All values are given in eV. 144

7.3 The binding energies for $[M_{Ce'}–V_O^{\bullet\bullet}–M_{Ce'}]$ defect clusters. All values are given in eV. 144

8.1 A comparison of the surface energies for the low index surfaces of CeO_2 obtained in this report with literature values. All values are given in J/m^2. 153

8.2 The reduction energy for a series of vacancy localisations on the (100) surface. The letters denote the relative position of each Ce(III) ion to the vacancy, i.e. nearest neighbour (NN), next–nearest neighbour (NNN) etc. All energies are given in eV. 155

8.3 The reduction energy for a series of vacancy localisations on the (110) surface. The letters denote the relative position of each Ce(III) ion to the vacancy, i.e. nearest neighbour (NN), next–nearest neighbour (NNN) etc. All energies are given in eV. 157

8.4 The reduction energies for a series of vacancy localisations on the (111) surface. The letters denote the relative position of each Ce(III) ion to the vacancy, i.e. nearest neighbour (NN), next–nearest neighbour (NNN) etc. All energies are given in eV. 158

8.5 The chemical potential dependent defect formation energies for the low index surfaces of CeO_2. All energies are given in eV. 159

8.6 The chemical potential dependent doping energies for the different charge compensation schemes on the low index surfaces of CeO_2. The energies for the $[La'_{Ce}+O^{\bullet}_{O}]$ compensation scheme have all been multiplied by two, so that the number of La(III) ions present is consistent throughout. All energies are given in eV. 165

8.7 The shift in core level energies for O holes and peroxide ions on the La–doped low index surfaces of CeO_2. All energies are given in eV. . . 166

8.8 The distance between important defect features and the chemical potential dependent reduction for the La–doped low index surfaces of CeO_2 that have been charge compensated with a peroxide ion. All distances are given in Å and all energies are given in eV. 171

8.9 The distance between important defect features and the chemical potential dependent reduction energy for the La–doped low index surfaces of CeO_2 with the vacancy compensation mechanism. All distances are given in Å and all energies are given in eV. 177

8.10 The chemical potential dependent values of the reduction energy of the pure surfaces and the La–doped surfaces with the vacancy and peroxide charge compensation scheme. Structure (a) refers to the configuration of La(III) ions that matches the lowest vacancy compensation scheme, while structure (b) represents the the La(III) configuration that matches the lowest energy peroxide compensation mechanism for that surface. All values are given in eV. 179

8.11 The energies for reduction and for the concurrent conversion of CO, NO_2 and NO on the pure surfaces and the La–doped surfaces with the vacancy and peroxide compensation mechanisms. The reduction of the La–doped (vacancy) surfaces are based on the lowest energy reduction vacancy. Two different structures are tested for the La–doped (100) and (111) surface with the peroxide compensation mechanism, where (a) the position of the La(III) ions match the lowest energy vacancy compensation structure and (b) the position of the La(III) ions match the lowest energy peroxide compensation structure. Since the position of the La(III) ions is the same for both defects, only one energy is given for the (110) surface. All energies are given in eV. 182

Chapter 1

Introduction

1.1 Climate Change and the Environment

The past decades of environmental research have all pointed to one conclusion: the climate is undergoing severe and drastic changes.[2] Evidence suggests that the last half of the 20th century was warmer than any other 50 year period within the past 500 years, and the average temperature in the Northern Hemisphere during this period was probably higher than any other time in the past 1,300 years.[3] The average surface temperature has increased by 0.7°C,[4] while the world's oceans have experienced a mean warming of 0.06°C.[5] Although it is expected for some fluctuations to appear in global temperatures over long time periods,[6] natural factors can no longer account for these rapid changes. The conclusion that must be drawn from this is that global warming is a man–made phenomenon.[7]

1.1.1 Greenhouse Gases and CO_2

Life on Earth relies on the presence of greenhouse gases in the atmosphere: energy from the sun strikes the planet's surface and radiates back into space; greenhouse gases help retain sufficient heat to maintain an average temperature of around 15°C. These gases, which include water vapour, methane, carbon dioxide, carbon monoxide, nitrogen dioxide, nitric oxide, and ozone, have affected Earth's climate, and in

turn organic life, which adapted over millions of years to live comfortably under ambient conditions. Despite the importance of these gases for maintaining a habitable climate, within the past 150 years human industry has increased the concentration of atmospheric greenhouse gases. Perhaps the most significant greenhouse gas for climate change is CO_2. Although other pollutants are potentially more damaging to the environment, for example, methane, CH_4, is roughly twenty times more damaging than similar concentrations of CO_2, the higher abundance of the latter makes it a primary concern for climate change. Historically, concentrations of CO_2 have fluctuated between $\sim$ 170 and 300 ppm for the last 2.1 million years, and in the last thousand years, up to the onset of the industrial revolution, levels were between $\sim$ 276 and 284 ppm. During the middle of the 19th century, however, the use of fossil fuels at an industrial scale became ubiquitous, forcing the level of atmospheric CO_2 to drastically increase and, in 2009, the concentration increased to roughly 385 ppm, which corresponds to about 818 billion metric tons of CO_2 in the atmosphere.[8]

The higher CO_2 concentrations, with the subsequent climate change, has had both a drastic, and detrimental impact on the environment, with both natural and managed ecosystems under threat. The changes in temperature and precipitation, along with associated loss of habitat, impinge heavily on animal populations all over the world. For example, it was observed that although milder winters reduced mortality rates among sheep and feral goats in Norway, this led to increased competition for food which resulted in a precipitous decline in population the following spring.[9] Agricultural production is under threat as well due to increasing scarcity of water, insects, which thrive under the higher temperatures, and the spread of plant diseases.[10] The loss of a stable system of food production would have disastrous consequences for the global population, from famine to economic collapse, particularly for developing nations whose economy is highly dependent on agriculture. The loss of arable land also forces populations to migrate, which has been linked with the spread of infectious diseases.[11] Furthermore, higher ambient temperatures promote the reproduction of bacteria, and increasing rates of infection.[12]

The section of the lower stratosphere referred to as the Ozone layer plays a vital function in preserving life on Earth. The comparatively high concentrations of O_3 found in this layer help prevent biologically harmful UV radiation from reaching the surface of the planet. The depletion of the Ozone layer due to chloro–fluoro–carbons (CFCs) is a well documented process. Levels of CFCs have actually been declining in recent years[13] but unfortunately the integrity of the O–zone layers remains under threat. Due to radiative cooling, higher levels of greenhouse gases actually cool the stratosphere, which promotes certain O–zone depleting processes,[14] thus hindering the recovery of the O–zone layer despite lower concentrations of CFCs. The world's seas, oceans and coastal regions are also threatened; the melting of the ice caps is causing a rises in sea levels, making many areas uninhabitable and high concentrations of CO_2 are actually acidifying oceans which is disastrous for marine ecology.[15]

1.2 Reduction of Green House Gases

All of the examples in the previous section point to one conclusion; that the levels of greenhouse gases must be drastically reduced as soon as possible to prevent catastrophic and irreversible damage to the climate. Due to its significant contribution to climate change, the reduction of CO_2 is a primary concern for the protection of the environment. In this section, the various methods reducing the levels of atmospheric pollutants shall be discussed.

1.2.1 CO_2 Sequestration

One method for dealing with excess CO_2 is to capture and store it, which is referred to as carbon sequestration. There are a wide variety of methods for carbon sequestration, including biological, chemical or physical processes. Examples of biological process include: reforestation, where atmospheric CO_2 is converted to biomass;[16] mixing ocean layers to trigger algal blooms;[17] and encouraging the growth of phytoplankton through iron fertilisation.[18] However, there are certain drawbacks for these techniques. Trees

and algae act as carbon stores when they are alive, but when they die, or are consumed, they may become carbon exporters. Therefore, they are used as temporary storage or as a way of better controlling the release of CO_2. For iron fertilisation, the excessive growth of phytoplankton could seriously affect marine ecosystems and therefore its use should be carefully considered. Chemical CO_2 sequestration generally refers to the process of converting CO_2 into a stable, solid carbonate. Various "chemical scrubbers" are prevalent in industrial processes to reduce the amount of CO_2 emissions.[19,20] Physical CO_2 sequestration often refers to the processes that occur to CO_2 that has been captured through chemical or biological processes. For example, CO_2 that has been converted to biomass is sometimes then buried underground, mimicking the process which originally created fossils fuels.

1.2.2 Catalysis

An alternative method for dealing with greenhouse gases is to employ catalytic processes to convert the pollutants into environmentally benign species. For example, volatile organic compounds (VOCs) are a common byproduct of many industrial processes. Two methods to reduce emissions of VOCs are by eliminating solvents from the industrial process or thermal incineration. The former, however, is not always feasible and the latter requires high operating temperatures and often produces noxious byproducts such as NO_x (x=1,2). By employing catalysts, VOC combustion can be achieved under milder conditions while simultaneously avoiding the production of NO_x.[21] Althought the combustion of VOCs does result in the production of CO_2, the release of VOCs into the atmosphere would be far more devastating. Silylium–carborane catalysts have been employed to de–fluorinate perfluoralkyls at ambient temperature, removing a highly destructive CFC from the industrial waste streams.[22] Other harmful by–products, such as NO and N_2O, can be converted into stable and environmentally benign N_2 with V_2O_5 catalysts.[23] It also possible to catalytically recycle emissions, by converting CO_2 back into fuels such as methane and methanol.[24,25] On a smaller scale, three–way–catalysts (TWCs) are an ubiquitous, and mandatory, feature of modern

automobiles.[26] These TWCs, also known as catalytic converters, reduce the levels of automotive emission by simultaneously converting CO and NO_x to CO_2 and N_2.

Although catalysts are undeniably valuable assets in the fight against climate change, several problems persist. For example, most catalyst can only efficiently function at lower temperatures and when there is only a medium level of throughput, which would rule them out from certain industrial processes. Furthermore, while the products from these catalytic reactions are less harmful than the reactants, they are not necessarily entirely benign, e.g. although a catalytic converter will reduce levels of toxic CO, one of the products will be CO_2 which remains, as discussed previously, detrimental to the environment.

1.3 Energy Production in the Green Age

Further to the extensive damage that the use of fossil fuels has inflicted on the environment, there is also the fact that petroleum is a finite resource. Some reports have even claimed that peak oil (the point at which global oil production begins to decline) could occur as soon as 2015.[27] As the double threat of peak oil and climate change loom closer, it is vital to develop new methods of renewable and environmentally friendly energy production. Although a great deal of progress still needs to be made, the utilisation of renewable sources of energy has increased drastically in recent times, and, as of 2010, energy production from renewable resources stood at roughly 16 % of global energy production, and comprised almost a fifth of electricity production.[28]

1.3.1 Wind Energy

Wind farms produce renewable energy from wind turbines that are erected, either at onshore or offshore locations, to harness wind energy, converting it to electricity. Wind farms have been adopted all over the world, and in Ireland 192 wind farms produce 2232.31 MW of energy, approximately 15.5% of Ireland's electricity demand as of 2012. [29] The major advantages of wind power is that once the turbines are constructed

they require no fuel and emit no pollution. The cost of manufacture, transport and contruction of a wind farm is recouped in a mere few months, whereupon the turbines will continue to function for years with little maintainence required. However, there are disadvantages to wind power. The most obvious is, of course, its dependence on the wind: variable weather conditions mean that energy production can stall when there's no wind and suddenly surge when it picks up again. Therefore, careful consideration must be taken so that alternate energy sources are available when wind levels are low and that the grid is capable of handling sudden surges in energy production whenever the wind rises. Most of the other problems with wind farms tend to be personal or anecdotal in nature, e.g. people have objected to wind farms on aesthetic grounds or turbines have been linked with the deaths of bats and birds. Wind turbelence caused by turbine blades have also been said to affect local air temperatures, which could have an impact on nearby crop production.[30]

1.3.2 Hydroelectric Energy

The world's oceans and rivers are also abundant sources of renewable energy, with hydroelectricity being the most widely used form of renewable energy.[31] The basic principles of hydropower have existed for hundreds of years, whereby the potential energy of water (from tides, the flow of a river or from a stored reservoir) is converted into electric energy. Water was perhpas the first power source, with water wheels being powered by the flow of rivers. Modern hydroelectic dams are extraordinary feats of engineering, where vast reservoirs power massive arrays of turbines, producing thousand of mega–watts of energy. For example, the Three Gorges Dam in China, possibly the largest power station ever built, commands a reservoir with a capacity of $39.3\,\mathrm{km}^3$ and contains 37 massive turbines for a total electrical generating capacity of 22.5 GW, and currently obtains an annual output of 80 TWh. A major advantage of hydroelectricity is that it produces no emissions, apart from those associated with construction of the dam, but there are further benefits to these types of power plants. Hydroelectric dams have highly flexible output levels and are able to quickly alter energy production based

on current demand. The low running costs, coupled with long operating lifetime, also ensure the energy produced from hydroelectricity is incredibly cheap. Despite these positives, there are certain disadvantages associated with hydroelectricity. The major problems arise from the construction of the large reservoirs necessary for the operation of the hydroelectric dam, which submerges extensive tracts of land upriver. This causes the destruction of vast areas of habitatable land, disrupting local ecosystems and forcing the relocations of thousands, if not millions, of people. Furthermore, if the dam itself were to fail then significant amounts of damage would be caused to the areas downriver.

1.3.3 Solar Energy

Perhaps the most abundant source of renewable energy is the one which life on Earth has depended on since it emerged; the Sun. There are two main processes for harnessing the Sun's energy for the purpose of energy production, concentrated solar power (CSP) and photovoltaics.

CSP is an indirect method of energy production: vast arrays of mirrors focus the suns energy to a point where it drives a heat engine, such as steam turbine. Although a relatively new type of power plant in the field of renewable energy, with only 1.9 GW of potential output installed world wide, as of March 2012,[32] interest is growing and many new CSP plants are scheduled to open soon.

For photovoltaic devices, the Sun's energy is converted directly into electricity through the photovoltaic effect. This method of energy production is far more prevalent than CSP, with solar panels fast becoming ubiquitous in everyday life. One of the positive aspects of photovoltaics is that they can be applied to a wide range of applications, from tiny panels on a calculator to power plants with vast arrays of panels, producing megawatts of energy. Furthermore, the cost of solar panels has been steadily decreasing over the years and has reached the point were they are now affordable to private households for personal energy production. The major advantage of solar power is that its source, the Sun, provides vast amounts of energy, up to $1000\,\mathrm{W/m^2}$ at the

equator, and is expected to continue doing so for billions of years to come.

Once the CSP station or photovoltaic unit has been constructed, it will produce no more emmissions and require very little maintenence over their life cycle. However, the problem with this technology is that different areas of the Earth receive different amounts of solar energy, and, of course, none at night, which limits the area where efficient of solar power plants could be constructed. Additionally, the amount of solar radiation falling on a certain area will vary according with time of day, year and also upon the weather. Consequently, solar power output is more variable than other forms of renewable energy. Furthermore, although the price is falling, the cost of manufacture still remains high. In addition, some newer solar panels are made from rare and toxic materials, such as cadmium telluride, further raising the cost, and creating issues with the disposal of solar panels at the end of their life time. A final point is that although greats strides have been taken in this area, photovoltaics remain incredibly inefficient at converting solar energy, with the average efficiency for commercially available cells only being in the range of 14–19 %.

While the various methods of energy production mentioned here are extremely important and widely employed, there is one major consideration that has yet to be discussed. Once these environmentally friendly plants start producing energy, what then? Unless the energy is used immediately, it runs the possibility of going to waste. Furthermore, for smaller scale and mobile applications, a personal power plant is not a feasible option. Therefore, methods must be employed to convert the electricity generated into other forms, such as kinetic or chemical energy, allowing the energy generated to be utilised wherever and whenever it is needed.

1.4 Energy Storage

One method of energy storage has been previously mentioned; the reservoirs for hydro-electric dams are in fact huge stores of potential energy. Some dams are also designed so that excess energy produced can power pumps that returns water from the bottom

of the dam to the reservoir, thus converting electricity back to potential energy. An alternate form of mechanical energy storage is compressed air. Excess off–peak energy is used to compress and store air, which is then released at peak times to power turbines. Additionally, the compressed air is readily transportable in high pressure gas cylinders, increasing the range of applications available. For example, compressed air engines are becoming feasible,[33] and major automobile companies are actively researching hybrid fuel/compressed air cars.

Another form of mechanical storage are flywheels, which use electrical or kinetic energy to spin the flywheel, thus saving it as rotational energy. There are several drawbacks to flywheels, mainly that they will lose energy through friction, either on the bearings or from wind resistance, meaning they are not efficient for long–term storage. Additionally, storing larger amounts of energy necessitates making the flywheel larger and/or increasing the speed it spins at. However, a larger flywheel would be bulky, limiting its application, e.g. a flywheel in a car would negate any fuel savings through its increased weight, and there are limits to how fast the flywheel can be spun before it breaks apart. Recent developments in materials, such as carbon fibre, mean that flywheels may soon become light and strong enough for smaller scale operations. Indeed, the car company Volvo have recently tested flywheels for their next generation of automobiles, where kinetic energy is transferred to the flywheel during braking, and have demonstrated a large increase in fuel efficiency.[34]

A more direct method of storing electrical energy is the use of capacitors, which store electric energy in an electrostatic field. Capacitors are used in energy production to help reduce fluctuations in the output, but are not suitable for large scale storage and instead they are more appropriate for smaller applications. For example, capacitors, in conjunction with a solar panel, can provide twenty four hour power to public amenities, such as street lights, parking meters and compactors in dustbins.

One of the most commonly encountered forms of energy storage is the battery, which stores electrical energy as chemical energy. While undoubtedly useful, and ubiquitous in everyday life, there are many problems with batteries. Batteries are often constructed

from highly toxic chemicals, such as lead and cadmium, which means that serious consideration must be taken for their disposal. Even rechargeable batteries have a limited life span and must eventually be disposed of. Batteries are also expensive, and their large weight and volume limits their applications. Furthermore, the charging rate of batteries limits their applications. The battery in the Tesla Model S, one of the first commercially available electric cars, requires, at minimum, twenty minutes to charge sufficiently.[35] Compared to a car powered by a traditional internal combustion engine, which can be refilled in minutes, this a large investment of time for the average consumer.

1.4.1 Chemical Storage as Fuels

Chemical fuels are the most ubiquitous form of energy storage. Fossil fuels, such as coal, natural gas and petroleum are all formed from organic matter that has been subjected to millennia of pressure and heat underground. They can almost be thought of as solar energy from thousands of years ago, stored in chemical bonds by ancient flora and fauna. As previously stated, fossil fuels are a finite resource and alternative forms of energy are desperately needed. One possible solution are biofuels, which are crops specifically grown for the purpose of converting them to fuel, such as ethanol or biodiesel. The advantage of biofuels over traditional fossil fuels are that they can be grown from renewable and sustainable sources, produce fewer harmful emission than fossil fuels and, due to the carbon required to produce the biomass in first place, can be considered a carbon neutral process.[36]

The advantages of chemical fuels are that they easily converted into mechanical energy, are easily transportable and have a high energy density per volume. Most power plants still burn fossil fuels, producing steam to power turbines and thus represent the majority of worldwide production of electricity.[37] Furthermore, the comparative stability of chemical fuels means that, despite the advances previously mentioned in battery production, they are currently the only practical energy source for the majority of forms of transportation. Biofuels, despite having some advantages, also have

significant drawbacks as a source of energy, which can be detrimental to both human populations and the environment. For example, the allocation of farmland for biofuels reduces the amount available for food production. A report from the World Bank suggested that the dramatic increase in food prices since 2002 could be a direct result of the increase in biofuel production.[38] Additionally, in order to remain sustainable and carbon neutral, extreme care must be taken in order to maintain the quality of the soils where biofuel crops are grown.[36] For the overall goal of reducing the levels of atmospheric CO_2, it could possibly more effective to just convert the farmland set aside for the production of biofuels into woodland.[39] As an alternative to these hydrocarbon–based fuels, another chemical storage medium exists that avoids many of the problems associated with the former two: hydrogen.

1.4.2 Production and Storage of Hydrogen Fuel

As a form of chemical storage, hydrogen possesses many desirable properties: it produces no emission, beyond water; although not as energy dense per volume as traditional hydrocarbon fuels, hydrogen does have the largest energy density per mass; and it is present on Earth, mainly as H_2O, in such abundance that it is, effectively, infinitely sustainable. Switching from a traditional hydrocarbon fuel economy could potentially solve many of the problems facing the world and its climate, providing a clean and plentiful source of energy. Unfortunately, there are many obstacles to the formation of the hydrogen fuel economy.

Firstly, molecular hydrogen is not present in significant quantities on Earth, however, many natural reservoirs exist, such as water, where hydrogen is bonded to oxygen. The consequence of this is that energy is required to separate the hydrogen, meaning that it is not a primary fuel source, as with fossil fuels, but rather an energy transfer medium. Several methods of hydrogen production exist, including electrolysis of water, steam reformation from hydrocarbons and as a by–product from chemical processes. Therefore, to be a truly green method of energy production, the energy needed to form hydrogen fuel must come from a renewable energy source, such as solar or hydroelectric

power, the burning of carbon neutral biofuels, or by the direct photo–splitting of H_2O.

The second major obstacle for hydrogen fuel is storage. For practical applications, hydrogen must be stored either under high pressure, or even liquefied, in order to provide sufficient energy density per unit volume. However, the mass of a high pressure cylinder serves to reduce the efficiency of a vehicle, and furthermore, due to the small size of hydrogen, it tends to diffuse through the containing material, compromising its structural integrity. This raises additional problems, either from asphyxiation or, due to the high flammability of hydrogen, from the risk of explosion. Alternatively, it is possible to store hydrogen as a hydride, which is subsequently decomposed at the point of use.[40] There are two major considerations that must be taken into account when considering hydrides as a method of storing hydrogen. Firstly, the hydrides must be stored under quite harsh conditions, limiting the ease of transportation. Secondly, at the point of use, the hydride must decompose to release the hydrogen fuel, and the rate of this decomposition is a major limiting step in the utility of this storage method. Another approach is to store hydrogen in solid, porous materials.[41] This process has the advantage that the adsorbed hydrogen molecules do not undergo dissociation or recombination and hence will not suffer from the kinetic limitations of the hydride storage systems. The final hurdle for the hydrogen economy is that the infrastructure is currently not in place for the distribution and exploitation of hydrogen as an energy source. To do so would require a major investment of time and money and a concerted effort from governments world wide to move away from traditional hydrocarbon fuels. Despite all of these drawbacks, the use of hydrogen as fuel is highly desirable and remains an active area of research.

1.5 Fuel Cells

Fuel cells are devices that directly convert chemical energy to electrical energy and heat. There are several distinct advantages of fuel cells as a method of energy production. The lack of a mechanical stage in the production of electricity means that fuels cells are

highly efficient and have minimal noise output. Furthermore, traditional combustion engines have trouble utilising H_2 fuels, whereas fuel cells are readily capable of doing so. There are several different examples of fuel cells, each with their own properties and applications, such as the proton exchange membrane fuel cells, which operate at low temperatures and are generally considered for transport applications, or molten carbonate fuel cells,[42] which operate at higher temperatures and are better suited for stationary power generators.

1.5.1 Solid Oxide Fuel Cells

Another type of fuel cell that operates at higher temperatures, ~1200 K, is the solid oxide fuel cell (SOFC).[43–45] In addition to the advantages common to fuel cells, they are among the most effective, displaying efficiencies of up to 85 %,[43] and they are extremely versatile in terms of the fuel they can use, ranging from hydrogen to traditional carbon–based fuels. This means SOFCs are a viable method of energy production, for both in the long and the short term.

1.5.2 Operation of an SOFC

Figure 1.1 displays a schematic of an SOFC. Typically, several of these cells would be linked together, supported and separated by an interconnect material. The SOFC is constructed so that the air and fuel sides are separated by an impermeable electrolyte material and the casing of the fuel cell itself. Air is injected at one side where it is allowed to flow by the cathode, and molecular oxygen adsorbs to the surface where it is reduced to O^{2-} ions. The cathode should exhibit both electronic and ionic conductivity: the former to provide and distribute electrons for the reduction reaction and the latter to aid in transporting the anions to the electrolyte. The ions are then absorbed by, and subsequently diffuse through, the electrolyte. An ideal electrolyte material should display high ionic conductivity and little to no electronic conductivity, as the latter can short circuit the operation of an SOFC. Additionally, the electrolyte material should be

stable across a range of chemical environments, as the two sides of an SOFC represent reducing and oxidising environments, and a thermal expansion coefficient that matches well with the cathode and anode materials.[46] At the anode, the anions oxidise the fuel, which for the example in Figure 1.1 would be H_2 to H_2O. The anode material should be porous, similar to the cathode, to allow better penetration by the fuel, aiding in its reduction. Most anodes for SOFCs are cermets, i.e. ceramic and metal composites such as Ni metal and YSZ.[47] As with the cathode, the anode should be both an ionic conductor, to transport charged species from the electrolyte, and an electronic conductor to disperse the electric current caused by the oxidation of the fuel. The equations for the reduction and oxidation reactions are shown below:

$$H_2 + O^{2-} \rightarrow H_2O + 2e^-, \tag{1.1}$$

$$\frac{1}{2}O_2 + 2e^- \rightarrow O^{2-}. \tag{1.2}$$

For the oxidation reaction, Equation 1.1, the right hand side shows that the oxidation of H_2 has left behind two excess electrons. This oxidation of H_2 drives the electrical current, which flows through an external circuit, providing electrical energy, before reaching the anode, where they aid in the reduction of O_2 (Equation 1.2). This is why the electrolyte should not be an electronic conductor; electrons should only flow from the cathode to the anode through the external circuit and conduction through the electrolyte would short circuit the operation of the fuel cell.

1.5.3 Current Materials used in SOFCs

Currently, the industry standard components of a fuel cell are: $La_{1-x}Sr_xMnO_3$ (LSM) for the cathode; yttria–stabilised zirconia (YSZ) for the electrolyte; and a cermet material, such as Ni/YSZ, for the anode. $LaMnO_3$ has a perovskite structure and is is an intrinsic p–type conductor, and by replacing a La(III) site with a Sr(II), some of the Mn(III) ions will become Mn(IV) to conserve charge, making LSM a mixed ionic/electronic conductor.[48] The major advantages of LSM is that it has very high electronic conductivity, with conductivities as high as 485 S/cm at 1273 K.[49] The poros-

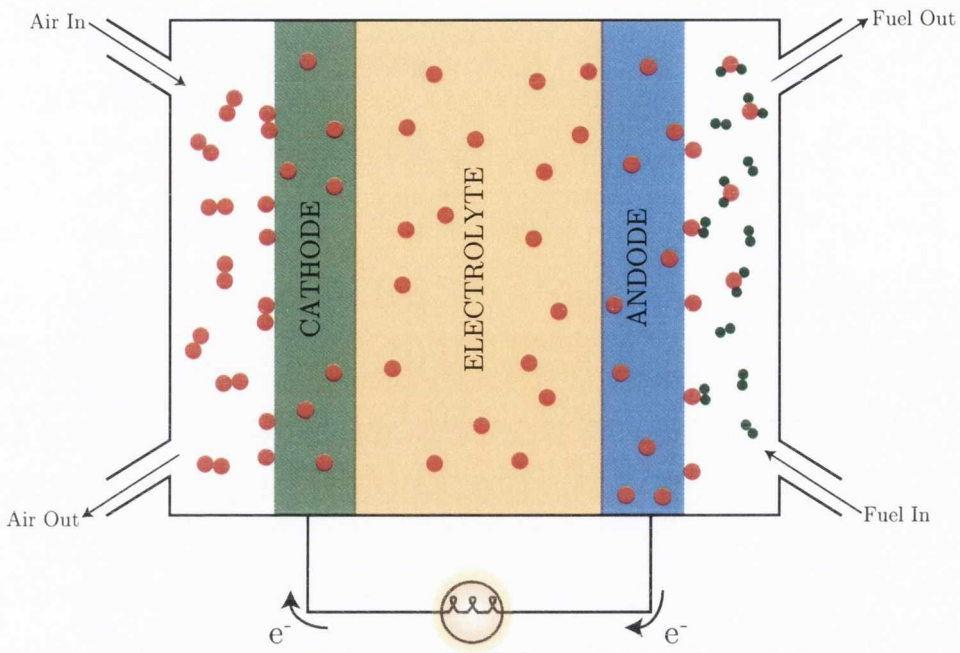

Figure 1.1: A schematic diagram of a SOFC. The red spheres represent oxygen atoms. The fuel, in this case hydrogen, is represented by the green spheres.

ity of the LSM cathode is also of importance, as increased porosity will decrease the electronic conductivity,[50] however, the cathode should be porous in order to increase the surface area available for the reduction of O_2, and help O ions reach the electrolyte. LSM also displays good electrochemical activity for the reduction of O_2, with activation energies for the electrocatalytic reaction of $\sim$180 KJ/mol.[51] Furthermore, LSM is compatible with standard YSZ electrolytes,[52] as well as potential new materials such as Gd–doped CeO_2, and retains its structural integrity over long periods of time.[53]

The cubic phase of zirconia is only stable at high temperatures, but it can be stabilised at lower temperatures through the introduction of Y(III). Typically, 8–10 mol% of Y(III) is present in YSZ electrolytes, as this is this is the minimum required to stabilise the cubic structure and higher levels of doping reduce ionic conductivity, either through interactions between dopants and oxygen vacancies or through vacancy ordering.[54] YSZ is stable across a wide range of temperatures and chemical potentials, which are ideal properties for an SOFC electroylte, and displays sufficient ionic conductivity ($\sim 1 \times 10^{-2}$ S/cm) at $\sim$1200 K.[55,56]

As previously mentioned, SOFC anodes are usually cermets, as this combination produces a material with high ionic and electronic conductivity, which is also catalytically active for fuel oxidation/combustion. Furthermore, cermets are often made with the ceramic material employed in the electrolyte in order to enhance the chemical stability and match the thermal expansion coefficients between the electrolyte and the anode. As such, Ni/YSZ cermets are perhaps the most commonly employed anode as it displays the necessary ionic and electronic conductivity with high catalytic activity for the oxidation of fuel.

1.5.4 Problems with Current SOFC Materials

Although these materials are the current standard components for SOFCs, there are still significant problems associated with their use. The electronic conductivity of LSM is highly dependent on the oxygen partial pressure: for high oxygen partial pressures, the conductivity remains constant, but this drops precipitously for oxygen partial pressures below 10^{-5} bar,[57] although this environment is not typical for SOFC cathodes. More importantly, LSM is chemically active with YSZ, and forms insulating layers of $La_2Zr_2O_7$ and $SrZrO_3$, limiting ionic conductivity from the cathode to the electrolyte.[58] There are also distinct disadvantages to the Ni/YSZ cermet anode, as it is prone to Ni agglomeration over time,[59] is not redox stable[60] and, for hydrocarbon fuels, suffers from carbon deposition.[47]

In addition to these drawbacks, there is the fact that an SOFC constructed from these materials will only operate at elevated temperatures, roughly 1200 K. There is a major impetus to reduce the operating temperature of SOFCs, as this would reduce the problem of lattice expansions, and hence mismatches, between the electrolytes and the electrodes. It would also allow fuel cells stacks to be constructed with a greater density of cells, and for cheaper materials to be used for the interconnects. Furthermore, lowering the temperature that the SOFC needs to be heated to before it begins operation means that start–up and shut–down times would be significantly reduced, along with greater overall durability and stability for all components. Unfortunately, in the tem-

perature range of 500 K–1000 K, the so–called intermediate–temperature range,[56] LSM cathodes suffer from considerable polarization resistance, as much as 2000 ohm cm^2, while YSZ electrolytes display insufficient ionic conductivity.[61]

1.5.5 Development of Intermediate Temperature SOFC

Currently, there is a large amount of research into developing improved materials for SOFCs to allow them to operate in the intermediate temperature range. One method for improving the mixed conductivity of LSM cathodes is to combine it with an ionic conductor, e.g. LSM–YSZ.[58] Alternatively, new perovskite materials have been researched, such as $La_{0.70}Sr_{0.30}CoO_{3-\delta}$ (LSC), which displays high ionic conductivities across a wide range of temperatures.[62] Unfortunately, LSC, similar to LSM, is chemically active with traditional ZrO_2 based electrolytes, and will form insulating layers at the boundaries at the cathode/electrolyte interface. Other materials that have been considered include $(Bi_2O_3)_{1-x}(Er_2O_3)_x$–Ag composites,[63] $Ln_{1-x}Sr_xCo_{1-y}Fe_yO_{3-\delta}$, (where Ln=Pr, Nd, Gd),[64] and $Sm_{0.5}Sr_{0.5}CoO_{3-\delta}/Co_3O_4$.[65] All these cathodes displayed good performance, even at the lower end of the intermediate temperature range. For anodes made from cermet materials, Sn/Ni and Cu/Ni alloys have been found to have increased resistance to carbon deposition when employing hydrocarbon fuels compared to Ni–based materials.[66,67] Ag based cermets have been found to perform particularly well, showing high performance with almost no carbon deposition, however, such anodes would be too expensive for commercial purposes.[68] Recently, novel anode materials with perovskite crystal structures have been proposed, with examples such as $La_{0.70}Sr_{0.30}Cr_{1-x}Ni_xO_3$[69] and Cu–$Gd_{0.2}Ce_{0.8}O_2$–$La_{0.2}Sr_{0.7}TiO_3$[70] being promising candidates for the next generation of anode materials.

Perhaps the biggest limiting factor for SOFCs in the intermediate temperature range is finding electrolyte materials with sufficiently high ionic conductivity, typically greater than 1×10^{-3} S/cm.[45] Due to their desirable mechanical properties, ZrO_2 based electrolytes are still being considered, and improving their conductivities at lower temperatures remains an active area of research. One method for increasing conductivity

is to form composite electrolytes of YSZ with alternative electrolyte materials, such as Gd–doped CeO_2 (GDC).[71] It was found that combing YSZ with GDC produced an electrolyte that displayed almost 3×10^{-3} S/cm at 873 K, which represented an improvement of 200% and 50% over single component YSZ and GDC electrolytes respectively. This enhancement of O^{2-} diffusion was linked to fast transport along the interfaces of the two materials. An alternative method for ZrO_2 based electrolytes is to find new dopants that will stabilise the cubic phase. Sc–doped ZrO_2 (SSZ) has received interest recently, and results indicate that it could surpass tradiontal YSZ electrolytes.[72] Another potential electrolyte material is Bi_2O_3, which displays the highest known ionic conductivity, $\sim$ 2.30 S/cm at 1073 K.[73] Unfortunately, this is only observed for the δ–phase of Bi_2O_3, which has a fluorite structure, but is only stable in the range of 1003 K to 1077 K, severely limiting its use. The introduction of dopants can stabilise δ–Bi_2O_3 at lower temperatures, but at the cost of reduced conductivity. $Bi_{0.80}Er_{0.20}O_{1.5}$[74] and $Bi_{0.75}Y_{0.25}O_{1.5}$[75] displayed conductivities of 0.23 S/cm and 0.11 S/cm at 923 K, sufficient for SOFC applications, however, they were also prone to phase separation, forming low conductivity phases over time. Recenlty, δ–Bi_2O_3 has been grown on YSZ substrates, to increase the thermal stability,[76] however, it was found that if the temperature went over 623 K the structure underwent a transition from δ to γ, drastically reducing the ionic conductivity, and making this material unsuitable for the intermediate temperature range. As such, Bi_2O_3 remains a far from optimal choice for the electrolyte material. Perovskite oxides have also shown considerable promise as electrolytes, displaying high conductivities, such as 2.92×10^{-2} S/cm for $La_{0.80}Sr_{0.20}Ga_{0.90}Mg_{0.10}O_{2.85}$ (LSGM) at 873 K.[77] However, under reducing conditions, extra phases will appear in LSGM,[78] reducing ionic conductivity while introducing electronic conductivity.[79] Furthermore, LSGM is known to react with Ni–based anodes, forming highly resistive layers of $LaSrGa_3O_7$ and NiO,[80] limiting the use of LGSM in convential SOFCs. Oxides with the apatite crystal structure have also been explored for new electrolyte materials. Studies have found that these materials display conductivities comparable to perovskite based materials, e.g. 3.50×10^{-2} S/cm for $La_{7.67}Y_2(GeO_4)_6O_{2.51}$ at 1073 K,[81] however,

synthesising high quality apatite materials is currently extremely difficult, requiring high temperatures ($> 1873\,\mathrm{K}$),[56] necessitating new synthesis methods in order make them viable candidates for SOFC electrolytes. There remains one major electrolyte material that has yet to be fully discussed: CeO_2, otherwise known as ceria.

1.6 Ceria

1.6.1 CeO_2 as a Catalyst

In the field of environmentally friendly technologies, CeO_2 has emerged as an important material for a variety of applications. As previously mentioned in Section 1.2.2, catalysts are often employed for the reduction of harmful pollutants, and CeO_2 is effective in this role[82–85] and as a support for other catalysts[86–90] due to its high thermal stability, self-decoking properties (which prevent poisoning of the catalyst),[91,92] and high oxygen storage capacity (OSC). OSC refers to the ability of CeO_2 to release O_2 under reducing conditions and absorb O_2 under oxidising conditions[93–95], which is a result of the comparative ease of O vacancy formation in CeO_2.[96,97] In Kröger–Vink notation, the reduction of CeO_2 is given by:

$$O_O^x + 2Ce_{Ce}^x \rightarrow V_O^{\bullet\bullet} + 2Ce_{Ce}' + \frac{1}{2}O_2(g), \tag{1.3}$$

where O_O^x is an O^{2-} ion and Ce_{Ce}^x is a Ce^{4+} ion at their respective lattice sites, and the superscript, x, denotes that these ions are charge neutral with respect to their position. On the right hand side of Equation 1.3, $V_O^{\bullet\bullet}$ represents an oxygen vacancy and Ce_{Ce}' is a Ce^{3+} ion. The vacancy is an area of zero charge at a lattice site where there should be a formal charge of 2-, giving the vacancy an effectively doubly positive charge, represented by the superscript of $\bullet\bullet$. Similarly, the Ce^{3+} ions have an effective charge of $1-$ relative to the lattice site, which the $'$ superscript represents. The formation of a neutral oxygen vacancy thus leaves behind two excess electrons which localise on neighbouring Ce ions, reducing them from 4+ to 3+. This reduction provides oxygen for oxidation reactions, while forming vacancy sites that can aid in reduction reactions.

One of the most common uses for CeO_2 is in the catalytic converter in automobiles, where it mainly acts as a support for the Pt, Pd and Rh catalysts, either taking in or releasing oxygen depending on the environment it is in. Furthermore, CeO_2 can also contribute to 'three–way catalysis', i.e. the simultaneous conversion of CO and NO_2/NO to CO_2 and NO/N_2.[82,84]

The redox catalysis of CeO_2 has been extensively investigated. A Fourier–transform infrared spectroscopy study discovered frequencies that corresponded with the adsorbed CO forming carbonate species,[98] which are easily desorbed as CO_2 above room temperature. Since CeO_2 is a heterogeneous catalyst, a proper understanding of its surface chemistry is vital for explaining how it affects catalytic processes. Results of transition electron microscopy found that nanorods will expose the (110) and (100) surfaces, nanocubes the (100) surface and nano–octahedra the (111) surface.[99] Raman spectra of these materials found that nanorods and nanocubes were more easily reduced than the nano–octahedra, indicating that the (100) and (110) surface are more reactive than the (111). Another study which explored the varying surface reactivities of CeO_2, compared CO oxidation on nanorods versus nanoparticles, which predominantly express the (111) surface.[85] It was found that nanocubes were far more effective for CO oxidation, which would be expected from the lower reduction energies measured for the (100) and (110) surfaces. The reduction of NO_2 proceeds in a similar fashion to the oxidation of CO, in that adsorbed NO_2 forms a nitrate species, and additional energy is required in order to produce NO or N_2.[100] Atomic force microscopy[101] and ultraviolet photoelectron spectroscopy[102] both observed that it is necessary for the surface of CeO_2 to be partially reduced, as this creates vacancy sites where NO_2 can adsorb, forming the nitrate species. This adsorption is also associated with the re–oxidation of the CeO_2 surface, as evidenced by the disappearance of peaks associated with Ce(III) ions in the UPS spectrum after NO adsorption.[102]

Theoretical studies have also explored CO adsorption on the surface of CeO_2. GGA+U studies found that adsorbed CO would form a carbonate species, partially reducing the surface,[103,104] in agreement with experimental observations. Density of

state calculations also demonstrated that the interaction of the adsorbed CO would reduce Ce(IV) ions to Ce(III),[103] similar to that which is observed for the formation of an O vacancy (Equation 1.3). This further demonstrates the formation of the carbonate species is an intermediate step in the oxidation of CO to CO_2, forming an O vacancy on the surface of CeO_2. Together with CO adsorption, Scanlon *et al.*[103] also investigated NO_2 adsorption on CeO_2. In agreement with the experimental results, it was found that NO_2 will only adsorb to a surface that has been reduced. In contrast with experimental results, however, there was no formation of a nitrate species. A GGA study investigated NO adsorption on the (100) and (110) surfaces and also observed that NO will not adsorb on stoichiometric/unreduced CeO_2.[105] It was also observed that NO adsorbed more strongly to the (111) surface than the (110). Previous studies have shown that the (111) surface is the most stable,[106,107] and therefore the reduced (111) surface would have a significant driving force to return to its stoichiometric configuration, hence NO is strongly adsorbed, which serves to re–oxidise the surface.[102]

CeO_2 catalysts have also been shown to be useful for the oxidation of hydrocarbons, such as methane, ethane, propane and n–butane,[108,109] hydrogen combustion,[110] steam reforming[111] and for water–gas–shift reactions.[88] In these examples, CeO_2 acts as an oxygen reservoir, providing a steady stream of oxygen to aid in the reactions. Interestingly, Zhao and Gorte[109] found that the rate of oxidation of n–butane had a dependence on the partial oxygen pressure at low temperatures, which disappeared at higher temperatures. It was reasoned that at elevated temperatures, the rate of diffusion of oxygen in CeO_2 was sufficient that bulk oxygen become available for the reaction.

A large range of aliovalent dopants have been considered for improving the catalytic properties of CeO_2. Pd(II) and Pt(II) dopants have been shown to enhance the OSC of CeO_2,[112] which theoretical evidence suggests is due to the formation of under–coordinated O ions upon doping.[113] Trivalent dopants, such as La(III) and Pr(III), have been shown to be particularly effective for soot oxidation,[83] and La– and Nd–doped

CeO_2 catalysts have also displayed enhanced conversion of CO to CO_2 compared to pure CeO_2.[114] It is generally considered that the introduction of a trivalent dopant to CeO_2 will result in the formation of an O vacancy, called a charge compensating vacancy (CCV), in order to conserve charge.[115,116] In Kröger–Vink notation, the doping of CeO_2 with trivalent cations is given by:

$$2Ce_{Ce}^{x} + O_{O}^{x} + M_2O_3 \rightarrow 2M'_{Ce} + V_{O}^{\bullet\bullet} + 2CeO_2 \tag{1.4}$$

where M'_{Ce} is a trivalent dopant at a Ce(IV) lattice site, hence it has an effective formal charge of 1-. Although ionic compensation of the charge is considered more favourable than electronic compensation in the bulk, on the surfaces the latter may be more favourable, similar to the charge compensation scheme seen in Li–doped MgO, [117] where the charge associated with the Li(I) dopant is compensated electronically through the formation of an O–hole:

$$2Ce_{Ce}^{x} + 2O_{O}^{x} + M_2O_3 + \frac{1}{2}O_2 \rightarrow 2M'_{Ce} + 2O_{O}^{\bullet} + 2CeO_2. \tag{1.5}$$

The results from a PBE+U study by Yeriskin and Nolan agreed with this theory, finding electronic compensation to be more stable than forming a CCV on the La–doped (110) and (111) surfaces,[118,119] with a later study reporting similar results for Al(III), Sc(III), Y(III) and In(III) on the (110) surface.[120] Furthermore, these studies discovered another defect structure that also appears more stable than the CCV, which is:

$$2O_{O}^{x} + Ce_{Ce}^{x} + M_2O_3 \rightarrow O_{O}^{\bullet} + V_{O}^{\bullet\bullet} + Ce'_{Ce} + 2M'_{Ce} + 2CeO_2. \tag{1.6}$$

where the charge associated with the dopants is compensated through the formation of an O vacancy, an O hole and a Ce(III) ion. However, these studies applied a $+U$ correction of 7 eV to the O $2p$ states, which may be excessively high, and hence these defect states may be influenced by the U value.

1.6.2 CeO_2 as an SOFC Electrolyte

CeO_2 is also a promising candidate for electrolyte materials with high conductivities in the intermediate temperature range ($\sim$ 773-1073 K).[56] CeO_2 is one of the most widely

studied potential materials for SOFC electrolytes due to its high thermal stability and ionic conductivity.[121–123] Unfortunatlye pure CeO_2 displays a rather low ionic conductivity ($\sim 3.13\times10^{-3}\,Scm^{-1}$), and is dependent on the presence of intrinsic O vacancy defects.[124] Furthermore, these intrinsic O vacancies have been linked with creating electronic conductivity in CeO_2, which short–circuits the operation of the fuel cell.[125] The most common method for increasing the ionic conductivity of CeO_2 is the introduction of trivalent dopants. As seen in Equation 1.4, the introduction of two trivalent cations creates a CCV, which can act as a pathway for ionic diffusion. X–ray diffraction results from several experimental studies have confirmed that such dopants are readily taken into bulk, with CeO_2 able to maintain is fluorite structure up to quite high levels of doping.[126–137]

Typically, Rare–earth cations are chosen as the dopants in CeO_2, as their ionic radii match closely with that of Ce(IV), 0.97 Å, causing minimum distortion of the CeO_2 lattice, which experimental[138] and theoretical[116,139] studies have indicated is an important factor in achieving high ionic conductivities. Using a two–point DC method, [127] ionic conductivities in $Ce_{0.80}M_{0.2}O_{2-\delta}$ (M = Y(III), Gd(III), Sm(III), Nd(III), La(III)) at 1073 K were measured at 3.96×10^{-2} S/cm for Y(III), 5.11×10^{-2} S/cm for Gd(III), 6.54×10^{-2} S/cm for Sm(III), 3.91×10^{-2} S/cm for Nd(III) and 4.49×10^{-2} S/cm for La(III). These high conductivities are also maintained at 873 K, with the lowest being found as 0.59×10^{-2} S/cm for Nd(III) and the highest for Sm(III), at 1.59×10^{-2} S/cm. Electrochemical impedance spectroscopy also measured high conductivities in 20% Sm–doped CeO_2, ranging from 1.60×10^{-2} S/cm to 3.20×10^{-2} S/cm depending on how the samples were synthesised.[128] A study on Sm–doped CeO_2 found that it had higher conductivity than Gd(III), Dy(III) and Er(III) at the same level of doping (10 mol%), while at 30 mol%, the conductivity of Dy–doped CeO_2 was higher than 10 mol% Y–doped CeO_2, which was attributed to an increase of the grain boundary conductivity. For Er–doped CeO_2, increasing the doping level of Er(III) reduced the ionic conductivity, which x–ray diffraction and scanning electron microscopy determined was due to the formation of Er_2O_3 phases.[129] $Ce_{0.80}Gd_{0.20}O_{1.90}$ was found to have a conduc-

tivity of 1.00×10^{-2} S/cm and 2.40×10^{-2} S/cm at 973 K and 1073 K respectively using AC impedance measurements, which is more than sufficient for an intermediate–temperature SOFC electrolyte.[130] A study by Zha *et al.*[133] investigated the effect of dopant concentration on the ionic conductivity. In agreement with previous work, they found that the ionic conductivity of Sm–doped CeO_2 was greater than Gd–Doped CeO_2, and in both cases the maximum conductivity was found for 15 mol% doping. Recently, an electrolyte made from a nanopowder of $Ce_{0.85}Dy_{.015}O_{0.925}$ was found to have a very high conductivity of 7.42×10^{-2} S/cm at 823 K, making it a highly promising new material for SOFC applications.[137]

Theoretical methods have been employed to probe the movement of oxygen ions in CeO_2, such as kinetic Monte Carlo, which uses energetic data of a system to create an event table, which is used to influence the subsequent, semi–random testing of the ensemble.[140] The advantage of this technique is that Monte Carlo calculations are not computationally demanding, which allows the use of highly accurate computational techniques to describe the electronic structure. Gopal and van de Walle studied the thermodynamics of intrinsic O vacancies in CeO_2 with GGA+U and Monte Carlo calculations. They determined that the concentration of O vacancies increases with the temperature and that the O vacancies tended to form clusters along the $\langle 110 \rangle$ and $\langle 111 \rangle$ directions. Dholabhai *et al.*[141] employed kinetic Monte Carlo techniques with DFT+U calculations to measure the O vacancy diffusion (cations were kept stationary), in Pr–doped CeO_2. They obtained conductivity data which was in reasonable agreement with experimental studies and they found that the conductivity is limited at higher dopant concentrations due to the formation of dopant–vacancy–dopant clusters.

An alternative method employed to model the movement of ions in CeO_2 is molecular dynamics. To avoid the cost of *ab initio* calculations, potential models are often constructed that try to reproduce the correct behaviour of the ions within the system, allowing the calculations to model larger systems and longer time periods, usually in the order of nanoseconds.[142] MD studies of pure CeO_2 observed little ionic diffusion, which was dependent on the concentration of O vacancies.[143,144] It was also noted that

diffusion only occurred through movement of an O ion to a neighbouring vacancy along the ⟨100⟩ direction:[143] interstitial anions could occur (such as a Frenkel defect) but the recombination time was far less the the rate of diffusion, meaning that they are unlikely to significantly contribute to ionic conductivity.[144] Force–field MD studies have also investigated doped CeO_2 systems. Similar to the studies of pure CeO_2, diffusion in doped systems occurs through a hopping mechanism along the ⟨100⟩ direction, except, instead of intrinsic O vacancies, the presence of the dopants leads to the formation of CCVs which promote ionic conductivity.[115,145] It was also observed that at higher dopant concentrations, the CCVs tend to cluster mostly along the ⟨111⟩ and ⟨110⟩ directions due to large short term repulsions between CCVs.[146] In agreement with experimental work, all these studies demonstrate an important factor for doped CeO_2 electrolyte materials: ionic conductivity in CeO_2 doped with trivalent cations will increase with increasing dopant concentration, and hence higher CCV concentrations, until an upper limit is reached. At this stage, the dopants and CCVs will form clusters, 'trapping' them and limiting further ionic diffusion.[129,135,136,147]

From all these studies, it is apparent that CeO_2 is highly suitable for SOFC applications in the intermediate–temperature range. In addition to the high conductivity, doped CeO_2 has high mechanical strength[126,127] and tends not to react with the other components of an SOFC under typical operating temperatures.[148,149] Although it is generally found that Gd(III) and Sm(III) are the best dopants for improving conductivity in CeO_2, there is some disagreement between the stated values, and new materials, such as Dy–doped CeO_2,[137] have displayed conductivities higher than some Gd–/Sm–doped systems. These discrepancies may be a result of different synthesis and analytical methods, and therefore it would be beneficial for a study to determine the effect of trivalent dopants on the conductivity of CeO_2, as this could definitively determine the effect and individual dopant has on CeO_2. An oft overlooked fact is how a dopant affect the reducibility of CeO_2. A suitable dopant should not increase the concentration of intrinsic O vacancies in CeO_2, as these have been linked with causing unwanted electronic conductivity in CeO_2. Preferentially, the dopant should even sup-

press the formation of intrinsic vacancies, ensuring the electrolyte is further resistant to reduction.

1.7 Thesis Outline

In these times of increasing concern for the environment, CeO_2 has emerged as an important material for a wide array of applications in the field of green technology. However, there still remains a significant impetus to refine and enhance these technologies in order to satisfy future demand. By exploring intrinsic and extrinsic defects in CeO_2, a greater insight of its properties will be gained, which will provide invaluable information for how to enhance CeO_2–based catalysts and fuel cell materials.

Details of the computational methods employed are discussed Chapter 2 to provide an overview of the quantum mechanical theories upon which they based, and discuss their advantages and limitations. Chapter 3 will discuss the Vienna *ab initio* simulation package, VASP,[150–152] through which all calculations were performed. This chapter will also discuss the various techniques that were employed to analyse the calculated data and the insight they provide on the atomic and electronic structure of the materials studied.

In Chapter 4, a range of intrinsic defects in CeO_2 are studied in order to gain a full insight of its defect chemistry. The relative stability of each defect across a variety of chemical environments and temperatures is also investigated in order to describe how CeO_2 behaves under real world conditions.

A series of trivalent dopants in CeO_2 are investigated with static calculations in Chapter 5. The relative attraction of the dopants for the CCV, as well as their affect on the reducibility of CeO_2, are calculated in order to screen potential candidates for SOFC applications. Carrying on from this work, Chapter 6 employs *ab initio* molecular dynamics to investigate doped CeO_2, and assess the efficacy of the techniques employed in the previous chapter for assessing trivalent dopants.

Chapter 7 further explores the electronic structure of pure and doped CeO_2. The

nature of defects within the band gap are investigated and how they affect the efficiency of CeO_2 based field effect transistors. The chemistry of the CeO_2 surfaces are discussed in Chapter 8, with an in depth analysis of the nature and structure of surface defects is carried out, along with a discussion of how they influence catalytic reaction on CeO_2.

Finally, Chapter 9 summarises the results presented in this thesis. The significance of these results, the potential pathways they open for future research will also be discussed.

Chapter 2

Computational Theory

2.1 Quantum Chemistry Methods

2.1.1 Schrödinger Equation

The quantum structure of a physical system can be determined through the Schrödinger equation.[153] In its time–independent form it is written as:

$$\hat{H}\Psi = E\Psi \tag{2.1}$$

where Ψ is the wavefunction, E is the energy of the system and $\hat{H}$ is the Hamiltonian, which takes the form:

$$\hat{H} = -\frac{\hbar}{2m_i}\nabla_i^2 + V(r) \tag{2.2}$$

where i is an index over all particles in the system, $\bar{h}= \frac{h}{2\pi}$, the Laplacian $\nabla_i^2 = \left(\frac{\delta^2}{\delta x_i^2} + \frac{\delta^2}{\delta y_i^2} + \frac{\delta^2}{\delta z_i^2}\right)$ is the kinetic energy operator and $V(r)$ is the potential energy operator of the system as a function of its coordinates.

If we multiply both sides of Equation 2.2 by the complex conjugate of the wavefunction and integrate over all space the equation becomes:

$$\int \Psi^* \hat{H}\Psi \, \delta\tau = \int \Psi^* E\Psi \, \delta\tau. \tag{2.3}$$

As E is a scalar value, it can be removed from the integral and thus Equation 2.3 becomes:

$$E = \frac{\int \Psi^* \hat{H}\Psi \delta\tau}{\int \Psi^* \Psi \delta\tau}. \tag{2.4}$$

This is known as the expectation value, i.e. it is the average value of a system's energy. An exact solution to the Schrödinger equation would therefore yield the ground state energy and wavefunction of a system. The wavefunction produced by the Schrödinger equation does not have any physical meaning, but its square gives the probability of finding an electron in space, i.e. it provides the electron density. Exact solution to the Schrödinger equation can be found for systems that contain only one electron (e.g. H, He^+, Li^{2+}) but because there's no way to analytically calculate electron-electron interactions, it is impossible to achieve an exact solution for more complicated systems. Therefore, a quantum chemical analysis of a complex system must employ a series of approximations to solve the Schrödinger equation.

2.1.2 The Born-Oppenheimer Approximation

A full solution to the Schrödinger equation would treat the system as a whole, i.e. it would account for both the nuclei and the electrons present. To simplify the calculations, the Hamiltonian is expressed as a series of kinetic and potential energy terms:

$$\hat{H} = \hat{T}_{nuc} + \hat{V}_{nuc-nuc} + \hat{V}_{nuc-elec} + \hat{T}_{elec} + \hat{V}_{elec-elec}, \tag{2.5}$$

where $\hat{T}_{nuc}$ and $\hat{T}_{elec}$ are the kinetic energy operators of the nuclei and electrons respectively and $\hat{V}_{nuc-nuc}$, $\hat{V}_{nuc-elec}$ $\hat{V}_{elec-elec}$ are the potential energy operators of nuclei–nuclei, nuclei–electron and electron–electron interactions. A further approximation that can be made to Equation 2.5 is to treat the nuclei as being stationary in space relative to the electrons due to the nuclei moving significantly slower, thus removing the $\hat{T}_{nuc}$ term from Equation 2.5. This fixing of the nuclei in space is, in essence, the Born–Oppenheimer approximation.[154] This still leaves the $\hat{V}_{nuc-nuc}$ term, but since the nuclei are now fixed it is therefore a constant field and need only be calculated once per each atomic configuration with the equation:

$$\hat{V}_{nuc-nuc} = \sum_{A<B} \frac{e^2 Z_A Z_B}{r_{AB}} \tag{2.6}$$

where e is the charge of an electron, Z_A and Z_B are the nuclear charges of atoms A and B, and r_{AB} is the distance between the two nuclei. This simplifies Equation 2.5 to

an electronic Hamiltonian, $\hat{H}_e$, with three terms:

$$\hat{H}_e = \hat{V}_{nuc-elec} + \hat{T}_{elec} + \hat{V}_{elec-elec}, \tag{2.7}$$

where:

$$\hat{V}_{nuc-elec} = -\sum_{A}^{M}\sum_{i}^{N}\frac{Z_A}{r_{iA}}, \tag{2.8}$$

$$\hat{T}_{elec} = -\sum_{i}^{N}\frac{1}{2}\nabla_i^2, \tag{2.9}$$

and

$$\hat{V}_{elec-elec} = \sum_{i>j}^{N}\frac{1}{r_{ij}}. \tag{2.10}$$

Where M and N are the total number of nuclei and electrons respectively, and i and j are any two electrons under consideration. The first two terms are comparatively easy to calculate. The final term, however, remains too complex to calculate and must undergo further approximations. Almost all quantum chemical calculations of the ground state include the Born–Oppenheimer approximation. The approximation only fails when dealing with quantum effect on light particles, e.g. quantum tunneling of hyrdogen atoms.

2.1.3 The Variational Principle

The variational principle states that for a trial wavefunction, Ψ_t, the calculated trial expectation value, E_t (2.4), will always be higher than the ground state energy, E_0, calculated from the ground state wavefunction, Ψ_0. Expressed as an equation, the variational principle is:

$$\langle \Psi_t \mid \hat{H} \mid \Psi_t \rangle = E_t \geq E_0 = \langle \Psi_0 \mid \hat{H} \mid \Psi_0 \rangle. \tag{2.11}$$

In essence, this means is that any energy calculated from a trial wavefunction will be higher in energy than the true ground state. Therefore, if a new trial wavefunction provides a lower energy then it is considered more accurate than the previous one. Hence the quality of a calculation can be improved by varying the wavefunction until the lowest energy solution is obtained. However, there is no way to determine whether a trial wavefunction is close to the true wavefunction.

2.1.4 Hartree–Fock Approximation

As previously mentioned, it is only possible to solve the Schrödinger equation for single electron systems. In an attempt to solve multi–electron problems, Hartree developed a simplification in 1928 involving a one electron Hamiltonian which assumed that the electron–electron interactions were independent of the other factors:

$$h(i) = -\frac{1}{2}\nabla_i^2 + \sum_A^M \frac{1}{r_{iA}} \quad \text{and} \quad \hat{H}_{ii} = \sum_i^N h(i). \tag{2.12}$$

Solutions to this equation can be found and this results in a series of spin orbitals which satisfy the equation

$$h(i)\chi_\eta(x_i) = \epsilon_\eta \chi_\eta(x_i) \tag{2.13}$$

with the interpretation that electron i occupies a spin orbit χ_j with energy ϵ_j. The full wavefunction (known as the Hartree product) is obtained from the product of the spin orbitals:

$$\Psi(x_1 \dots x_N) = \chi_i(x_1)\chi_j(x_2)\chi_k(x_3)\dots\chi_\eta(x_n). \tag{2.14}$$

and the resulting energy is:

$$\langle \Psi \mid \hat{H} \mid \Psi \rangle = \epsilon_i + \epsilon_j + \epsilon_k \dots \epsilon_\eta = E \tag{2.15}$$

Although Hartree was able to calculate the ground state and excited state of many atomic systems, there were still some major problems with this method. The first was the lack of electron–electron interactions. These interactions were reintroduced by considering the probability density of the electrons, i.e. the square of the wavefunctions. Each electron is considered to move through a potential field created by the nuclei and all the other electrons in the systems, thus averaging the electron–electron interactions. This is referred to as the mean–field approach. However, the field created by the electrons is determined by the wavefunctions which have yet to be calculated. To carry out the calculation, first an initial guess of the wavefunctions are made. It is then possible to solve the equations and produce a new set of wavefunctions and hence a new potential. The calculations can then be repeated with the new set of orbitals

replacing the original guess. This cycle is repeated until the answers produced are self–consistent, i.e. the outputs produced from one cycles match those of the previous cycle, within a given level of accuracy. This technique is the so–called Hartree self–consistent–field method.

The second major problem with the Hartree approach was that the wavefunctions in this approximation are unphysical. The Hartree–product is symmetric with respect to electron exchange, i.e. swapping the position of two electrons in Equation 2.14 yields the exact same wavefunction, therefore it does not obey the Pauli exclusion principle.

Taking helium as an example, there are two possible Hartree wavefunctions, given by:

$$\Psi = \chi_i(x_1)\chi_j(x_2) \text{ and } \Psi = \chi_i(x_2)\chi_j(x_1) \tag{2.16}$$

where χ_i could be the $1s$ α (spin–up) orbital and χ_j the $1s$ β (spin–down) orbital for the ground state. It is obvious that the two Hartree wavefunctions are formed merely by swapping the electrons. However, they both possess the same sign and hence they do not obey the Pauli exclusion principle. By combining the two Hartree products it is possible to generate a wavefunction that satisfies the condition:

$$\Psi = \frac{1}{\sqrt{2}}[\chi_i(x_1)\chi_j(x_2) - \chi_i(x_2)\chi_j(x_1)] \tag{2.17}$$

where $\frac{1}{\sqrt{2}}$ is a normalization constant. The wavefunction in 2.17 now obeys the Pauli exclusion principle, as swapping the electrons results in changing the sign of the wavefunction:

$$\frac{1}{\sqrt{2}}[\chi_i(x_2)\chi_j(x_1) - \chi_i(x_1)\chi_j(x_2)] = -\frac{1}{\sqrt{2}}[\chi_i(x_1)\chi_j(x_2) - \chi_i(x_2)\chi_j(x_1)] = -\Psi \tag{2.18}$$

When these equations were first developed there was not a proper understanding of the indistinguishability of electrons, the cause of the antisymmetric wavefunction, and there formed the notion of the 'exchange' of electrons. As a result, the energy term associated with this phenomenon is referred to as the exchange energy. The effect of this on the total energy calculations will be discussed later.

For helium, determining the wavefunction through inspection is simple enough but this method is not practical for larger systems. For a system containing N electrons

and η spin orbitals, the wavefunction can be defined as the determinant of a matrix of the orbitals. This is usually known as a Slater determinant, named for J. C. Slater. For large matrices, writing out the full matrix and subsequent determinant would be too cumbersome so instead only the leading diagonal is written with the normalisation constant (equal to $\frac{1}{\sqrt{N!}}$) assumed. Thus an N dimensional Slater determinant takes the form:

$$\Psi = |\chi_i(x_1)\chi_j(x_2)\dots\chi_\eta(x_N)| \tag{2.19}$$

An advantage of expressing wavefunctions as a Slater determinant is that it obeys the Pauli exclusion principle; doubly occupying an orbital causes the determinant to disappear:

$$\Psi = \frac{1}{\sqrt{2}}\begin{vmatrix} \chi_i(x_1) & \chi_i(x_1) \\ \chi_i(x_2) & \chi_i(x_2) \end{vmatrix} = \frac{1}{\sqrt{2}}[\chi_i(x_1)\chi_i(x_2) - \chi_i(x_2)\chi_i(x_1)] = 0 \tag{2.20}$$

The final form of the energy is given by the equation:

$$E = 2\sum_{i=1}^{N}\hat{H}_{ii} + \sum_{i=1}^{N}\sum_{j=1}^{N}(2J_{ij} - K_{ij}) \tag{2.21}$$

where $\hat{H}_{ii}$ is the sum of the one electron Hamiltonians from Equation 2.12. The last two terms in Equation 2.21 are the electron–electron interactions and are known as the *Coulomb term* and the *exchange integral*. They take the form:

$$J_{ij} = \int\int \chi_i(x_1)\chi_j^*(x_2)\frac{1}{r_{12}}\chi_i(x_1)\chi_j^*(x_2)\,d\tau_1\,d\tau_2 \tag{2.22}$$

and

$$K_{ij} = \int\int \chi_i(x_1)\chi_j^*(x_2)\frac{1}{r_{12}}\chi_j(x_1)\chi_i^*(x_2)\,d\tau_1\,d\tau_2 \tag{2.23}$$

While J_{ij} represents the classical repulsion between electrons, K_{ij} has no classical analogue and is a quantum mechanical effect that results from the antisymmetric wavefunction. K_{ij} is a negative term, hence it lowers the total energy of the system, and is the most computationally expensive part of a Hatree–Fock calculation.

2.1.5 Roothaan–Hall Equations

For complex systems, we can define the molecular orbitals in terms of atomic orbitals. These basis functions, known as the linear combination of atomic orbitals, take the form:

$$\Psi_i = \sum_{\mu} C_{\mu}^{i} \phi_{\mu} \tag{2.24}$$

where ϕ_μ are the basis functions and C_μ^i are the coefficients of atomic orbital μ in molecular orbital i. The form of the basis functions need not be directly modeled on atomic orbitals. For example, gaussian functions can be used to construct atomic–orbital like basis functions. Working independently, Roothaan and Hall developed a set of matrix equations known as the Roothaan–Hall equations. These are an alternate way to represent the HF equations and take the form:[155]

$$FC = SC\epsilon \tag{2.25}$$

where F is a modified Fock matrix, constructed from single–electron operators, S is the overlap matrix of basis functions, C is the matrix of the coefficients, C_μ^i, and ϵ is the diagonal matrix of orbital energies, ϵ_i.

2.1.6 Limitations of the Hartree–Fock Approach

The HF approach is still regularly employed for quantum chemical calculations. It is known to provide highly accurate results, within a few percent of experiment, for molecular properties such as interatomic distances and bond angles. However, the HF approach suffers from serious limitations that severly hinder its usefulness. Perhaps the biggest limitation of the HF approach is the *electron correlation problem.* This difference in energy was defined by Lowdin as the *correlation energy.*[156] The problem arises because the Hamiltonian is solved with an approximate wavefunction which treats the electrons in an averaged fashion and thus the instantaneous position of electrons with respect to each other is largely ignored. In reality, electrons, being charged species, try to avoid each other and therefore at any instant there is less chance of finding

electrons close to each other than the electron density would suggest and consequently electron localisation is overestimated in HF.

The first type of correlation is dynamical correlation and deals with the actual motion and interactions of two electrons, i.e. the probability of finding one electron at a certain position is dependent on the position of the other electrons. The second type is non–dynamical correlation which occurs when there are degenerate states around the highest occupied molecular orbital. In HF, one state will be occupied instead of treating all the states equally. Dynamical correlation is typically around 0.1% of the total energy. The result of this is that HF can model structural properties with a reasonable level of fidelity but often completely fails in the calculations of reaction energetics; a reaction involves the breaking of bonds and the redistribution of electrons, both of which are processes that are highly affected by electron correlation. Furthermore, certain properties are dependent on correlation, e.g. van der Waals interactions depend strongly upon the dynamical movement of electrons, and cannot be calculated by a mean–field approach.

Another problem with HF is its scaling cost, which scales according to N^3, where N is the number of particles in the system. This factor coupled with the electron correlation problem makes the HF approach wholly unsuitable for large scale simulations, such as crystals. Methods for improving the description of correlation, such as configuration interaction, coupled cluster and Møller–Plesset perturbation theory have been developed but such methods are even more computationally expensive, making their application to solid state calculations unfeasible. An alternative theory that can be applied to calculations on the solid state, and also deal with the electron correlation problem, is density functional theory (DFT).

2.1.7 Density Functional Theory

Density functional theory (DFT) states that the energy of a system can be derived from its electron density. The original theory is based on the Thomas–Fermi model, but it was in 1964 that the validity of DFT was proven by Hohenberg and Kohn

(HK). The HK theorems state that (i) the ground state energy of a many electron system is determined by the electron density and (ii) the exact total energy of a many electron system is given by the exact ground state electron density. Furthermore, they demonstrated that all ground state properties could be derived from this density. One advantage of DFT is immediately apparent: whereas previous approaches had to deal with $3N$–dimensional systems (N being the number of electrons), DFT only needs to optimise the electron density function, $\rho(r)$, which is always 3–dimensional, significantly simplifying the calculation. Similarly to how the Hamiltonian was dealt with in Equation 2.5, before performing a DFT calculation the energy term is split into its constituent parts:

$$E[\rho(r)] = T[\rho(r)] + E_{elec-elec}[\rho(r)] + E_{nuc-elec}[\rho(r)] \tag{2.26}$$

where $T[\rho(r)]$ is the kinetic energy, $E_{elec-elec}[\rho(r)]$ are the electron–electron interactions and $E_{nuc-elec}[\rho(r)]$ are the electron–nuclear interactions. An alternative form of Equation 2.26, in which the terms that only depend on the electron density, $\rho(r)$, are grouped together, is written as:

$$E[\rho(r)] = F[\rho(r)] + \int \rho(r) V_{ext}(r)\, dr \tag{2.27}$$

where the second term is the interaction between the electron density and the potential field created by the nuclei, $V_{ext}(r)$. The first term, which contains the kinetic energy and the electron–electron interactions, is known as the *Hohenberg and Kohn universal functional*. If the the form of $F[\rho(r)]$ was known exactly, then finding the exact ground state energy would be a simple case of minimising the energy with respect to $\rho(r)$. Unfortunately, the exact nature of $F[\rho(r)]$ is not known.

A computational scheme based on the HK formalism was later developed by Kohn and Sham.[157] They achieved this by reintroducing the wavefunction to the calculations. One of the first problems encountered during previous attempts was the difficulty of calculating the kinetic energy. The solution offered by Kohn and Sham (KS) was to consider a fictitious, non–interacting system generated from a wavefunction that would

have the same ground state energy as the fully interacting system.

$$\rho_{KS}(r) = \sum_{i}^{N} |\psi_{KS}|^2 = \rho_{exact}(r) \tag{2.28}$$

The kinetic energy is then split into the energy associated with the non–interacting system (T_s) and a correction term (T_c) to account for electron–electron interactions. Part of the kinetic energy can now be calculated in same way as HF;

$$T[\rho(r)] \rightarrow T_s + T_c[\rho(r)] \quad \text{where} \quad T_s = -\frac{1}{2}\sum_{i}\langle \chi_i \left|\nabla^2\right| \chi_i\rangle. \tag{2.29}$$

The electron–electron interactions are also split into two two–electron term; the first is a classical Hartree energy between two electron densities; the second term, E_{NC}, deals with the non–classical electron interactions, i.e. the exchange and correlation energies;

$$E_{elec-elec}[\rho(r)] = \frac{e^2}{2}\int\int \frac{\rho(r)\rho(r')}{|r-r'|} dr\, dr' + E_{NC}[\rho(r)] \tag{2.30}$$

The Hohenberg–Kohn functional, from 2.27, now has the form:

$$F[\rho(r)] = T_s[\rho(r)] + J[\rho(r)] + E_{XC}[\rho(r)] \tag{2.31}$$

in which the term $J[\rho(r)]$ is the classical Coulomb interactions while $E_{XC}[\rho(r)]$ is the non–classical elements (exchange and correlation) of the electron–electron interactions and is defined as:

$$E_{XC}[\rho(r)] = (T[\rho(r)] - T_s[\rho(r)]) + (E_{elec-elec}[\rho(r)] - J[\rho(r)]) = T_C[\rho(r)] + E_{NC}[\rho(r)] \tag{2.32}$$

In DFT, exchange and correlation are in–built, as opposed to HF wavefunction methods where the two effects are separate. It is now possible to derive the single particle KS equations and, from this set of single particle orbitals, produce a Slater determinant which has a density equal to the density of the system being studied. The total energy, in terms of the wavefunctions, is now:

$$E[\rho(r)] = T_S[\rho(r)] + J[\rho(r)] + E_{XC}[\rho(r)] + E_{Ne}[\rho(r)] \tag{2.33}$$

where:

$$T_S[\rho(r)] = \sum_{i=1}^{N}\langle \chi_i \left|\nabla^2\right| \chi_i\rangle \tag{2.34}$$

and:

$$J[\rho(r)] = \frac{1}{2}\sum_{i=1}^{N}\sum_{j=1}^{N}\int\int |\chi_i|^2 \frac{1}{r_{ij}} |\chi_j|^2 \, dr_1 \, dr_2 \tag{2.35}$$

and:

$$E_{Ne}[\rho(r)] = -\sum_{i=1}^{N}\int \sum_{A}^{M} \frac{Z_A}{r_{iA}} |\chi_i|^2 \, dr_1. \tag{2.36}$$

The next step is to determine a set of orbitals, $\chi_i(r)$, that provide the minimum energy for equation 2.33, i.e. the variational principle, under the constraint that all the orbitals are orthonormal. This produces a set of single particle equations similar to those found in the HF approach. In the equations, a potential acts upon the wavefunction to produce the eigenvalues and eigenvectors:

$$\left(-\frac{1}{2}\nabla^2 + \left[\int \frac{\rho(r)}{r_{12}} \, dr_2 + V_{XC}(r) - \sum_{A}^{M} \frac{Z_A}{r_{1A}}\right]\right) \chi_i = \epsilon_i \chi_i \tag{2.37}$$

which gives:

$$\left(-\frac{1}{2}\nabla^2 + V_{eff}(r)\right) \chi_i = \epsilon_i \chi_i \tag{2.38}$$

where V_{XC} is the exchange–correlation potential, and V_{eff} is the effective potential experienced in the system. This defines the Kohn–Sham one electron operator for the total energy. Similar to the HF approach, V_{eff} is dependent on the orbitals, which are what is being calculated, and hence an iterative approach starting from an initial guess is required (self–consistent field theory). DFT could be an exact method for calculating the energy of system, however, the form of the $E_{XC}[\rho(r)]$ functionals are not known and have only been calculated for a free electron gas and thus must otherwise be approximated. DFT therefore contains approximate exchange and correlation energies, as opposed to the HF approach which contains the exact exchange energy but completely ignores correlation. Despite this limitation, DFT has become a popular choice for calculations of the solid state, and many methods have been devised for improving $E_{XC}[\rho(r)]$, some of which will be discussed in the following section.

2.1.8 Exchange–Correlation Functionals

The Kohn–Sham approach is capable of calculating much of the electronic energy of a system exactly, with the remaining terms collected together in the $E_{XC}[\rho(r)]$

functional. The accuracy of DFT calculations is therefore highly dependent on the $E_{XC}[\rho(r)]$ functional. Fortunately, comparatively simple approximations of $E_{XC}[\rho(r)]$ can be employed which provide reasonable results.

The majority of $E_{XC}[\rho(r)]$ functionals are based on a uniform electron gas model, in which a hypothetical system containing an infinite number of electrons that are free to move in an electrically neutral environment. A large body of energy versus density data on these systems has been amassed from quantum–Monte–Carlo calculations and thus accurate exchange and correlation energies are readily available within this model. $E_{XC}[\rho(r)]$ can be written as

$$E_{XC}[\rho(r)] = \int \rho(r)\epsilon_{XC}[\rho(r)]\, dr \tag{2.39}$$

where $\epsilon_{XC}[\rho(r)]$ is the exchange–correlation energy per electron. Therefore, by integrating $\epsilon_{XC}[\rho(r)]$ over all points in the system the total exchange–correlation energy can be calculated.

One method for applying the exchange–correlation contributions from the electron gas model to a real system is the local density approximation (LDA). The LDA approach is based upon the assumption that at any position r in a system, the exchange–correlation energy is equal the exchange–correlation energy of a homogeneous electron gas of the same density. Bloch and Dirac[158,159] developed equations that relate the exchange portion of the energy, ϵ_X, to the density and hence this value is easily calculated. However, because no such equation exists for the correlation portion, ϵ_C, these energies were taken from the quantum–Monte–Carlo calculations.[160] Subsequently, Vosko, Wilk and Nusair were able to develop an interpolation formula with this data from which LDA correlation energies could then be calculated.[161] The major assumption of the LDA approach is that the exchange–correlation energy is only dependent upon the density at point r. Hence, LDA–DFT has been found to be effective for calculations on systems with uniform electron densities but conversely it is less accurate for systems where the electron density changes rapidly, such as localised defects in solid state materials.[162,163] Furthermore, the LDA approach suffers from other drawbacks, most

noticeably the fact that it overbinds the electrons causing an underestimation of the bond lengths whilst overestimating ionisation and atomisation energies.

A number of attempts to improve on LDA were based on the idea that the exchange–correlation energies could be improved if they were not solely derived from the local density, but also on the gradient of the density at that point. Perhaps the most successful of these corrections is the generalised gradient approximation (GGA) which adds a term involving the gradient of the density, $\delta(\rho(r))$, often as a correction to LDA energies. The GGA approach has been found to provide more accurate results than LDA, especially in systems with inhomogeneous electron densities. There can be considered to be two main types of GGA functionals. The first type, such as the Lee–Yang–Parr[164] correlation and Becke's[165] exchange functionals, are derived from experimental data. Therefore, such functionals could be considered *semi–empirical* in nature, although it is perhaps better to think of them as parameterised as the experiment data is only used to fit parameters which are independent of the of atoms being studied. However, the parameters in these functionals are derived from data on molecules containing only atoms from the first three row of the periodic table and as such may not be suitable for calculations on heavier elements. The other type of functionals do not depend on empirical data and are instead based on the physics of the exchange and correlation functionals. Examples of such functionals include the those of Perdew and Wang[166] and Perdew–Burke–Ernserhof (PBE).[167]

2.1.9 The DFT+U Approach

The effectiveness of DFT for computational solid state calculations has made it one of the most popular methods for theoretical physicists and chemists. However, despite the simplicity and accuracy of LDA and GGA calculations, both suffer from some serious limitations, mostly due to the approximate nature of the $E_{XC}[\rho(r)]$ functional. When calculating the electron–electron interactions, an electron interacts with a field made up of all the electrons, therefore there exists an interaction between the electron and itself. In the Hartree–Fock approach, the exchange integral (Equation 2.23) is

calculated exactly, hence removing this interaction. However, in DFT the exchange is only approximated which means that for a single electron the Coulomb and exchange terms may not necessarily cancel each other, resulting in the spurious interaction of an electron with itself. This error is termed the self–interaction error (SIE). For molecules, this is not necessarily a problem as they tend to have a fairly delocalised electronic structure, but for solid systems containing highly localised electrons the SIE can have a severe impact on the accuracy of the calculations. One method for improving accuracy is the DFT+U approach, which counteracts the SIE while only marginally impinging on the computational cost.

DFT+U was originally developed to model highly correlated systems, i.e. systems where strong Coulombic forces lead to localised electronic states, which are strongly affected by the SIE. The use of the word correlated in this context should not be confused with the correlation energy as defined by Löwdin[156] which is the difference in energy between the HF energy and the true ground state energy.

In order to illustrate how the DFT+U approach works, it is instructive to see how the SIE affects the energy in standard DFT. Figure 2.1 demonstrates the change in energy of a single atom as an electron is added from (or removed to) an external reservoir. Although the energy change between integer charges should be a linear value, DFT predicts a value which is continuous and lower in energy than the exact value. This discrepancy results in non–integer occupation of an orbital being artificially lower in energy, hence the tendency of DFT to inaccurately model the structure of systems known to have localised electronic states.[163,168,169]

To account for the SIE, the DFT+U approach introduces an empirical Hubbard model correction to the DFT energy. In practice, the Dudarev[170] version is often used, which has the form:

$$E_{\mathrm{DFT}+U} = E_{\mathrm{DFT}} + \frac{U}{2}\sum_{I,\sigma} \lambda^{I\sigma}(1-\lambda^{I\sigma}) \tag{2.40}$$

where $\lambda^{I\sigma}$ is the occupation of an orbital with a specific angular momentum (σ) on a specific atom (I) and U is the parameter that controls the size of the correction. This

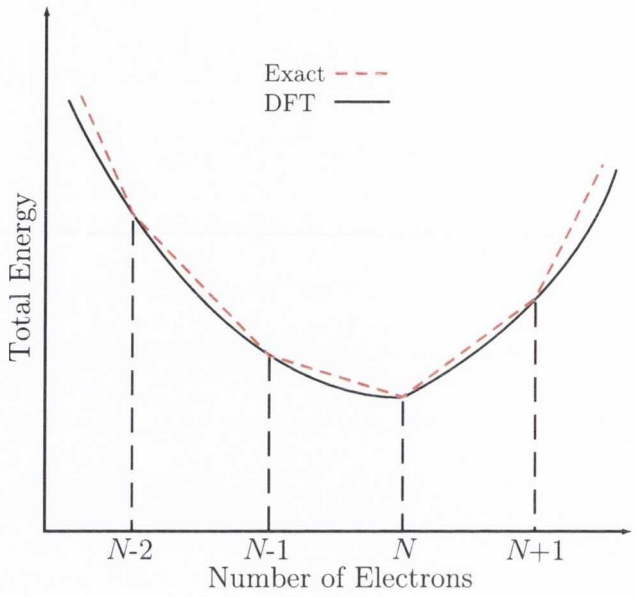

Figure 2.1: The change in energy as a function of the number of electrons, N, in a system for a DFT and an 'exact' calculation.

parameter, the so–called $+U$ correction, acts as an energetic penalty to the partial occupation of orbitals: when the occupation of an orbital is zero or one, the final term on the right hand side of Equation 2.40 disappears, but when the orbitals are partially occupied the term is non–zero, raising the energy of the system and thus encouraging integer occupation of the orbitals.

This is illustrated schematically in Figure 2.2. In this hypothetical system there are three p–orbitals. In the first case, one electron is shared between the orbitals. With the $+U$ correction applied there is an energy penalty of $\frac{U}{2}(3 \times (\frac{1}{3} \times \frac{2}{3})) = \frac{1}{3}U$ for this configuration. In the second example, one electron fully occupies one orbital and there is no penalty for the configuration, thus DFT+U favours the localised system.

The main advantage of DFT+U is that it counteracts the SIE error without raising the computational cost, in comparison to standard LDA/GGA calculations, thus making it a very popular method. Unfortunately, it does have some drawbacks, perhaps most notably with the $+U$ parameter itself. The value of U should be 'large enough' that it corrects the SIE, yet 'small enough' that it doesn't over–penalise delocalisation, but it is hard to determine what constitutes a suitable value. One method is to fit

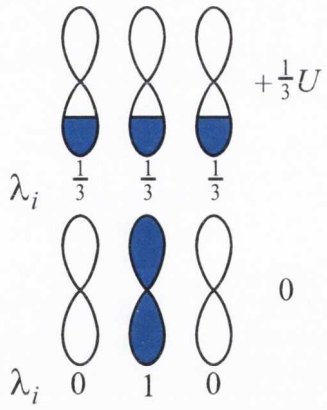

Figure 2.2: A diagram that demonstrates how the $+U$ approach counteracts the SIE using three p orbitals as an example. In the top example, a single electron partially occupies three p orbitals, adding a penalty of $\frac{1}{3}U$ to the energy. In the bottom example, one electron fully occupies a p orbital and no energetic penalty is applied.

U to the experimental band gap, but in most cases this not an appropriate method for determining U. Firstly there is a band gap error inherent to DFT calculations that results in calculated band gaps being significantly lower than experimental values.[171] This error is not entirely dependent on the SIE, so varying the value of U should not be expected to fix it in the first place; secondly, fitting to the band gap often leads to excessively high values of U which can lead to localised defect states that bear little to no relationship to experimental results.[163,172] A more appropriate method for selecting a U value is to fit to the specific features observed through experiment. For example, electron defects usually give rise to defect states in the band gap which can be detected through UPS/XPS. A value of U can then be selected which recreates the defect state's *relative* position in the band gap, thus reproducing the correct description of the defect state. For certain defect states, such as oxygen holes in CeO_2, there is a dearth of spectroscopic data in the literature. In such instances the U value can be determined through the use of an *ab initio* procedure, such as constrained DFT.[173] In this thesis, a Koopmans–like approach, based on the procedure originally developed by Lany and Zunger,[174] was employed to determine the U value for such states. This attempts to restore the linear behaviour of energy with occupation and will be discussed in a

subsequent chapter.

2.2 Solid State Simulations

2.2.1 Periodic Boundary Conditions

For a macroscopic crystal system, a direct solution to the Schrödinger equation would be impossible to determine due to the sheer number electrons involved. Fortunately, it is possible to take advantage of the regular structure of crystal systems to make the problem solvable. Crystal structures are made up of regular repeating units, so it is possible to solve the Schrödinger equation for one of these finite units. This simulation cell is defined by its lattice vectors (a, b and c), lattice angles (α, β and γ) and positions of the atoms. When performing a calculation, this simulation cell is expanded periodically in all three dimensions, as demonstrated in Figure 2.3. The edges of the cell are therefore under periodic boundary conditions i.e. if a atom was to 'move off' of one side of the cell, it would 'reappear' at the opposite side. This approach uses space group information to help reduce the number of calculations needed.

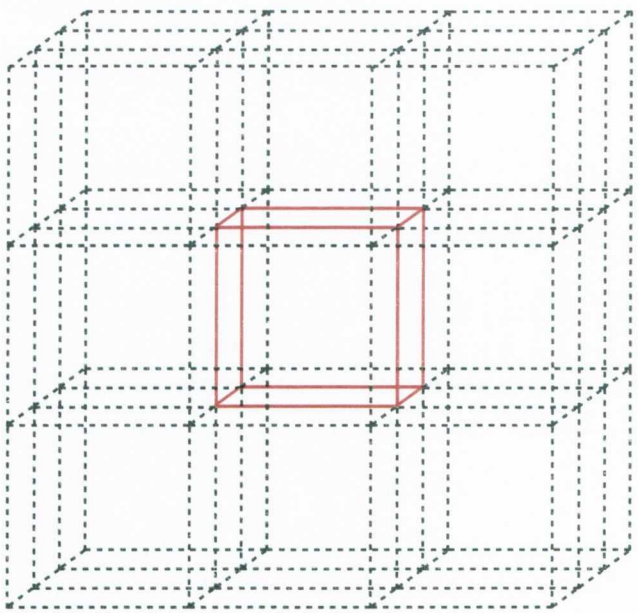

Figure 2.3: A 3×3×3 expansion of the a simulation cell (red cube) representing the periodic boundary conditions for a quantum–chemical calculation.

2.2.2 Basis Sets and Pseudopotentials

The accuracy of a quantum chemical calculation is highly dependent on the mathematical representation of the wavefunction. These representations, known as basis sets, are often constructed from a linear combination of functions to match the expected behaviour of the wavefunctions. For calculations on solid–state, periodic structures, a plane wave basis set is particularly advantageous.[175] A basis set constructed from plane waves, of the form e^{ikx} (where x is the position vector, k is the wave vector and i is the imaginary number), is independent of the position and number of atoms in the cell and is only dependent on the magnitude of the simulation cell itself. Thus, it is not biased towards any particular system and does not suffer from the basis set superposition error that affects localised basis sets, such as Gaussian functions.

In a plane wave basis set, the wavefunction is expressed as a linear combination of plane waves with differing reciprocal lattice vectors. In theory, this Fourier series could fully describe a given system but only with an infinite basis set. Instead, a cutoff energy is introduced that places an upper threshold on the frequency (kinetic energy) of the plane waves, thus making the basis set finite. The plane wave cutoff energy must be optimised for a given system to provide adequate convergence. Therefore optimising the plane wave basis set is far easier than for localised basis sets, as only this single factor needs to be optimised.

For practical purposes, only the valence electrons are represented by the plane wave basis set. The wavefunction of electrons near the nuclei would experience rapid oscillations and therefore modelling them would require an excessively high cutoff energy. One solution to this problem is to employ what is known as a pseudopotential. The pseudopotential replaces the strong potential near an ionic nucleus with a weaker pseudopotential. The pseudopotential is derived from all–electron calculations and parameterised so that the resulting pseudo–wavefunction it forms will match the all-electron wavefunction beyond a certain radius (Figure 2.4). As the pseudo–wavefunction is smoother than the all electron wavefunction below the cutoff radius, r_c, a smaller plane wave cutoff energy is required.

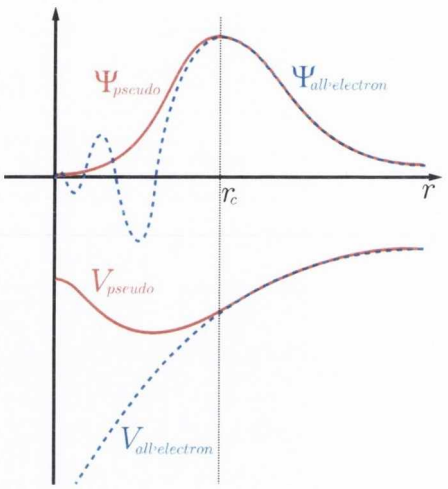

Figure 2.4: A representative comparison between the pseudopotential, V_{pseudo}, and its resulting pseudowavefunction, Ψ_{pseudo}, (solid red lines) and the all–electron potential, $V_{all-electron}$, and wavefunctions, $\Psi_{all-electron}$ (dashed blue lines). The cut–off radius r_c (black dashed line) is the radius beyond with the pseudo– and all–electron wavefunctions will match each other.

A variation of this, known as the Projector Augmented-Wave (PAW) method, was developed by Blöchl[176]. PAW is an all-electron approach, in which the core states are represented with localised basis sets while the valence states are represented by plane waves. The effect of the core states is then projected onto the valence electrons. The major advantage of this method is that it is possible to achieve the accuracy of an all-electron calculation while retaining the numerical efficiency of pseudopotentials. In addition, PAW is able to provide the correct nodal behavior of valence electron wavefunctions.

2.2.3 Brillouin Zone and *k*–Points

To simplify the calculation of the electronic structure, Bloch's theorem is applied to the wavefunction. Bloch's theorem states that the wavefunction of a particle in a periodic system (e.g. an electron moving through the periodic potential of the ions in a crystal lattice) may be written as the product of a plane wave and a periodic function, $u(r)$,

which possesses the same periodicity as the potential:

$$\Psi(r) = e^{ikx}u(r). \tag{2.41}$$

The value k in Figure 2.41 is the wave vector that links the phase relationship of the wavefunction between repeated unit cells. The first Brillouin–zone is the region along "k–space" where the eigenvalues of the Hamiltonian can be labeled uniquely within a $\frac{2\pi}{a}$ range along the k–lattice (Figure 2.5). The significance of this with respect to the Bloch's theorem is that the solutions of the wavefunction can be characterised solely from their behaviour within the Brillouin–zone.

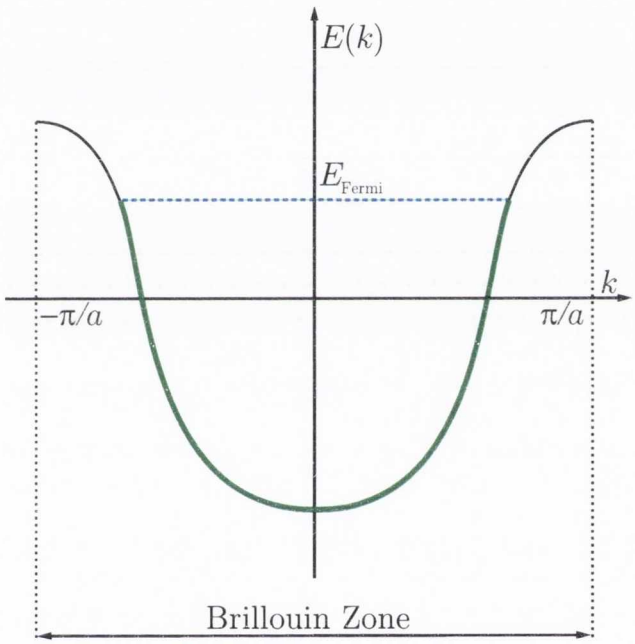

Figure 2.5: A representation of a band structure within the first Brillouin–zone. The area highlighted in green represents filled states and the blue line represents the Fermi level (E_{Fermi}).

During a DFT calculation the electron density is calculated at every iterative step. Ideally, this would be achieved by integrating the squared magnitudes of the Kohn–Sham eigenfuctions over the Brillouin–zone. Such a process would be computationally expensive so instead the integral is approximated by taking the sum over a series of selected k–points. Due to the fact the wavefunction varies smoothly over reciprocal

space, it is only necessary to sample a selection of representative points in order to get an accurate approximation of the total energy.[177] For non–metals, whose valence band maximums (VBMs) tend to be fully occupied, only a small number of k–points are required (k–point density $\approx 0.04\,\text{Å}^{-1}$). The occupation of the VBM in metals, however, will vary more and therefore a larger number of k–points are needed ($\approx 0.01\,\text{Å}^{-1}$). To ensure sufficient convergence, the k–point sampling is increased until the change in energy between calculations is sufficiently small. In this thesis the method used to generate the k–point meshes is that of Monkhorst and Pack,[178] which is able to utilise regular k–point meshes (where the k–points are evenly spaced from the origin) and special k–point meshes (where the regular mesh is offset from the origin).

2.2.4 Electronic Optimisation

Three main components are required to begin a DFT calculation; the lattice vectors, atomic coordinates and the total number of electrons. Figure 2.6 is a schematic that represents how the optimistion of the electronic and geometric structures are carried out. The first step is to produce a trial charge density and wavefunction. The values for these are either taken from a previous calculation or are randomly generated if there are no previously calculated values. The Hamiltonian is then constructed as a sum of the kinetic energy ($T[\rho(r)]$), potential energy ($J[\rho(r)]$) and the exchange–correlation energy ($E_{XC}[\rho(r)]$). The next step is the most time consuming part of the process: diagonalisation of the Kohn–Sham equations to obtain the eigenvalues. The diagonalisation of $N \times N$ matrix scales with a factor of N^3 and the use of a plane wave basis set further increases the problem. As such, this portion of the calculation can take up to 90% of the total time. In this thesis, all calculations were solved using a the iterative blocked Davidson algorithm which only solves for a subset of eignvalues.[179]

From the solutions of Kohn–Sham equations a new charge density and wavefunction are generated. The energy of the new configuration is calculated, and if the value is within a specified threshold from the starting energy the wavefunction is considered converged, the new forces are calculated and the ionic positions are updated. If the

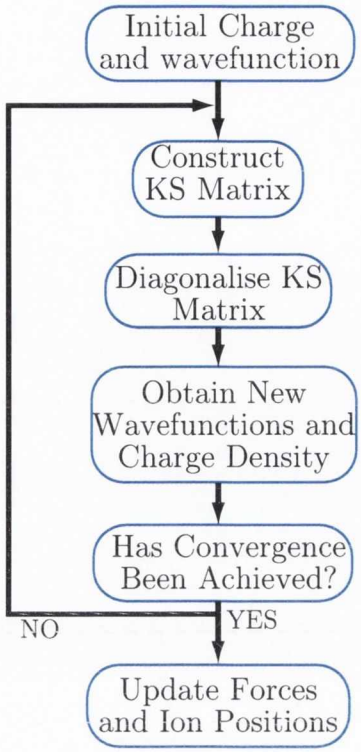

Figure 2.6: A workflow diagram demonstrating a typical DFT self–consistent calculation.

energy difference is not within a specified threshold, the new wavefunction and density are used as the new input and the self–consistent procedure repeats until convergence is achieved.

2.2.5 Force Model and Geometry Optimisation

A force is classically defined as the first derivative of energy with respect to position. For an ion in a system, the force can be calculated by moving it in all directions and working out the derivative numerically. For a system with N atoms this would require a total of 6N calculations and is therefore an inefficient method. To simplify the situation, the calculations in this thesis employ the Hellmann–Feynman theorem[180] which states that the force on an atom in a system is merely the classical electrostatic force felt by the nucleus. The advantages of this approach is that the force on all the ions can be calculated with only one call to the energy sub–routine and the forces can

be calculated directly from the wavefunctions which have been previously calculated.

A disadvantage of this approach is that the derivative of the basis set with respect to the volume of the cell is ignored which introduces an extra force to the pressure calculation, termed the Pulay stress.[181] For a plane wave basis set, Pulay stress is not always a concern as the plane waves are not atom specific. However, Pulay stress becomes an important factor for calculations were the volume of the system changes. For example, if the size of a lattice were to increase, the reciprocal lattice would shrink and thus alter the plane wave cut off. For these calculations extra care must be taken to ensure the Pulay stress is accounted for.

Once the forces have been calculated they are used to perform relaxations. The minimisation techniques used in this thesis were the Quasi–Newton approach and molecular dynamics (MD) as implemented in the VASP code. In theory, the ground state ionic configuration is reached when the net force on each ion is zero, but in practice these relaxations are carried out until previously determined convergence criteria are met.

2.2.6 Energy Minimisations: From Steepest Descent to Quasi–Newton

The minimisation of the energy is an iterative procedure, and at each step the energy is reduced until a minimum is achieved. One of the most basic forms of energy optimisation is the method of steepest (or gradient) descent, which generally takes the form:

$$x_{n+1} = x_n - \lambda g_n \tag{2.42}$$

where x is the position of the atoms at steps n+1 and n. λ, a numerical value, is the step size between each configuration and can be varied at each step to optimise the efficiency of a calculation. g_n is the gradient at the position x_n and hence the method follows the path of the negative gradient towards the minimum. While this process is robust and simple, a major disadvantage is that the path of descent is orthogonal to the gradient contour at a given point. As a consequence, when the minimum lies

within a narrow valley it will take many small steps to find the minimum. It is worth pointing out that each step only depends upon the gradient at that point, i.e. it is independent of the previous steps in the calculation. By including information about the gradient from previous steps, the optimisation can be improved, requiring fewer steps to reach the minimum.

The Newton–Raphson method is referred to as a second–order derivative method as it relies on the second derivative of the function. Taking the Taylor expansion around a function, $f(x)$, to the second derivative gives:

$$f(x + \Delta x) = f(x) + f'(x)\Delta x + \frac{1}{2!}f''\Delta x^2. \tag{2.43}$$

The maxima/minima of the function can be found by taking the first derivative of Equation 2.43 with respect to Δx:

$$f'(x) + f''(x)\Delta x = 0. \tag{2.44}$$

Since $\Delta x = x_{n+1} - x_n$, Equation 2.44 can be rewritten to give the Newton–Raphson equation:

$$x_{n+1} = x_n - \frac{f'(x)}{f''(x)}. \tag{2.45}$$

To relate Equation 2.45 to the system studied in this report, it is rewritten as:

$$x_{n+1} = x_n - B_n^{-1} \cdot g_n \tag{2.46}$$

where x_{n+1} and x_n are the positions of an atom, B_n^{-1} is the inverse Hessian matrix, i.e. a square matrix of the partial second derivative, and g_n is the gradient.

Although the Newton–Raphson method is an improvement over the gradient descent approach, it remains impractical due to the computational cost associated with calculating the inverse of the Hessian matrix. Instead, the Quasi–Newton approach may be used. In this method, Equation 2.46 is still used but instead of calculating the inverse Hessian matrix at every step, it begins with an identity matrix and subsequently builds up an approximation of the inverse Hessian through information from the previous steps. Several ways exist to calculate the approximate matrix, for example

the Davidon–Fletcher–Powell formula which is shown below:

$$B_{n+1}^{-1} = B_n^{-1} + \frac{\Delta x \cdot \Delta x}{\Delta x \Delta g} - \frac{(B_n^{-1} \cdot \Delta g) \cdot (B_n^{-1} \cdot \Delta g)}{\Delta g \cdot B_n^{-1} \cdot \Delta g} \tag{2.47}$$

A full discussion of and derivation of Equation 2.47 and similar methods for approximating the inverse Hessian can be viewed in Polak (1971).[182] The important point about such approximations is that they are dependent on the changes in the forces, displacement of the ions and the previous inverse Hessian matrix. Therefore, as the calculations proceeds each iteration improves the estimated inverse Hessian matrix until it more closely matches the exact one, assuming the original approximation holds.

2.2.7 Molecular Dynamics

Molecular Dynamics employs Newton's second law of motion to describe the movement of atoms in a system. Atoms and molecules are assigned velocities and hence it is possible to model the evolution of the system over time. Newton's second law of motion states that the force acting upon an object is proportional to its acceleration, i.e. $\boldsymbol{F} \propto \boldsymbol{a}$. Therefore, for an atom, i, with a mass a m_i, experiencing a force $\boldsymbol{F}$ will undergo an acceleration given by:

$$\boldsymbol{F} = m_i \cdot \boldsymbol{a}_i \tag{2.48}$$

Consider an atom with a velocity of $\boldsymbol{v}_i t$: if there are no external forces acting on it then its position after a change in time, Δt, will merely be $\boldsymbol{v}_i t \Delta t$. However, when an constant external force acts on the atom the velocity and positions after the time step will become:

$$\boldsymbol{v}_i(t + \Delta t) = \boldsymbol{v}_i(t) + \boldsymbol{a}_i(t)\Delta t \tag{2.49}$$

$$\boldsymbol{r}_i(t + \Delta t) = \boldsymbol{r}_i(t) + \boldsymbol{v}_i(t)\Delta t + \frac{1}{2}\boldsymbol{a}_i \Delta t^2 \tag{2.50}$$

Unfortunately, Equations 2.49 and 2.50 only work when the force remains constant and as such are not directly applicable to real systems. The force on an atom is dependent on the instantaneous position of all the other atoms in the systems and hence does not remain constant. This would necessitate the time step being infinitesimally

small and practical considerations requires the time step to be of finite size. Therefore, once the forces are calculated, algorithms are used to integrate Newton's laws of motion over the finite time step and thus determine the positions and velocities of the atoms.

One of the most basic integrations algorithms is the Verlet algorithm.[183] In this approach, information regarding the positions and accelerations at the current and previous time steps, t and $t - \Delta t$ respectively, to determine the news positions and accelerations at the subsequent time step, $t + \Delta t$. This is achieved by taking the third order Taylor expansion at position $t + \Delta t$ and $t - \Delta t$:

$$\boldsymbol{r}_i(t + \Delta t) = \boldsymbol{r}_i(t) + \boldsymbol{v}_i(t)\Delta t + \frac{1}{2}\boldsymbol{a}_i(t)\Delta t^2 + \frac{1}{6}\boldsymbol{b}_i(t)\Delta t^3 + \vartheta\Delta t^4 \tag{2.51}$$

$$\boldsymbol{r}_i(t + \Delta t) = \boldsymbol{r}_i(t) - \boldsymbol{v}_i(t)\Delta t + \frac{1}{2}\boldsymbol{a}_i(t)\Delta t^2 - \frac{1}{6}\boldsymbol{b}_i(t)\Delta t^3 + \vartheta\Delta t^4 \tag{2.52}$$

where $\boldsymbol{b}_i$ is the third derivative of $\boldsymbol{r}_i$ with respect to t and ϑ is an accuracy parameter. By summing Equations 2.51 and 2.52 together, the positions at time $t + \Delta t$ can be calculated:

$$\boldsymbol{r}_i(t + \Delta t) = 2\boldsymbol{r}_i(t) - \boldsymbol{r}_i(t - \Delta t) + \boldsymbol{a}_i(t)\Delta t^2 + \vartheta\Delta t^4. \tag{2.53}$$

The Verlet algorithm does not explicitly calculate the velocities, however, they can be derived from knowledge of the trajectories. This is done by subtracting Equation 2.52 from Equation 2.51.

$$\boldsymbol{r}_i(t + \Delta t) - \boldsymbol{r}_i(t + \Delta t) = 2\boldsymbol{v}_i(t)\Delta t + \vartheta\Delta t^3 \tag{2.54}$$

$$\boldsymbol{v}_i(t) = \frac{\boldsymbol{r}_i(t + \Delta t) - \boldsymbol{r}_i(t - \Delta t)}{2\Delta t} + \vartheta\Delta t^2 \tag{2.55}$$

The algorithms are very simple and easy to implement but are not without their drawbacks. Looking at the truncation errors in Equation 2.53 and Equation 2.55, for former's is of the order of Δt^4 whereas the latter is of the oder Δt^2. Therefore, while the position algorithm is accurate and stable, the velocity algorithm is far less accurate.

An alternative to this algorithm is the Verlet leapfrog algorithm. For this algorithm the velocities are calculated at half–integer time steps:

$$\boldsymbol{v}_i(t + \frac{1}{2}\Delta t) = \frac{\boldsymbol{r}_i(t + \Delta t) - \boldsymbol{r}_i(t)}{\Delta t} \tag{2.56}$$

$$\boldsymbol{v}_i(t - \frac{1}{2}\Delta t) = \frac{\boldsymbol{r}_i(t) - \boldsymbol{r}_i(t - \Delta t)}{\Delta t}. \tag{2.57}$$

Rearranging Equation 2.56 provides an expression for calculating the new positions, based on the old positions and the half–integer time step.

$$\boldsymbol{r}_i(t + \Delta t) = \boldsymbol{v}_i(t + \frac{1}{2}\Delta T)\Delta T + \boldsymbol{r}_i(t) + \vartheta \Delta t^4 \tag{2.58}$$

Furthermore, starting from Equation 2.53, by subtracitng $\boldsymbol{r}_i(t)$ from both sides, dividing across by Δt and the substituting in Equation 2.56 and Equation 2.57, it possible to achieve an expression for determining the velocity at the half–integer time steps:

$$\boldsymbol{v}_i(t + \frac{1}{2}\Delta t) = \boldsymbol{v}_i(t - \frac{1}{2}\Delta t) + \boldsymbol{a}(t)\Delta t + \vartheta \Delta t^3. \tag{2.59}$$

This is where the algorithm gets its name from; because the velocities are calculated at the half–integer time steps, they are said to 'leap–frog' over the positions. The main advantages of this over the previous Verlet algorithm is that it now has a numerical precision of Δt^3, as opposed to Δt^2, and it reduces problems associated with calculating positions over long time steps. However, because the position and the velocity are not calculated at the same time, it is not possible to calculate the potential and kinetic energy contributions to the total energy at the same time. This problem is overcome by employing the following equation:

$$\boldsymbol{v}_i(t) = \frac{1}{2}\left[\boldsymbol{v}_i(t + \frac{1}{2}\Delta t) + \boldsymbol{v}_i(t - \frac{1}{2}\Delta t)\right] \tag{2.60}$$

An additional problem inherent to all these algorithms is the simple fact that the algorithms require knowledge from the previous step and hence are not self–starting. Therefore, for the initial step velocities need to be assigned to the atoms. The velocities are randomly assigned to the atom under the constraint that the system starts at the required temperature and the simulation cell has no translational momentum.

2.2.8 Molecular–Dynamics Ensembles

The conditions under which a system evolves during a MD run are defined by a statistical ensemble. The first such ensemble that will be discuss is the microcanonical, or

NVE, ensemble which holds the number or particles, volume and energy constant. In this ensemble, the constant value, derived from the Hamiltonian, H, takes the form:

$$H_{NVE} = U + K.E. \tag{2.61}$$

where U and K.E. are the potential and kinetic energies respectively. In this work, the microcanonical ensemble is used to equilibrate the systems being studied. During this run, the system is allowed to reach an equilibrium from the initial positions and velocities. From there, data is collected over a sufficiently long time period to observe desired properties.

This work makes use of one of the alternate ensembles, the canonical, or NVT, ensemble which also keeps the number of particles and the volume constant. Instead of keeping the energy constant, the temperature is fixed by coupling the system to a temperature bath. Several temperature baths exist, but this work exclusively uses the Nosé–Hoover thermostat.[184] The temperature of a system at a time t, $T(t)$, can be calculated by:

$$T(t) = \frac{\sum_{i=1}^{N} m_i \boldsymbol{v}_i^2(t)}{k_B f} \tag{2.62}$$

where f is the number of degrees of freedom, which is $3N$-3 for periodic systems. Therefore, by adjusting the forces of the system the temperature can be modified to match an external temperature, T_{ext}. This change in velocity is given by:

$$\frac{d\boldsymbol{v}(t)}{dt} = a(t) - \chi(t)\boldsymbol{v}(t) \tag{2.63}$$

where χ is a friction coefficient whose value is controlled by:

$$\frac{d\chi(t)}{dt} = \frac{fk_b}{Q}(T(t) - T_{ext}) \tag{2.64}$$

where Q is the effective mass of the temperature bath. The value of Q determines the strength of the coupling between the two systems: a large value of Q leads to small coupling while smaller values increase the coupling. The definition of Q is given by :

$$Q = fk_B T_{ext} \tau_T^2 \tag{2.65}$$

where τ_T is a specified time constant, termed the relaxation constant. For the NVT ensemble, the conserved quantity, the Helmholtz free energy (derived from the Hamiltonian), is defined as:

$$H_{NVT} = U + K.E. + \frac{1}{2}Q\chi(t)^2 + \frac{Q}{\tau_T^2}\int_0^1 \chi(s)ds \tag{2.66}$$

where s the effective coordinate of the thermostat, and ensures that the total energy between the heat bath and the system remains conserved.

When an MD calculation moves from the "equilibration run" (NVE ensemble) to the "production run" (NVT ensemble), the configurational energy and temperature will begin to oscillate, but the average values will remain constant to those of the NVE ensemble. Thus it is possible to sample a wider range of energy states, resulting in more thermodynamically reasonable values. In this thesis, results were extracted from instantaneous times steps, without employing any time step averaging.

Chapter 3

Computational Methodology

3.1 Vienna *ab initio* Simulation Package (VASP)

All calculations presented in this thesis were carried out with the Vienna *ab initio* Simulation Package (VASP).[150–152] VASP is a quantum mechanical code commonly used for a wide variety of electronic structure calculations. One major advantage of the VASP code it that is can implement a wide variety of quantum mechanical modeling techniques such HF, DFT, DFT+U, Hybrid–DFT and quantum–MD. Furthermore, it contains its own set of optimized PAW pseudopotentials for each element. From there a series of electronic and structural minimisations, i.e. optimisations, are carried out until the systems is deemed to be properly minimised. Subsequently additional properties of the material under study can be calculated, e.g. band structure, density of states, charge density, etc.

3.2 Structural Optimization and Convergence

For self–consistent calculations on solid state materials, the three major factors that determine the precision of the results are; (i) resolution of the basis set, (ii) the k–point sampling density and (iii) sufficient optimisation of the geometry. A flow chart representing the full process of structural optimisation can be seen in Figure 3.1. For each system studied, the convergence was tested against the k–point density and the

plane wave cutoff to ensure suitable values were used. For the plane wave cut–off, to model rapid changes in electron density a high plane wave cut–off is needed. Since the major focus of this study is CeO_2, a high cut–off is needed to model oxygen due it being a lighter atom and hence the valence electrons are close to the core of the atom. To determine the value for the cutoff energy, a series of calculations were performed, where the only variation was the value of the cutoff, until the energy difference between results was deemed sufficiently small (less than 0.01 eV change per formulae unit between cut–offs). For calculations on bulk structures, a plane wave cutoff of 500 eV was used. For the more complex calculations of surfaces, the plane wave cutoff was reduced to 400 eV as it was found to still provide adequate convergence while keeping computational costs to a minimum.

For each system studied in this report, the initial structures were based on experimental results. A series of optimisations were carried out at range of different volumes, while the atom positions, lattice vectors and lattice angles were allow to relax under the constraint of constant volume. The optimisations were carried out until the data bracketed a minimum and the equilibrium volume was then calculated by fitting the energy vs. volume data to the Murnaghan equation of state.[185] Once the equilibrium volume was determined, the system underwent a final optimisation at that volume.

3.3 Electronic Structure Calculations

3.3.1 Band Structures

The band structure of a solid material describes the states of electrons in solid materials and how the energy of these states varies across phases of k–space. To calculate the band structure from DFT calculations, the Kohn–Sham eigenvalues are extracted from the calculation and are plotted as a function of k. From the band structure numerous electronic properties of the material can be determined, including the band–gap, optical absorbance, position of defect states, etc.

To perform a band structure calculation in VASP, the charge density and wave-

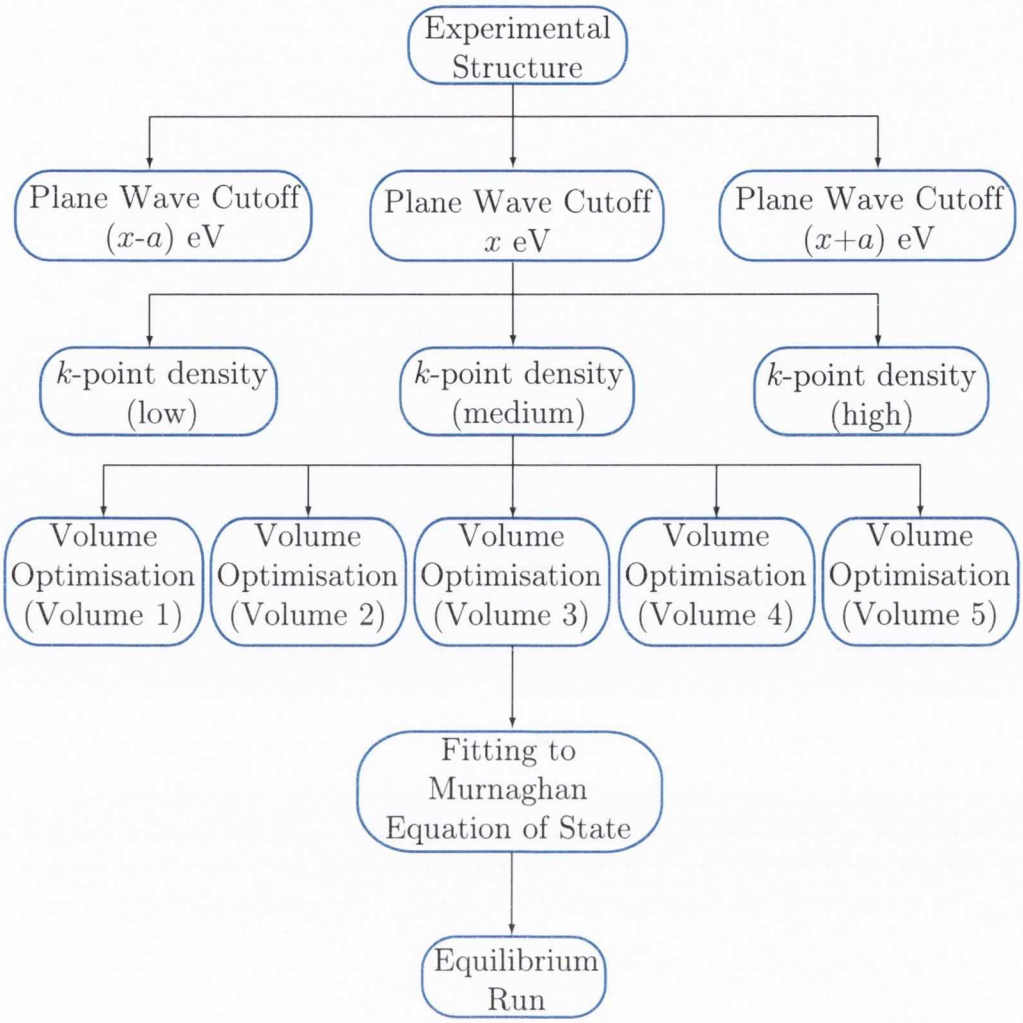

Figure 3.1: A flow chart demonstrating the structural optimisation and convergence procedure.

functions are calculated self–consistently with a homogeneous k–point mesh. A non self–consistent calculation is performed while the charge density is kept constant and the eigenvalues at k–points along the lines of high symmetry in the reciprocal cell are obtained. The eigenvalues are then plotted against these k–points to produce the band structure.

Theoretically, to be entirely accurate a band structure should be calculated along all possible k–points. However, doing so would require an infinite number of vectors and hence is not feasible. Instead, the band structure is calculated along certain lines of the Brillouin–zone which are unique to the crystal class and the change of the band energies over these lines is plotted. The Brillouin–zone of a material is specific to its

space group. For example, the fluorite structure has a $Fm\bar{3}m$ space group (# 225) and its high symmetry points in the Brillouin–zone are shown in Figure 3.2. The energy can then be plotted over a path that visits the points of high symmetry (e.g. the band structure in Chapter 4 follows the path $\Gamma \rightarrow$X$\rightarrow$W$\rightarrow$ $\Gamma \rightarrow$L$\rightarrow$W). The coordinates for the high symmetry points were taken from Bradley and Cracknell.[1]

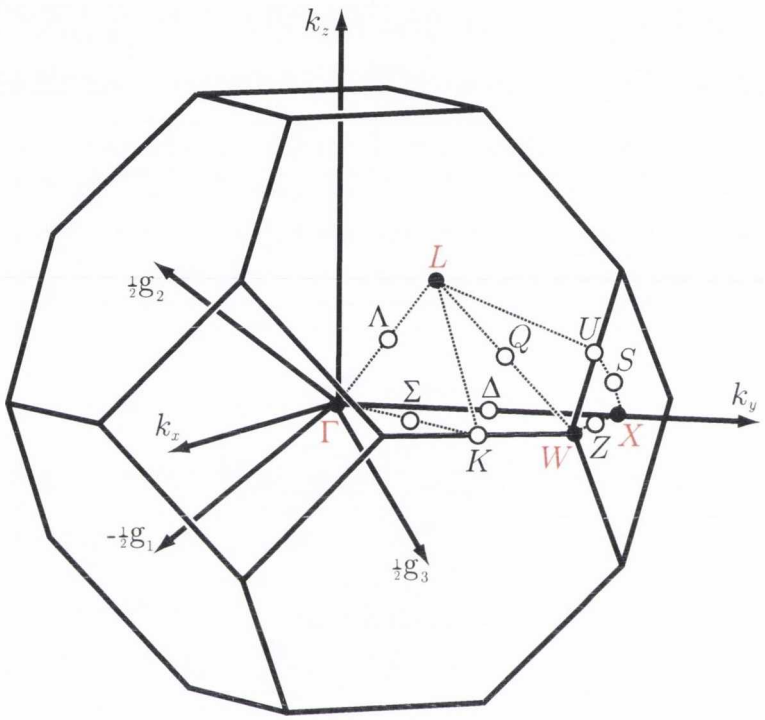

Figure 3.2: The Brillouin Zone for the $Fm\bar{3}m$ space group (from Bradley and Cracknell [1]). Γ = (0,0,0), X = (0, $\frac{1}{2}$, 0), W = ($\frac{1}{2}$, $\frac{1}{2}$, 0), L = ($\frac{1}{4}$, $\frac{1}{4}$, $\frac{1}{4}$).

3.3.2 Electronic Density of States

Another method to analyse the electronic structure of a material is the electronic density of states (EDOS). The EDOS can be considered an integrated form of the band structure, i.e. it displays the density of the eigenvalues as a function of energy. While the EDOS does provide information about the total electronic structure of the system it is not ion specific and hence it is not possible to determine to which ion each state is associated with. To elucidate matters, it is possible to calculate a partial electronic density of states (PEDOS) where the EDOS is decomposed in terms of the ions and

the l and m quantum numbers. To achieve this the wave functions are projected onto the atoms using spherical harmonics. The radius around a certain ion to which the wavefunction will be associated with is determined by the user, and in this thesis they are set as the PAW radii.

3.4 Defect Calculations

Many properties of a material are the result of defects and impurities present in the system. For a crystalline material, such defects are likely to be low in concentration and randomly distributed throughout the system. Therefore in most instances modeling a defect in a single unit cell will not produce accurate results: due to the small number of atoms in the cell, the introduction of a single defect would reflect a large defect concentration and furthermore the small size could mean that, due to periodic boundary conditions, the defect will interact with its own image. To be able to model low defect concentrations, the unit cell is expanded into a supercell of sufficient size which then is treated under periodic boundary conditions. In practice it is not always possible to have a supercell of sufficient size due to the complexity of the calculation and the computational resources available. This section will detail the techniques employed to calculate defects in supercells.

3.4.1 Formation Energy of a Neutral Defect

The formation energy of a neutral defect is calculated from

$$\Delta H_{\mathrm{f}}(\mathrm{D}) = (E^{\mathrm{D}} - E^{\mathrm{H}}) + \sum_i n_i(E_i + \mu_i) \tag{3.1}$$

where E^{H} is the total energy of the host supercell and $E^{(\mathrm{D},0)}$ is the energy of the neutral (charge state of 0) defect cell. E_i are the elemental energies, i.e. the energies of the constituent elements in their standard states (e.g. Ce(s) and O_2(g)) and n is the number of atoms of an element added to (positive) or taken from (negative) an external reservoir. μ_i are the chemical potentials of the elements and are to used to

Element	E_i
O_2(g)	-9.88/-2.66
Ce(s)	-4.05
Al(s)	-3.74
Ga(s)	-2.91
Sc(s)	-6.33
Sb(s)	-4.12
In(s)	-2.56
Tl(s)	-2.25
Y(s)	-6.67
La(s)	-4.93

Table 3.1: The calculated elemental energies, E_i, for a range of species investigated in this thesis. Two values are given for O_2(g) due to the two values of U that were applied to the O $2p$ states. The first is for U=0.0 eV and the second is for U=5.5 eV. All values are given in eV.

approximate the formation of defects under different growth conditions. The values of the the elemental energies employed within this thesis are shown in Table 3.1. The calculation of the chemical potentials will be discussed further on in this section.

3.4.2 Chemical Potential Limits

The chemical potentials will vary with the environment, e.g. the experimental growth conditions of the oxide. In principle these values should be treated as a variable but, in practice, limits are placed on the chemical potentials to reduce the number of calculations needed. By varying the chemical potentials of different species, it is possible to model different equilibrium growth conditions within the global constraint of the calculated enthalpy of formation of the host. The formation enthalpies were calculated from the calculated energies of the bulk cells and their constituent elements. Within

this study of CeO_2, using PBE+U calculations on CeO_2, with U values of 5.0 eV and 0 eV place on the Ce $4f$ and O $2p$ states respectively, this yields:

$$\mu_{Ce} + 2\mu_O = \Delta H_f(CeO_2) = -10.5\,eV. \tag{3.2}$$

The upper bound of μ_O, i.e. Ce-poor/O-rich conditions, is determined by the formation of O_2(g):

$$\mu_O = 0\,eV, \rightarrow \mu_{Ce} = -10.5\,eV. \tag{3.3}$$

The lower bound of μ_O, i.e. Ce-rich/O-poor conditions, is determined by the formation of Ce_2O_3:

$$2\mu_{Ce} + 3\mu_O \leq \Delta H_f(Ce_2O_3) = -18.97\,eV. \tag{3.4}$$

By solving Equations 3.2 and 3.4 simultaneously the chemical potentials for Ce-rich/O-poor conditions are obtained:

$$\mu_O = -2.03\,eV,\ \mu_{Ce} = -6.44\,eV. \tag{3.5}$$

3.4.3 Temperature and Pressure Dependence of Defect Formation

All static DFT calculations are carried out at a temperature of 0 K. Therefore, the calculated defect formation enthalpy would differ from the formation enthalpy of a material under real–world conditions, e.g. typically a CeO_2 electrolyte in an SOFC would experience temperatures of ~500-1000 K and partial oxygen pressures ranging from P=10^{-10} atm (anode end) to P=0.2 atm. To relate the calculated values to working conditions, temperature and pressure dependence analyses are performed.

For CeO_2, the effect of temperature and pressure on the defect formation energies are estimated by considering the enthalpic and entropic contributions to the oxygen chemical potential μ_O in the O_2 gas phase. The direct effects of temperature and pressure on μ_{Ce}, $\Delta H_f(CeO_2)$ and $\Delta H_f(Ce_2O_3)$ are neglected as these are either small ($P\Delta V$ terms) or are expected to cancel as the vibrational frequencies of the reference materials will be relatively insensitive to temperature ($T\Delta S_{vib}$). However, μ_{Ce} will be

affected by the condition $\mu_{Ce} + 2\mu_O = \Delta H_f(CeO_2)$. As the only concern is the change in μ_O, it is necessary to only take into account the effect of the partial oxygen pressure. The change to μ_O can be expressed as:[186]

$$\Delta\mu_O(T,P) = \frac{1}{2}\left\{C_p(T-T_0) - T\left[S_0 + C_p \ln\frac{T}{T_0}\right] + k_B T \ln\frac{P}{P_0}\right\} \tag{3.6}$$

In the above equation the constant-pressure specific heat capacity per diatomic molecule is taken as $C_p{=}\frac{7}{2}k_B$, derived from the ideal gas law, and the experimental value for the $O_{2(g)}$ standard entropy is $S_0 = 205\,\mathrm{J\,mol^{-1}\,K^{-1}}$. The reference temperature (T_0) and pressure (P_0) are set to 298 K and 1 atm respectively (standard temperature and pressure). Once the temperature and pressure dependence of the formation energies is calculated it is then possible to estimate the defect concentrations as a function of temperature, assuming Arrhenius-type behavior.

3.4.4 Formation Enthalpy of Charged Defects

Impurities and point defects can lead to the formation of new defect levels in the band gap of a material. The presence of the defect levels can be identified experimentally and the nature and type of defect present identified. However, there is no definite way of identifying experimentally if a defect level is caused by a particular defect. Therefore computational techniques are becoming increasingly popular in identifying these defect levels. However, it is generally not possible to compare the single particle levels (SPLs), i.e. the raw eigenvalues (Kohn–Sham states) of the defect state in the band structure, that are calculated because experimental data is usually based on transitions from one charge state to another. To calculate the formation energy of a defect with a charge state of q the following equation is used:

$$\Delta H_f(\mathrm{D,q}) = (E^{\mathrm{D,q}} - E^{\mathrm{H}}) + \sum_i n_i(E_i + \mu_i) + q(E_{\mathrm{Fermi}} + \epsilon^H_{\mathrm{VBM}}) + E_{\mathrm{align}}[q] \tag{3.7}$$

where $E^{\mathrm{D,q}}$ is the total energy of the defective cell. E_{Fermi} ranges from the VBM to the conduction band maximum (CBM). $\epsilon^H_{\mathrm{VBM}}$ is the eigenvalue of the VBM of the host bulk. $E_{\mathrm{align}}[q]$ is the correction terms which accounts for (i) the alignment between the

VBM of the host bulk with the defective supercell and (ii) the finite-size-cell effects that occur in calculations of charged defects. $E_{\text{align}}[q]$ is calculated using the 'sxdefectalign' program, which is based on the correction scheme developed by Freysoldt *et al.*[187] This scheme cancels the interaction betweens images of the charged defects and aligns the electrostatic potential to the bulk material. These are calculated from the local potentials of the defect and a reference cell, the pure bulk, and the only extra parameter required for this scheme is the dielectric constant. DFT is known to have problems calculating dielectric constants, and therefore it is taken from experimentally determined values (e.g. for CeO_2 ε=24.5).[188]

3.4.5 Thermodynamic Transition Levels

To compare computational results with experiment, the thermodynamic ionization (transition) levels $\epsilon_D(q/q')$. These are defined as the Fermi level at which two charge states, q and q', will have the same formation energy. To calculate them, the following equation is used:

$$\epsilon_D(q/q') = \frac{\Delta H^f(D,q) - \Delta H^f(D,q')}{q' - q}. \tag{3.8}$$

These transition levels can be compared to experimentally derived trap levels.

3.4.6 Transition Level Diagrams

A transition level diagram displays a plot of the formation energy of a defect as a function of the Fermi level. Such graphs are commonly found in computational studies on semiconductors and although they are an effective way of displaying the properties of defects, understanding the information presented can be difficult.

An example of a transition level diagram is displayed in Figure 3.3. The figure displays two plots showing the formation energy versus E_{Fermi} at constant chemical potentials, cation–rich/anion–poor, (3.3(a)), and cation–poor/anion–rich, (3.3(b)). Defects usually have many different charge states (dashed lines) but for the sake of clarity only the lowest energy charge state (solid lines) at each value of E_{Fermi} is plotted. It is

possible that a certain charge state will not be stable across the Fermi level and hence will not be observed experimentally. These defects are known as negative U defects, [189] where U in this instance is defined as the difference between ionisation energy and electron affinity. Therefore, a defect is considered a negative U defect if it can trap a second electron (or hole) more strongly than the first. An example of such a defect can be see in Figure 3.3: the +1 charge state for the anion vacancy remains unstable at all values of E_{Fermi}.

When an n–type defect is formed, extra electrons are introduced to the VBM. These electrons aren't stable, so the E_{Fermi} is pushed higher in the band gap until the electron localises on a defect (the positive slopes seen in Figure 3.3). Conversely, p-type introduce holes to, or near, the VB, which serves to lower E_{Fermi} (the negtaive slopes in Figure 3.3). When the formation energies of the defects are equal, they are in equilibrium with each other. These points, the thermodynamic ionisation (transition) levels, as calculated from Equation 3.8, are represented on the graph by the solid dots. The positions of the transition levels relative the VBM or CBM are good indicators of the conductivity of the system. Defects with ionisation levels $\sim 30\,\text{meV}$ from the band edges are called shallow defects and are important for conductivity. If the transition levels of an n–type defect are close to the CBM, then the system is a good n–type conductor as electrons associated with these defects, known as shallow donors, can be thermally excited into the conduction band (CB). For p–type defects, unoccupied transition levels close to the VBM are indicative of good p–type conductivity, allowing the facile promotion of holes states to the VB from these shallow acceptor levels.

The material that Figure 3.3 describes would be a n–type conductor under cation–rich/anion–poor conditions. At all ranges within the band gap, the n–type defect has the lowest formation energy and will therefore be the dominant defect. The fact that the (+2/0) transition level is very far from the CBM indicates that the conductivity in this material will be dependent on the polaronic hopping of the electron. As the system moves to cation–poor/anion–rich conditions, the p–type defect begins to dominate at lower Fermi levels. However, p–type conduction would not be possible in this system

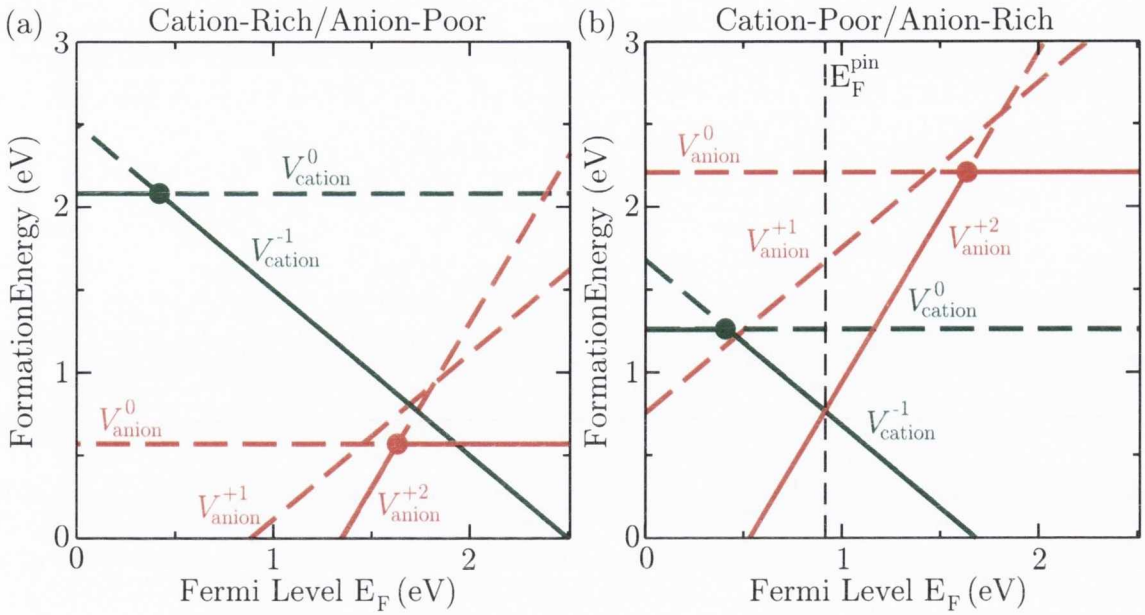

Figure 3.3: A model transition level diagram for a representative material under (a) cation–rich/anion–poor conditions and (b) cation–poor/anion–rich. n–type defects are described by the colour red lines whereas the p–types are denoted by green. The solid circles represent the transition levels ($\epsilon_D(q/q')$). The dashed line shows the Fermi pinning energy.

due to the crossover of the acceptor and donor states, depicted in 3.3(b). At his point, the effects of the n– and p–type defects, which serve to raise and lower E_{Fermi} respectively, cancel each other out and E_{Fermi} is pinned at that energy.

3.5 Mean Square Displacement Plots and the Nernst–Einstein Equation

The mean square displacement (MSD) is a statistical method that describes the average structural difference between two systems. In molecular dynamics, it can be used to calculate the average movement of an ion over a certain time frame. The MSD is calculated with the equation:

$$MSD(t) = \langle \sum_{i=1}^{N} [\boldsymbol{r}_i(t) - \boldsymbol{r}(0)]^2 \rangle \tag{3.9}$$

However, the calculations performed in this thesis all employed periodic boundary conditions. Therefore, if an atom where to diffuse across one side of the cells, its periodic image is mapped to the opposite side of the cell. As such, it is impossible to track the diffusion of atoms across periodic cells from only their position. However, it is possible to obtain the MSD by mapping the position to the velocity of the atoms.

An example of an MSD plot for a notional binary oxide is shown in Figure 3.4. The plot shows that the line representing the cation remains constant throughout with only minimal movement. This suggests that the cations are experiencing thermal vibrations but remain at their lattice sites. The line representing the O anions, however, increases over the time period, reaching $\sim$8 Å^2. This indicates that the O ions are diffusing freely through the solid material. The MSD plots presented in this thesis were all calculated from a single time origin

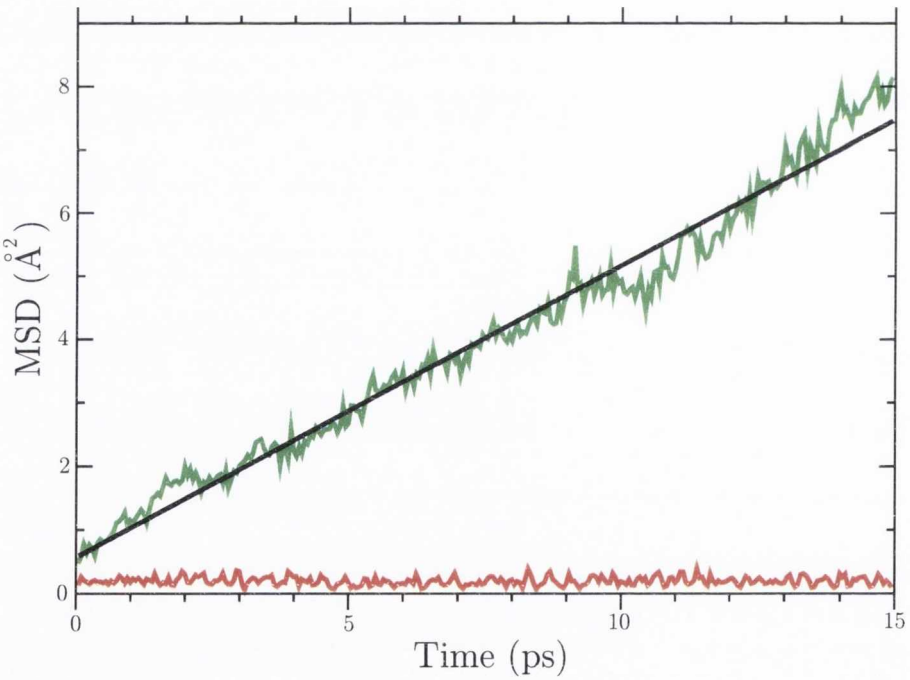

Figure 3.4: An example of an MSD for a theoretical oxide material, AO. The red lines show the MSD of the cations while the green lines indicate the MSD of the O anions.

Perhaps one of the most important pieces of information that can be derived from the MSD plot is the diffusion coefficient, D, which is the displacement of a species per unit time. The diffusion coefficient is easily calculated as it is simply sixth of the slope

of the MSD plot. Once the value of D is known, it become possible to estimate the ionic conductivity through the Nernst–Einstein relation:

$$\sigma_{\mathrm{NE}} = \frac{c^2 \rho D}{k_B T} \tag{3.10}$$

where c is the charge of the mobile species, ρ is the density of charge carriers in the system and T is the temperature of the system. Once these values are known, it is possible to compare them to experiment values.

3.6 Radial Distribution Function

The radial distribution function is a statistical method that can be used to determine how the concentration of atoms changes as a function of the radius around a reference atom. For MD simulations, it is used to describe the average structure of the simulation cell across the entire run, providing information such as the average nearest–neighbour distance between ions. The RDF is calculated with the following equation:

$$\mathrm{RDF} = \frac{1}{4\pi r^2 \Delta r} \frac{n_{ij}(r)}{\rho_j} \tag{3.11}$$

where n_{ij} is the number of atoms of type j that are between a distance of r to $r+\Delta$ from the reference atom, i, and ρ_j is the number concentration of atoms of type j. Equation 3.11 is actually the partial radial distribution function, which calculates the RDF between two specified species. An example of an RDF for a notional oxide, AO, is shown in Figure 3.5, where the RDF is plotted between oxygen anions and the cations A. Two peaks are present in the plot, one from just under 2.00 Å to 3.50 Å, and the second from 3.50 Å to just under 5.50 Å. The peaks represent the nearest neighbour and next–nearest neighbour distance between A and O respectively. Since the atoms are moving during a MD run, there's no set bond length, due to the constant vibration, or even diffusion, of the anions, hence the peaks encompassing a wide range of values. The first peak shows that the A–O bond length will vary by ~1.68, but the majority of ions will possess a bond length of about 2.27 Å. The fact that the RDF goes almost to 0.00 at 3.50 Å indicates that the NN and NNN positions between the atoms is very

well defined. This would suggest there are no O ions occupying interstitial sites, and that diffusion in the system occurs through a discrete hopping mechanism between neighbouring lattice sites.

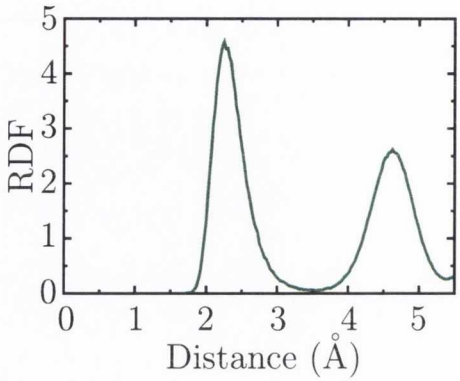

Figure 3.5: An example of an RDF for a theoretical oxide material, AO. The green line shows the plot of the RDF between A and O.

Chapter 4

Analysis of Intrinsic Defects in CeO_2

4.1 Introduction

CeO_2 is an important material for a wide range of different applications, including: catalysis, both as an active catalysts and as a support material; the electrolyte material in SOFCs; gas sensing; and high–κ dielectric applications. All of these properties are a consequence of defects present in CeO_2 and hence exploring the chemistry of such features is an active area of research. In the area of intrinsic defects, previous work has concentrated on O vacancies in CeO_2, with only a handful of studies having investigated the properties of other intrinsic defects. Theoretical data on Ce vacancies by Fernandes *et al*, using LDA/GGA+U calculations, with the full–potential linear muffin–tin–orbial method, predicted that these defects would be semi–metallic in nature,[190] contrary to similar defects in other metal oxides.[174,191,192] The structure of Frenkel defects has been investigated[144,193] and their effect on ionic conductivity was investigated through molecular dynamics calculations, which suggested that such defects are more likely to recombine than contribute to conductivity.[144] Yasunaga *et al.*[194,195] investigated CeO_2 surfaces under electron radiation determining that O and Ce interstitials were present, but their exact structure and impact on the intrinsic properties of CeO_2 was

not investigated. It has also been shown that CeO_2 will display intrinsic ferromagnetism when synthesised as a thin film.[196–198] However, the cause of this phenomenon has yet to be determined.

In this chapter PBE calculations with on–site Coulomb correction (PBE+U) are employed to explore the properties of intrinsic defects within CeO_2. Using a Koopmans–like approach, a suitable U value for the O $2p$ states was determined, enabling the accurate modelling of p–type defects. For the first time, information on the formation energies and also the geometry and electronic structure of each defect is also provided. Defect concentrations are then assessed as a function of temperature and O partial pressure.

4.2 Computational Methods

As discussed in Chapter 2, standard LDA and GGA functionals are incapable of correctly modeling systems with localised electronic defects due to the inherent SIE.[163,168,169] Therefore the PBE+U method[170] was employed to approximately correct the SIE associated with PBE calculations.[170,199,200] Previous theoretical work found that the expected structure of reduced CeO_2 could be reproduced by introducing a $+U$ correction with $U\{\text{Ce } 4f\}$=5.0 eV.[106] The U value from different calculations are not always directly comparable, as each functional will have a different SIE and each programs' implementation of the U correction will differ in how they determine orbital occupations. However, subsequent studies demonstrate that values of $U\{\text{Ce } 4f\}$=5.5 eV[201], 4.5 eV[107] and 5.0 eV[97,106,202–204] can accurately model the ground state properties of pure and reduced CeO_2. Accurate descriptions of CeO_2 and reduced CeO_2 have also been obtained with hybrid-DFT techniques.[205,206] These methods reduce the SIE error by introducing a small amount of the exact non-local Fock exchange to the approximate DFT exchange-correlation functionals. However, it was deemed that the PBE+U method with $U\{\text{Ce } 4f\}$=5.0 eV was more suitable as this method will reduce the SIE without the high computational overhead associated with hybrid–DFT in a

plane wave basis set.

Previous studies on metal oxides have shown that when employing LDA(GGA) to model O–derived p-type defect states, such as localised holes, it is necessary to account for the SIE associated with the O $2p$ states which can be accomplished using the $+U$ approach.[162,168,174,191,192] Previous studies used a $U\{\text{O } 2p\}$ value of 7 eV,[118,119] but this value was derived for MgO.[168] Because it was expected that some of the defects studied may lead to the formation of localised holes on oxygen anions, it was necessary to determine a suitable value of $U\{\text{O } 2p\}$ for CeO_2.

To determine the U value for the O $2p$ states an *ab initio* fitting procedure used by Morgan and Watson was employed,[191] similar to the Koopmans-like procedure developed by Lany and Zunger.[174] This method is based on the requirement that for a self–interaction free system the energy change when an electron is added or removed should be linear (cf. Section 2.1.9).[207] For this condition to be met, the addition of an electron to a hole state (with N electrons) must satisfy

$$E(N+1) - E(N) = e_i(N) \tag{4.1}$$

where $E(N)$ is the energy of the system with a self-trapped hole (the +1 charge state), $E(N+1)$ is the energy of the neutral system with the same structure as the $E(N)$ system and $e_i(N)$ is the eigenvalue of the hole state relative to the VBM. Included in the calculation of the charged cell are two corrections; a core-level alignment and an image charge correction which were calculated with the "sxdefectalign" program as described in Section 3.4.4. When $E(N+1) - E(N)$ and $e_i(N)$ are plotted against U (Figure 4.1), it is observed that at $U\{\text{O } 2p\}$=5.5 eV the requirement of Equation 4.1 is satisfied, indicating that the SIE of the system has been overcome. This suggests that the value of $U\{\text{O } 2p\}$=7 eV that was used previously by Yeriskin and Nolan[118,119] would not satisfy Equation 4.1 and hence would over–stabilize/localise O holes in CeO_2.

The defect formation energies, $\Delta H_f(\text{D})$, are calculated according to Equation 3.1 in Chapter 3. In Section 3.4.2, it was demonstrated how to calculate the chemical potential limits when $U\{\text{Ce } 4f\}$=5.0 eV and $U\{\text{O } 2p\}$=0 eV, hereafter denoted as

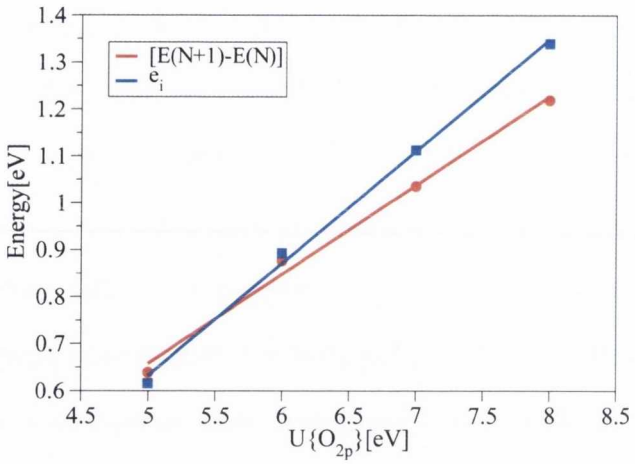

Figure 4.1: The variation of the electron addition energy , $E(N+1) - E(N)$ (red line, red circles), and the hole state eigenvalue (relative to the VBM), e_i (blue line, blue squares) of the +1 charge state of CeO_2, as a function of $U\{O_{2p}\}$. For all calculations $U\{Ce_{4f}\}$=5.0 eV.

$U_{Ce,O}$=$\{5.0,\ 0.0\}$ eV. To reiterate, the results were $\mu_O = 0\,eV, \mu_{Ce} = -10.5\,eV$ at the O–rich/Ce–poor limit and $\mu_O = -2.03\,eV$, $\mu_{Ce} = -6.44\,eV$ at the O–poor/Ce–rich limit.

For calculations where $U_{Ce,O}$=$\{5.0,\ 5.5\}$ eV, the formation energies are: $\Delta H_f(CeO_2) = -9.67\,eV$, $\Delta H_f(Ce_2O_3) = -17.7\,eV$, which sets the chemical potentials at the Ce-poor/O-rich limit as: $\mu_O = 0\,eV$, $\mu_{Ce} = -9.67\,eV$, and at the Ce-rich/O-poor limit to $\mu_O = -1.64\,eV$, $\mu_{Ce} = -6.39\,eV$.

The effect of temperature and pressure on the formation energies were calculated according to the method described in Section 3.4.3.

4.3 Bulk Properties

The lattice constant of CeO_2 for $U_{Ce,O}$=$\{5.0,\ 0.0\}$ eV ($U_{Ce,O}$=$\{5.0,\ 5.5\}$ eV) was calculated to be 5.494 Å (5.477 Å), which is within 1.5% (1.2%) of the experimental lattice constant of 5.41 Å.[208] The Ce–O bond length, 2.377 Å (2.372 Å), also agrees with the experimental bond length, being within 1.5% (1.2%) of the recorded value of 2.343Å.

[209] The band structure and PEDOS were calculated for $U_{Ce,O}$={5.0, 0.0} eV and $U_{Ce,O}$={5.0, 5.5} eV and minimal differences were observed between them (Figure 4.2). The calculated band gap was found to be 2.45 eV (2.51 eV). These values are significantly lower than experimentally determined band gap, which have been reported to be 2.76 eV,[210] 3.31 eV,[211] and 3.60 eV.[212] This is not unexpected as GGA is well known to underestimate band gaps despite accurately describing the ground state properties.[171] By integrating the PEDOS, it was found that 11.8% (12.4%) of the electrons in the valence band are associated with Ce states, showing that there is no significant redistribution of the electrons upon the introduction of $U\{O_{2p}\}$.

4.4 Defect Structure

All defect calculations in CeO_2 were carried out in simulation cells with the same lattice parameters as the pure bulk cell. Furthermore, each defect was calculated using both $U_{Ce,O}$={5.0, 0.0} eV and $U_{Ce,O}$={5.0, 5.5} eV. For each of the defects investigated several possible structures and spin states were calculated to determine the lowest energy structure.

4.4.1 Oxygen Vacancy

During the formation of an oxygen vacancy, two excess electrons are localised onto nearby Ce ions, reducing them from Ce(IV) to Ce(III).[106,107,201,203] In Kröger–Vink notation this is

$$O_O^x + 2Ce_{Ce}^x \rightarrow V_O^{\bullet\bullet} + 2Ce'_{Ce} + \frac{1}{2}O_2(g), \tag{4.2}$$

where O_O^x represents a neutral O ion on an O lattice site, Ce_{Ce}^x is a neutral Ce atom (i.e. Ce(IV)) on a Ce lattice site, $V_O^{\bullet\bullet}$ is a doubly positively charged vacancy at an oxygen lattice site and Ce'_{Ce} is singly negatively charged cerium (i.e. Ce(III)) at a cerium lattice site. The excess electrons occupy previously empty $4f$ states on the Ce ions. This is supported by experimental studies, which have found distinctive $4f$ peaks deep in the band gap of reduced CeO_2.[93,213,214] For the calculations of an

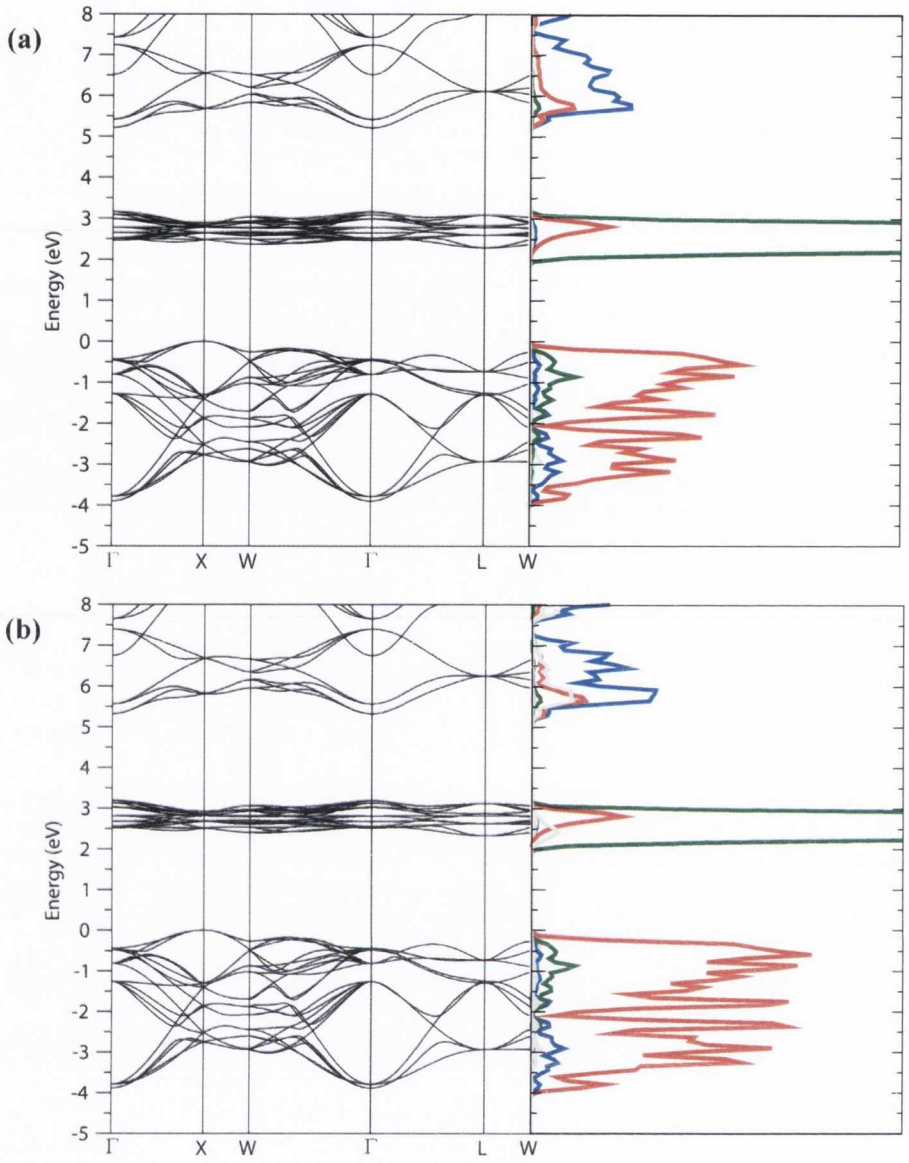

Figure 4.2: The band structure and PEDOS of pure CeO_2 for (a) $U_{Ce,O}$={5.0, 0.0} eV and (b) $U_{Ce,O}$={5.0, 5.5} eV. The VBM is set to 0 eV. The blue lines represent Ce $5d$ states, the green lines Ce $4f$ states and the red lines O $2p$ states. All other states are shown in grey.

oxygen vacancy in CeO_2, the structures obtained for the two different cases when $U_{Ce,O}$={5.0, 0.0} eV and $U_{Ce,O}$={5.0, 5.5} eV were found to be very similar, Figures 4.3(a) and (b) respectively. There was almost no difference in energy between the ferromagnetic and anti-ferromagnetic configurations (<0.1 meV) and therefore only the ferromagnetic configuration of the excess electrons is displayed. The vacancy is

an area of effective positive charge, and hence, the eight neighbouring oxygen ions move off their lattice site towards the vacancy, while the neighbouring Ce ions move away from the vacancy. For calculations where $U_{Ce,O}$={5.0, 0.0} eV ($U_{Ce,O}$={5.0, 5.5} eV) the neighbouring oxygen which is only coordinated to Ce(IV) ions moves by 0.22 Å (0.30Å), the oxygen ion bridging the two Ce(III) ions by 0.04 Å (0.03Å) and the four oxygens which are coordinated to one Ce(III) ion by 0.19 Å (0.12Å), all towards the vacancy. The two Ce(III) ions move 0.09 Å (0.13Å) whereas the Ce(IV) ions move a distance of 0.16 Å (0.18Å). The variation in the relaxation of the oxygen ions can be related to the Ce(III) ions having a lower charge than the Ce(IV) ions, leading to longer Ce(III)-O bond.

Figures 4.3(c) and (d) shows the EDOS for an oxygen vacancy in CeO_2, with a ferromagnetic arrangement of electrons, when $U_{Ce,O}$={5.0, 0.0} eV and $U_{Ce,O}$={5.0, 5.5} eV respectively. It can be observed in these figures that there are only very minor differences between the two cases. We can see that between the O $2p$ dominated valence band and the Ce $4f$ dominated conduction band a new defect peak has appeared, made up of occupied Ce $4f$ states, which indicates the presence of Ce(III) ions. The EDOS for the anti–ferromagnetic configuration displays a similar Ce $4f$ defect peak, albeit with one peak spin up and the other spin down. Both the position and nature of the defect peak are consistent with previous experimental[93] and theoretical[106,202,215,216] work.

4.4.2 Cerium Interstitial

The addition of a Ce interstitial introduces four extra electrons to the system. There are two different ways for the excess electrons to localise; either the electrons localise on four of the Ce ions neighbouring the vacancy, reducing them from Ce(IV) to Ce(III)

$$4Ce_{Ce}^{x} + Ce(s) \rightarrow 4Ce'_{Ce} + Ce_{i}^{\bullet\bullet\bullet\bullet}, \tag{4.3}$$

or one electron remains on the interstitial ion while three of the neighbouring Ce ions are reduced

$$3Ce_{Ce}^{x} + Ce(s) \rightarrow 3Ce'_{Ce} + Ce_{i}^{\bullet\bullet\bullet}. \tag{4.4}$$

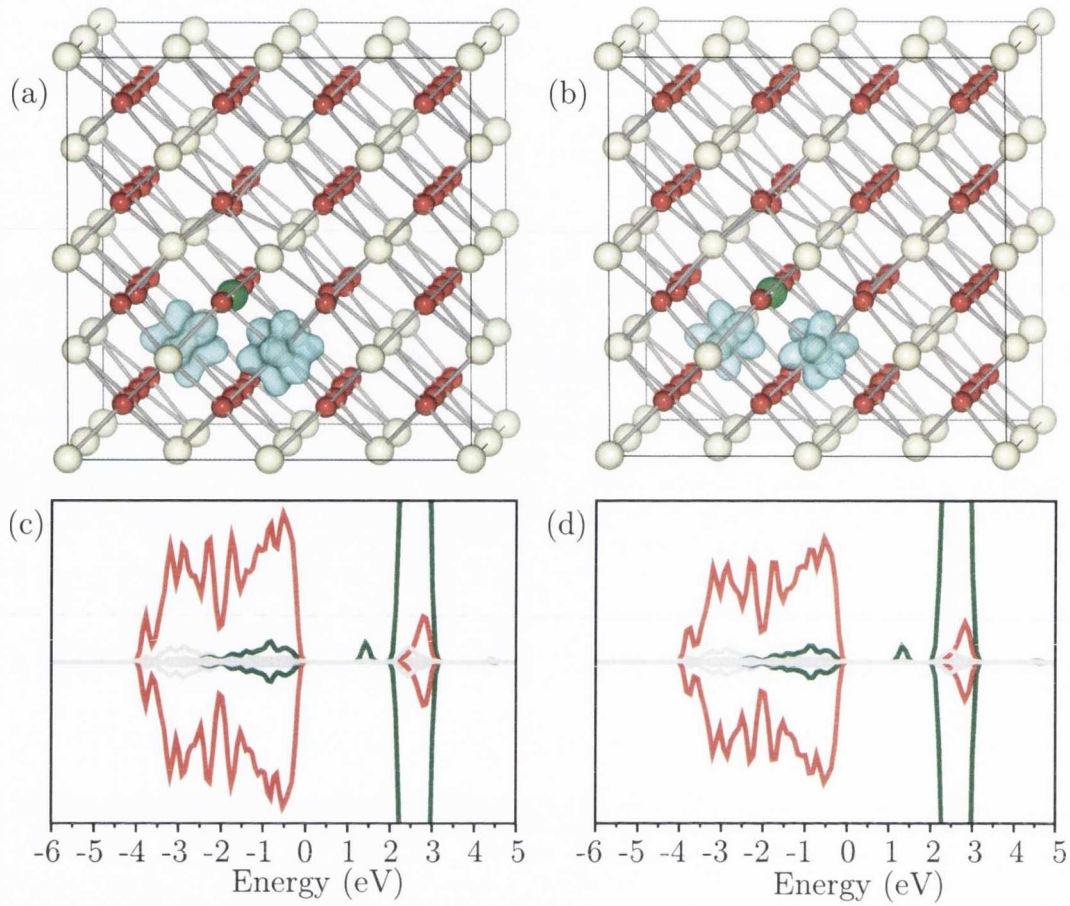

Figure 4.3: The structure with spin-density plot when (a) $U_{Ce,O}$={5.0, 0.0} eV and (b) $U_{Ce,O}$={5.0, 5.5} eV and the density of states of an O vacancy in CeO_2 with (c) $U_{Ce,O}$={5.0, 0.0} eV and (d) $U_{Ce,O}$={5.0, 5.5} eV. Ce atoms are represented by white spheres, O atoms are represented by red spheres and the position of the vacancy is represented by the light green sphere. The isosurface is shown in blue and is set to 0.05 e/Å^3. For the EDOS, the Ce 4*f* and O 2*p* states are represented by the green and red lines respectively. All other states are shown in grey.

Figures 4.4 (a) and (b) shows the structure, spin density and EDOS for the cerium interstitial when $U_{Ce,O}$={5.0, 0.0} eV and $U_{Ce,O}$={5.0, 5.5} eV respectively. Once again, minimal differences exist between the structures. The lowest energy was found when the excess electrons localise according to Equation 4.4 in an anti-ferromagnetic configuration (Figures 4.4(b) and (c)). For $U_{Ce,O}$={5.0, 0.0} eV ($U_{Ce,O}$={5.0, 5.5} eV), the singlet configuration was lower in energy than the quintet and triplet states by

240 meV (450 meV) and 90 meV (140 meV) respectively. The eight oxygen ions neighbouring the interstitial ion remain on their lattice sites. The six Ce ions that neighbour the interstitial relax away from it by 0.25 Å for the Ce(III) ions and 0.32 Å for the Ce(IV) ions for both values of $U\{O_{2p}\}$.

The EDOS for when $U_{Ce,O}$={5.0, 0.0} eV and $U_{Ce,O}$={5.0, 5.5} eV, Figures 4.4(e) and (f) respectively, shows defect peaks made up of occupied Ce $4f$ states between the valence and conduction bands, which are due to Ce(III) ions. A partial charge analysis of the defect peaks show that the lowest energy peak in the spin up state is attributed to the interstitial Ce(III) ion. The remaining peaks, which are all at a similar energy, are due to the three Ce(III) ions neighbouring the interstitial, one in the spin up state and two in the spin down state.

4.4.3 Cerium Vacancy

The formation of a neutral Ce vacancy removes four electrons from the lattice. This creates holes in the valence band which are expected to localise on the O $2p$ states, as these states dominate the VBM. In Kröger–Vink notation this would be

$$Ce_{Ce}^{x} + 4O_{O}^{x} \rightarrow V_{Ce}^{''''} + 4O_{O}^{\bullet} + Ce(s). \tag{4.5}$$

Figures 4.5 shows the structures of a Ce vacancy for (a) $U_{Ce,O}$={5.0, 0.0} eV and (b) $U_{Ce,O}$={5.0, 5.5} eV. Both structures are shown with the overall spin in the quintet state, as this spin configuration was found to be marginally lower in energy than the triplet or singlet states (8.5 meV and 11.4 meV respectively). When $U_{Ce,O}$={5.0, 0.0} eV the spin density is delocalised over the eight oxygen ions neighbouring the vacancy, however, when $U_{Ce,O}$={5.0, 5.5} eV we obtain a different picture with localised holes on four of the O ions neighbouring the vacancy. This is a result of the SIE: in the former case the SIE associated with the O states delocalises the hole states over the eight neighbouring O ions. When the $+U$ correction is applied to the O $2p$, the localised electronic structure is achieved. For $U_{Ce,O}$={5.0, 0.0} eV the eight O ions that neighbour the Ce vacancy move away from the vacancy by between 0.13 and

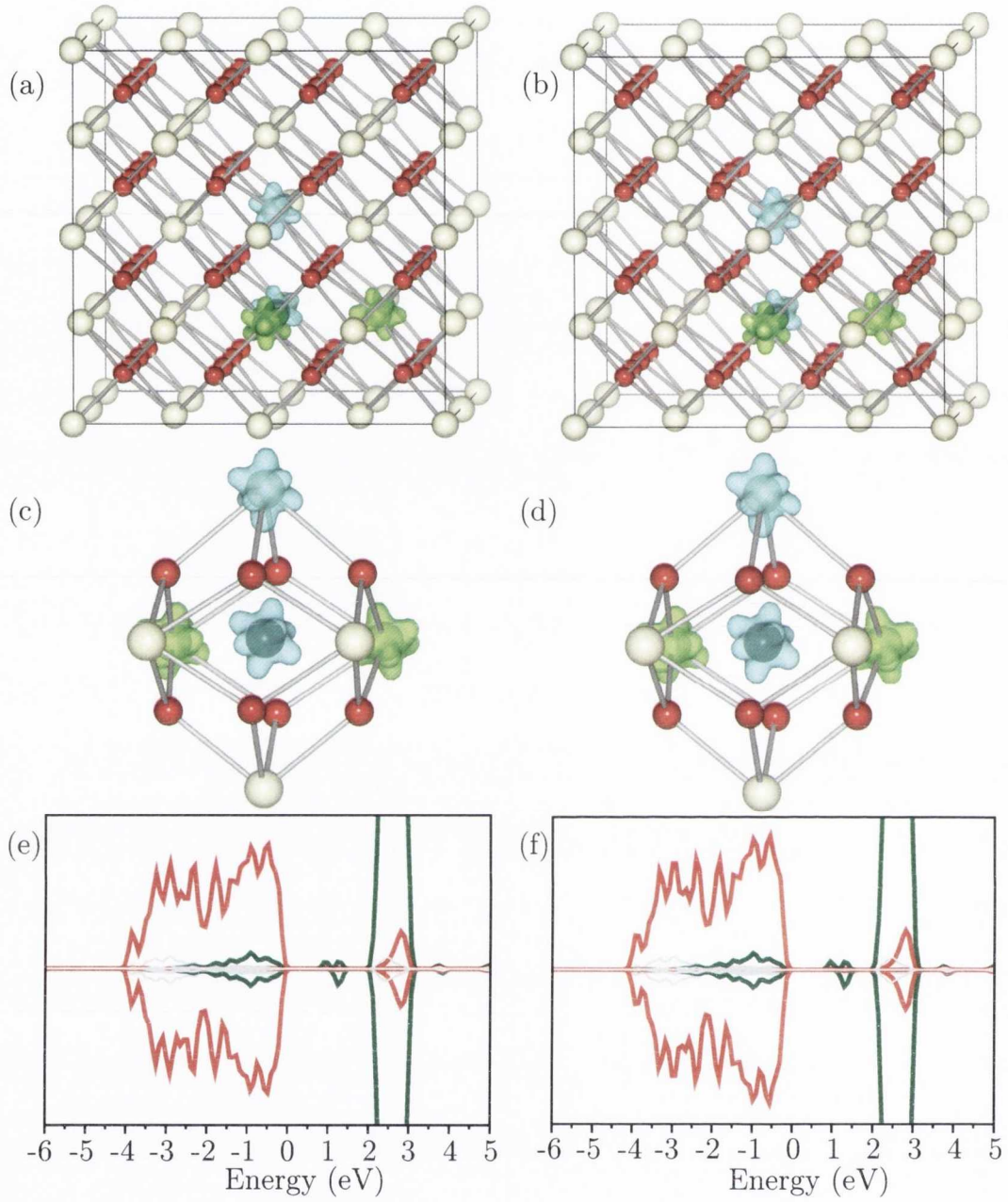

Figure 4.4: The full simulation cell when (a) $U_{\mathrm{Ce,O}}$={5.0, 0.0} eV and (b) ($U_{\mathrm{Ce,O}}$={5.0, 5.5} eV) and the local structure of a Ce interstitial with a partial charge–density plot of the defect peaks for (c) $U_{\mathrm{Ce,O}}$={5.0, 0.0} eV and (d) $U_{\mathrm{Ce,O}}$={5.0, 5.5} eV and the density of states of a Ce interstitial in CeO_2 when (e) $U_{\mathrm{Ce,O}}$={5.0, 0.0} eV and (f) $U_{\mathrm{Ce,O}}$={5.0, 5.5} eV. The Ce interstitial is represented by the black sphere and the blue isosurface represents the spin-up electrons and the green isosurface represents the spin-down electrons. The isosurfaces are set to 0.05 e/Å^3.

0.14 Å. When $U_{Ce,O}$={5.0, 5.5} eV the O^x ions relax away from the cerium vacancy by 0.26 Å whereas the $O^\bullet$ ions relax towards the vacancy by 0.03 Å leading to an increased Ce(IV)-$O^\bullet_O$ bond (2.44 Å) since the $O^\bullet$ ions are less negatively charged than the O^x ions.

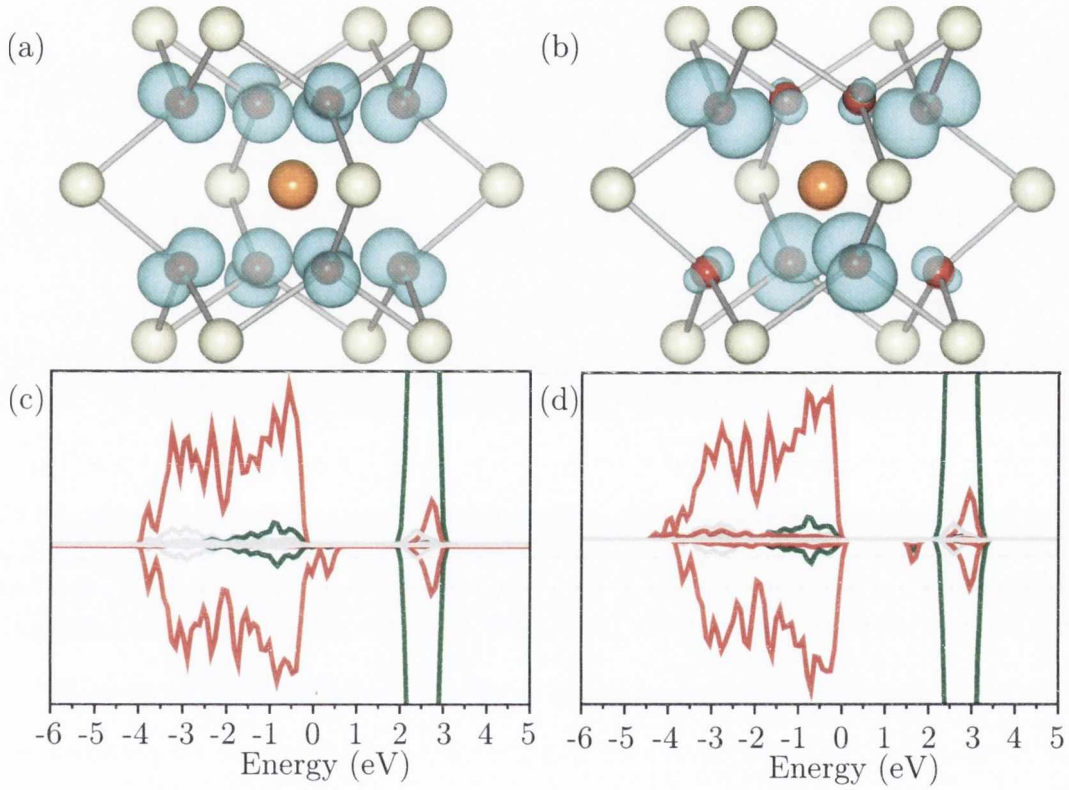

Figure 4.5: The local structure around a Ce vacancy in CeO_2 when (a) $U_{Ce,O}$={5.0, 0.0} eV and (b) $U_{Ce,O}$={5.0, 5.5} eV and the density of states for a cerium vacancy with (c) $U_{Ce,O}$={5.0, 0.0} eV and (d) $U_{Ce,O}$={5.0, 5.5} eV. The position of the Ce vacancy is represented by the orange sphere. The isosurfaces are set to 0.05 e/Å^3. In the EDOS, the Ce 4*f* states are the green lines and the O 2*p* states are the red lines. All other states are represented by the grey lines.

The EDOS for a Ce vacancy when $U_{Ce,O}$={5.0, 0.0} eV, (Figure 4.5(c)) indicates that the Ce vacancy is semi-metallic in nature, similar to the EDOS of Fernandes *et al.*[190] However, the EDOS when $U_{Ce,O}$={5.0, 5.5} eV (Figure 4.5(d)) shows a defect state within the band gap primarily composed of empty O 2*p* orbitals from the O holes indicating that the metallic solution is a result of failing to account for the SIE.

This is similar to previous studies on cation vacancies in other metal oxides with O $2p$ dominated valence bands that have applied corrections for the SIE.[162,168,174,191,192]

4.4.4 Oxygen Interstitial

It might be expected that the introduction of an O interstitial would form localised holes on the interstitial ion and the neighbouring oxygen ions:

$$O_O^x + \frac{1}{2}O_2(g) \rightarrow O_O^\bullet + O_i'. \tag{4.6}$$

However the interstitial ion could relax from its original position towards the lattice O ion, forming a peroxide ion and hence no holes would be observed

$$O_O^x + \frac{1}{2}O_2(g) \rightarrow (O_2)_O^x. \tag{4.7}$$

Figure 4.6 (a) shows the structure of the O interstitial for $U_{Ce,O}$={5.0, 0.0} eV and Figure 4.6 (b) displays the structure for $U_{Ce,O}$={5.0, 5.5} eV. When $U_{Ce,O}$={5.0, 0.0} eV ($U_{Ce,O}$={5.0, 5.5} eV) the interstitial ion moves 0.84Å,(0.80Å) towards a lattice O ion, which moves 0.10Å (0.10Å) towards the interstitial position. The resulting O–O bond length of 1.45Å, (1.48Å) is characteristic of a peroxide species.[217] The formation of a peroxide upon the introduction of an O interstitial has also been observed in other close–packed metal oxides, such as Al_2O_3,[218] SnO_2,[219] TiO_2,[191,220] and ZnO.[221] Since the O interstitial forms a peroxide ion, there are no unpaired electrons on any O ions. Therefore, the presence of the U value on the O $2p$ states does not significantly affect the structure from the case where $U_{Ce,O}$={5.0, 0.0} eV.

Peaks corresponding to the peroxide (which are O $2p$ in nature) can be seen in the EDOS (Figures 4.6(c) ($U_{Ce,O}$={5.0, 0.0} eV) and (d) ($U_{Ce,O}$={5.0, 5.5} eV)) between -6 and 0 eV. Integrating these peaks gives approximately 10 electrons, suggesting occupation of a σ, two π and two π^* orbitals, as expected from the MO diagram of a peroxide ion. Furthermore, the peak at ~4.4 eV corresponds to the empty σ^* orbital of the peroxide ion, which has been observed previously in SnO_2.[219]

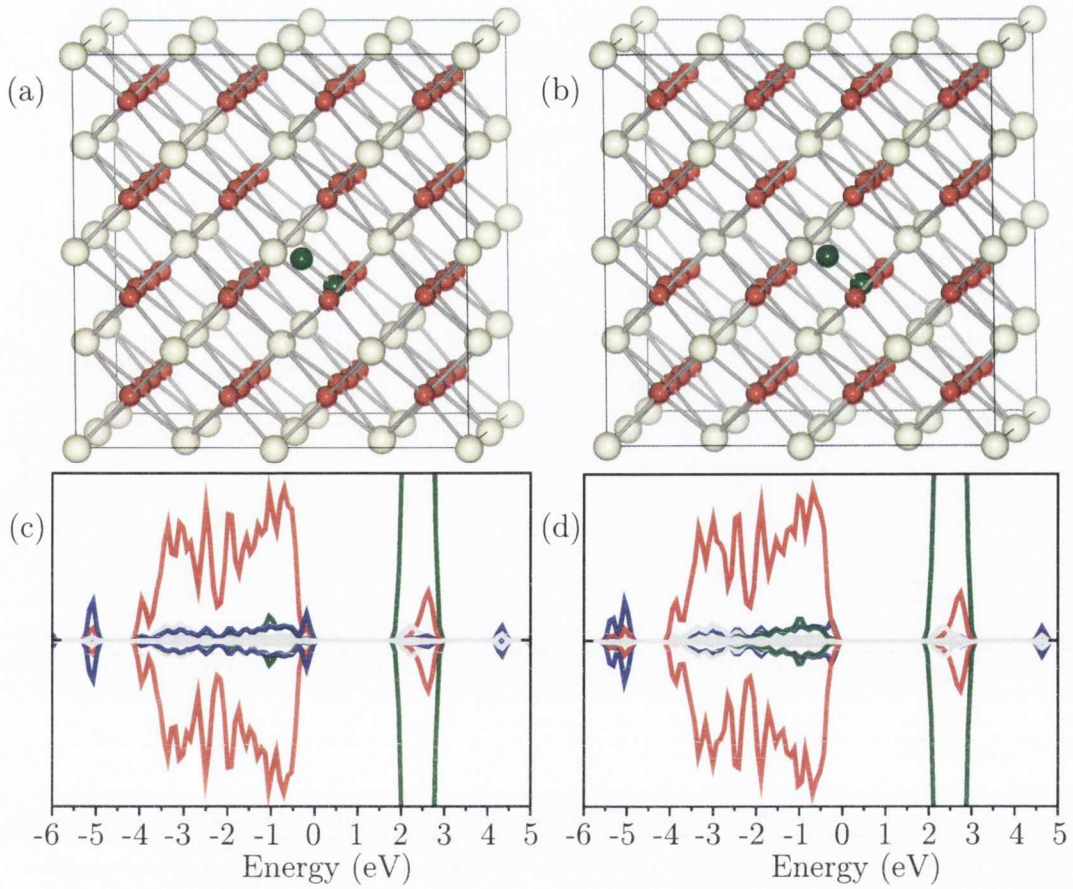

Figure 4.6: The structure when (a) $U_{\mathrm{Ce,O}}$={5.0, 0.0} eV and (b) $U_{\mathrm{Ce,O}}$={5.0, 5.5} eV and the density of states with $U_{\mathrm{Ce,O}}$={5.0, 0.0} eV and $U_{\mathrm{Ce,O}}$={5.0, 5.5} eV of a peroxide ion in CeO_2. The peroxide ion is represented by the dark green spheres. In the density of states the Ce $4f$ states are shown in green and the O $2p$ for lattice O ions in red. The purple lines represent the O $2p$ states associated with the peroxide ion and have been magnified by $\times 5$ to aid clarity.

4.4.5 Anion Frenkel and Schottky Defects

In Kröger–Vink notation, an anion Frenkel defect is denoted by

$$\mathrm{O}_{\mathrm{O}}^{\mathrm{x}} \rightarrow V_{\mathrm{O}}^{\bullet\bullet} + \mathrm{O}_{\mathrm{i}}^{\prime\prime}, \tag{4.8}$$

and a Schottky defect by

$$\mathrm{Ce}_{\mathrm{Ce}}^{\mathrm{x}} + 2\mathrm{O}_{\mathrm{O}}^{\mathrm{x}} \rightarrow V_{\mathrm{Ce}}^{\prime\prime\prime\prime} + 2\mathrm{V}_{\mathrm{O}}^{\bullet\bullet} + \mathrm{CeO}_2. \tag{4.9}$$

The structures and EDOS for the anion Frenkel and the Schottky defects are shown in Figure 4.7 and Figure 4.8 respectively. For both of these defects, the structure and EDOS remained largely unchanged between the $U_{Ce,O}$={5.0, 0.0} eV and $U_{Ce,O}$={5.0, 5.5} eV cases. For both defects, the position of the vacancies and interstitials were varied to determine the lowest energy configuration. For the anion Frenkel defect we found that there was a minimum distance the oxygen interstitial had to be from its corresponding vacancy, below which they would spontaneously recombine. Figures 4.7(a) and (b) shows the first stable anion Frenkel defect, which occurs when the oxygen interstitial is 7.17 Å from the corresponding oxygen vacancy. In the EDOS, Figures 4.7(c) and (d), a new peak appears in the band-gap, made up of O_{2p} states with a small contribution from Ce_{4f} states. The charge density associated with the defect peak is shown in 4.7(a) and (b) and suggests the orbitals of the interstitial O^{2-} ion and neighbouring lattice O ions are perturbing each other, shifting their levels to a higher energy in the density of states.

For the Schottky defect it was found that the cerium and oxygen vacancies will form defect clusters, as shown in Figure 4.8(a) and (b), which is 2.47 eV more stable than for a dispersed arrangement of the vacancies. The presence of a Schottky defect does not affect the EDOS with respect to the pure bulk.[97]

4.5 Defect Formation Energies

The chemical dependent defect formation energies are shown in Table 4.1. It should be noted that these energies are for the formation of the defect clusters seen in the previous section, and therefore contain energies of interaction between the various components of the defect. For example, the formation energy of the O vacancy contains the attraction energy between the effectively positive vacancy and the effectively negative Ce(III) ions. Under Ce-rich/O-poor conditions the formation energy of O vacancies is significantly lower than any of the other defects. However, under Ce-poor/O-rich conditions the peroxide ion has the lowest formation energy, with O vacancies having the second

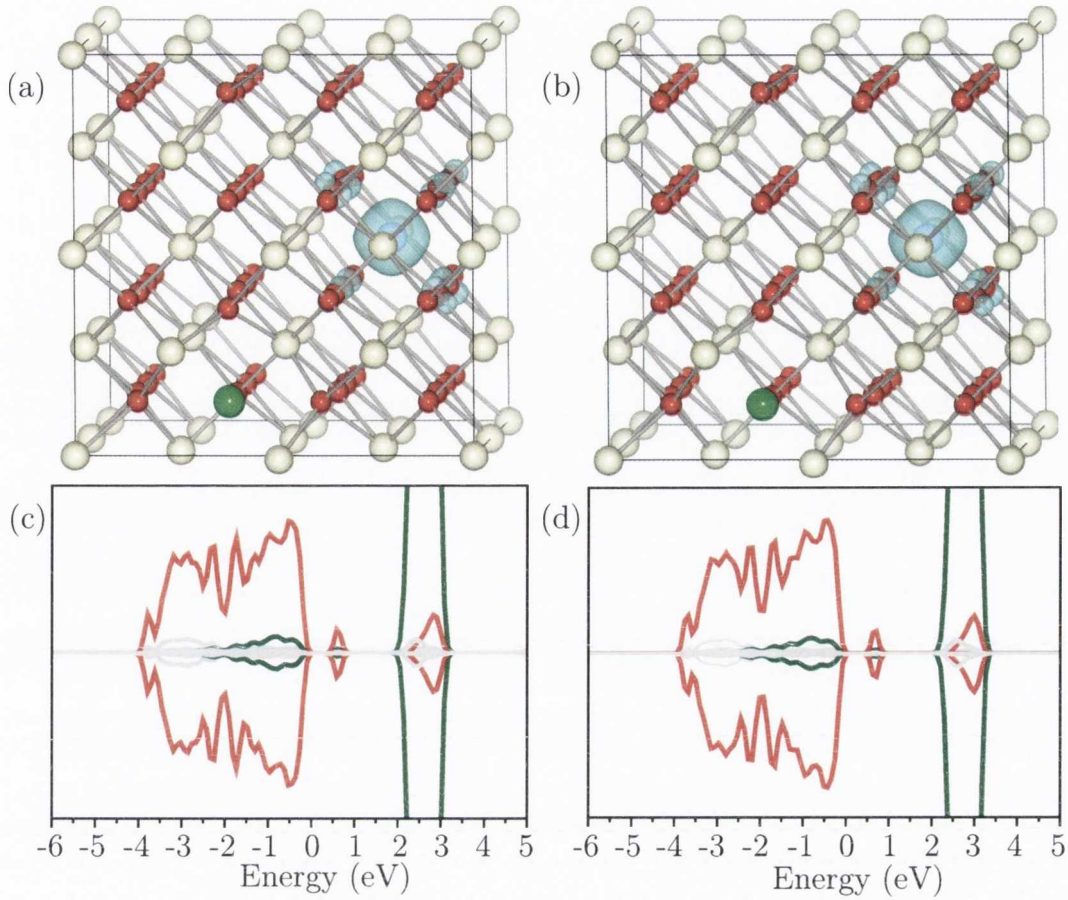

Figure 4.7: The (a) structure with partial charge-density of the defect peaks and (b) density of states of an anion Frenkel defect in CeO_2 when $U_{Ce,O}$={5.0, 5.5} eV. The O vacancy is represented by the light green sphere and the O interstitial is represented by the purple sphere. The isosurface is set to 0.05 e/Å^3. The green lines in the EDOS show the Ce 4f states while the red lines are the O 2p states.

lowest energy. In all cases the formation energy for Ce vacancies and Ce interstitials are much higher than the other defects.

Comparison of the results for $U_{Ce,O}$={5.0, 0.0} eV and $U_{Ce,O}$={5.0, 5.5} eV shows only small differences in the formation energies. The exception to this is for the Ce vacancy where the formation energy is lower by 2.16 eV at the Ce-rich/O-poor limit and by 1.38 eV at the Ce-poor/O-rich when $U_{Ce,O}$={5.0, 5.5} eV. This is because Ce vacancies lead to the formation of localised holes on neighbouring oxygen ions. Without the correction to the O 2p states the SIE leads to a unrealistic delocalisation of the

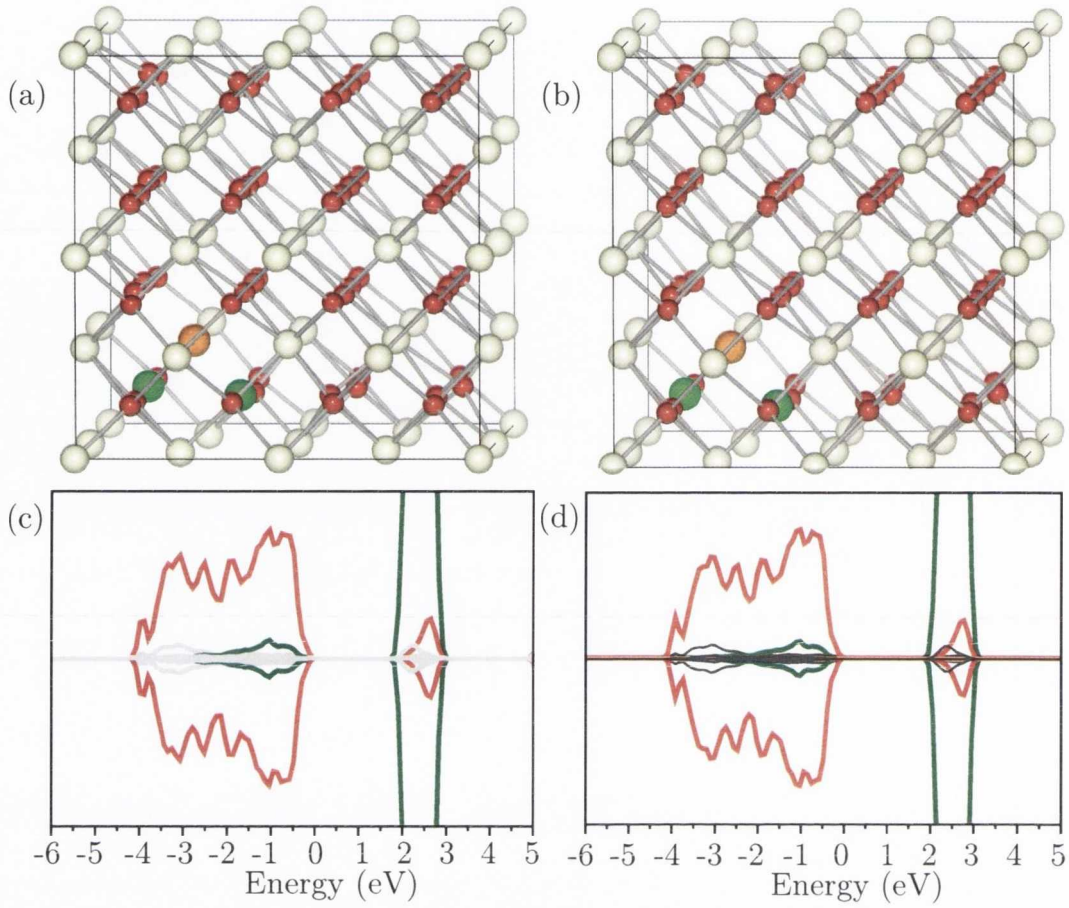

Figure 4.8: The (a) structure and (b) density of states of a Schottky defect in CeO_2 when $U_{Ce,O}$={5.0, 5.5} eV. The Ce vacancy is represented by the orange sphere and the O vacancies are represented by the light green spheres. The Ce $4f$ states and the O $2p$ states are represented by the green an red line respectively in the EDOS.

charge over the O ions but when the SIE is counteracted a localised electronic structure is obtained.

Figure 4.9 shows the change in concentration of the defects with temperature for $U_{Ce,O}$={5.0, 5.5} eV using the methodology outlined in Section 3.4.3. The O partial pressures are set at P=10^{-10} atm (Figure 4.9(a)) and P=0.2 atm (Figure 4.9(b)) to represent defects in CeO_2 under very low O partial pressure (e.g. SOFC anode) and air (e.g. SOFC cathode with air as the source of O_2).[56] At both high and low O partial pressures the most abundant defect will be oxygen vacancies. At higher temperatures there are small concentrations of anion Frenkel and Schottky defects while the con-

Defect	$U_{Ce,O}$={5.0, 0.0} eV		$U_{Ce,O}$={5.0, 5.5} eV	
	O–poor	O–rich	O–poor	O–rich
O vacancy	0.57	2.60	0.58	2.22
Ce interstitial	5.96	10.02	6.03	9.31
Ce vacancy	10.35	6.29	8.19	4.91
O interstitial (peroxide)	3.76	1.73	3.50	1.86
Anion Frenkel	3.89	3.89	3.96	3.96
Schottky	3.58	3.58	3.66	3.66

Table 4.1: The chemical potential dependent free energies for the formation of the defect clusters, for $U_{Ce,O}$={5.0, 0.0} eV and $U_{Ce,O}$={5.0, 5.5} eV. N.B. O–poor also implies Ce–rich and vice versa. All energies are given in eV.

centration of Ce vacancies is negligible. At very high temperatures, and low O partial pressures, there are small concentrations of Ce interstitials. Under high partial O pressure the concentration of peroxide ions is significantly higher than at low pressure, however at the typical operating temperature of a solid oxide fuel cell (≈500-1000 K) the concentration of O vacancies is far greater.

4.6 Discussion

The SIE is a major obstacle to the accurate modelling of defects in solids and its effect on n-type defects in CeO_2 has been extensively modelled. However, the study of the SIE with respect to p-type defects has not received as much attention. To address this discrepancy, an *ab initio* fitting procedure was employed determine a U parameter for the O $2p$ states in CeO_2. Using the derived value of U{O $2p$}=5.5 eV it was possible to model localised electron holes on the O anions, yielding electronic structures similar to studies of other wide-gap metal oxides with O $2p$ dominated valence bands in which the SIE has been corrected.[168,174,191,192] If U{O $2p$} is not included when modeling Ce vacancies, the SIE leads to a unrealistic delocalised defect which is semi–metallic

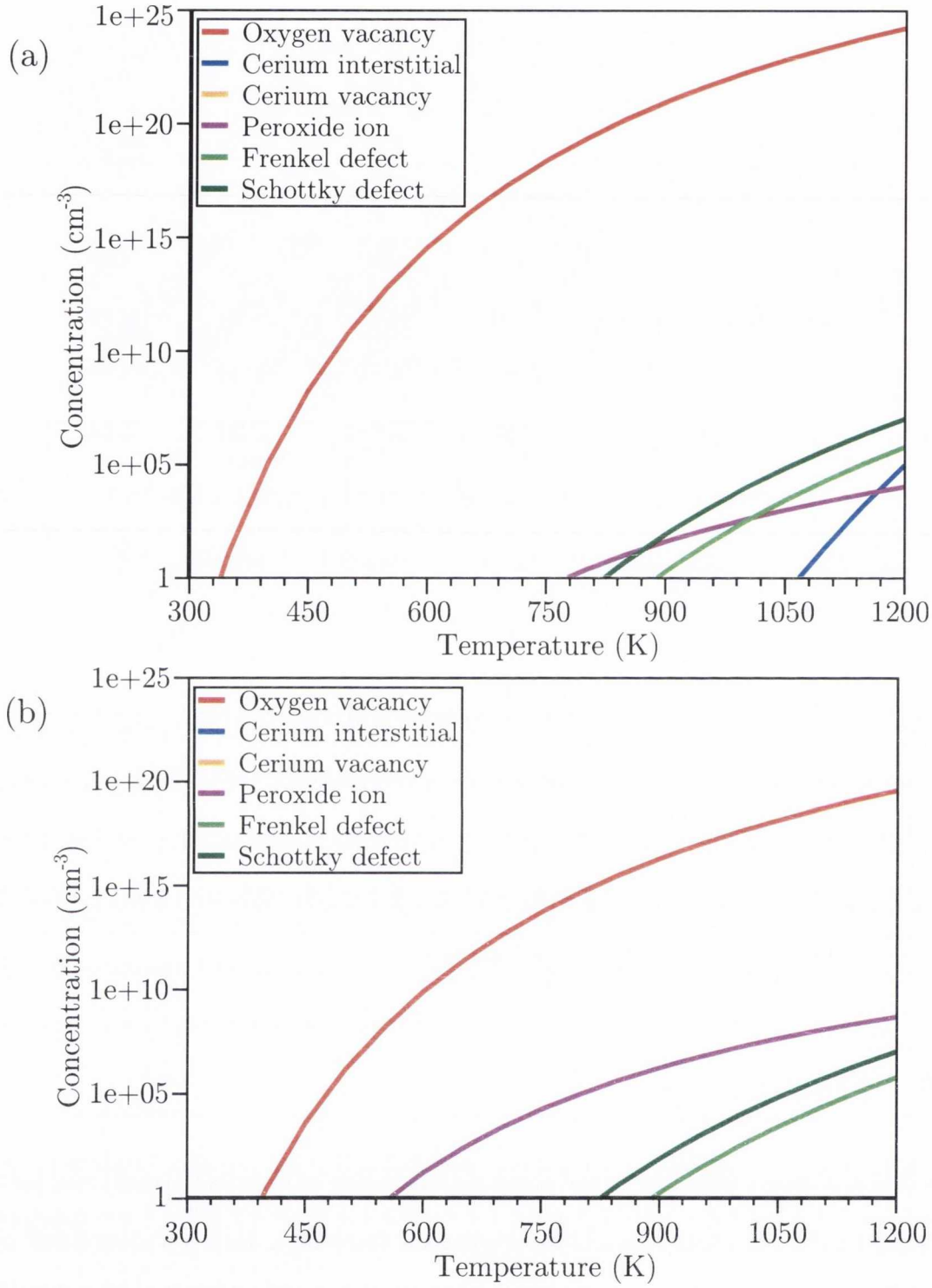

Figure 4.9: The temperature dependence of concentration of intrinsic defects in CeO_2 at O partial pressures of (a) $P = 10^{-10}$ atm and (b) $P = 0.2$ atm.

in nature.[190] The $U\{\mathrm{O}\ 2p\}$ value is therefore essential for modeling defects that form localised oxygen holes in CeO_2.

It was found from the temperature dependence analyses (Figure 4.9) that the defect with the greatest concentration in CeO_2 was the O vacancy. In terms of catalysis, the importance of the OSC of CeO_2 is well understood, as at higher temperatures there will be a high concentration of O released from CeO_2, allowing the catalysis of oxidation reactions, while the O vacancies can act as sites for reduction reactions.[93–97] For SOFC applications, O vacancies will also act as pathway for ionic conduction by allowing neighbouring O ions to hop from their lattice position and fill the vacancy site. As the temperature and number of vacancies increase, ionic conductivity will also increase. The formation of a neutral O vacancy leads to the reduction of two Ce(IV) ions to Ce(III) which could lead to electronic conductivity. While this may be advantageous for catalytic applications, it is detrimental to the operation of an SOFC as it will short circuit the cell. It was also found that there was no energy difference between a ferromagnetic and anti-ferromagnetic arrangement of the excess electrons. Therefore oxygen vacancies are unlikely to be the cause of the observed ferromagnetism in CeO_2.

The formation energy of Ce interstitials is prohibitively high and therefore their concentration in CeO_2 is very low, only appearing at low concentrations at elevated temperatures and low O partial pressures. This is in contrast to materials such as TiO_2, which can exhibit concentrations of cation interstitials comparable to that of anion interstitials at high temperatures or low partial O pressures.[162,222] Due to their high formation energy, 5.96/6.03 eV at the O–poor limit when $U_{Ce,O}$={5.0, 0.0} eV/$U_{Ce,O}$={5.0, 5.5} eV, Ce interstitials are unlikely to have any impact on the catalytic properties or the ionic conductivity of CeO_2. Furthermore, the four Ce(III) ions created by the formation of the interstitial defect will preferentially arrange their spins in a singlet state and therefore these defects are also unlikely to contribute to ferromagnetism.

The concentration of Ce vacancies is predicted to be negligible in CeO_2 and are therefore unlikely to contribute to catalysis or conductivity. Fernandes *et al.* suggested that this defect could partly account for the intrinsic ferromagnetism in CeO_2 despite the low concentration due to a large magnetic moment.[190] The results presented in this chapter show that a quintet arrangement for the oxygen holes around a Ce vacancy

is indeed the most stable configuration, however, it is only lower in energy than the singlet state by 11 meV, far lower than the previously reported stabilisation energy of 221 meV.[190] The discrepancy between these results is most likely due to previous work not taking into account the SIE for the O $2p$ states and hence having stronger interactions between the spins of the electrons delocalised over the same O sites.

O interstitials in ceria result in the formation of peroxide ions with neighbouring lattice O ions. At low O partial pressures the concentration of peroxide ions is low, but at higher O partial pressures the concentration increases significantly. However, since O interstitials are trapped as peroxide ions they are unlikely to contribute to the OSC. Furthermore, these are unlikely to be mobile defects and will not contribute to ionic conductivity.

At elevated temperatures there will be a small concentration of anion Frenkel defects. The results for the anion Frenkel defect agree with previous work, which has shown that they can be present within CeO_2,[223] but are liable to undergo pair recombination unless the O interstitials are sufficiently far from their corresponding O vacancies.[144] The oxygen vacancies of an anion Frenkel defect could act as pathways for ionic diffusion but since the concentration of such defects is very low in CeO_2, their contribution will be insignificant. This is in contrast to other materials with the flourite structure, such as CaF_2, where Frenkel defects do contribute to ionic conductivity due to lower formation energies.[224]

There will be a small concentration of Schottky defects at high temperatures. It was found though that the lowest energy structure of the Schottky defect is when the O vacancies and the Ce vacancy cluster together. This preference for forming clusters, together with a low concentration, suggests that Schottky defects will not significantly contribute towards the ionic conductivity of CeO_2.

4.7 Conclusions

PBE+U was used to investigate the properties of intrinsic defects within CeO_2. Using an *ab initio* fitting procedure, based on Koopmans' theorem, a value of $U\{$O $2p\}$=5.5 eV was found to be suitable for modelling localised O holes in CeO_2. When this U value was applied to the defect calculations, it was possible to model localised O holes in CeO_2. Furthermore, it was shown that to accurately model electronic defects in CeO_2, it is necessary to include U on both the Ce $4f$ and O $2p$ states. This is an important result for future research on defective CeO_2 where there is the possibility of forming localised holes and/or localised electrons.

It was determined that O vacancies will have the lowest formation energies under O–poor conditions while O interstitials (peroxide ions) will have the lowest formation energy at the O–rich limit. To relate these results to real world operating conditions we carried out a temperature dependence analysis under high and low O partial pressures. The results presented in this work have shown that under these conditions O vacancies will always be the most abundant defect in CeO_2. Furthermore it was demonstrated that at the dilute limit, none of the considered defects studied can account for the apparent ferromagnetism observed in CeO_2.

Chapter 5

The Structure and Reducibility of CeO_2 Doped with Trivalent Cations

5.1 Introduction

As discussed in Chapter 1, doping CeO_2 with trivalent cations is a common method for increasing the ionic conductivity of CeO_2. In this chapter, a series of trivalent dopants will be tested with CeO_2 to determine which system will be most effective for SOFC applications. As the local structure around the dopant ions could strongly influence the movement of ions in CeO_2, and hence the ionic conductivity, it is therefore vital to obtain a detailed knowledge of the structure of doped CeO_2. For example, the CCV and dopant ions may preferentially form defect clusters, with a strong binding energy between the vacancy and the dopants hindering ionic conductivity by 'trapping' the vacancies next to the dopants. Force–field based molecular dynamics studies have shown that while diffusion of the O anions do take place in doped CeO_2, the O vacancies are preferentially attracted to the dopant ions, e.g. Y(III),[225] Gd(III)[145] and La(III).[115] However, these studies disagree over the degree of association between vacancies and dopants. Cheng *et al.* stated that for Y-doped CeO_2, O vacancies would preferentially lie at a next–nearest neighbour position with respect to the Y(III) cations.[225] In contrast, Inaba *et al.* and Hayashi *et al.* determined that dopant–vacancy–dopant clusters

would form for Gd-, La- and Y-doped CeO_2.[115,145]

The structure of doped CeO_2 has also been investigated using DFT calculations, for example Andersson *et al.* used PW91–DFT to model CeO_2 doped with the trivalent rare-earth ions.[116] Their results indicated that dopants with a low association energy for O vacancies would lead to the largest increases in ionic conductivity. For the rare–earth dopants, they determined that the lowest association energies were for ions with ionic radii of ~ 1.08 Å, e.g. Sm(III) (1.08 Å) and Pm(III) (1.09 Å). A PBE+U study by Nakayama and Martin[226] also investigated the relationship between ionic radii and ionic conductivity for trivalent rare-earth dopants. They found that dopants with smaller radii had a tendency to trap vacancies next to them, but larger dopants hindered the movement of O ions. Hence, dopants with intermediate ionic radii, such as Y(III) (1.02 Å), would be most suitable for fuel cell applications.[116] However, one area that Nakayama and Martin failed to cover is that the dopants may form dopant-vacancy-dopant clusters: the association energies they calculated were only between a vacancy and a single dopant. The effect of dopants on the CeO_2 lattice was also investigated through DIPPIM–MD and PW91–DFT simulations by Marrocchelli *et al*, who reported that there are two important factors for how trivalent cations affect lattice distortions;[139] firstly, the formation of the O vacancy and secondly, the difference between the ionic radii of the host cation, Ce(IV), and the dopant cations. The former causes a contraction in the lattice, due to electrostatic interactions, whereas the latter leads to lattice expansion through steric effects. Marrocchelli *et al.* determined an ionic radius of a trivalent dopant, 1.03 Å, for which the electrostatic and steric effects would cancel each other out which is consistent with the experimental work of Kim who calculated this value as 1.038 Å.[138] This radius is referred to as the critical ionic radius, r_c.

As mentioned in Chapter 1, the advantage of the CCVs in doped CeO_2 is that they introduce pathways for ionic diffusion without creating Ce(III) ions, which can act as carriers for electronic conductivity. Since it is important to avoid electronic conductivity, the dopants chosen should not increase the reducibility of CeO_2, meaning the dopants should not make it easier to form intrinsic O vacancies. Experimental studies

have investigated the reducibility of trivalently doped CeO_2, but there are discrepancies between the results. Zając and Molenda, using thermogravimetric techniques, studied the reducibility of CeO_2 doped with Y, Nd, Sm, Gd and Dy. They determined that the concentration of O vacancies did not vary between different dopants, but only as a function of the concentration of dopant ions.[227] However, Yahiro *et al.* investigated the electronic conductivity of CeO_2 doped with Sm, Gd, Yb and La as a function of partial O pressure. They too carried out a thermogravimetric analysis, but in contrast to the work of Zając and Molenda, they found that the concentration of O vacancies present, and therefore the reducibility of doped CeO_2, varied between dopants at the same level of concentration, with Sm–doped CeO_2 displaying the most resistance to reduction.[228]

In this chapter, the lowest energy structures for a variety of trivalent dopants in CeO_2 are calculated, with a particular focus of the association between dopant ions and oxygen vacancies. Finally, the effect of these dopants on the reducibility of CeO_2 is explored to determine whether it is the dopant radius, or alternate factors, that affects the formation of O vacancies. This information will prove useful for choosing the most effective dopants for SOFC applications.

5.2 Computational Methods

All calculations were carried out with the same methods employed in Chapter 4. To account for the SIE, $U_{\mathrm{Ce,O}}$=$\{5.0, 5.5\}$ eV was employed. Although no p–type defects were calculated in this chapter, the U value for the O $2p$ states was used to maintain consistency with other work in this thesis. Several of the dopants studied (Pr, Nd, Eu, Gd, Dy, Ho, Er and Tm) also have unpaired $4f$ electrons. Therefore, U=5 eV was also applied to their $4f$ states: although this value may not be the most suitable choice for all the dopants, it should provide sufficient electron localisation to model the correct electronic structure, allowing for a comparison of the doped systems.

All defect calculations were carried out in a 2×2×2 expansion of the optimised 12

atom unit cell (96 atoms) and employed a 2×2×2 k-point mesh. To create the doped cells, two Ce ions were replaced with two trivalent dopant ions (Al, Ga, Sc, Sb, In, Lu, Tl, Tm, Er, Ho, Y, Dy, Tb, Gd, Eu, Nd, Pr, Bi or La), giving a dopant concentration of 6.25 mol%, and a CCV was created to conserve the charge balance. The position of the CCV was varied (Figure 5.1 to determine the lowest energy structure for the doped cells. The doping energy, E_{dop}, was calculated according to the method described in Section 3.4.1. The association energy, E_{ass}, between the dopants and the the CCV is calculated by finding the difference between the structure where the CCV is far away from the dopants and the lowest energy structure. To model reduced CeO_2, an additional O ion was removed from the system. The position of this vacancy was also varied to determine how the presence of the dopants affects the reduction energy, E_{red}, throughout the cell.

5.3 Structure of Doped Ceria

The first step was to determine the most stable structure of doped CeO_2. A range of different locations were tested for the CCV to determine where it would preferentially lie with respect to the dopants: firstly, with the CCV nearest–neighbour to the dopants (Figure 5.1(a)); secondly, with the CCV next nearest–neighbour to the dopants (Figure 5.1(b)); thirdly, with the CCV nearest–neighbour to a single dopant (Figure 5.1(c)); and finally, with the CCV far away from the dopants (Figure 5.1(d)). For each CCV position, E_{dop} was calculated, Table 5.1, and the location with the lowest value of E_{dop} was deemed the most stable structure. The analysis of the lowest energy structure revealed that the defect structure could be grouped according to the ionic radius of the dopant ions. The values displayed in Table 5.1 are listed in order of increasing ionic radii, but for the specific radii, cf. Table 5.2. For Al– and Ga– doped CeO_2, the CCV preferentially forms in the nearest neighbour position to one of the dopants, and ~5.47 Å from the other, as seen in Figure 5.2. When doped with Sc(III), Sb(III), In(III), Tl(III), Lu(III), Tm(III), Er(III), Ho(III), Y(III), Dy(III), Gd(III), Eu(III) or

Bi(III), the doped cells adopt the structure seen in Figure 5.3, where the CCV is nearest neighbour to both the dopant cations. For the remaining dopants, La(III), Pr(III) or Nd(III), the CCV lies in the next-nearest neighbour position with respect to both the dopants (Figure 5.4).

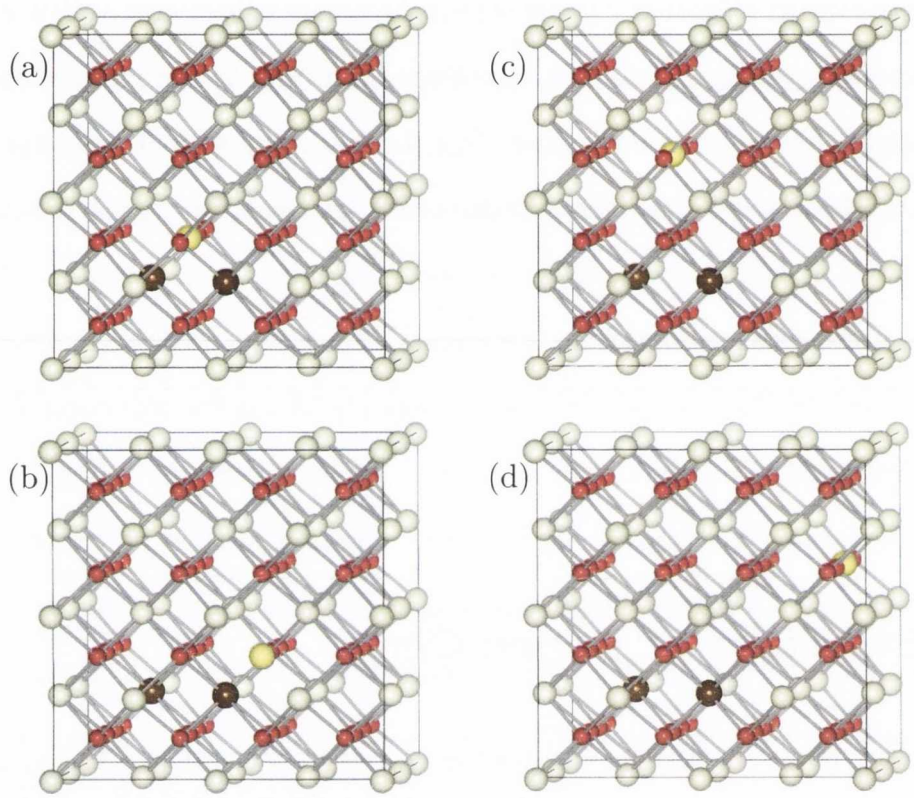

Figure 5.1: Starting configurations for doped CeO_2 with a CCV placed (a) nearest-neighbour to the dopants (NN–CCV), (b) next nearest-neighbour to the dopants (NNN–CCV), (c) nearest–neighbour to one of the dopants (NN–1–CCV) and (d) far away from the dopants (far–CCV). Ce, O and dopant ions are shown in white, red and brown respectively. The position of the CCV is denoted by the yellow sphere.

Al(III) and Ga(III) have the smallest ionic radii of the dopants studied and hence there is more space for distortion of the lattice, similar to small divalent dopants in CeO_2.[113,229] The Al(III) and Ga(III) ions that are nearest neighbour to the CCV move 0.91 and 0.80 Å respectively from the original Ce(IV) lattice position, while the other Al(III) and Ga(III) ions move 0.75 and 0.56 Å respectively. It is of interest to note that the local structures around the Al(III) and Ga(III) dopants have similar bond lengths

dopant	E_{dop}				E_{ass}
	NN–CCV	NNN–CCV	NN–1–CCV	Far–CCV	
Al	4.70	4.76	4.56	8.49	3.93
Ga	4.51	4.33	4.26	7.07	2.81
Sc	2.19	2.28	2.66	3.20	1.01
Sb	2.19	2.86	2.67	3.49	1.30
In	0.99	2.12	1.58	2.16	1.17
Lu	1.32	2.15	1.66	2.01	1.11
Tl	2.40	3.35	2.94	3.51	0.69
Tm	0.44	1.06	0.76	0.99	0.55
Er	0.86	1.39	1.16	1.37	0.51
Ho	0.83	1.34	0.99	1.45	0.62
Y	0.76	0.91	1.29	1.61	0.85
Dy	0.13	0.63	0.43	0.60	0.48
Gd	0.70	0.98	0.89	1.06	0.37
Eu	0.65	0.76	1.12	0.90	0.25
Nd	0.56	0.49	0.65	0.76	0.27
Pr	0.42	0.35	0.52	0.64	0.29
Bi	1.25	1.58	2.07	2.49	1.24
La	0.67	0.52	1.14	1.30	0.78

Table 5.1: The values of E_{dop} for trivalent dopants in CeO_2 for different locations of the CCV and the E_{ass} between the dopant and the CCV. The most stable structure (i.e. lowest E_{dop} energy) is highlight in blue. All energies are given in eV.

and bond angles to those observed in their native oxides. In Al_2O_3, two neighbouring Al ions are linked by two bridging O ions, matching that which is observed in Al–doped CeO_2. However, an asymmetric electrostatic field is created since only one of the dopant ions neighbours the CCV, and hence the structure is somewhat distorted compared to that seen in Al_2O_3. Comparing values obtained in this study (with experimental values

for the native oxides), the average Al–O bond length is 1.84 Å (1.97 Å and 1.85 Å), the Al–Al distance is 2.69 Å (2.79 Å), the Al–O–Al bond angles are 93.82° and 93.39° (93.63°) and the O–Al–O bond angles are 85.87° and 86.93° (86.37°). It should be noted that in Al_2O_3, the Al cations have an octahedral coordination but in doped CeO_2 the Al(III) ions have tetrahedral coordination. This is likely caused by the CeO_2 lattice not being able to distort sufficiently to achieve full octahedral coordination for the relatively shorter Al–O distance and hence the tetrahedral structure. In Ga_2O_3, Ga(III) has two coordination environments, octahedral and tetrahedral. The defect structure of Ga(III) dopants in CeO_2 has many similarities with the octahedrally coordinated Ga(III) ions in Ga_2O_3, although with tetrahedral coordination. Once again comparing the calculated structural values (with experiment)[230], the average Ga–O bond length is 1.97 Å (2.00 Å), the Ga–Ga distance is 2.91 Å (3.03 Å), the Ga–O–Ga bond angles are 95.72° and 94.50° (99.10°), and the O–Ga–O bond angles are 85.81° and 83.92° (80.92°). The defect structure does not share many similarities with the tetrahedrally coordinated Ga(III) ions in Ga_2O_3, which have Ga–O bond length of 1.88 Å, a Ga–Ga distance of 3.10 AA, Ga–O–Ga bond angles of 105.62° and 111.08° and O–Ga–O bond angles of 111.08° and 122.00°. Similar to Al-doped CeO_2, the structure of the dopants seen in Ga-doped CeO_2 differs slightly from the native oxide due to the asymmetric electrostatic field around the dopant cluster. Furthermore, Ga(III) also adopts a tetrahedral coordination structure as the host lattice cannot distort sufficiently to allow the dopant cations to achieve octahedral coordination.

As the ionic radii of the dopants increases they are more constrained to lattice positions and hence the defect structure around the dopants bears less relation to the structure of the cations in their native oxides. For Sc(III), Sb(III), In(III), Tl(III), Lu(III), Tm(III), Er(III), Ho(III), Y(III), Dy(III), Gd(III) and Eu(III) the CCV is located nearest neighbour to the two dopants (Figure 5.3). These dopants encompass a wide range of ionic radii that are either less, or not significantly larger, than 1.03 Å, the ionic radius given by Marrocchelli *et al.* at which a trivalent dopant in CeO_2 will cause neither expansion or contraction of the host lattice.[139] Due to the minimal

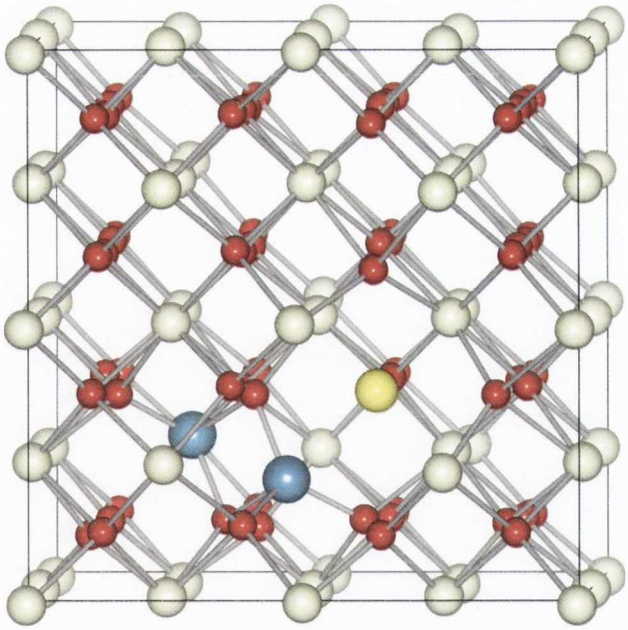

Figure 5.2: Lowest energy structure for Al and Ga-doped CeO_2. The dopant cations are represented by the grey spheres.

distortion of the lattice, the M(III)–O bond lengths do not differ significantly from the Ce–O bond length of 2.37 Å.[231] Furthermore, as the CCV can be considered an area of effective positive charge and the trivalent dopants are less positively charged than the host Ce(IV) cations, it is more favourable to have the CCV nearest neighbour to the dopants than to four Ce(IV) ions (Figure 5.3). The M(III)–M(III) distances for these dopant range from 4.05 Å for Tl(III) to 4.15 Å for Y(III). This is similar to the Ce(III)–Ce(III) distance in reduced CeO_2 (4.07 Å) when the O vacancy neighbours the Ce(III) ions, compared to the Ce(IV)–Ce(IV) distance of 3.89 Å.

As the ionic radii increases beyond 1.03 Å, there appears to be a threshold around 1.07Å beyond which steric effects of the dopants on their surroundings overcomes the electrostatic effects of the CCV. This is the case for Nd(III), Pr(III) and La(III), where it becomes energetically favourable for the CCV to be in the next-nearest neighbour position (Figure 5.4). The M(III)–O bond length increase to an average of 2.45 Å (Nd(III) and Pr(III)) and 2.46 Å (La(III)), compared to the Ce–O bond length of 2.37 Å.[231] The exception to this is the O anion that bridges the two dopants cations and also neighbours the CCV. The O ion moves towards the CCV, which is an area

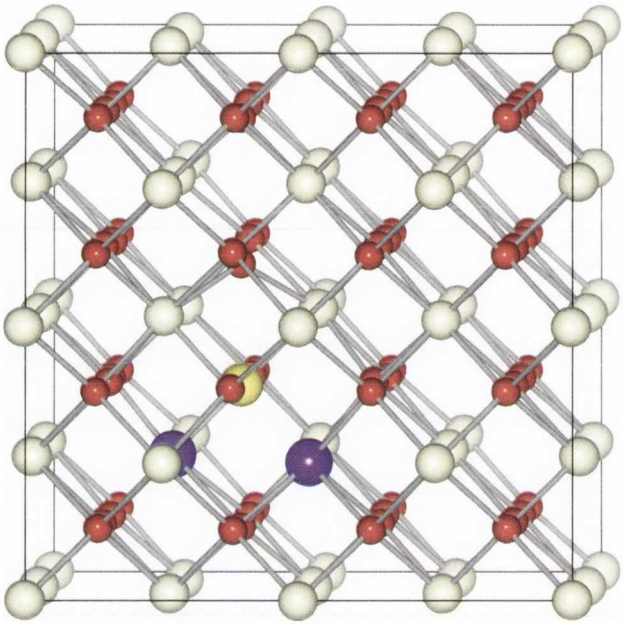

Figure 5.3: Lowest energy structure for Sc, Sb, In, Tl, Lu, Tm, Er, Ho, Y, Dy, Gd, Eu and Bi-doped CeO_2. The dopant cations are represented by the purple spheres.

of effective positive charge, increasing the M(III)–O bond length to 2.59 Å (Nd(III)), 2.60 Å (Pr(III)) and 2.63 Å (La(III)). The M(III)–M(III) distances are 3.89 Å (La), 3.86 Å (Pr) and 3.85 Å (Nd), which closely match the Ce(IV)–Ce(IV) distance of 3.87 Å seen in bulk CeO_2.

An exception to the relationship between ionic radius and defect structure was found for Bi–doped CeO_2. The ionic radius of Bi(III) is similar to La(III), however, the CCV was found to preferentially form in the nearest–neighbour position. Previous studies have shown that the highly asymmetric structure of α-Bi_2O_3 is a result of the lone–pairs on the Bi(III) ions.[232,233] The charge density around the CCV and the dopants is displayed for Y– and Bi–doped CeO_2 in Figure 5.5 (a) and (b) respectively. The electron density around the Y(III) ions is clearly symmetric whereas the Bi(III) ions possess an asymmetric electron density that is oriented towards the CCV. This asymmetric density is likely a result of the lone–pairs, further evidenced by the calculated PEDOS.

In the α–Bi_2O_3 PEDOS, Figure 5.6, there are two major interactions between the cations and the anions in the regions between -10.5 eV to -7.5 eV and -5 eV to the VBM. The region between -10.5 eV to -7.5 eV is considered to be a bonding interaction be-

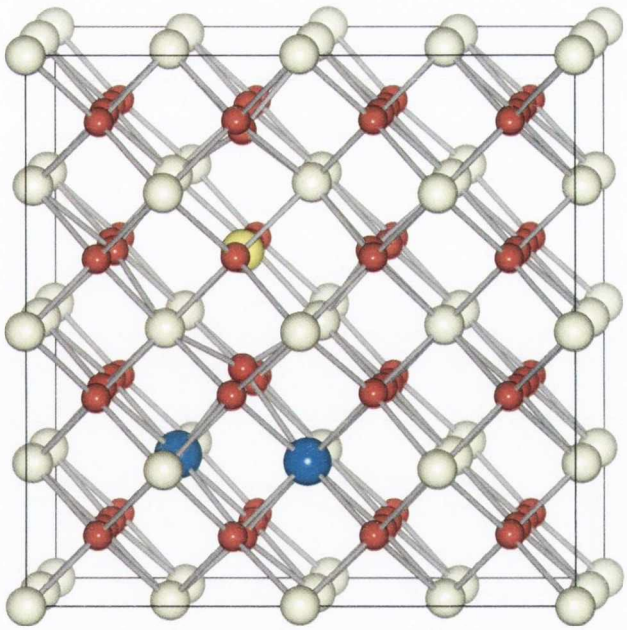

Figure 5.4: Lowest energy structure for Nd, Pr and La-doped CeO_2. The dopant cations are represented by the blue spheres.

tween the Bi 6*s* and O 2*p* states. The second region can be further split into two parts: between -5 eV to -1.5 eV there is an interaction the Bi 6*p* and O 2*p* states and from -1.5 eV to the VBM there is also a contribution from the Bi 6*s* states. This interaction of Bi 6*s* and O 2*p* is a filled anti–bonding interaction that is stabilised through coupling to the filled Bi 6*p* states, thus creating the distinctive lone pairs observed in α-Bi_2O_3. [232] In the calculated PEDOS for Bi-doped CeO_2, Figure 5.7, similar interactions between the Bi 6*s* states and the O 2*p* states are observed at $\sim$ -9 eV and at the top of the valence band. These peaks correspond with the previously identified bonding and anti–bonding interactions between Bi 6*s* and O 2*p* states, along with some mixing of Bi 6*p* states with the latter, confirming the presence of lone pairs in Bi–doped CeO_2. In Bi_2O_3, as well as other materials containing Bi(III), Pb(II) and Sn(II), the formation of lone–pairs has been shown to greatly reduce the energy in the system. [232,233] Therefore, it is more stable to have the CCV nearest-neighbour to the Bi(III) ions and form lone–pairs, despite the size of the Bi(III) ions. It should be noted that the charge density observed for Y–doped CeO_2 matches that which is observed for the other dopants studied. The only exception is Sb(III) which also displays lone pairs in

CeO_2, however the ionic radius of Sb(III) is in the range where it would be expected that the CCV would be in the nearest neighbour position, regardless of the presence of lone pairs.

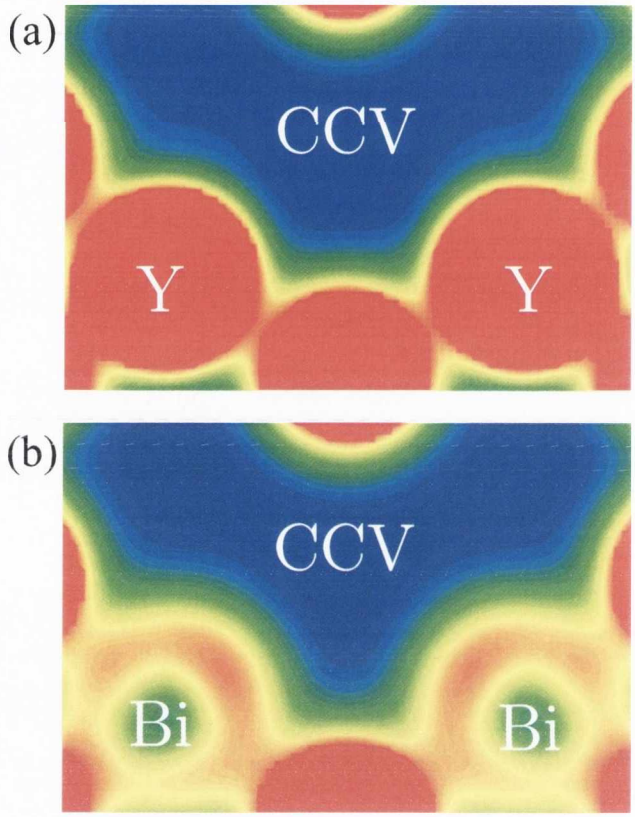

Figure 5.5: The charge density around the (a) Y(III) and (b) Bi(III) cations and CCV in doped CeO_2. The charge density plot ranges from 0.0 (blue) to 0.4 (red)e/Å^2.

In Table 5.2 the calculated E_{ass} between the dopants and the CCV are displayed. For SOFC applications, this energy should be as small as possible, as larger values would trap the CCV at the dopant ions and thus hinder ionic conductivity. Al– and Ga-doped CeO_2 have the largest values of E_{ass}, 3.93 eV and 2.81 eV respectively, indicating that they would not be suitable for SOFC applications. Sb– and Bi-doped CeO_2 have the next highest E_{ass} at 1.30 eV and 1.24 eV respectively. The comparatively higher values found for these dopants are likely due to the extra stability associated with the lone pairs on the cations which would be lost if the CCV was to move away from the dopants, restoring a symmetric coordination environment. All the rare–earth dopants and Y(III) have low values for E_{ass}, with Eu(III), Nd(III) and Pr(III) having

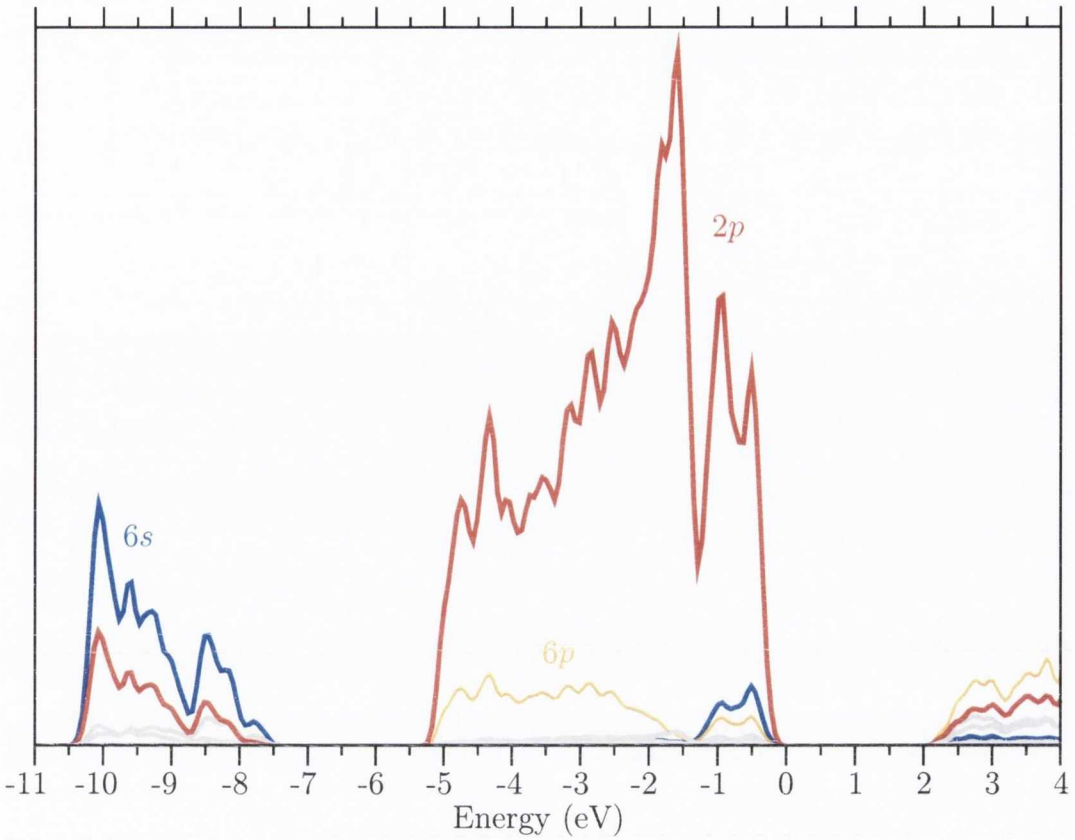

Figure 5.6: The electronic density of states for α–Bi_2O_3. The blue lines represent Bi $6s$ states, the orange lines Bi $6p$ states and the red lines O $2p$ states. All other states are shown in grey. The top of the valence band has been is aligned to 0 eV.

particularly low values, even lower than Gd(III), which is commonly quoted as one of the best trivalent dopants for SOFCs. Therefore, O anions in these doped materials should be comparatively free to move and hence should display good ionic conductivity.

5.4 The Effect of Dopants on the Reducibility of CeO_2

The operation a SOFC requires that the electrolyte is a purely ionic conductor; any electronic conductivity can serve to short–circuit the cell. Since the formation of O vacancies can cause electronic conductivity in CeO_2, the dopants should not increase the concentration of such defects, i.e. it should not make the material more reducible.

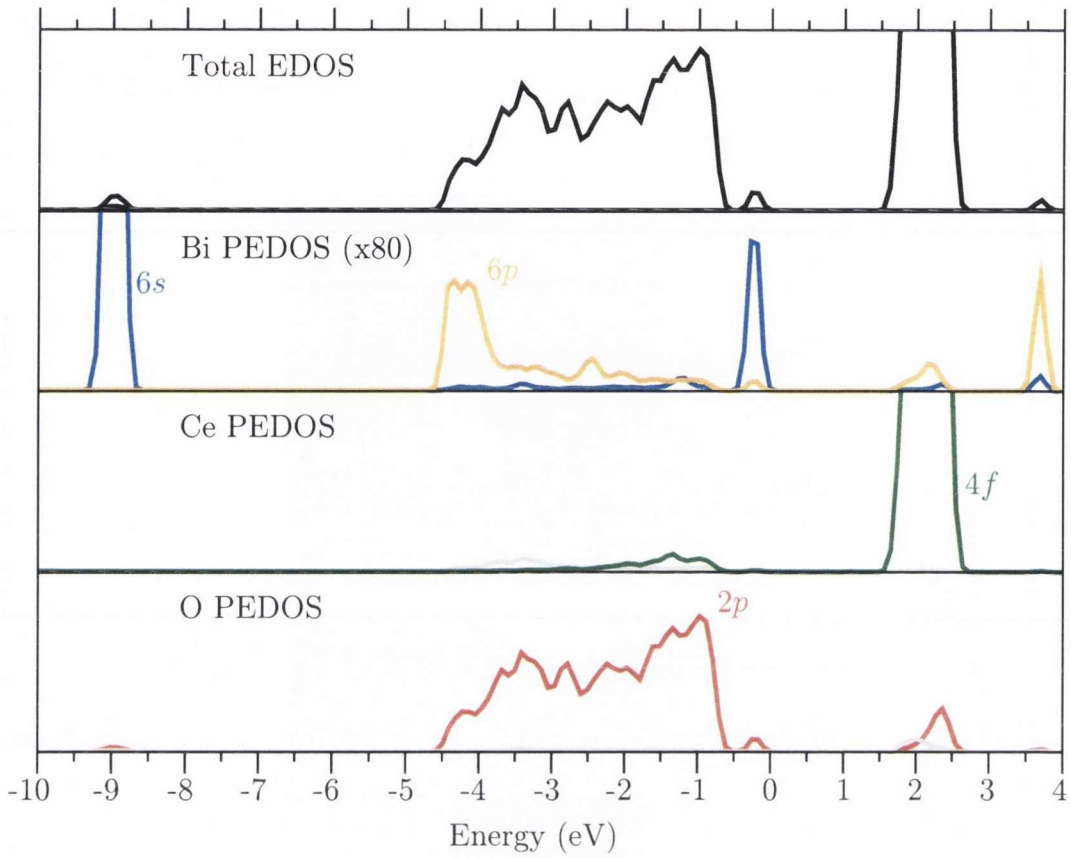

Figure 5.7: The electronic density of states for Bi–doped CeO_2. The blue lines represent Bi $6s$ states, the orange lines Bi $6p$ states, the green lines Ce $4f$ states and the red lines O $2p$ states. The height of the Bi states have been magnified $\times 80$ for clarity. The top of the valence band has been is aligned to 0 eV.

Therefore, an additional O vacancy was introduced to the doped systems to determine their affect on the reducibility of CeO_2. For most dopants, two different positions were tested: one with the vacancy near to the dopants and another further away (Figure 5.8 (a) and (b)). For Al– and Ga–doped CeO_2 an extra position for the reduction was also carried out, Figure 5.8(c). This O ion was chosen because it is under–coordinated, compared to other Bulk O ions, due to the coordination of Al(III) and Ga(III), and previous work on divalently doped CeO_2 has shown that it is easier to remove under–coordinated oxygen ions from CeO_2.[113,229] The values of E_{red} and their relation to pure CeO_2 are displayed in Figure 5.9. The smaller dopants, Al(III) and Ga(III) (shown in the inset), do not significantly affect the E_{red} for a nearby, fully coordinated O ion,

but for under–coordinated O ions, the energy is far lower, in line with previous work on divalently doped CeO_2 which showed that it is easier to remove under–coordinated O ions from doped CeO_2.[113,229] Furthermore, the energy is also reduced for O ions far away from the dopant ions. When the CCV is nearest neighbour to the dopant ions (Sc, Sb, In, Tl, Tm, Er, Ho, Y, Dy, Gd, and Bi), the E_{red} is largely unaffected. As the ionic radii of these dopants are closer to that of Ce(IV), the CeO_2 lattice is not greatly distorted by their presence and hence only minor changes to E_{red} are observed. An exception to this is Eu–doped CeO_2 which shows a drastic decrease in E_{red} when the vacancy forms near the dopants. The reason for this becomes apparent upon studying the electronic structure. It was found that excess electrons associated with the formation of the neutral oxygen vacancy will preferentially localise on the Eu(III) ions, reducing them to Eu(II), instead of the Ce(IV) ions. This result is to be expected as Eu(II) ions are know to be relatively stable. For Nd(III), Pr(III) and La(III) the energy to form an O vacancy near the dopants is significantly higher than for pure CeO_2 but for an O vacancy away from the dopants the energy is significantly lower. However, the doped CeO_2 cells considered in this report only correspond to a doping level of 6.25 mol%. From the literature, the highest levels of ionic conductivity in trivalently doped CeO_2 have been found for doping levels of between 15 mol% and 20 mol%.[129,234–236] Therefore this lowered E_{red} at these distances away from the dopant ions would become increasingly insignificant as the dopant concentration increases.

It would have been expected that as the reduction vacancy moved farther away from the dopants, E_{red} would be closer to the undoped bulk E_{red} of 2.23 eV. However, from the results it is evident that that is not always the case. It is possible that the energy difference is due to a long range lattice strain effect caused by the dopants, but it could also be due to an image interaction between the simulation cells, which would suggest that the 2×2×2 cells used in these calculations are too small. To test the suitability of the 2×2×2 cell, a 3×3×3× simulation cell of La–doped CeO_2 was created and three O vacancy positions were tested; the first two were the same distance from the dopants to the O vacancies as in the 2×2×2 cell and the third was placed

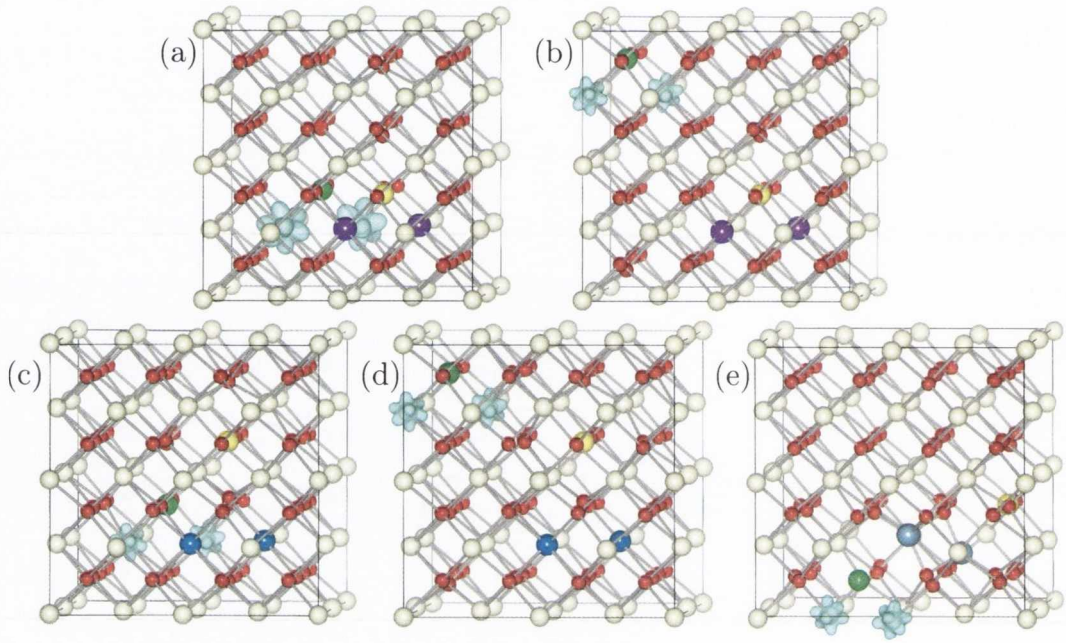

Figure 5.8: The positions tested for an intrinsic vacancy in doped CeO_2. The positions are (a) vacancy near dopants with a NN-CCV, (b) vacancy far from dopants with a NN-CCV, (c) vacancy near dopants with a NNN-CCV, (d) vacancy far from dopants with a NNN-CCV and (e) an alternate position (Al and Ga–doped CeO_2 only). The position of the intrinsic vacancy is represented by the green sphere. The isosurfaces are shown in blue and are set to 0.05 e/Å^3.

further away than the previous two. It was found that E_{red} at the first two positions were unchanged from the 2×2×2 cell while the third vacancy had the same E_{red} as bulk CeO_2. Hence the difference in energy between the E_{red} in doped and pure CeO_2 was not due to an insufficiently large simulation cell.

5.5 Discussion

The results demonstrate that the structure of doped CeO_2 is dependent on the ionic radius of the dopants. When the dopants are much smaller than the host cations, e.g. Al(III) and Ga(III), the dopant cations ions are comparatively free to move off the lattice site leading to distortion in the CeO_2 lattice. Furthermore, the bond lengths and angles in the defect clusters formed by these dopants have similarities with those of the

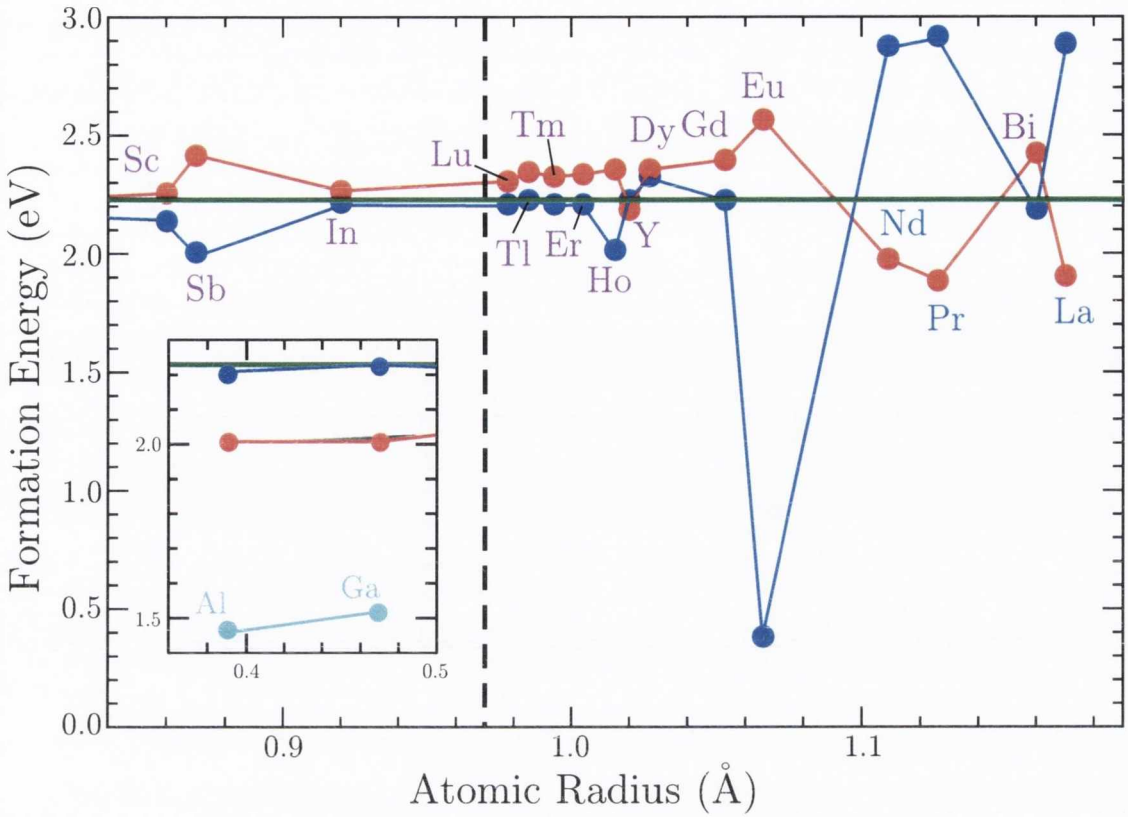

Figure 5.9: The E_{red} values for doped CeO_2. The blue and red lines represent vacancies formed close to and far from the dopant cations respectively. As the radii of Al(III) and Ga(III) are significantly smaller than the other dopants studied, the results for these two dopants are shown in an inset on the graph, with additional results for removing an under–coordinated O ion (light blue). The green line represents the E_{red} for pure CeO_2 and the black dashed line indicates the ionic radius of Ce(IV).

cations in their native oxides. As the ionic radius of the dopant cations increase, the dopant cations are more constrained and less deformation of the lattice occurs. For ionic radii up to 1.07 Å, it was observed that the lowest energy structure is when the CCV neighbours the dopants. This is likely because the CCV experiences less electrostatic repulsion from the dopant cations than from the Ce(IV) ions. As the ionic radius increases beyond 1.07 Å the steric effects of the dopants will begin to dominate and eventually the CCV is forced away from the dopants to the next nearest–neighbour position. An exception was found in the case of Bi–doped CeO_2. Despite having a larger ionic radius than La(III), the lowest energy structure was found for a CCV

neighbouring the dopants. It was determined when the CCV is nearest neighbours to the dopants, lone–pairs form on the Bi(III) and Sb(III) ions, stabilizing the structure.

The results on the E_{red} of doped CeO_2 would suggest that the ionic radius of the dopant is not directly responsible for any observed changes, similar to the results of Zając and Molenda.[227] Instead, the largest effect on the reducibility is how the dopants change the structure of the lattice. The increased distortion created by the Al(III) and Ga(III) dopant ions lead to under-coordinated O ions which are far easier to remove from the lattice than fully coordinated ions. For Nd, Pr and La–doped CeO_2 it becomes harder to remove oxygens ions close to the dopants, most likely due to steric strain between the dopants and Ce(III) ions. For the remaining dopants, which cause the least distortion to the lattice, we find that E_{red} is mostly unchanged from pure CeO_2 and appears to be largely insensitive to the ionic radii.

To help summarize the results, some of the cells in Table 5.2 have been shaded according to the following criteria: E_{dop} less than 1.50 eV; E_{ass} less than 0.65 eV; and do not decrease E_{red}. These criteria were selected to provide a good framework for comparing the dopants and determining which are best suited for SOFC applications. The E_{red} value for the vacancy further away from the dopants has not been included as, at the higher levels of doping generally seen in experimental studies, this value should be of little importance. It is apparent that neither Al(III) or Ga(III) would be suitable dopants for SOFC applications: they have high values of E_{dop}, a high value of E_{ass} and they decrease the E_{red} of CeO_2, increasing the amount of intrinsic O vacancies, and hence Ce(III), that can short circuit the operation of an SOFC. This is perhaps not surprising, as Al– and Ga–doped CeO_2 has been linked to enhanced OSC.[237,238] From the remaining dopants Sc(III), Sb(III), In(III), Lu(III), Tl(III), and Bi(III) are poor choices for fuel cell applications. Sb(III) and Bi(III) have very high values of E_{ass},[239] a result of the stabilizing effect of lone–pairs on the dopant ions. In the case of Sc(III), In(III), Lu(III) and Tl(III) their moderate E_{ass}, coupled with high E_{dop} values of Sc(III) and Tl(III), makes them less desirable compared to other dopants studied. The experimentally measured activation energies for ionic conductivity in

Sc– and Lu–doped CeO_2 were measured to be 1.24 eV[240] and 0.88 eV[241] respectively. These are both higher than the values of E_{ass} that have been presented, however, this is likely because E_{ass} is the energy difference between two different configurations, and doesn't calculate the energy barrier for ionic diffusion. Despite this, E_{ass} is still a good measure for screening dopants in CeO_2. The study by Omar *et al.*[241] found that Lu–doped CeO_2 had the highest activation energy out of the Rare Earth dopants studied (Lu(III), Er(III), Er(III), Y(III), Dy(III), Gd(III), Nd(III)), which agrees with the values of E_{ass}. There is not much discussion of doped CeO_2 featuring In(III) and Tl(III) ions in the literature, as their smaller ionic radius would perhaps be better suited for materials such as zirconia, where there would be less mismatch between the dopants and the host cation (Zr(IV) = 0.84 Å).[242,243] For Eu(III), the reduction energy has been significantly lowered due to the reduction of Eu(III) to Eu(II). This would suggest that Eu may act as a divalent dopant in CeO_2. Eu(III) may still be suitable for SOFC applications; Eu–doped CeO_2 has been experimentally observed to be a good ionic conductor,[136] which suggests the facile formation of the second vacancy without the formation of Ce(III) is beneficial for ionic conductivity. Y(III) and La(III) could be potential dopants for SOFC electrolytes; they exhibit low E_{dop} and while their E_{ass} values are not as low as other dopants, neither are they excessively high. Experimental studies have calculated the activation energy if Y– and La–doped CeO_2 to be 0.78 eV[241] and 0.75 eV[136] respectively, which closely match the E_{ass} values of 0.85 eV and 0.78 eV. Additionally, the presence of La(III) in CeO_2 is shown to increase E_{red}, which would help to avoid short–circuiting the operation of an SOFC by preventing the formation of intrinsic O vacancies. Of the remaining dopants investigated in this study, Tm(III), Er(III), Ho(III) are reasonable candidates for SOFC applications. They all have low E_{dop} and exhibit very low E_{ass} values with the CCV. Furthermore, none of them significantly lower the E_{red} of CeO_2 and thus do not increase unwanted electronic conductivity. Tm(III) and Ho(III) have not received much attention experimentally, most likely because both of them are very rare, even among the Rare Earth elements. Er(III) is far more abundant, and it has been observed to be a good ionic conductor

at low temperatures, it is surpassed by other dopants, e.g. Dy(III) and Gd(III). The difference between in E_{ass} between Er(III) and these two dopants is 0.03 eV for Dy(III) and 0.14 eV for Gd(III), which matches well with the differences in experimentally calculated activations energies, which are 0.04 eV and 0.11 eV respectively.[241] Out of all the dopants studied, Dy(III), Gd(III), Nd(III) and Pr(III) would be the most promising candidates for SOFC applications. As seen in Table 5.2, they are the only dopants that fall under the desired criteria in all cases. Their low E_{dop} ensures that they are readily incorporated into CeO_2 whilst their low E_{ass} indicates that the CCV is unlikely to be trapped by the dopant cations, aiding conductivity. These values tended to be lower than the values of E_a seen in experiment, however, as previously stated E_{ass} only describes the relative attraction between dopants and the CCV, and does not deal with the energy barriers associated with ionic diffusion, but it is still useful for a qualitative assessment of the dopants. Gd(III) doped CeO_2 has been widely studied, and its effectiveness for SOFC applications is well known.[130,133,147] A study by Balaguer *et al.*[136] measured the activation energy and conductivity for a series of rare earth dopants and found the activation energy for Nd(III) was slightly lower than for Gd(III), which corresponds with the calculated values of E_{ass}, although the conductivity in Gd(III) doped CeO_2 was slightly higher. Dy(III) has been shown to be an effective co–dopant for CeO_2,[244] as well as in singly doped systems, where it displaying high conductivities at low temperatures,[137] that are even comparable to Gd(III).[129] The E_{ass} of Dy(III) is 0.10 eV higher than for Gd(III), which matches quite well with the experimentally observed difference in activation energies (~0.07 eV).[241] Furthermore, Dy(III) and Gd(III) do not lower E_{red} and Nd(III) and Pr(III) actually raise it, helping to prevent any unwanted electronic conductivity in CeO_2. These results demonstrate that a combination of E_{dop}, E_{ass} and E_{red} provide a good basis for assessing the suitability of dopants for fuel cell applications. Although the E_{ass} values did not necessarily match the activation energies in experimental studies, there was good agreement between the relative values of E_{ass} and the activation energies for the dopants, and hence it is a suitable method for determining whether or not a particular

doped system will display sufficient conductivity.

Dopant	Ionic Radius[245]	E_{dop}	E_{ass}	E_{red} (Near)
Al	0.39	4.56	3.93	-0.77
Ga	0.47	4.26	2.81	-0.71
Sc	0.87	2.19	1.01	-0.09
Sb	0.86	2.19	1.03	-0.22
In	0.92	0.99	1.17	-0.01
Lu	0.98	1.32	1.11	-0.02
Tl	0.98	2.40	0.69	0.00
Tm	0.99	0.44	0.55	-0.02
Er	1.00	0.86	0.51	-0.02
Ho	1.01	0.83	0.62	-0.21
Y	1.02	0.76	0.85	0.00
Dy	1.03	0.13	0.48	0.10
Gd	1.05	0.70	0.37	0.00
Eu	1.07	0.65	0.25	-1.84
Nd	1.11	0.49	0.27	0.65
Pr	1.13	0.35	0.29	0.69
Bi	1.16	1.25	1.24	-0.04
La	1.17	0.52	0.78	0.66

Table 5.2: A summary of the ionic radii, E_{dop}, E_{ass} and E_{red} for the trivalent dopants studied in this report. The ionic radii are given in Å and energies are given in eV. The values of E_{red} given are relative to the E_{red} of pure CeO_2, 2.23 eV. The blue shading indicates the properties which are best suited for SOFC applications according to the previously decided criteria.

5.6 Conclusions

PBE+U calculations have been applied to a series of trivalent dopants in CeO_2. They demonstrate that the structure of doped CeO_2 is highly dependent on the ionic radius of the dopants: smaller dopants will adopts a structure similar to that of their native oxide; intermediate sized dopants will occupy Ce lattice sites and form a charge compensating vacancy (CCV) that neighbours them; larger dopants will also occupy Ce lattice sites and the CCV will be positioned at a next–nearest neighbour site. The effect of the dopants on the reducibility of CeO_2 was also tested. The results indicate that the radius of the dopants only affects the reducibility of CeO_2 in as much as it determines the defect structure: in doped CeO_2, cells that share similar defect structures also had similar values of E_{red} regardless of the differences between ionic radii.

From the range of dopants considered in this study, Dy(III), Gd(III), Nd(III), Pr(III) would be the most promising for SOFC applications. Firstly, they all exhibit low doping energies, meaning that they will easily form solid solutions with CeO_2. Secondly, the level of association between the dopant cations and the CCV are all exceptionally low. This ensures the CCV will not become trapped by the dopant cations, promoting good ionic conductivity. Finally, these dopants either do not affect the reduction energy of CeO_2 (Dy(III) and Gd(III)) or raise it (Nd(III) and Pr(III)) which serves to limit unwanted electronic conductivity in CeO_2.

Chapter 6

Ionic Conductivity in Doped CeO_2

6.1 Introduction

Perhaps the most important property for an SOFC electrolyte is the ionic conductivity: the operation of the fuel cell is dependent on the rapid diffusion of O anions through the electrolyte, from the cathode to the anode. Although there is much information that can be gained from static calculations, they can't fully describe the dynamical motion of ions through a crystal lattice over time. Furthermore, standard DFT calculations are carried out at 0 K, whereas for CeO_2–based electrolytes, the operational temperature range for these materials is ~500–1000 K.[45] Therefore, to gain additional insight into how trivalent dopants affect the ionic conductivity of CeO_2, complementary techniques must be employed that can measure the dynamical motion of anions in CeO_2.

Following advances in computational processing power, *ab initio* MD has emerged as a viable technique, offering an alternative to force–field MD.[246] These calculations employ *ab initio* calculations to obtain the electronic structure, providing highly accurate potential fields for the MD simulations. The disadvantage of the approach, compared to traditional force–field MD is that the electronic structure calculations can still be costly, which limits the practical applications of *ab initio* MD. Therefore, it is often used to test the suitability of force fields[247] or on very small systems over small time periods, e.g. a 64 atom system with a production run of $\sim$ 40 ps.[248]

In this chapter, CeO_2 systems doped with a series of trivalent cations (In(III), Y(III), Bi(III) and La(III)) are explored with *ab initio* MD calculations in order to determine how the presence of dopants affects the ionic conductivity. Due to the nature of *ab intio* MD, only short production runs are feasible, but the high accuracy of the technique is sufficient to provide useful information on doped CeO_2 materials.

6.2 Computational Methods

All electronic structure calculations were carried out with the PBE+U functional, as described in previous chapters. No localised electronic states were present in any of the calculations, however, $U_{Ce,O}$=$\{5.0, 5.5\}$ eV was employed to maintain consistency with previous results. To reduce the computational cost, the plane wave cut–off was reduced to 400 eV, and the convergence criteria for the SCF calculations was reduced to a difference of 1×10^{-5} eV between steps. For the MD calculations, a time step of 5.0 fs was used.

All MD simulations were carried out in a 2×2×2 expansion (96 atoms) of the unit cell of CeO_2. Four dopant atoms, either In(III), Y(III), Bi(III) or La(III) were introduced into the system, thus creating two CCVs, giving a dopant concentration of 12.50 mol%. The dopants were chosen from the results of the previous chapter. Firstly, only dopants with closed shell electronic structures were chosen, allowing the use of non–spin polarised calculations, vastly reducing the computational cost. Furthermore, using closed shell systems eliminates the problem of spin or charge hopping. Secondly, all the dopants chosen had low doping energies (see E_{dop} in Table 5.2), indicating that these dopants are readily soluble in CeO_2. Finally, these dopants encompass a range of ionic radii and association energies, thus providing an overview of how these factors affect ionic diffusion. Two different configurations were tested for each dopant: one where the dopants form clusters (Figure 6.1 (a)) and one with the dopants dispersed throughout the cell in order to try and maximise the distance between them (Figure 6.1 (b)). Each system underwent an equilibration run (NVE ensemble), where the

temperature was scaled to the target temperatures, either 1073 K, 1573 K, 2073 K, 2323 K, 2573 K or 3073 K, for ~5 ps. Once the system reached equilibrium, i.e. the system did not fluctuate more than ~ 250 K from the target temperature, the systems underwent the production run (NVT ensemble) for 25 ps. During the production runs, the temperatures of the systems fluctuated, due to the small size of the simulation cells. However, the average temperatures across the enetire runs remained very close to the target temperatures. Upon completion of the simulation, the output files were analysed to allow the calculation of the mean–square displacement (MSD), radial distribution function (RDF), and the coordination number of the ions. Since the calculations are carried out with a constant volume, the direct effect of thermal expansion of the lattices can not be simulated. To overcome this shortcoming, the lattices were expanded based on experimentally derived thermal expansion coefficients (TEC), and the volumes of each cell are shown in Table 6.1. The TEC for La(III), 11.80×10^{-6} /K,[249] and Y(III), 11.02×10^{-6} /K,[250] were both taken from literature values, however, no such data was found for In– and Bi–doped CeO_2. Instead, the same TEC as La(III) was employed for Bi(III), due to the closeness of their ionic radii (1.16 Åand 1.17 Å). Although the ionic radii of In(III) and Y(III) are not too close, it was found that there is little difference in the lattice constants for In– and Y–doped CeO_2, 5.406 Å [250] and 5.403 Å [251] respectively, and therefore the same TEC as Y(III) was used for In(III). The change in lattice constant due to the presence of the dopants was not modeled. Tests on La– and Y–doped CeO_2 found that the change in lattice constants at 6.25 mol% were quiet small, less than 0.3 %, whereas the changes due to thermal expansions were in the order of ~2.5–3.5 %. Assuming the changes in lattice constant as a function of dopant concentration are linear, the changes at 12.50 mol% would still be far smaller those due to thermal expansion, and hence, only the latter are accounted for. Chapter 7 contains a more complete discussion of the change in lattice constant due to the presence of dopant cations.

	Volume (Å^3)		
Dopant	2073 K	2323 K	2573 K
In(III)/Y(III)	1406.86	1418.26	1429.72
Bi(III)/La(III)	1413.55	1425.79	1438.11

Table 6.1: The volume of the simulation cells for doped CeO_2.

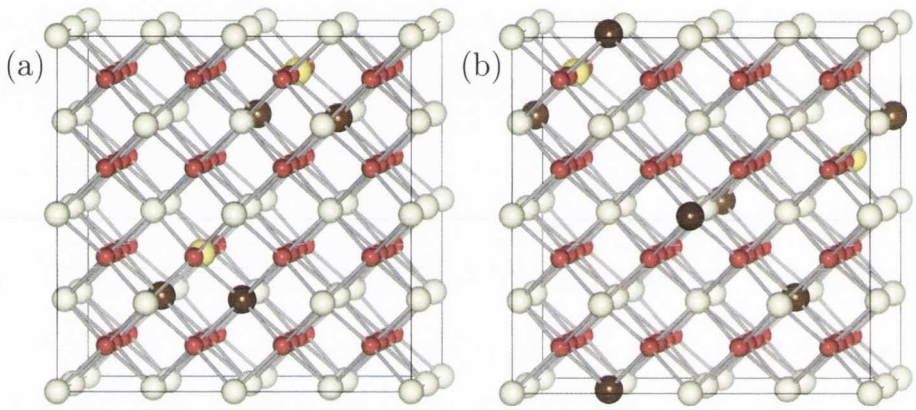

Figure 6.1: The starting structures for the *ab initio* MD simulations with a (a) clustered and (b) dispersed arrangement of the dopant cations. The dopants (In(III), Y(III), Bi(III) and La(III)) are represented by the brown spheres, the Ce(IV) ions by the white spheres and the O ions by the red spheres. The yellow spheres indicate the position of the CCVs.

6.3 Mean–square Displacement Plots and Diffusion Coefficients.

The MSDs were calculated accoring to the methods described in Section 3.5. Figure 6.2 displays the MSD plot for Y–dispersed at (a) 1073 K and (b) 3073 K. Both of these plots are representative of what occurs in all the systems studied at these temperatures. For calculations at 1073 K, no ionic diffusion occurs even over extended periods of time; the only motion that is observed are thermal vibrations of the ions on their lattice sites (Figure 6.2(a)). Similarly, the MSD plot at 1573 K also displayed no ionic conductivity, and therefore these results were discarded. Conversely, simulations carried out

at 3073 K, such as Figure 6.2(b), displayed very high levels of ionic conductivity over comparatively short time periods. However, closer examination of the structure over the time period revealed that ionic diffusion at these high temperatures was occurring not only the ⟨100⟩ direction, but also along the ⟨110⟩ and ⟨111⟩ directions. Previous studies have determined that ionic diffusion in CeO_2 under typical SOFC operating conditions only occurs along the ⟨100⟩ direction,[115,142] indicating that the high conductivities observed at 3073 K are due to an alternative, high temperature diffusion mechanism, or even perhaps the preliminary stages of melting. Therefore, the results for simulations at this temperature were discarded. The results presented in the rest of this chapter come from the MD simulations at 2073 K, 2323 K and 2573 K: these temperatures provide the necessary kinetic energy so that ionic diffusion can be measured within the time frame of the simulation while maintaining, for much of their run time, the expected movement of the ions along the ⟨100⟩ direction.

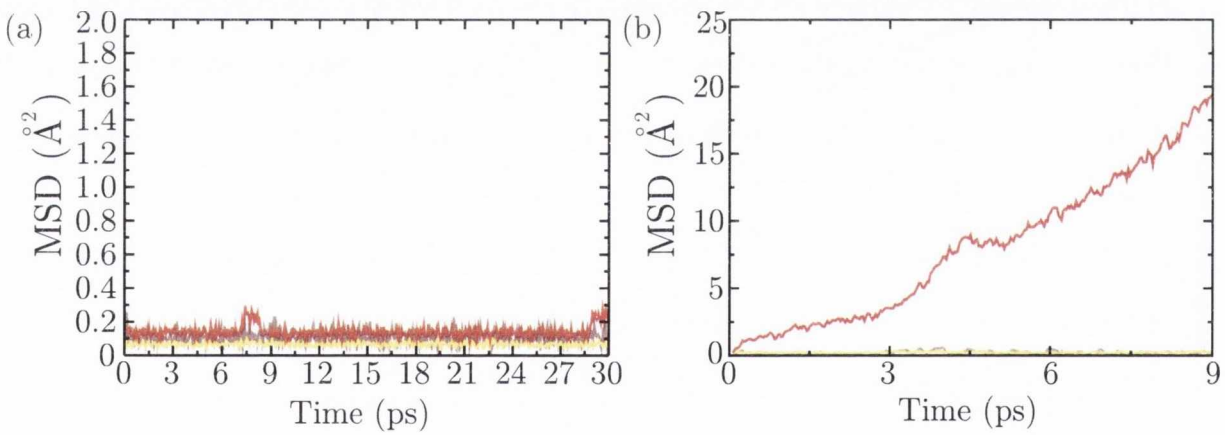

Figure 6.2: The MSD plot of Y–dispersed at (a) 1073 K and (b) 3073 K. The brown, yellow and red lines represent the movement of the dopant cations, the Ce(IV) cations and the O anions respectively.

The MSD plots for the doped systems at 2073 K, 2323 K and 2573 K are shown in Figure 6.3. The plots for the dopants and Ce(IV) ions are omitted, as only thermal vibrations were observed for these species. For the clustered systems, Figure 6.3[I], and dispersed systems, Figure 6.3[II], the diffusion of the anions increases as a function

of temperature. As previously mentioned, diffusion in CeO_2 takes place along $\langle 100 \rangle$ direction, as O ions hop from their lattice site to fill a neighbouring vacancy.[115,142] An increase in temperature should equate to a steady increase in conductivity as each ion has more kinetic energy, increasing the chance of the ions diffusing. For the most part, the MSD increase at a steady rate over the time period, indicating that a single diffusion mechanism is present over this time. However, there are a few exceptions. The MSD of La–clustered at 2073 K (Figure 6.3(d)[I]), is seen to level off at $\sim$ 9 ps with only thermal vibrations of the O anions observed thereafter. For the In–clustered systems (Figure 6.3(a)[I]) and Bi–clustered (Figure 6.3(c)[I]) at 2573 K, there are points where the slope of the MSD sharply increases, indicating a drastic increase in ionic conductivity at $\sim$12.50 ps and $\sim$10 ps for the In– and Bi–clustered systems respectively.

The diffusion coefficients, D, are calculated from the MSD plots ($D=\frac{1}{6}slope$[MSD], see Section 3.5) and are displayed in Table 6.2. At 2073 K, D is higher for the dispersed configurations than for the clustered ones, with the exception of In–doped CeO_2. However, as the temperature rises, the clustered systems display higher values of D compared to their dispersed counterparts. The results of Chapter 5 would suggest that conductivity would always be greater in the dispersed–dopant systems, as this would avoid the formation of the stable dopant–CCV–dopant clusters. A closer investigation of the structure is necessary to explain why this is not the case.

In Figure 6.3(d)[I], it was observed that after $\sim$ 9 ps, there was almost no diffusion in the system. Figure 6.4 displays the structure of the system at 15 ps and, taking into account for the periodicity of neighbouring cells, each CCV is is within $\sim$ 4.50 Å–4.75 Å of three La(III) dopants. Given the thermal vibration of the cations, this range of values corresponds to a next–nearest neighbour site with respect to the dopants, which the results of Chapter 5 showed was highly favourable for the CCVs in La–doped CeO_2. This fact accounts for the lack of diffusion and low diffusion coefficients observed for this system: the stability of the CCVs when they are NNN to La(III) hinders ionic conductivity, and eventually stops it by trapping the CCVs.

A closer investigation of the structure of the In–clustered system at 2573 K can be

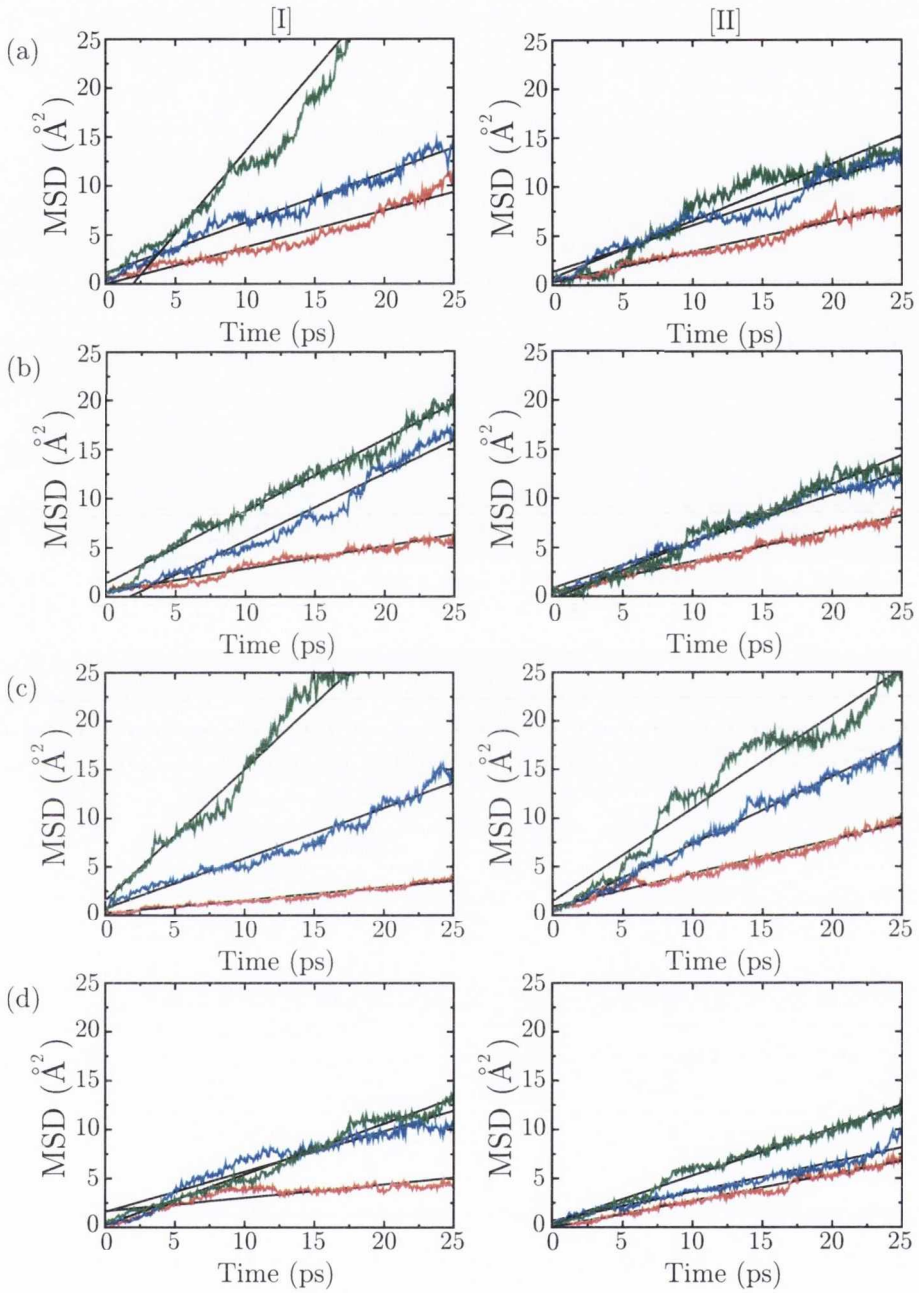

Figure 6.3: The MSD plot of O anions for [I] clustered and [II] dispersed arrangements of (a) In(III), (b) Y(III), (c) Bi(III) and (d) La(III) dopants in CeO_2. The simulations were carried out at 2073 K (red lines), 2323 K (blue lines) and 2573 K (green lines). The black lines show the slopes of the MSD plots.

Dopant	Configuration	Temperature		
		2073 K	2323 K	2573 K
In	Clustered	6.23	8.50	18.40
	Dispersed	5.12	7.86	9.66
Y	Clustered	3.87	11.40	12.20
	Dispersed	5.17	7.90	9.73
Bi	Clustered	2.21	8.62	19.60
	Dispersed	5.73	11.50	15.90
La	Clustered	2.29	6.90	8.35
	Dispersed	4.51	5.00	8.03

Table 6.2: The diffusion coefficients, D for doped CeO_2. All values for the diffusion coefficients are given in $10^{-6}\,cm^2/s$, and activation energies are given in eV.

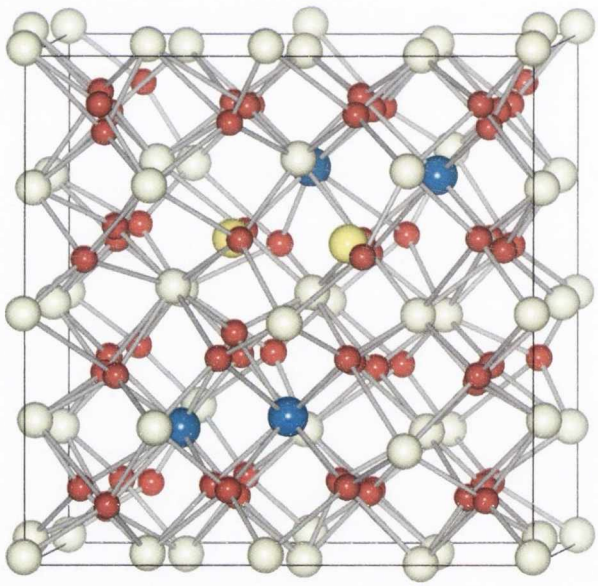

Figure 6.4: The structure of the La–clustered system at 2073 K at 15 ps. The Ce(IV), La(III) and O ions are represented by the white, blue and red spheres respectively. The position of the CCVs are shown by the yellow spheres.

seen in Figure 6.5. In the area around the CCV, Figure 6.5 (b), a neighbouring O ion has moved from its lattice site in the $\langle 100 \rangle$ direction towards the CCV, which is the

expected mechanism for ionic diffusion. However, in addition to this, an additional mechanism is present. In Figure 6.5 (c), an O ion, which neighbours neither of the CCVs, has moved from lattice site in the $\langle 111 \rangle$ towards an interstitial site, leaving behind a vacancy, which can act as a pathway for further ionic diffusion. The presence of this alternate, high temperature, diffusion mechanism is likely the cause of the high MSD slope and diffusion coefficient observed for this system.

Similar to the In–clustered system, the slope of the MSD for Bi–clustered system at 2573 K was also very high, and hence the high diffusion coefficient. Figure 6.6 (b) demonstrated that O ions are moving in the $\langle 100 \rangle$ to fill CCVs, but once again an alternative diffusion process in also present. For this diffusion mechanism, seen in Figure 6.6 (c), an O ion has moved form its lattice site in the $\langle 110 \rangle$ direction towards an interstitial site, leaving a vacancy which attracts another nearby O ion, and the formation of this new conduction pathway thus increases the ionic conductivity.

There are two major explanations for the appearance of these extra conduction mechanisms in In– and Bi–CeO_2 at high temperatures. The first is that the temperature is sufficiently high that Frenkel defects are actually stable. The results of Chapter 4 suggested there could be small concentrations of Frenkel defects within CeO_2 at higher temperatures, ~900–1200 K. Since these MD simulations are being carried out at temperatures over twice those values, it is not unreasonable that Frenkel defects are forming. The other possibility is that these systems are undergoing the early stages of sub–lattice melting. The melting point of CeO_2 is 2673 K,[252] which is very close to the target temperatures of the these systems. Furthermore, the smaller a simulation cell is, the greater the degree the temperature will fluctuate, further increasing the chance of melting. As such, the high diffusions observed in these systems appear only to be a result of the temperature, and are unlikely to be present under operating conditions typical to an SOFC electrolyte.

In regards to the diffusion coefficients being higher for the clustered systems at 2323 K and 2573 K than their dispersed counterparts, a possible explanation in the former system, the range of possible CCV–dopant distance is larger. Once a CCV is

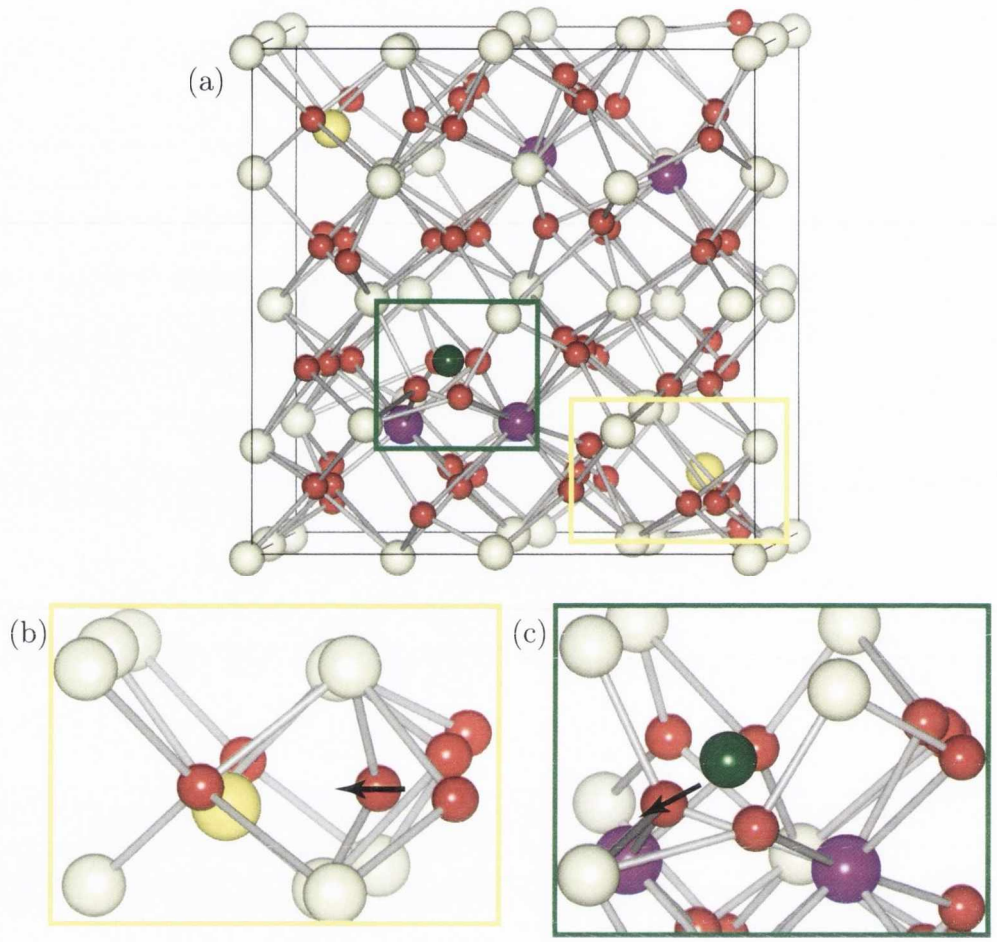

Figure 6.5: The (a) full simulation cell of the In–clustered system at 2573 K with close up views of the structure around (b) the CCV and (c) a vacancy caused by the formation of a Frenkel defect. The picture was taken at 17.50 ps. The In(III) ions are represented by the light purple spheres. The position of the CCVs are shown by the yellow spheres, and the green sphere represents a vacancy formed as a result of a Frenkel defect. The yellow and green boxes designate which section of the structure the close up views are showing. The motion of specific O ions are represented by the arrows.

free from the dopant–CCV–dopant cluster it is able to move throughout the system until it is captured at another cluster. In the dispersed systems, as a vacancy diffuses through the lattice there is a greater chance of it encountering a dopant cation, due to their dispersal, which overall slows the ionic diffusion compared to the clustered systems. Therefore, at the high temperatures these simulations are carried out under,

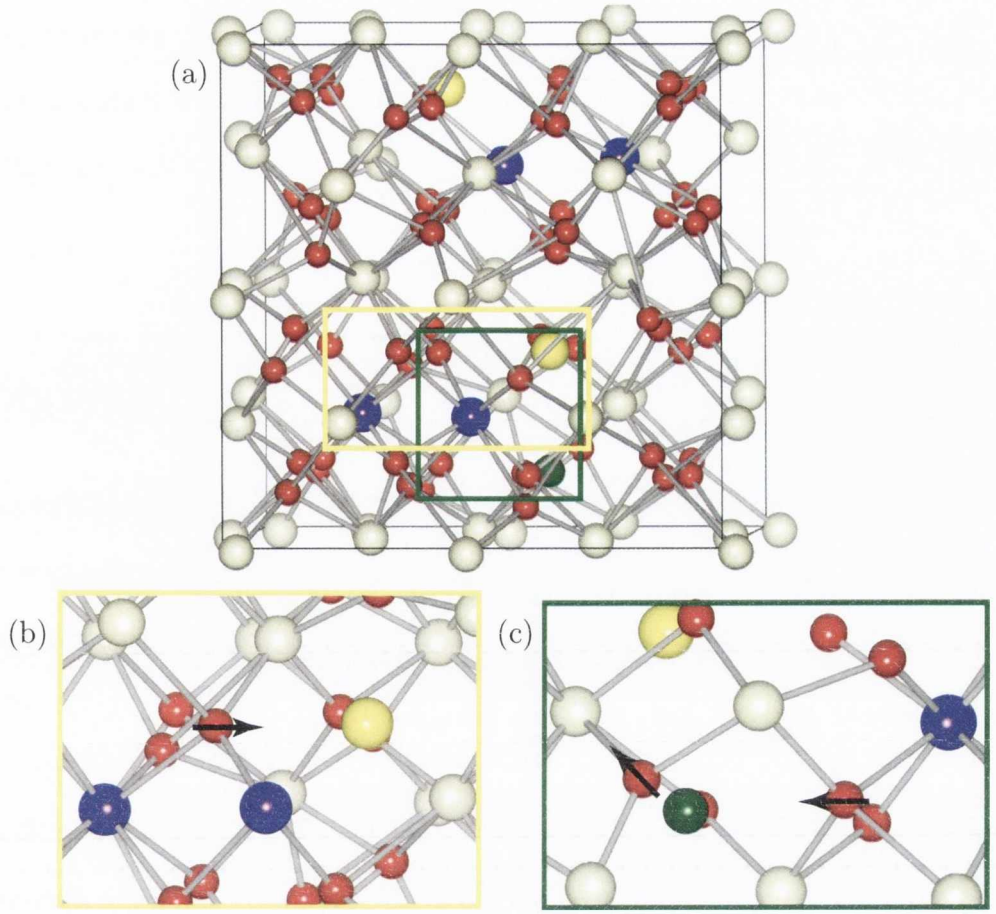

Figure 6.6: The (a) full simulation cell of the Bi–clustered system at 2573 K with close up views of the structure around (b) the CCV and (c) a vacancy caused by the formation of a Frenkel defect. The picture was taken at 22.75 ps. The Bi(III) ions are represented by the dark purple spheres. The position of the CCVs are shown by the yellow spheres, and the green sphere represents a vacancy formed as a result of a Frenkel defect. The yellow and green boxes designate which section of the structure the close up views are showing. The motion of specific O ions are represented by the arrows.

there is sufficient energy for the CCV to break free from the dopant clusters and high values of D are observed. As previously mentioned, the In–clustered systems has a higher value of D than the In–dispersed systems, even at 2073 K. A PBE study by Nakayama and Martin proposed that for trivalent dopants in CeO_2, those with small ionic radii would have a greater attraction for the CCV, but it would be easier for

O anions to diffuse by them. Since In(III) has the smallest radii out of the dopants studied in this chapter (0.92 Å), it is possible that at 2073 K there is already sufficient energy for easy diffusion around the dopant clusters to occur, and hence the high values of D observed in the In–clustered system at 2073 K.

6.4 Conductivity Plots and Activation Energies

The Nernst–Einstein equation (Section 3.5, Equation 3.10) can be employed to calculate the ionic conductivity, σ, from the diffusion coefficients. Figure 6.7 displays plots of $\ln(\sigma T)$ versus temperature for each sytem. The advantage of plotting the results in this manner is that the activation energy for ionic diffusion, E_a, can be calculated from the slopes of plots due to the relation $\sigma T = \sigma_0 e^{-\frac{E_a}{k_B T}}$, where σ_0 is the pre–exponential factor. The activation energies for each system are display in Table 6.3. In every case, E_a is significantly lower for the dispersed systems than the clustered ones. This demonstrates that the CCV is more strongly attracted to the dopants in the latter system, most likely due to the high stability of the dopant–vacancy–dopant cluster. The particularly high E_a for Bi–doped CeO_2 is likely a result of the lone–pairs associated with the dopants (see Section 5.3). An exception to this trend was observed for In–doped CeO_2. In Chapter 1.1, the association between the CCV and In(III) was higher than for Y(III), however, they were found to have the same value of E_a for the dispersed configuration and in the clustered system, the E_a of In(III) is lower than for Y(III). To determine the cause of this apparent discrepancy, a closer analysis of the structure of the systems will be carried out in the following sections.

6.5 RDFs and Structural Analysis

The RDFs were calculated over the entire runs (25 ps, 500 frames) in order to describe the relative position of the cations with respect to the anions. Figure 6.8 shows the plot of the RDF for Ce–O and La–O distance for the La–clustered system at (a) 2073 K, (b)

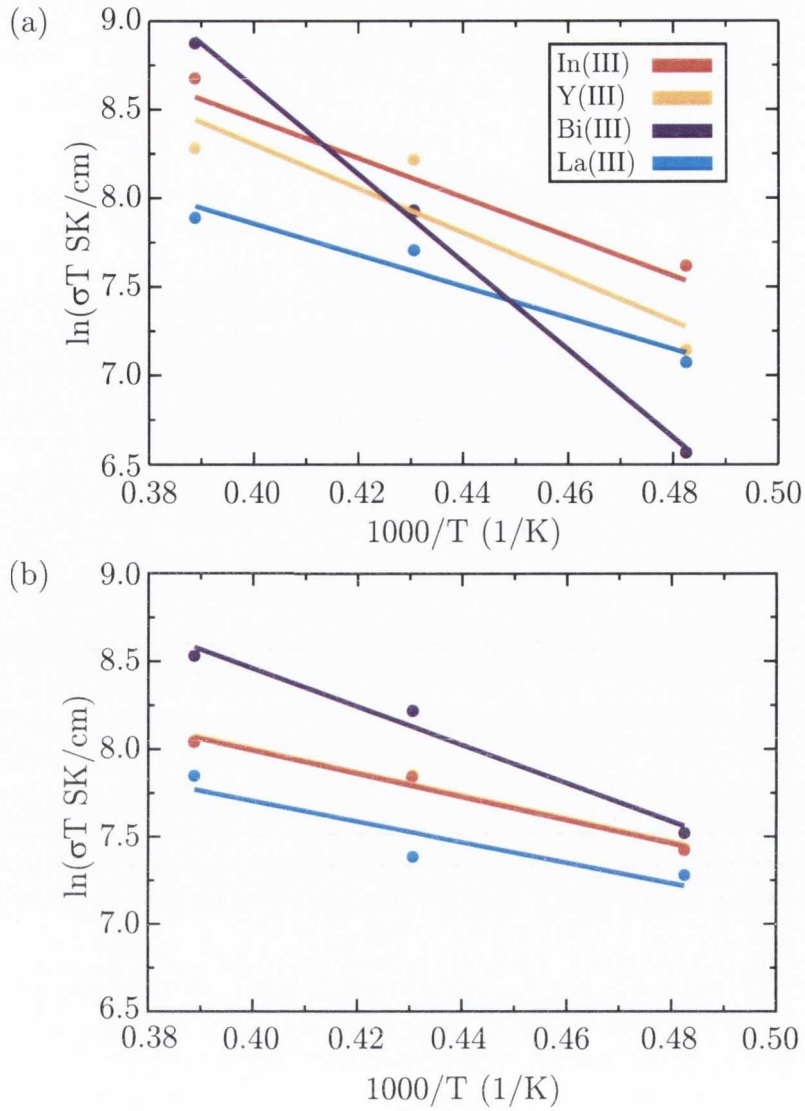

Figure 6.7: The plot of $\ln(\sigma T)$ versus $\frac{1000}{T}$ for the (a) clustered and (b) dispersed arrangement of dopants. The In–doped systems are represented by the red circles/lines, the Y–doped systems by the yellow circles/lines, the Bi–doped systems by the purple circles/lines and the La–doped systems by the blue circles/lines.

2323 K and (c) 2573 K, with minimal differences between the three temperature regimes observed. Similar results were found for the other dopant systems, and therefore RDFs are only given in Figure 6.9 for systems simulated at 2323 K, to serve as a representative example. Each RDF displays two peaks, one between ~1.80–3.50 Å, which are the nearest neighbour distances, and the second between ~3.50–5.50 Å, which show the next–nearest neighbour distances. The most likely M–O bond lengths are summarised

Dopant	Configuration	E_a (eV)
In	Clustered	1.33
	Dispersed	0.80
Y	Clustered	1.50
	Dispersed	0.80
Bi	Clustered	2.97
	Dispersed	1.31
La	Clustered	1.06
	Dispersed	0.71

Table 6.3: The calculated activation energies, E_a, for ionic diffusion in doped CeO_2.

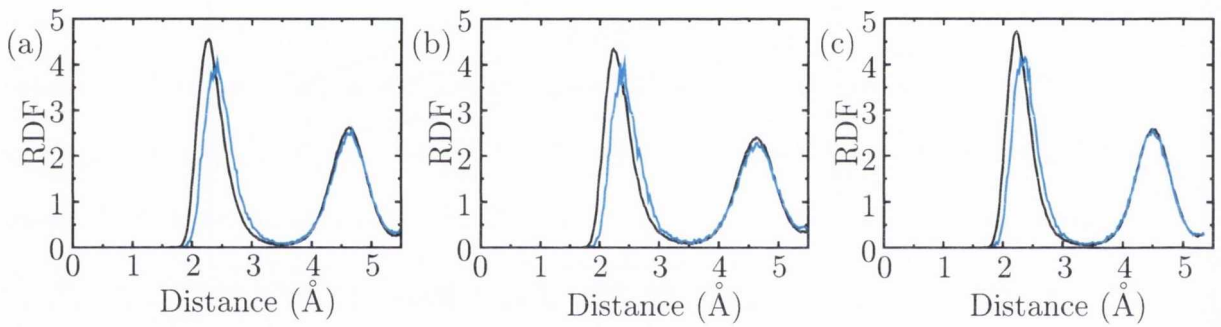

Figure 6.8: The RDF plot of Ce–O (black lines) and La–O (blue lines) for the La–clustered system at (a) 2073 K, (b) 2323 K and (c) 2573 K.

in Table 6.4. At 2073 K, the most likely Ce–O distance is 2.25 Å which is less than the value of the static lattice (2.37 Å, see Chapter 4). For the M–O distances, very few differences are observed between the RDFs for the clustered (Figure 6.9 [I]) and the dispersed (Figure 6.9 [II]). Furthermore, due to the short time span of the simulations, the peaks in the RDFs, especially for the dopants, are not always smooth. Therefore, the change in M–O distances between configurations may only be a result of the jaggedness of the peaks. In Figure 6.9 (a), it can be seen that the In–O distance is less than the Ce–O distance. For Y–doped (Figure 6.9 (b)) and Bi–doped CeO_2 (Figure 6.9 (c)), the RDFs of the M–O and Ce–O distances match very closely,

Dopant	Configuration	M–O (Å)		
		2073 K (Å)	2323 K	2573 K
In	Clustered	2.18	2.18	2.18
	Dispersed	2.16	2.16	2.16
Y	Clustered	2.22	2.22	2.22
	Dispersed	2.24	2.24	2.24
Bi	Clustered	2.29	2.29	2.29
	Dispersed	2.30	2.30	2.30
La	Clustered	2.42	2.42	2.42
	Dispersed	2.40	2.40	2.40

Table 6.4: The M–O bond lengths (M=In(III), Y(III), Bi(III), La(III)) and dopant cation coordination numbers for the doped CeO_2 systems.

with the former being slightly shorter and the latter slightly longer. Finally, the RDF for La–doped CeO_2, Figure 6.9 (c), show that the average La–O distance is greater than the average Ce–O distance. All these results are consistent with previous work concerning the critical ionic radius, r_c: this is the radius a dopant ion must have to cause neither expansion nor contraction of the host lattice, and for trivalent dopants in CeO_2 this value is 1.038 Å.[138] The radius of In(III), 0.92 Å, is lower than the r_c, which means the lattice will contract around the dopants and hence the shorter In–O distances. The radius of Y(III), 1.02 Å, is very close the the r_c, which accounts for the minimal differences observed between the Y–O and Ce–O distances observed in Figure 6.9 (b). When the radius of the dopant is higher than the r_c, as for Bi(III) (1.16 Å) and La(III) (1.17 Å), the lattice expands around the dopants, which leads to the longer La–O distances observed in Figure 6.9 (c) and (d).

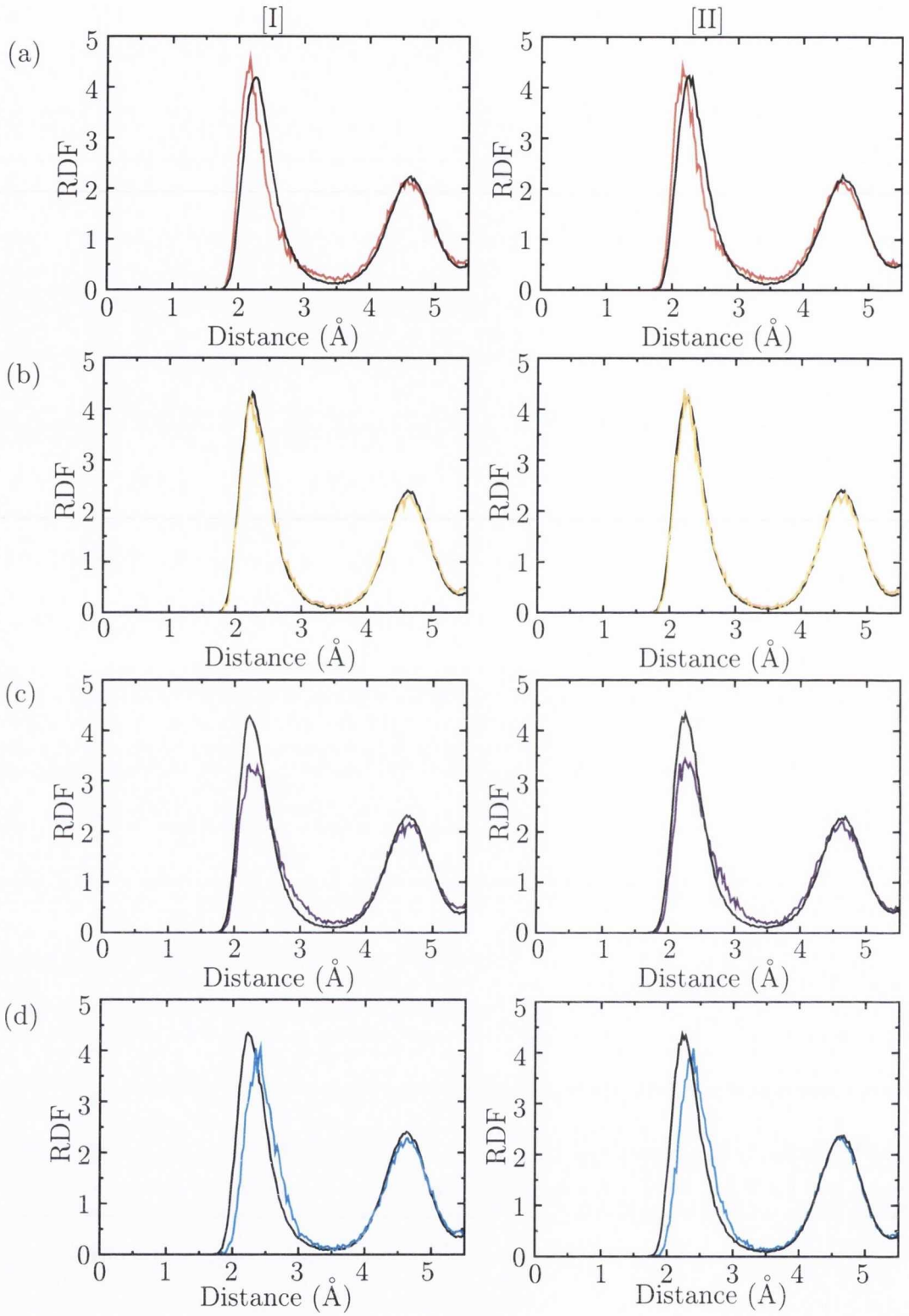

Figure 6.9: The RDF plots for [I] clustered and [II] dispersed dopant configurations in (a) In(III), (b) Y(III), (c) Bi(III) and (d) La(III) doped CeO_2 at 2323 K. The Ce–O distances are represented by black lines and the M–O distances are represented by the red (In(III)), yellow (Y(III)), purple (Bi(III)) and blue (La(III)) lines.

6.6 Coordination Analysis

To determine the coordination numbers of the dopants, the number of nearest neighbours for all the dopants in a single frame of the simulation was calculated and from that the average dopant coordination number was derived. These values were added up for all frames in order to give the average coordination number across the entire production run. Firstly, it was necessary to define what would be considered a nearest neighbour. From the RDF plots in Figure 6.9, it was found that the first peak, corresponding to the nearest neighbour distances, were within the range of ~1.80–3.5 Å. Therefore, any anion within 3.5 Å of a dopant ion was considered a nearest neighbour. The NN bond lengths and coordination numbers are shown in Table 6.5. The range of values that were expected for the dopants ions were: 7.00, when both CCVs are NN to two dopants; 7.25, when one dopant is NN to two dopants, and the other is NN to a single dopant; 7.50, for when either one CCV is NN two dopants while the other is NN to no dopants, or when both CCVs neighbour a single dopant; 7.75, when a single CCV is NN to one dopant; and finally, 8.00 when there are no CCVs NN to the dopants. Similarly, the range of coordination numbers for the Ce(IV) ions is expected to range from 7.86, when both CCVs neighbour two dopants, and 7.71, when the CCVs only neighbour Ce(IV) ions. However, there are a few instances were the coordination numbers exceed these value. Investigation of the structures revealed that at higher temperatures, there is such distortion within the lattice that some of the next–nearest neighbour anions had fallen within the defined radius, thus leading to the higher coordination numbers observed. For example, Figure 6.10 shows that in addition to the eight NN anions around the Y(III) ion, there is an O ion 3.28 Å away that is counted as also coordinated to the cation, giving it a coordination of nine.

For the In–doped systems, the coordination numbers suggest a high level of association between the dopants and the CCVs. For the In–clustered systems, the coordination number is 7.40 at 2073 K, which indicates that either both CCVs are NN to one In(III) ion, or one CCV is NN to two In(III) ions, which would correspond to a coordination

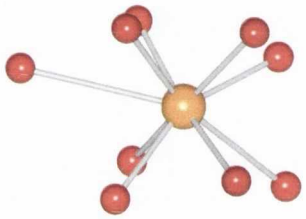

Figure 6.10: The local structure around an Y(III) ion (orange sphere) in the Y–dispersed system at 2573 K. The images is taken at a time of 13.80 ps.

Dopant	Configuration	Coordination Number					
		2073 K		2323 K		2573 K	
		M(III)	Ce(IV)	M(III)	Ce(IV)	M(III)	Ce(IV)
In	Clustered	7.40	7.88	7.33	7.76	7.28	7.72
	Dispersed	7.43	7.72	7.46	7.74	7.50	7.83
Y	Clustered	7.85	7.74	8.01	7.84	8.08	7.90
	Dispersed	7.85	7.72	7.92	7.90	8.27	8.16
Bi	Clustered	7.51	7.79	7.53	7.73	7.54	7.73
	Dispersed	7.64	7.73	7.61	7.72	7.67	7.75
La	Clustered	7.94	7.81	7.91	7.85	7.90	7.88
	Dispersed	7.96	7.80	7.92	7.85	8.23	8.11

Table 6.5: The coordination numbers of the cations in doped CeO_2.

number of 7.50. The fact that it is slightly lower means that occasionally three In(III) ions neighbour a CCV, corresponding to a coordination number of 7.25, which serves to reduce the overall average coordination number. As the temperature increases, it was found the the average coordination of In(III) ions in the system decreased, and furthermore, so did the average coordination of the Ce(IV) ions. The fact that both coordination numbers decrease is a result of the alternate diffusion mechanism discussed in Section 6.3, where O ions were observed moving to interstitial sites. This movement of O ions away from their lattice sites would reduce the coordination of the the cations in some time frames, reducing the average coordination overall. Therefore, as the tem-

perature increases, more of these interstitial O ions form, and hence the decrease in coordination with the increase in temperature. For In–dispersed systems, the coordination number is ~7.50, across the range of temperatures, which indicates that either each CCV is often NN to two In(III) ions or both are NN to a single In(III). Similar to the clustered system, this shows that there is a high level of association between In(III) and the CCVs. For the Y–doped systems, the coordination number of 7.85 at 2073 K suggests that the Y(III) ions are mostly coordinated to 8 O anions, with the vacancies only occasionally being nearest neighbours. At higher temperatures, the coordination numbers for both Y–doped systems are ~8, and therefore there is little preference of the CCV for either the Y(III) or Ce(IV) ions. The coordination numbers for both cations at 2323 K and 2573 K were higher than expected, but this was due to NNN ions being within the cut–off range due to movement of the ions. In Bi–doped CeO_2, the coordination numbers across all temperatures were ~7.50 and ~7.60 for the clustered and dispersed systems respectively, indicating that the two vacancies often neighboured the Bi(III) cations, likely caused by the favourable formation of lone pairs on the Bi(III) ions when a vacancy neighbours them. Furthermore, the Ce(IV) coordination numbers in these systems were consistent with the idea of the CCVs neighbouring the Bi(III) ions. The coordination number is slightly lower for the clustered systems due to the formation of Bi–CCV–Bi clusters being particularly favourable. Finally, the coordination numbers in La–doped CeO_2 were ~8 for each system studied. However, it was shown in Figure 6.4, Section 6.3, that the CCVs would preferentially lie, or be trapped, at a position NNN to the dopants, and therefore the NNN coordination numbers were calculated. Similarly for the coordination numbers, the number of NNN anions should range from 23, for when both CCVs are NNN to two La(III) ions, and 24, for no vacancies NNN to the dopants. For La–clustered, these values were 23.02, 23.17 and 24.37 at 2073 K, 2323 K, and 2573 K respectively, and in the La–dispersed system the values were 23.34, 23.38 and 24.08, again for 2073 K, 2323 K, and 2573 K respectively. For La–clustered at 2073 K, the value of 23.17 indicates the CCVs have indeed formed clusters with the La(III) ions at a NNN position. There is somewhat less association

at 2323 K, but the CCV is still often NNN to the La(III) ions, and at 2573 K there is no longer any significant association between the La(III) ions and the CCVs. A similar situation is observed for the La–dispersed system: there is some association between the La(III) ions and the CCV, although less than for the clustered configuration, which disappears at higher temperatures.

6.7 Discussion

To help summarise the results, Table 6.6 displays σ in order of increasing ionic conductivity. At first glance, ionic conductivity appears to be in contrast to what would be expected based on previous calculations of the activation energies. The expectations were that clustered systems would be more likely to trap the CCVs, thus reducing conductivity, and that lower activation energies values would lead to higher rates of ionic diffusion. At 2073 K, there is indeed less conductivity in the clustered systems, with the exception of In–clustered, but the ionic conductivity appears to increase as an inverse function of E_a. At 2323 K and 2573 K the clustered systems display higher conductivities than their dispersed counterparts, and once again, systems with lower activation energies often display lower conductivity than systems where the activation energy is higher. These apparent discrepancies are most likely caused by the high temperatures under which the systems are modelled. In both In– and Bi–doped systems, the coordination numbers of the dopant cations would suggest that they are often trapped by the dopants, and yet these systems display some of the highest levels of ionic diffusion. It was discovered that, in these systems, alternate diffusion mechanism a present, caused by the formation of Frenkel defects, which greatly increases the ionic conductivity. As for the higher conductivities in the clustered systems compared to their dispersed counterparts at 2323 K and 2573 K is mostly likely a result of the dopant configurations. Despite the fact that the clustered systems have higher activation energies, this is easily overcome at elevated temperatures, and once the CCVs are free to diffuse through the system there is less chance of one encountering another dopant than there is in

the dispersed system. CeO_2 based electrolytes typically operate at ~500–1000 K, and therefore most experimental results are taken from within this range. By extrapolating the slopes from Figure 6.7 back to lower temperatures, a description of these systems under typical operating conditions can be achieved.

2073 K		2323 K		2573 K	
System	σ	System	σ	System	σ
Bi–Clustered	0.34	La–Dispersed	0.69	La–Dispersed	0.99
La–Clustered	0.57	La–Clustered	0.96	La–Clustered	1.04
Y–Clustered	0.61	In–Dispersed	1.10	In–Dispersed	1.21
La–Dispersed	0.70	Y–Dispersed	1.10	Y–Dispersed	1.22
In–Dispersed	0.81	In–Clustered	1.19	Y–Clustered	1.54
Y–Dispersed	0.82	Bi–Clustered	1.20	Bi–Dispersed	1.98
Bi–Dispersed	0.89	Y–Clustered	1.60	In–Clustered	2.31
In–Clustered	0.99	Bi–Dispersed	1.60	Bi–Clustered	2.43

Table 6.6: The ionic conductivities, σ in doped CeO_2. All values are given in S/cm.

Table 6.7 displays the projected σ at 1073 K for each system, along with their activation energies and association energies (E_{ass}, calculated in Chapter 5). At this temperature, the order of σ matches better with was was originally expected: the dispersed systems display higher ionic conductivities, and the ionic conductivity increases with decreasing values for the association energy. The position of the dopant cations thus plays a vital role in determining the level of ionic conductivity in CeO_2. When the dopants are clustered together, they can form the highly stable dopant–CCV–dopant cluster, preventing the diffusion of O ions. In Chapter 5, Bi(III) ions were shown to have a very high level of association to CCVs, due to the fact that lone pairs form on the Bi(III) ions when the CCV neighbours them. Therefore, the Bi–doped systems are more likely to trap CCVs leading to very low conductivities, to the point that the projected conductivity of Bi–dispersed is even lower than the La–clustered system. The order of E_a matches the values of E_{ass} calculated in Chapter 5, with the exception

of In–doped CeO_2. This is despite the fact that the coordination number of In(III) in CeO_2 is lower than for the other other doped systems, suggesting a high association between the dopants and the CCVs, as expected from the high value of E_{ass}. Nakayama and Martin previously proposed that it would be easier for O anions to pass by dopants with smaller ionic radii. Therefore, the low E_a could be a result of small ionic radius of In(III), since although the In(III) tend to trap CCVs, this is balanced by the fact that O ions are comparatively freer to move by the dopant cations than in the other doped systems.

System	σ (S/cm)	E_a (eV)	E_{ass} (eV)
Bi–Clustered	1.02×10^{-5}	2.97	1.24
Y–Clustered	5.01×10^{-3}	1.50	0.85
In–Clustered	0.01	1.33	1.17
Bi–Dispersed	0.01	1.31	1.24
La–Clustered	0.02	1.06	0.78
In–Dispersed	0.08	0.80	1.17
Y–Dispersed	0.08	0.80	0.85
La–Dispersed	0.09	0.71	0.78

Table 6.7: The projected ionic conductivities, σ, with the activation energies, E_a, of doped CeO_2 at 1073 K.

Little research has been carried out for In–doped CeO_2, perhaps due to its scarcity, and it has not been considered for SOFC applications. The results of this chapter suggest that it may prove to be an effective dopant for increasing ionic conductivity, although it may be prone to forming In–CCV–In clusters at lower temperatures. Similarly, there has not been much discussion on Bi(III) as a dopant for CeO_2 based electrolytes. A study by Li *et al.* determined an E_a of 1.25 eV for CeO_2 doped with 14 mol% of Bi(III), similar to the value of 1.31 eV calculated for the Bi–dispersed system. They also measured the conductivity of Bi–doped CeO_2 to be $\sim9.41\times10^{-5}$ S/cm at 714 K, and an extrapolation from the plot of the conductivity of Bi–dispersed in

Figure 6.7 gives a value of 1.24×10^{-4} S/cm, a difference of ~24 %. Considering the elevated temperature of the simulations, and the fact that E_a is known to be dependent on temperature,[147] this is still a reasonable agreement. For Y–doped CeO_2, several experimental studies, all with a dopant concentration of 10 mol%, have determined E_a to be 0.60 eV,[253] 0.65 eV,[254] and 0.97 eV.[255] As can be seen, there is a large amount of disagreement between the experimental results, but the fact that the E_a calculated for Y–dispersed falls into the middle of this range further indicates the suitability of *ab initio* MD for screening potential dopants. The conductivities measure in these studies were 0.07 S/cm at 1000 K,[253] 2.00×10^{-3} S/cm at 833 K[254] and 0.06 S/cm at 773 K,[254], with the calculated conductivities at these temperatures being 0.06 S/cm, 0.02 S/cm and 0.01 S/cm, respectively. Although the latter two experimental results do not agree well with the calculated conductivities, it does show great agreement with the results of van Herle *et al*,[253] being within 14% of each other. Similarly for La–doped CeO_2 there is some agreement between experimental values of E_a, e.g. 0.75 eV [256] and 0.92 eV[257], with the calculated value of 0.71 eV. The conductivities measured from these experiments were 0.04 S/cm at 1000 K and 0.02 S/cm at 1073 K respectively, with the calculated conductivities being 0.07 S/cm at 1000 K and 0.09 S/cm at 1073 K. The good agreement with the former experiment is perhaps due to similar doping levels in the experiment and the calculations, 15 mol% and 12.5 mol% respectively, whereas the latter study used a doping concentration of 20 mol% of La(III). These results indicate that although E_a is dependent on temperature, high temperature *ab initio* MD simulations can produce conductivites that are comparable with experiment. Although some discrepancies exist, they are accurate enough to determine whether a dopant is suitable for SOFC applications, and its performance relative to other dopants.

6.8 Conclusions

The results show that the structure of the dopants is highly important, as systems where the dopants are dispersed had lower activation energies than those systems where

the dopants formed clusters, e.g. E_a=0.71 eV for La–doped CeO_2 with a dispersed arrangement of the dopants, and E_a=1.06 eV in the system where they were clustered together. Therefore, more ordered arrangements of dopants will tend to trap CCVs, hindering ionic conductivity at the typical operating temperatures of an SOFC. Bi–doped CeO_2 was found to display very little conductivity at lower temperatures, due to a high level of association between the dopants and the vacancies, and therefore is not suitable for SOFC applications. In(III) showed surprisingly high conductivity, being on par, or even higher, to equivalent Y–doped systems. However, In–doped systems did display alternative conduction mechanism, which may be the cause of this good conductivity, however, future experimental investigation of In–doped CeO_2 may prove fruitful. Out of all the dopant studied, La(III) displayed the lowest E_a of all the systems, making it a suitable candidate for SOFC electrolyte materials.[196–198]

Overall, this chapter has demonstrated that *ab initio* MD is useful for exploring the dynamic properties of materials. Despite the need for high temperatures and short simulations times, the results compare reasonably well with experiment, making these techniques a valuable method for exploring and comparing the properties of different systems.

Chapter 7

Trivalent Dopants for Improved High–κ Dielectric Behaviour in CeO_2

7.1 Introduction

CeO_2 has a vast array of potential uses, beyond catalysis and SOFC electrolytes, including such diverse applications as sunscreen[258] and anti–cancer therapies.[259] One of these alternate uses of CeO_2 is in the field of high–κ dielectrics.[260–266] Currently, HfO_2 is commonly used to replace SiO_2 in metal-oxide-semiconductor field-effect transistors (MOSFETs)[267–272] due to its moderate dielectric constant (14–18) and large band gap (5.8 eV).[270] However, there are some notable drawbacks to HfO_2–based MOSFETs. The main disadvantage is the large lattice mismatch between HfO_2 and the Si substrates, which can be as much as 6.39%.[273] Although stabilizing the cubic phase of HfO_2 by doping with yttrium can reduce this problem, the lattice mismatch still remains high.[269,270] Furthermore, defects at the interface, such as Hf–Si bonds, can also degrade the operation of the MOSFET.[269] As a result, large leakage currents have been observed in HfO_2 MOSFETs.[269] In terms of a replacement for both SiO_2 and HfO_2, CeO_2 has been found to be a good candidate due to its high dielectric constant (23-52)

[274–276], moderate band gap (2.76 eV-3.60 eV),[210–212] small equivalent oxide thickness, i.e. how thick a SiO_2 wafer would need to be to perform the same task as the high–κ dielectric (EOT = 3.8 Å)[275] and low mismatch with the Si substrate ($\Delta d < 1\%$).[261]

An important consideration when producing a MOSFET is the interface state density, D_{it}. This is a measure of the concentration of electrically active defects at the interface of the semiconductor and the oxide that can trap charge carriers. Therefore, to be effective for MOSFET applications, the D_{it} between CeO_2 and the Si substrate should be as low as possible.[261] As demonstrated in Chapter 4, the formation energy of an O vacancy in CeO_2 is quite low, which can result in the presence of Ce(III) ions at the CeO_2/SiO_2 interface. The presence of such defects may cause higher values of D_{it}, and indeed it has been found that CeO_2 MOSFETs grown under O–poor conditions have a greater leakage current than those grown under O–rich conditions.[261] It is therefore clear that a mechanism for suppressing the interface state density in CeO_2 is necessary to maximize the potential of CeO_2 for high-κ dielectric applications.

In this chapter, a series of intrinsic and extrinsic defects in CeO_2 are studied to determine its suitability for MOSFET applications. The results demonstrate: (i) the dominant intrinsic defect in CeO_2, $V_O^{\bullet\bullet}$, cannot be intrinsically compensated under Ce-rich/O-poor conditions, and can only be compensated at higher Fermi energies (E_{Fermi}) by Ce vacancies ($V_{Ce}^{''''}$) under Ce-poor/O-rich conditions, (ii) La(III) and Y(III) doping can effectively compensate the electrons left behind upon $V_O^{\bullet\bullet}$ formation through the formation of $[M'_{Ce}–V_O^{\bullet\bullet}–M'_{Ce}]$ complexes, and (iii) the addition of La(III) to CeO_2 increases the lattice constant, reducing the lattice mismatch with Si. Optimal growth conditions for La-doping to achieve maximally resistive CeO_2 with a low defect density are proposed.

7.2 Computational Methods

The defect formation energies were calculated according to the method described in Section 3.4.4. In addition to the chemical potentials for Ce and O, μ_M was also calcu-

lated, where M=Al, Ga, Sc, In, Tl, Y and La, using a method based on that of Varley *et al.*[277] In this process, the boundary of the chemical potentials are set as the formation enthalpy of M_2O_3: $\Delta H_{M_2O_3} = 2\mu_M + 3\mu_O$. As the overall system under consideration is CeO_2, the upper and lower limits of μ_O are kept the same as those calculated in Section 3.4.2 when calculating μ_M. The resulting metal chemical potentials are show in Table 7.1

	Ce–rich/O–poor	Ce–poor/O–rich
μ_{Al}	-4.42	-6.88
μ_{Ga}	-1.67	-4.13
μ_{Sc}	-5.85	-8.31
μ_{In}	-0.26	-2.72
μ_{Tl}	0.00	-1.04
μ_{Y}	-5.84	-8.30
μ_{La}	-5.51	-7.97

Table 7.1: The chemical potentials for M(III) cations (M=Al, Ga, Sc, In, Tl, Y and La). All energies are given in eV.

The thermodynamic transition/ionization levels of a defect, $\epsilon_D(q/q')$, corresponding to the Fermi-level energy at which the q and q' charge states of a defect are equal in energy, were calculated according to the method discussed in Section 3.4.5.

7.3 Intrinsic defects

The formation of point defects in a lattice can be compensated by ionic or electronic defects.[278] The structure and formation energy for the uncharged intrinsic defects was discussed in Chapter 4. The energy of the excess electrons and holes are determined by the electron chemical potential (Fermi level).

Figure 7.1 shows a plot of formation energy for all point defects under O–poor and O-rich conditions. Under O–poor growth conditions, it is clear that the dominant

defect will be the $V_O^{\bullet\bullet}$, which will not be compensated over the entire range of the band gap. $V_O^{\bullet\bullet}$ is a negative–U type defect, i.e. it exists only in the +2 and neutral charge states, consistent with the behaviour of $V_O^{\bullet\bullet}$ in a range of other wide band gap oxides.[279–285] The +2/0 ionization level is $\sim$ 0.9 eV below the conduction band minimum, meaning that $V_O^{\bullet\bullet}$ is a *deep* donor, which is mediated by the localized Ce(III) states present in the band gap.[286]

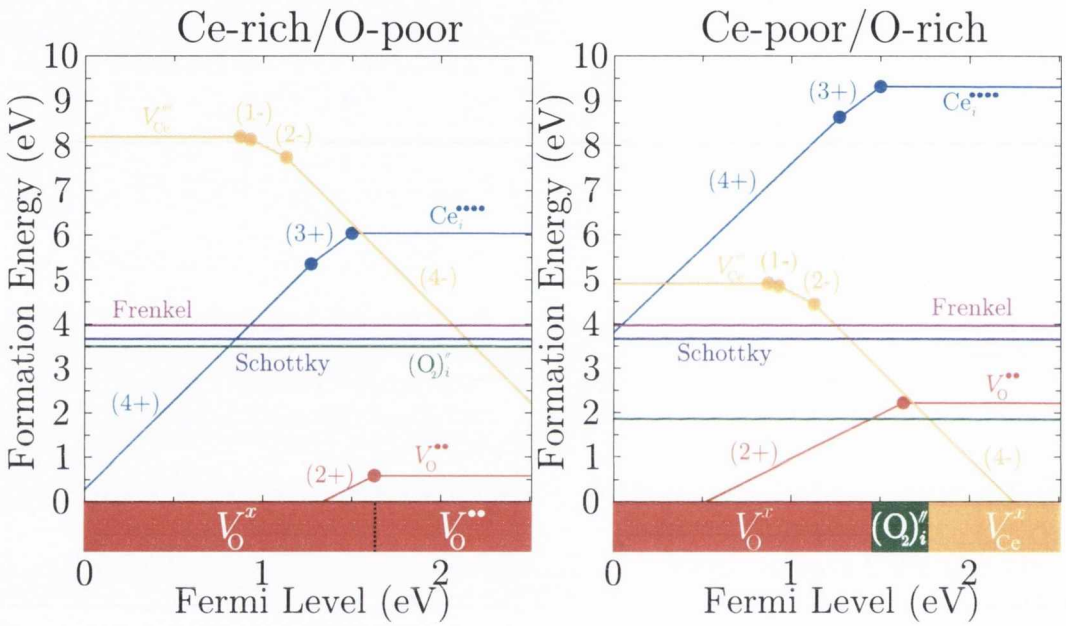

Figure 7.1: Formation energies for intrinsic defects under O–poor conditions (left panel) and O–rich (right panel) conditions. The coloured regions at the bottom indicate which defect is energetically preferred.

In an O–rich growth environment, $V_O^{\bullet\bullet}$ is the most stable defect up to 1.03eV below the CBM, where after the interstitial peroxide, $(O_2)_i''$, followed by the V_{Ce}'''' in the 4− charge state, V_{Ce}^x, start to dominate. Although the electrons formed upon $V_O^{\bullet\bullet}$ formation would be compensated at higher E_{Fermi} values, it is highly unlikely that E_{Fermi} could ever be raised high enough, due to the polaronic nature of reduced Ce seen in Chapter 4, which means that the Fermi level will be trapped near the Ce(III) states in the band gap.

7.4 Trivalent dopants

As discussed in Chapter 5, trivalent dopants will form CCVs to counteract the charge imbalance, which act as pathways for ionic diffusion and, in most cases, do not affect the reducibility of CeO_2. However, there is possibly an alternate charge compensation scheme, where the dopants' charge is compensated by the formation of an O hole. Taking a range of trivalent dopants (Sc, Y, La, Al, Ga, In, Tl), both ionic compensation ($[M'_{Ce}$–$V_O^{\bullet\bullet}$–$M'_{Ce}]$ formation) and electronic compensation ($[M'_{Ce}$–$O_O^{\bullet}]$) were tested.

For a single dopant cation in CeO_2, the charge is compensated by an O hole. For all the dopants studied, the most stable position for the hole was at an O ion next nearest–neighbour to the dopant cation (Figure 7.2). The structure for this compensation scheme has not changed significantly from the pure cell. The dopant cation remains at the lattice site and the O ions have moved away by ~0.07 Å. The greatest change in structure occurs for the O hole, which has moved ~0.25 Å away from the dopant.

From the results of Chapter 5, it was observed that the lowest energy structure depends on the ionic radius of the dopant ions. To reiterate: Al(III) and Ga(III) ions adopt a structure where the CCV neighbours only one of the dopants (Figure 7.3(a)); for Sc, Tl, Y and In–doped CeO_2, the CCV is found nearest–neighbour to both dopant cations 7.3(b); and in La–doped CeO_2 the CCV is at the next nearest–neighbour site with respect to the two dopants. Figure 7.3(c).

The formation energies for $[M'_{Ce}$–$V_O^{\bullet\bullet}$–$M'_{Ce}]$ and $[M'_{Ce}$–$O_O^{\bullet}]$ defects are shown in Figure 7.4 (solid lines). La(III) and Y(III) prove to be the most soluble dopants. Since single M'_{Ce} dopants formed localised O holes (polarons) neighbouring the dopant, the corresponding 0/-1 transition levels are deep in the band gap. This behaviour is to be expected for a material with an O $2p$–dominated VB[168,287] and has been observed in other oxide materials.[117,192] The La_{Ce}^{x} and Y_{Ce}^{x} charge states cross the V_O^x charge state near the middle of the band gap, indicating that La(III) and Y(III) doping can compensate the electrons from $V_O^{\bullet\bullet}$ formation, pinning E_{Fermi} in the band gap.

Although the formation energy of $[M'_{Ce}$–$O_O^{\bullet}]$ was lower than the formation energy

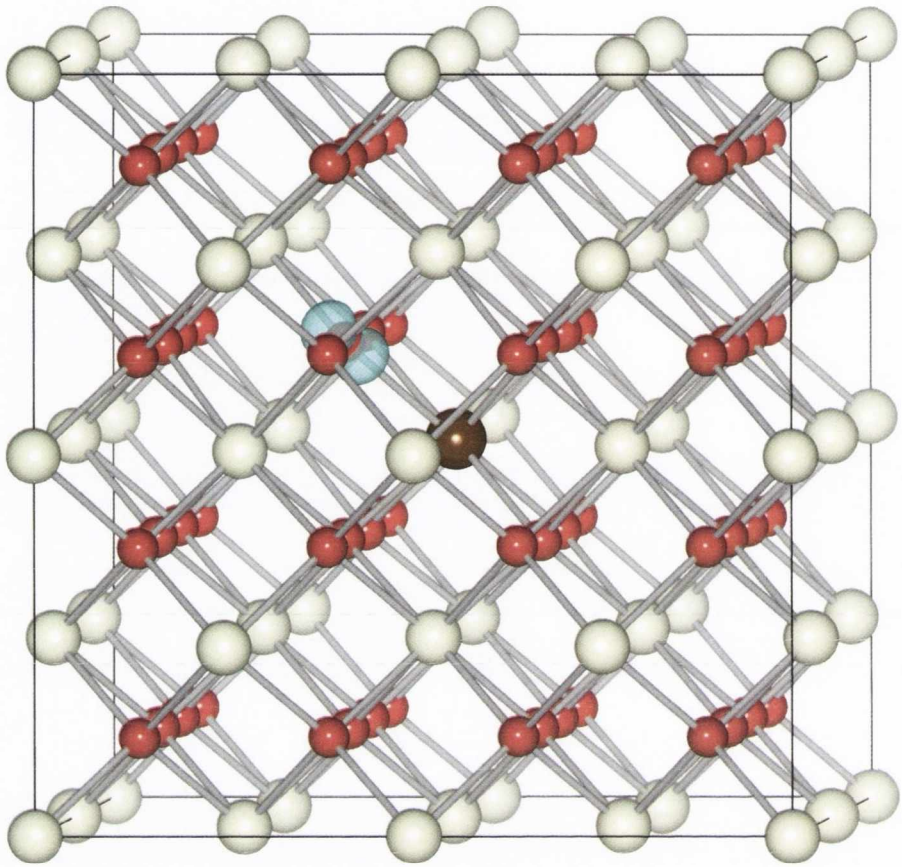

Figure 7.2: The structure of trivallently doped CeO_2 with electronic charge compensation. Ce ions are represented by the white spheres, O ions by the red spheres and the dopant ions by the brown sphere. The isosurface is shown in light blue and set to $0.05\,e/Å^3$.

of the $[M'_{Ce}–V_O^{\bullet\bullet}–M'_{Ce}]$ in all cases, this comparison is slightly misleading, as there are different numbers of M in each defect. To determine whether ionic (CCV) or electronic (O hole) compensation of the dopants is preferable, the relative stability of $[M'_{Ce}–V_O^{\bullet\bullet}–M'_{Ce}]$ and $[M'_{Ce}–O_O^{\bullet}]$ have been calculated from the equation:

$$2\Delta H_f[M_{Ce'} - O_O^{\bullet}] \xrightarrow{\Delta E} \Delta H_f\,[M_{Ce} - V_O - M_{Ce}] + \frac{1}{2}E(O_2). \tag{7.1}$$

The results of these calculations, shown in Table 7.2, are all negative which indicates that upon the introduction of trivalent dopants in CeO_2, the formation of the CCV is spontaneous and hence ionic compensation is preferable to electronic compensation.

To determine how strongly bound the dopant cations and CCV are, the binding

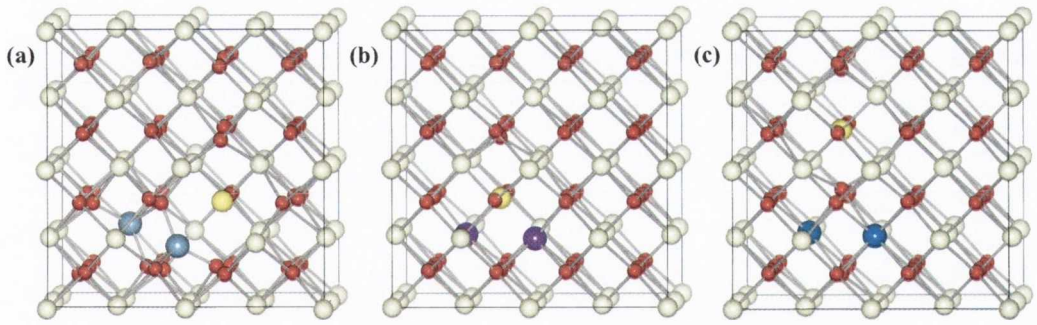

Figure 7.3: The converged structures of $[M'_{Ce}–V_O^{\bullet\bullet}–M'_{Ce}]$ defect clusters in CeO_2 with the CCV (a) nearest neighbour to one dopant (grey spheres; Al, Ga), (b) nearest neighbour to both dopants (purple spheres; Sc, Tl, Y, In) and (c) next–nearest neighbour to both dopants (dark blue sphere, La). The position of the CCV is represented by the yellow sphere.

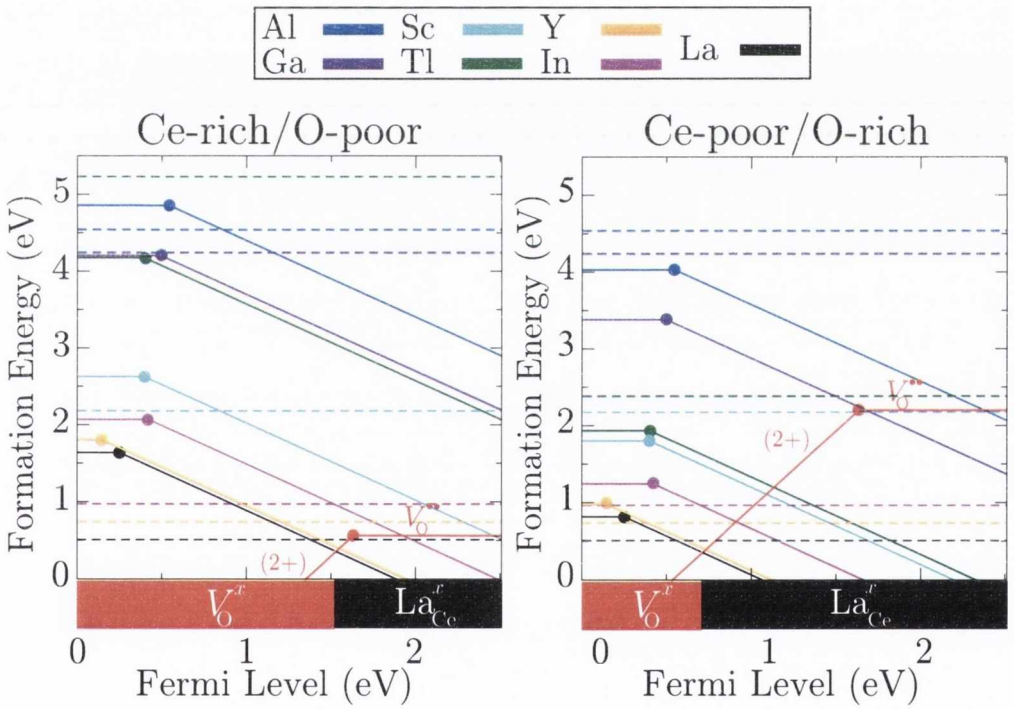

Figure 7.4: Formation energies for for trivalent dopants in CeO_2 under O-poor conditions (left panel) and O-rich (right panel) conditions. The full lines indicate the $[M'_{Ce}+O_O^{\bullet}]$ defects, with the dashed lines indicating the $[M'_{Ce}–V_O^{\bullet\bullet}–M'_{Ce}]$ formation energies. The coloured regions at the bottom indicate which defect is energetically preferred.

Dopant	Al	Ga	In	Tl	Sc	Y	La
ΔE (O–poor)	-4.86	-3.87	-2.87	-2.81	-2.77	-2.57	-2.46
ΔE (O–rich)	-6.51	-5.51	-4.51	-4.46	-4.41	-4.21	-4.10

Table 7.2: The stability of [M_{Ce}–V_O–M_{Ce}] defect clusters compared to [M_{Ce}–$O_O^{\bullet}$]. All values are given in eV.

energy of these complexes have been calculated, using:

$$E_b = \Delta H_f(V_O^x) + 2\Delta H_f(M_{Ce}^x) - \Delta H_f\left[M'_{Ce} - V_O^{\bullet\bullet} - M'_{Ce}\right]. \tag{7.2}$$

If the value of E_b is positive, then the dopant will preferentially form the [M_{Ce}–V_O–M_{Ce}] clusters instead of isolated V_O and M_{Ce} defects, with the results of this analysis shown in Table 7.3. The binding energy is positive in all cases, hence the thermodynamic driving force is for [M_{Ce}–V_O–M_{Ce}] formation.

Dopant	Al	Ga	In	Tl	Sc	Y	La
E_b	3.58	2.29	1.33	1.23	1.00	0.48	0.59

Table 7.3: The binding energies for [$M_{Ce'}$–$V_O^{\bullet\bullet}$–$M_{Ce'}$] defect clusters. All values are given in eV.

Under O–rich growth conditions, the energy to dope CeO_2 with La(III) or Y(III) is lower than the formation energy of the V_O, indicating that both dopants will act as an effective electron *killer*, therefore reducing the D_{it}, which is very beneficial for high-κ dielectric applications. Additionally, the incorporation of dopants into CeO_2 affects the lattice constant. As discussed in Chapter 5, Marrocchelli *et al.* determined that a trivalent dopant must have an ionic radius greater than 1.03 Å to cause overall expansion of the CeO_2 lattice.[139] To check this effect for Y– and La–doped CeO_2, a series of constant volume optimizations were performed on a 2×2×2 supercell, containing a [M_{Ce}–V_O–M_{Ce}] cluster ($Ce_{30}M_2O_{63}$). The resulting energy–volume data was fitted to the Murnaghan equation of state to obtain the new equilibrium lattice volume for the doped supercells (Figure 7.5). It was found that the lattice constant for La–doped

CeO_2 is increased by 0.29 %, whereas in Y–doped CeO_2 the lattice constant actually decreased by 0.08 %, in agreement with the results of Marrocchelli *et al.*[139]

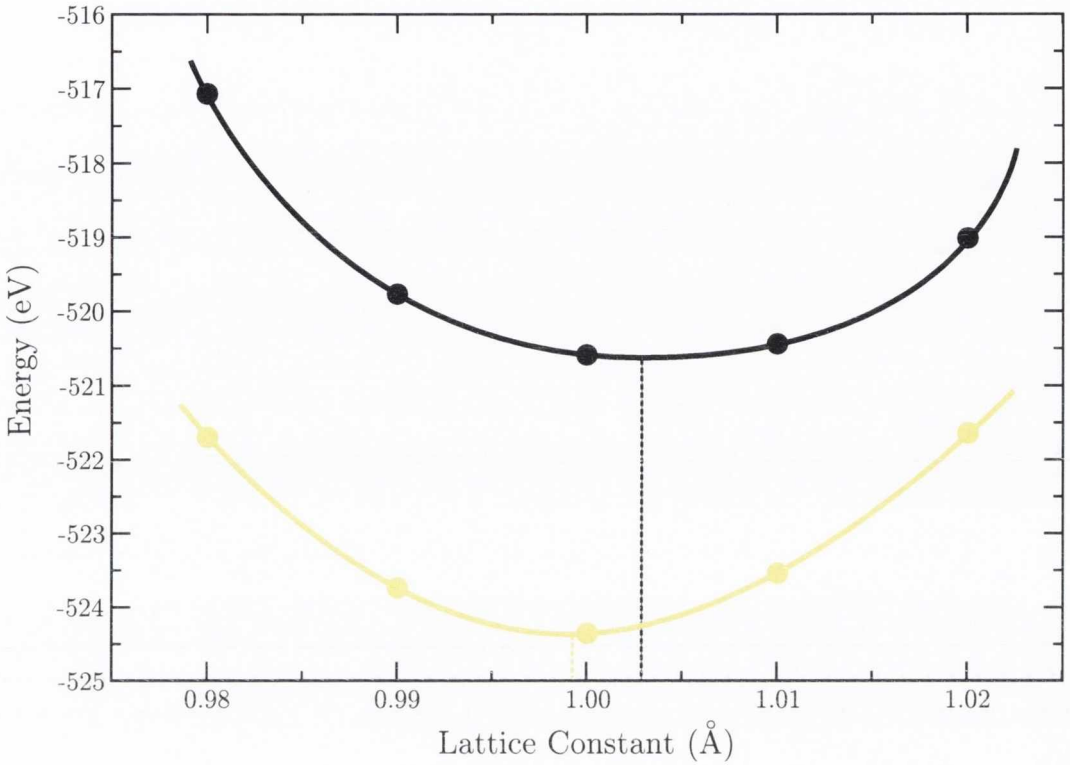

Figure 7.5: The fit of energy/volume data (circles) to the Murnaghan equation of state (solid lines) for La– and Y–doped CeO_2 (black and yellow respectively). The lattice constant is given relative to the lattice constant of CeO_2. The dashed lines indicated the equilibrium lattice volume.

7.5 Discussion

From the results show in Figure 7.1, it is apparent that under O–poor growth conditions, there will be a high concentration of $V_O^{\bullet\bullet}$ present, which could potentially trap charge carriers if present at the interface between the semiconductor and the oxide, thus increasing the D_{it}, which will be detrimental to high-κ applications. At O–rich conditions, the formation energy for $V_O^{\bullet\bullet}$ is increased which possibly accounts for the lower D_{it} seen in samples grown in an O–rich growth environment.[261] This suggests that

CeO_2 MOSFETs should be grown under O–rich conditions, however, there will still be a considerable amount of $V_O^{\bullet\bullet}$ present in the system (cf. the results of the temperature dependence analysis in Section 4.5). Therefore, to ensure optimum performance, the D_{it} must be further decreased.

It was shown that La_{Ce}^{x} and Y_{Ce}^{x} defects are capable of pinning the Fermi energy in the band gap and hence could act as "killers" for the excess electrons associated with $V_O^{\bullet\bullet}$, reducing D_{it}. However, the [M'_{Ce}–$V_O^{\bullet\bullet}$–M'_{Ce}] defect cluster was determined to be more stable than [M_{Ce}–$O_O^{\bullet}$] defects, therefore La(III) and Y(III) dopants would compensate excess electrons ionically as opposed to electronically. An additional advantage of doping with La(III) is that it causes expansion within the crystal lattice. This serves to decrease the lattice mismatch between CeO_2 (5.41 Å)[288] and Si (5.43 Å) [289] which further reduces the value of D_{it}.

7.6 Conclusions

In summary, a range of trivalent dopants in CeO_2 were studied as a means to lower the inherent density of electrons in the system, caused by V_O formation. The calculations predicted that La(III) and Y(III) are the best *electron killer* defects, being the most soluble trivalent dopants in CeO_2, compensating electrons ionically through [M'_{Ce}–$V_O^{\bullet\bullet}$–M'_{Ce}] formation. The incorporation of La(III) increases the lattice constant of CeO_2, lowering the already small lattice mismatch between CeO_2 and Si. Growth of La–doped CeO_2 under Ce-poor/O-rich conditions is expected to be optimal for production of highly resistive CeO_2. These results open up the possibility of La-doped CeO_2 as a replacement for SiO_2 in high-κ dielectric applications.

Chapter 8

Defect Chemistry on the Catalytically Active Surfaces of Pure and La–doped CeO_2

8.1 Introduction

Due to the importance of CeO_2 for many catalytic processes, there is a significant impetus to improve the operation of CeO_2 catalysts. Two common methods used to enhance the performance are optimisation of the synthesis and the addition of aliovalent dopants. The first method can enhance catalytic properties by altering the structure of the material, exposing the more reactive surfaces. For example, CeO_2 nanorods are more effective at oxidizing CO than CeO_2 nanocrystals, due to the nanorods preferential expression of the (100) and (110) surfaces,[85] whereas nanocrystals[106] expose the more stable (111) surface and are thus less effective. The presence of dopants can improve CeO_2–based catalysts in several ways, for example by creating under–coordinated O anions, thus increasing the reducibility,[113] or by increasing the number of catalytically active sites on the surface area.[290]

For the low index surfaces of CeO_2, the O vacancy remains the most studied intrinsic defect. This is probably because it is expected that these defects readily form on the

surfaces, similar to the bulk, and due to its importance for describing the OSC of CeO_2.[106,202,216,291] It is generally agreed that the reduction mechanism in CeO_2 is:

$$O_O^x + 2Ce_{Ce}^x \rightarrow V_O^{\bullet\bullet} + 2Ce'_{Ce} + \frac{1}{2}O_2(g), \tag{8.1}$$

where the excess electrons associated with the formation of the vacancy localise on nearby Ce(IV) ions, reducing them to Ce(III). However, there is still little agreement about the exact structure of the reduced low index surfaces. In bulk CeO_2 it is thought that the reduced Ce(III) ions neighbour the vacancy,[231] but scanning tunnelling microscopy studies have determined that this may not be the case for the surfaces, with the Ce(III) ions possibly forming away from the vacancy.[292,293] Theoretical studies are in agreement with this observation, showing the lowest vacancy formation energy on the (111) surface to be for a sub–surface O ion with the Ce(III) ions being next–nearest neighbour to the vacancy.[206,294] The (110) surface has displayed multiple configurations with comparable energies. Galea *et al.*[202] were the first to describe a "split–vacancy", where a neighbouring O ion moves to a position half way between its lattice site and the vacancy and the two Ce(III) ions are nearest neighbours but one is in a sub–surface position. A recent study by Kullgren *et al.* also observed the split–vacancy, however, both Ce(III) ions were on the surface, one nearest neighbour to the vacancy and the other in a next–nearest neighbour position.[291] In both the studies, it was found that energy differences between many of the configurations for the reduced surfaces were rather small, in the range of 0.05 eV. Although these varying cerium states have been explored on CeO_2, alternative oxygen states have yet to receive the same attention. Several studies have investigated and confirmed the presence of peroxide species on CeO_2 surfaces, but these have been solely related to adsorbed molecular oxygen.[99,295] In Chapter 4, peroxide ions were shown to be the most prevalent defect under O–rich conditions in bulk CeO_2, therefore the possibility exists that these defects may form intrinsically on the surfaces. The presence of such a competing defect could have a significant impact on our understanding of the catalytic properties of CeO_2.

The catalytic properties of CeO_2 can be enhanced through the addition of aliova-

lent dopants, with La(III) showing particular promise (see Chapter 1).[83,114] As demonstrated in Equations 1.4–1.6, there are several potential schemes to account for the charge difference resulting form the introduction of La(III), for example, by the formation of O holes (electronic compensation) or O vacancies (ionic compensation). Additionally, peroxide defects have been observed in several close–packed metal oxides,[191,218–221] which offers the possibility that a charge compensation scheme involving peroxide ions is also possible:

$$2O_O^x + 2Ce_{Ce}^x + M_2O_3 + \frac{1}{2}O_2 \rightarrow (O_2)_i'' + 2V_O^{\bullet\bullet} + 2M_{Ce}' + 2CeO_2. \tag{8.2}$$

To accurately describe how the dopants affect properties such as the reducibility and the adsorption of molecules, it is vital that the description of the doped surface is accurate. If a model is used that does not employ the lowest energy structure, then the accuracy of subsequent calculations may not be sufficient. Furthermore, an accurate model can provide new insights for experimental working, highlighting new features and potential reaction pathways.

The importance of the reducibility of CeO_2, and how it is affected by dopant cations, was an important area of consideration in Chapter 5. The discussion there focused on bulk CeO_2, and as such was more concerned with the reducibility with respect to the application of CeO_2 for SOFC electrolytes. In this chapter, the low index surfaces are being discussed with reference to heterogeneous catalysis where the reducibility of CeO_2 is still of great concern, as this factor influences the catalytic properties of CeO_2. Therefore, the effect of La(III) on the reducibility of CeO_2 must also be investigated. Additionally, CeO_2 is often employed to catalyse automotive emission, such as CO and NO_x,[296] and therefore a description of how the presence of La(III) affects reactions typically associated with these catalysts would be useful for assessing the utility of La–doped CeO_2 for catalysis.

In this chapter, PBE+U calculations are used to investigate the nature of oxygen states on pure and La–doped low index surfaces of CeO_2. The intrinsic and extrinsic defects of the (100), (110) and (111) surfaces are extensively studied to determine

their lowest energy structures. Additionally, a range of calculations are carried out on each one to determine how the dopants alter the energy required to form O vacancies. Furthermore, first principles energetics are employed to describe the how favourable catalytic oxidation and reduction reactions are on La–doped low index surfaces of CeO_2. These results will provide valuable information for future experimental and theoretical research on the surfaces of CeO_2 and elucidate the role La(III) plays in CeO_2 catalysts.

8.2 Computational Methods

All calculations were carried out with the same methods employed in previous chapters. The three low index surfaces of CeO_2 were constructed from the unit cell with the METADISE program.[297] All calculation on the surfaces were performed using the slab method: a slab containing a certain number of crystal layers is placed in a three–dimensional simulation cell with a vacuum gap perpendicular to the surface. The number of crystal layers needed must be large enough that the faces of the slab, which represent two surfaces, do not interact with each other. Therefore, for each surface the number of layers in the slab was varied until the energy difference between calculations was less than 0.01 eV. Furthermore, the vacuum gap was also tested to ensure it was sufficiently large that the slabs did not interact with their periodic images. The following simulation cells were utilized: the (100) surface was modelled with a (2×2) expansion; the (110) surface was modelled with a (2×3) expansion; and the (111) was modelled with a (4×4) expansion. Modelling surfaces is computationally expensive, therefore a plane–wave cut–off of 400 eV and a 1×1×1 Monkhorst–Pack k–point mesh were employed to reduce the cost. This value is lower than that used in the bulk for the (100) and (110) surfaces, but was found to provide suitable accuracy (< 0.005 eV energy difference per CeO_2 unit) compared to a denser k–point mesh while keeping the computational cost to a minimum. All calculations were deemed converged when the total force on each ion was < 0.01 eV/Å.

The surface energies, γ, were calculated according to the equation:

$$\gamma = \left(\frac{E_{surf} - E_{bulk}}{2\mathrm{A}} \right) 16.021\ \mathrm{J/m^2} \tag{8.3}$$

where E_{surf} is the energy of the slab, E_{bulk} is the energy of the bulk, A is the surface area of the slab and 16.021 is a factor to convert the answers into $\mathrm{J/m^2}$. All defect calculations were calculated according to Equation 3.1 in Chapter 3. The chemical potential employed are the same as those derived in previous chapters: at the Ce–poor/O–rich limit these are μ_{O}=0 eV, μ_{Ce}=-9.67 eV and μ_{La}=-7.97 eV and at the Ce–rich/O–poor limit they become μ_{O}=-1.64 eV, μ_{Ce}=-6.39 eV and μ_{La}=-5.51 eV.

In addition to the U value, the occupation matrix technique was used to aid in the localisation of spin states.[298] This method works by specifying the occupation within the $+U$ correction during the SCF cycle. This encourages the specified occupations and allows the system to be relaxed with this electronic distribution. The structure is optimised with the desired localisation, creating polaronic distortions around the defect. The occupation matrix is the turned off and the calculation is allowed to relax since total energies are incorrect with the occupation matrix active. The distortion introduced by the polarising distortion created when the occupation matrix was active encourage the localisation of the electron/hole at the desired site.

8.3 The Low Index Surfaces of CeO_2

The surface energies as a function of slab thickness are displayed in Figure 8.1. The (100) surface is a type III surface, i.e. it has a dipole moment perpendicular to the surfaces, and therefore half the surface O ions are removed from each side of the slab in order to remove the dipole. From these results, the following slab thicknesses were chosen: 13.10 Å for the (100) surface (120 atoms); 11.55 Å for the (110) surface (126 atoms); and 14.16 Å atoms for the (111) surface (240 atoms). For the (111) surface, it appears that a slab thickness of 9.24 Å was sufficiently large to converge the system, however, it was likely too small to model defects, as the surfaces of the slab would be close enough for defects on them to interact, especially for defects at sub–surface sites.

A slab 11.70 Å thick could also have been employed, however, by choosing the larger slab size there are atoms at the centre of the slab, which aids in maintaining symmetry in the lattice.

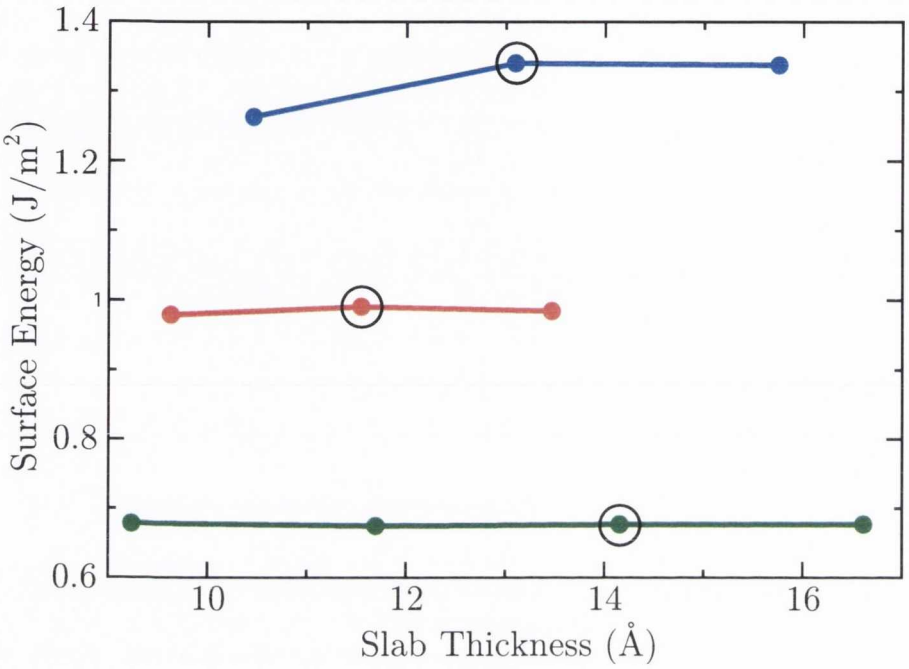

Figure 8.1: The variation of the surface energies a function of slab thickness. The (100), (110) and the (111) surfaces are represented by the blue, red and green lines respectively. The black circle indicate the slab size that was employed in subsequent calculations.

The pure surfaces of the low index surfaces of CeO_2 are shown in Figure 8.2, while their surface energies are displayed in Table 8.1 along with references from previous DFT studies. The surface energies in this report are slightly lower than the results of Fabris *et al*,[107] Skorodumova *et al.*[299] and Nolan *et al.*[106] but the (100) and (110) surface energies significantly lower than those reported by Marrocchelli and Yildiz.[300] The cause of the discrepancies between the result presented here and with the literature is probably due to the different computational techniques employed: Fabris *et al.* also used the PBE functional, whereas the other referenced works all employed the PW91 functional. In addition, Fabris *et al*, Nolan *et al.* and Marocchelli and Yildiz also included a $+U$ parameter on the Ce $4f$ states, 4.5 eV, 5.0 eV and 5.0 eV respec-

	Surface Energy		
Method	(100)	(110)	(111)
PBE+U (this work)	1.34	0.99	0.59
PBE+U [107]	N/A	1.06	0.72
PW91 [299]	1.41	1.05	0.68
PW91+U [106]	1.41	1.01	0.68
PW91+U [300]	1.65	1.39	0.64

Table 8.1: A comparison of the surface energies for the low index surfaces of CeO_2 obtained in this report with literature values. All values are given in J/m^2.

tively, whereas the calculations presented in this work used the PBE functional with a $+U$ parameter of 5.0 eV and 5.5 eV applied to the Ce $4f$ and O $2p$ states respectively. Consequently, each calculation will produce slightly different lattice constants, which would also cause changes in the calculated surface energies. Therefore the direct comparison of surface energies is not simple, however, the order of surface stability matches the previous theoretical studies, as well as experimental work,[301] i.e. (100) > (110) > (111).

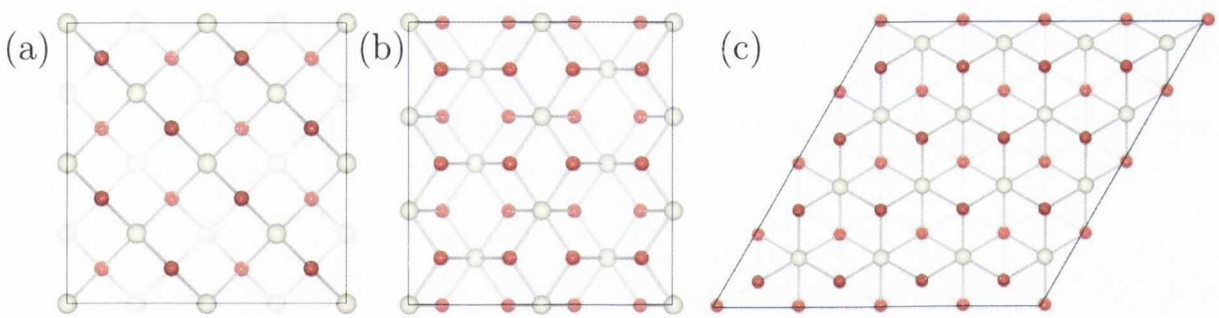

Figure 8.2: Plan view of the pure CeO_2 surfaces that were employed in the calculations, (a) (2×2) expansion of (100), (b) (2×3) expansion of (110) and (c) a (4×4) expansion of (111). The Ce cations and O anions are represented by the white and red spheres respectively.

8.4 Intrinsic Defects on the Pure CeO_2 Surfaces

To test the reducibility of CeO_2, O vacancies were created on the low index surfaces. In order to determine the most stable structure, several different position for the Ce(III) ions (i.e. the localisation of the excess electrons) were tested. Figure 8.3 shows the pure surfaces with the Ce ions and the vacancy sites labelled. These labels will be used to differentiate between the electron localisations. For example, a vacancy on the (100) surface when the Ce(III) ions are both neighbouring the vacancy will be referred to as the (100)[3,6] vacancy.

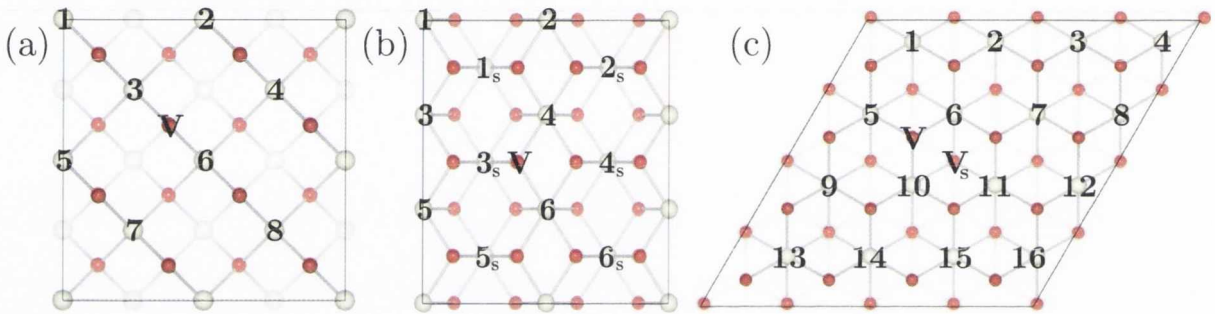

Figure 8.3: The (a) (100), (b) (110) and (c) (111) surfaces of CeO_2. The vacancies positions that were tested are denoted by the letter V. The Ce ions have been labelled to indicate where the excess electrons associated with vacancy creation localise. Subscript 's' denotes a sub–surface site.

The reduction energy, E_{red}, for the different vacancy localisation on the (100) surface are shown in Table 8.2. The most stable localisation was found for (100)[3,6], where both Ce(III) ions are nearest neighbour to the vacancy, similar to bulk CeO_2 (see Section 4.4.1). As the Ce(III) ions are positioned away from the vacancy, the general trend is that the reduction energy increases, which is likely due to Coulombic interactions. The vacancy is an area of effective positive charge, therefore it is favourable to have the Ce(III) ions neighbouring it, as they occupy a Ce(IV) site and therefore have an effective negative charge. The distance between the Ce(III) ions is also an important factor in determining the reduction energy. Since the Ce(III) ions are larger than Ce(IV) (1.14Å compared to 0.97Å), they will cause expansion in the

		E_{red}	
Ce(III) Position	Vacancy	O–poor	O–rich
NN,NN	3,6	-0.89	0.75
NN,NNN	3,7	-0.82	0.82
	3,5	-0.67	0.97
NN,NNNN	3,8	-0.59	1.05
	3,1	-0.19	1.45
NNN,NNN	5,2	-0.27	1.37
	5,7	-0.20	1.44
	5,4	-0.22	1.42
NNN,NNNN	1,5	-0.56	1.08
	1,7	-0.45	1.19
NNNN,NNNN	1,8	-0.04	1.59

Table 8.2: The reduction energy for a series of vacancy localisations on the (100) surface. The letters denote the relative position of each Ce(III) ion to the vacancy, i.e. nearest neighbour (NN), next–nearest neighbour (NNN) etc. All energies are given in eV.

lattice around them and therefore, it is favourable, whenever possible, to arrange the Ce(III) ions so that they are as far away from each other. For example, the Ce(III) ions are the same distance to the vacancy in (100)[3,8] and (100)[3,1], however, the Ce(III) ions are nearest neighbour in the latter configuration, which increases the reduction energy of the latter by 0.40 eV.

Table 8.3 displays the reduction energies for vacancies on the (110) surface. In contrast to the (100) surface and bulk CeO_2, the most stable vacancy, (110)[4,5], has Ce(III) neighbouring the vacancy while the other is at a next–nearest position, in agreement with previous studies.[291] As with the (100) surface, the reason for this is due to the fact that Coulombic attractions favour the Ce(III) ions being close to the vacancy, but the lattice strain increases when the Ce(III) ions are nearer to each other.

Therefore, the (110)[4,5] vacancy is perhaps the most stable configuration as it strikes a balance between these two factors. Another important feature of the (110) surface is the "split–vacancy", an example of which can be seen in Figure 8.4(b). First observed by Galea *et al.* this is where an O ion neighbouring the vacancy moves towards it, taking up a bridging position which is significantly more stable than a normal vacancy.[202] The only vacancy where this split–vacancy did not occur was for (110)[4,6], an NN-NN configuration of Ce(III), as it appears not to be stable between two Ce(III) ions, but when one Ce(III) occupies an NN position in the sub–surface, (110)[6,3_s], the more stable split–vacancy can form. To test whether the extra stability was due to the bridging O ion or the sub–surface Ce(III) site, the configuration (110)[3_s,4_s] was tested. Despite the fact that a split vacancy is formed, the reduction is much higher than for the other NN-NN vacancies, which suggest that sub–surface Ce(III) sites are not stable for the vacancies on the (110) surface.

The reduction energies for the (111) surface is shown in Table 8.4. For this surface, sub–surface vacancies were also tested. It was discovered that for similar configurations of the Ce(III) ions, the sub–surface vacancy was slightly more stable than the surface vacancy by ~0.03–0.05 eV. The reason for this is that when a vacancy is at a surface site, the three neighbouring O ions are in the sub–surface and are all four coordinated, whereas at the sub–surface vacancy site, three of the six neighbouring O ions are three coordinate surface O ions. In the latter case, the under–coordinated O ions are able to relax more freely, stabilising the sub–surface vacancy. It was found that the most stable vacancy was at a sub–surface site with the Ce(III) ions both NNN to the vacancy, in agreement with previous work.[302] On the (110) surface, the most stable vacancy, (110)[4,5], only had one Ce(III) at a NNN site, which is possibly a result of the slab sized used for the calculations. For the (2×3) expansion of the (110) surface, the only configuration where both Ce(III) ions are NNN to the vacancy, (110)[5,2], the Ce(III) ions are NN to each other, which is highly unfavourable due to lattice strain. Conversely, the (111) surface is modelled with a (4×4) expansion, and as such there is sufficient space on the surface for both Ce(III) ions to occupy a site NNN to the

		E_{red}	
Ce(III) Position	Vacancy	O–poor	O–rich
NN,NN	$6,3_s$	-0.89	0.75
	4,6	-0.82	0.82
	$3_s,4_s$	-0.65	0.99
NN,NNN	4,5	-1.12	0.52
	6,5	-1.09	0.55
NN,NNNN	6,2	-0.57	1.07
NNN,NNN	3,5	-1.03	0.61
NNN,NNNN	5,2	-1.03	0.61
NNNN,NNNN	1,2	-0.94	0.70

Table 8.3: The reduction energy for a series of vacancy localisations on the (110) surface. The letters denote the relative position of each Ce(III) ion to the vacancy, i.e. nearest neighbour (NN), next–nearest neighbour (NNN) etc. All energies are given in eV.

	E_{red}		
Ce(III) Position	Vacancy	O–poor	O–rich
Surface Vacancy			
NN–NN	5–10	-0.19	1.48
NN–NNN	5–11	-0.34	1.30
NN–NNNN	5–15	-0.09	1.55
NNN–NNN	9–11	-0.56	1.08
Sub–surface Vacancy			
NN–NN	10–11	-0.16	1.45
NN–NNN	11–5	-0.37	1.27
NN–NNNN	6–14	-0.14	1.50
NNN–NNN	5–15	-0.60	1.04

Table 8.4: The reduction energies for a series of vacancy localisations on the (111) surface. The letters denote the relative position of each Ce(III) ion to the vacancy, i.e. nearest neighbour (NN), next–nearest neighbour (NNN) etc. All energies are given in eV.

vacancy.

It was demonstrated that a peroxide ion is stable within bulk CeO_2 (See Section 4.4.4) and therefore a defect with two Ce(III) ions and a peroxide ion replacing two lattice O ions ($[Ce'_{Ce}–(O_2)''_i+2V_O^{\bullet\bullet}–Ce'_{Ce}]$) was tested to see if peroxide defects were stable on the low index surfaces. A wide range of different configurations were tested for the two defects by varying the position of the Ce(III) ions and the O vacancy/peroxide ion to determine the most stable structure. It was found that the peroxide would only form when the O ions forming the peroxide were nearest neighbours to the Ce(III) ions. The formation energies for these intrinsic surface defects are summarised in Table 8.5. Under O–poor conditions, the O vacancy is more stable than the peroxide ions on all surfaces, with formation energies of -0.89 eV (100), -1.12 eV (110) and -0.60 eV (111) for the vacancies compared to 0.35 eV (100), 0.30 eV (110) and 1.14 eV (111). However,

	(100)		(110)		(111)	
	O–poor	O–rich	O–poor	O–rich	O–poor	O–rich
$[Ce'_{Ce}– V_O^{\bullet\bullet}–Ce'_{Ce}]$	-0.89	0.75	-1.12	0.52	-0.60	1.04
$[Ce'_{Ce}–(O_2)''_i+2V_O^{\bullet\bullet}–Ce'_{Ce}]$	0.35	0.35	0.30	0.30	1.14	1.14

Table 8.5: The chemical potential dependent defect formation energies for the low index surfaces of CeO_2. All energies are given in eV.

O–rich conditions stabilise the peroxide defect, and for the (100) and (110) surfaces it is now more stable than the O vacancy by 0.40 eV (100) and 0.22 eV (110). On the (111) surface, the O vacancy is still more stable, but now only by 0.10 eV.

The lowest energy vacancy and peroxide defects for each surface are shown in Figure 8.4. For the vacancy defects (Figure 8.4 (a)–(c)), the position of the vacancy and its distance from the Ce(III) ions are in agreement with previous studies of the (100),[106] (110)[291] and (111)[302] surfaces. For the peroxide defects, two neighbouring O ions move from their lattice positions to an interstitial site and form a peroxide anion, $(O_2)''_i$, (Figure 8.4 (d)–(f)), while two neighbouring Ce(IV) ions are reduced to Ce(III). On the (100) surface two O ions move 1.91 Å from their lattice sites; on the (110) surface two O ions move 0.74 Å from their lattice positions; and on the (111) surface, a sub–surface O ion and a surface O ion move 0.64 Å and 0.90 Å, respectively, from their lattice sites. The resulting O–O bond lengths are 1.50 Å (100), 1.53 Å (110) and 1.53 Å (111), all of which are characteristic of a peroxide species.[217]

8.4.1 Vibrational Frequencies of Surface Peroxide Species

To calculate the vibrational frequencies of the peroxide ions, a set of calculations were performed where the O ions of the peroxide underwent a series of displacements along three directions while the rest the ions were kept stationary. The frequencies could then be calculated from the second derivative of the energy of the ions. The calculated vibrational frequencies of the O–O stretch in the intrinsic peroxide ions were 864 cm^{-1}, 802 cm^{-1} and 834 cm^{-1} on the (100), (110) and the (111) surfaces respec-

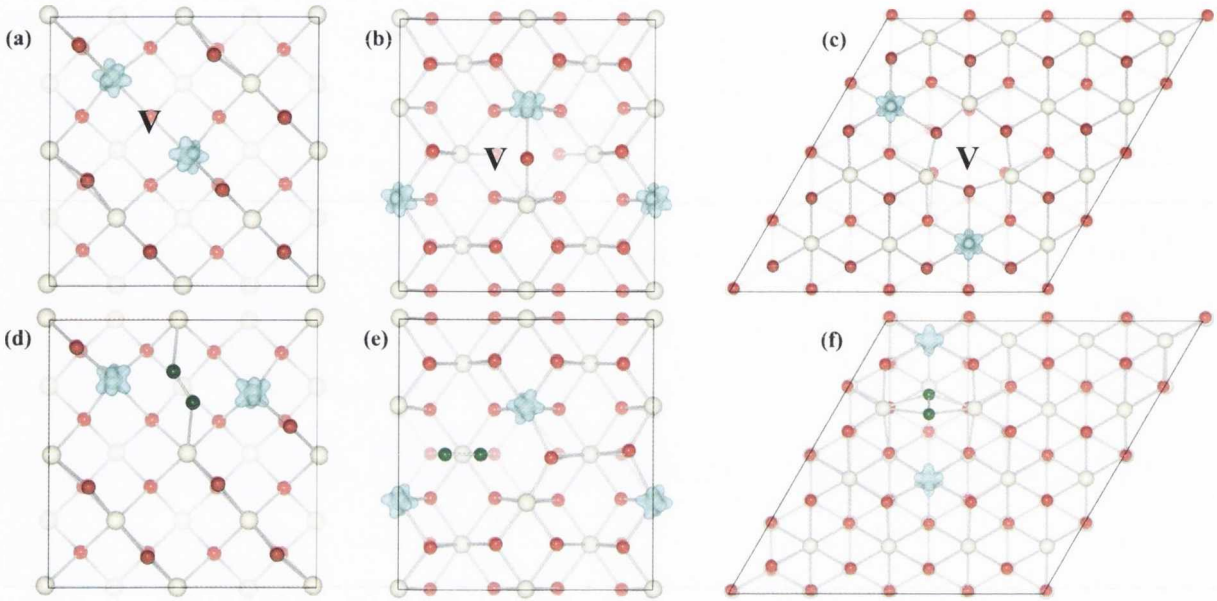

Figure 8.4: The low index surfaces of CeO_2 displaying the structures and spin density plots of the O vacancy defect on the (a) (100), (b) (110) and (c) (111) surfaces and the peroxide defect on the (d) (100), (e) (110) and (f) (111) surfaces. The Ce and O ions are represented by the white and red spheres respectively. The position of the vacancy is denoted by the letter V. The peroxide ion is represented by the dark green spheres. The isosurfaces, shown in blue, show the spin electrons on the Ce(III) ions and are set to $0.05\,e/Å^3$

tively. In previous spectroscopic studies of CeO_2 surfaces, peaks at ~877–831 cm^{-1} in the Raman spectra were assigned to O–O stretching of peroxide species from adsorbed O_2 molecules.[99,295] Wu *et al.*[99] observed these peroxide peaks in the Raman spectra of nanorods, which express the (100) and (110) surfaces, and nanocubes, which only expose the (100) surface. In contrast, extremely weak peaks at these frequencies were seen for nano-octahedra, whose surfaces are exclusively (111) in nature. The results presented in this chapter demonstrate that intrinsic peroxide defects readily form on the (100) surface, and the vibrational frequencies match experimentally determined values. Therefore, the peaks observed may be from intrinsic peroxide ions on the (100) and not due to adsorbed species. Furthermore, the lack of peaks for the (111) surfaces is in agreement with the energetic data presented in Table 8.5, which shows that the perox-

ide ion is not stable on the (111) surface. The calculated peroxide vibration frequency on the (110) surface does not match the experimental values. However, the experimental peaks associated with (110) surfaces were higher in frequency than those of the (100) surfaces, which Wu *et al.* claimed was a result of the defects forming clusters on the (110) surface, whereas they remained isolated on the (100). Since only isolated defects were calculated, this could account for the disparity between the experimental and calculated frequencies. The possibility of the intrinsic surface peroxide species being present in reduced CeO_2 at high oxygen partial pressures may be significant for understanding CeO_2 catalysis, as previous studies have only considered reactions through the O vacancy[202,303,304] or through adsorbed peroxo/superoxo species.[295,305,306]

8.5 Defect Structures of La–doped CeO_2

8.5.1 One La(III) per Surface

The first defect structures considered were charge compensating oxygen holes ($[La'_{Ce}+O^{\bullet}_{O}]$). The lowest energy structure for this defect on the three surfaces are shown in Figure 8.5 (a)[I–III]. For each of the three low index surfaces the introduction of a single dopant ion generates a hole state, i.e. an $O^{\bullet}$, which is most stable on a surface O ion neighbouring the La–dopant. It was found that O holes formed away from the dopant were not stable, and would tend to delocalise. This is likely because the La(III) ion and the O hole have, within the CeO_2 lattice, an effective negative and positive charge, respectively, hence having the hole next to the dopant ion helps to stabilise it.

8.5.2 Two La(III) per Surface

For the $[2La'_{Ce}+2O^{\bullet}_{O}]$ defect a series of calculations were carried out to determine the optimum position of the dopants and the holes. The lowest energy defect structures for each surface are shown in Figure 8.5 (b)[I–III]. As for a single La(III) dopant, the holes will preferentially form on O ions neighbouring the dopants, as the opposite effective

charges help to stabilise the defects. In all cases, the La(III) ions occupied next–nearest positions on the surface relative to each other, with La–La distances of 5.47 Å, 5.48 Å and 6.62 Å on the (100), (110) and (111) surfaces respectively.

For the compensation mechanism $[2La'_{Ce}+V_O^{\bullet\bullet}+O_O^{\bullet}+Ce'_{Ce}]$, the charge is balanced by an O vacancy, an O hole and a Ce(III) ion. The lowest energy structures for this compensation mechanism can be seen in Figure 8.5 (c)[I–III]. On the (100) surface, the vacancy forms 4.63 Å from one of the La(III) and 5.99 Å from the other. The Ce(III) ion neighbours the vacancy and is 3.70 Å and 3.82 Å from the La(III) ions. The O hole moves 2.08 Å from the lattice site to a bridging site, 2.12 Å from the vacancy. This is probably a result of the effective positive charge of the vacancy, which attracts the neighbouring O hole. Furthermore, there is less attraction between the O hole and the Ce(IV) ions than for a O anion, allowing the hole to move from its lattice site. On the (110) surface the vacancy forms next to one of the La(III) ions, reducing a neighbouring Ce(IV) to Ce(III), with the O hole neighbouring the other La(III) ion. For the (111) surface, the vacancy preferentially forms at a sub–surface O site with the dopant ions next–nearest neighbour to it. The Ce(III) ion also resides at a next–nearest neighbour site to the vacancy while the O hole is on a surface O ion, nearest neighbour to a La(III) ion. The defect structures on the (110) surface is in agreement with previous work,[118,119] however, the (111) surface structure presented here was found to be more stable than the originally proposed structure. The (100) surface was not investigated in previous studies and therefore there is nothing to compare it to.

Upon the introduction of two La(III) ions, another compensation mechanism is possible where two O ions will move from their lattice sites and form a peroxide ion, thus compensating the charge ($[2La'_{Ce}+(O_2)''_i+2V_O^{\bullet\bullet}]$). The most favourable configurations found are shown in Figure 8.5 (d)[I–III]. For all surfaces, two O ions move from their lattice positions to form the peroxide ion at an interstitial site. On the (100) surface, the surface O ion neighbouring each dopant ion moves 1.91 Å to form the peroxide ion. For the (110) surface, two surface O ions move 0.74 Å towards each other and form the peroxide. The peroxide ion on the (111) surface is formed between a sub–surface and

a surface O ion, which move from their lattice sites by 0.90 Å, and 0.64 Å respectively. The resulting O–O bond lengths are 1.50 Å (100), 1.53 Å (110) and 1.53 Å (111), all of which are characteristic of a peroxide species.[217]

Finally, several different configuration were tested for the $[2La'_{Ce}+V_O^{\bullet\bullet}]$ scheme, the most commonly studied structure for trivalently doped CeO_2.[226,304,307,308] The lowest energy structures are shown in Figure 8.5 (e)[I–III]. On the (100) surface, a surface O ion is removed with the two La(III) dopants 2.46 Å from the vacancy. On the (110) surface, the O ion neighbouring the vacancy moves from its lattice position to a bridging position between a La(III) and a Ce(IV) ion, forming a split vacancy.[202,291] The two La(III) ions are 2.36 Å and 5.80 Å from the bridging O ion. For the (111) surface, Figure 8.5 (e)[III], the vacancy lies at a sub–surface O lattice site and the two La(III) ions are 4.58 Å from the vacancy.

8.6 Doping Energies of Doped CeO_2 surfaces

The La–doping energy for these charge compensation mechanisms are displayed in Table 8.6. Under O–poor conditions, the O vacancy is the preferred compensation mechanism on all surfaces, with doping energies of -1.10 eV, -1.28 eV and -0.70 eV for the (100), (110) and (111) surfaces respectively. At the O–rich limit, however, the preferred compensation mechanism on the (100) and (110) surfaces is now a peroxide ion, with doping energies of -1.50 eV for the (100) surface and -1.34 eV on the (110) surface. Vacancy compensation is still more stable for the (111) surface, with a doping energy of -0.70 eV compared to -0.64 eV for the peroxide ion. The O vacancy and O hole structure, $[2La'_{Ce}+V_O^{\bullet\bullet}+O_O^{\bullet}+Ce'_{Ce}]$, is the second most stable defect under O–poor conditions, but still far less stable compared to O vacancy by itself. Under O–rich conditions it becomes the least stable of all the charge compensation schemes studied. Charge compensation through O holes was found to be unstable under O–poor conditions, but is significantly stabilised under O–rich conditions, and for the (100) surface it is the second most stable compensation mechanism after peroxide

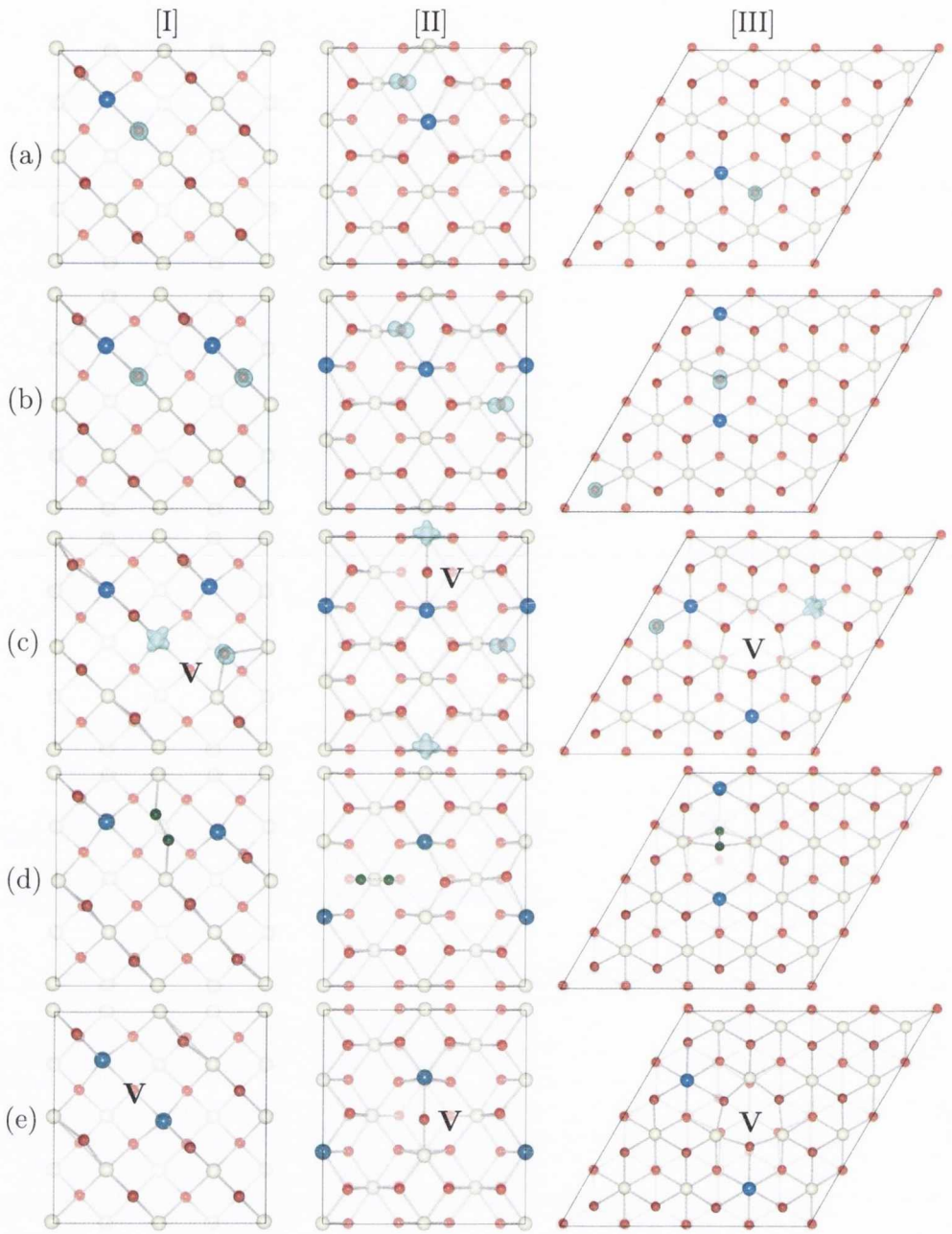

Figure 8.5: The low index surfaces of La–doped CeO_2 with spin density plots displaying charge compensation through the formation of (a) an O hole (one La(III)), (b) two O holes (two La(III)), (c) a vacancy, an O hole and a Ce(III) ion, (d) a CCV and (e) a peroxide ion on the [I] (100), [II] (110) and [III] (111) surfaces. Where applicable the position of the O vacancy is denoted by the letter V. The La(III) ions and the peroxide ions are represented by the dark blue and green spheres respectively. The isosurfaces, showing the excess spin of the O holes and Ce(III) ions, are shown in light blue and are set to $0.05\,e/Å^3$.

	(O–poor)			(O–rich)		
	(100)	(110)	(111)	(100)	(110)	(111)
$[La'_{Ce}+O^{\bullet}_{O}] \times 2$	0.40	0.58	1.38	-1.24	-1.04	-0.26
$[2La'_{Ce}+ 2\ O^{\bullet}_{O}]$	0.44	0.54	1.29	-1.19	-1.09	-0.34
$[2La'_{Ce}+V^{\bullet\bullet}_{O}+O^{\bullet}_{O}+Ce'_{Ce}]$	-0.60	-0.52	0.30	-0.60	-0.52	0.30
$[2La'_{Ce}+(O_2)''_{i}+2V^{\bullet\bullet}_{O}]$	0.14	0.30	1.00	-1.50	-1.34	-0.64
$[2La'_{Ce}+V^{\bullet\bullet}_{O}]$	-1.10	-1.28	-0.70	-1.10	-1.28	-0.70

Table 8.6: The chemical potential dependent doping energies for the different charge compensation schemes on the low index surfaces of CeO_2. The energies for the $[La'_{Ce}+O^{\bullet}_{O}]$ compensation scheme have all been multiplied by two, so that the number of La(III) ions present is consistent throughout. All energies are given in eV.

compensation. It is worth noting that the doping energy for two isolated holes on the (100) surface was lower than for two clustered holes, i.e. $[La'_{Ce}+O^{\bullet}_{O}] \times 2$ is more stable than $[2La'_{Ce}+ 2\ O^{\bullet}_{O}]$, suggesting that it is unfavourable for La(III) ions to cluster on the (100) surface.

These results are in clear contrast with the work of Yeriskin and Nolan, who claimed that the $[2La'_{Ce}+V^{\bullet\bullet}_{O}+O^{\bullet}_{O}+Ce'_{Ce}]$ is a stable defect.[118,119] The stability of these defects was further tested by calculating the energy required to convert Ce'_{Ce} and $O^{\bullet}_{O}$ to Ce^{x}_{Ce} and O^{x}_{O}, essentially switching to the vacancy compensation mechanism, but keeping the same configuration of La(III) as those seen in Figure 8.5 (c). The energy required was calculated to be -0.43 eV, -0.74 eV and -1.00 eV for the (100), (110) and (111) surfaces respectively, i.e. the excess electron will spontaneously neutralize the O hole. This emphasizes the fact that this compensation mechanism is *not* stable and will never form.

	(100)	(110)	(111)
$O_O^{\bullet}$	-1.43	-1.18	-1.53
$(O_2)_i''$	-1.67	-1.73	-2.22

Table 8.7: The shift in core level energies for O holes and peroxide ions on the La–doped low index surfaces of CeO_2. All energies are given in eV.

8.6.1 Oxygen Core Levels on the Low Index Surfaces

An x–ray photoelecton spectroscopy (XPS) study by Fleming *et al*[309] investigated La–doped CeO_2 nanocrystals, which predominantly express the (111) surface but also have significant contributions from the (110) and the (111) surfaces. They discovered a peak in the O 1*s* spectra displaying a binding energy 1.5–1.8 eV higher than the average O 1*s* contributions. In contrast to the results presented in this paper, they suggested it may be due to a charge compensating mechanism featuring O holes. To compare to the XPS data, the shift in O 1*s* core levels between O holes/peroxide and surface O anions was calculated. The O 1*s* core level shifts for both hole states and peroxide ions are shown in Table 8.7. It was found that these 1*s* core levels were lower in energy than the average of the other surface O 1*s* core levels, which would correspond to the higher binding energies observed experimentally. For O holes, the shift in core level energies only matches that which was observed by Fleming *et al.* for holes on the (111) surface, however, the energetic data suggests that such defects are not stable on the (111) surface. For the peroxide ions on the surfaces, the shifts in core level energies on the (100) and (110) surface are within the experimentally observed range, and hence the peaks observed by Fleming *et al.* are likely to be due to a peroxide compensation mechanism, and not O holes. Peaks corresponding to the calculated peroxide shift on the (111) surface were not seen, but their absence is explainable. Under all conditions, the O vacancy is the most stable charge compensation scheme on the (111) surface and hence no peaks associated with peroxide defects on this surface are observed.

8.7 Reduced La–doped surfaces

Having determined the lowest energy structures for the La–doped surfaces, a series of additional vacancies were created on each one to determine how the dopants affect the reduction energy, E_{red}, of La–doped CeO_2. For the (100) and (110) surfaces, the peroxide ion is the most stable compensation scheme under Ce–poor/O–rich environments whereas under Ce–rich/O–poor conditions compensation is via the O vacancy. Therefore, the effect of both compensation mechanisms on the reduction energy was tested for the (100) and (110) surface. For the (111) surfaces, additional vacancies were only introduced to the surface with the compensating vacancy as it is more stable than the peroxide ion mechanism under all conditions. To aid in the comparison with the pure surfaces, the relaxed structures of the lowest energy vacancy for the three surfaces is shown below in Figure 8.6.

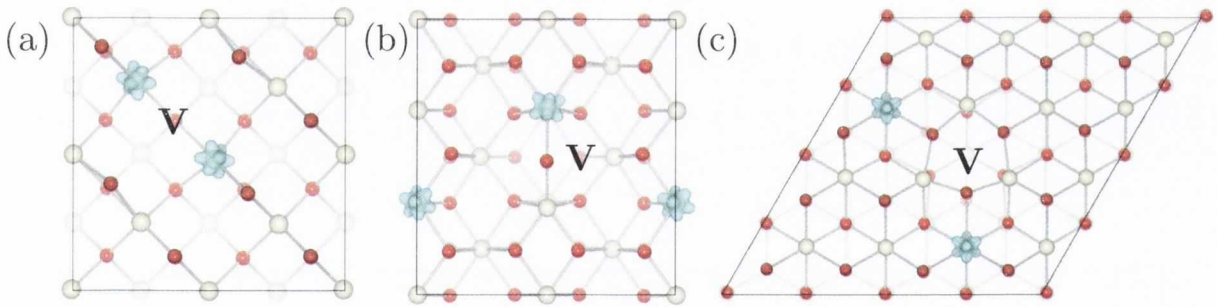

Figure 8.6: The low index surfaces of CeO_2 displaying the structures and spin density plots of the O vacancy defect on the (a) (100), (b) (110) and (c) (111) surfaces. The Ce and O ions are represented by the white and red spheres respectively. The position of the vacancy is denoted by the letter V. The isosurfaces, shown in blue, show the spin electrons on the Ce(III) ions and are set to $0.05\,e/Å^3$

8.7.1 Reduction of surfaces with a peroxide charge compensation mechanism

The structures of peroxide compensated La–doped (100) surfaces that have been reduced, along with the reduction energies, E_{red}, relative to the pure surfaces, are shown in Figure 8.7. For the most stable vacancy, Figure 8.7(a), the reduction energy was 0.41 eV higher than for the undoped surface (the relative reduction energy for the surfaces is the same regardless of whether the environment is O–poor or O–rich). For the second configuration, Figure 8.7 (b), the reduction has increased by 0.89 eV over the pure surface. The peroxide–Ce(III) distances are 4.52 Å (Figure 8.7 (a)) and 5.99 Å (Figure 8.7 (b)). These results indicate that, for the peroxide compensated La–doped (100) surface, the reduction energy is lower for shorter peroxide–Ce(III) distances. Due to the size of the surface used in this study, the La(III)–Ce(III) distances were largely the same for all the vacancies (~4.65 Å) and hence the effect of this distance on the formation energy can not be determined.

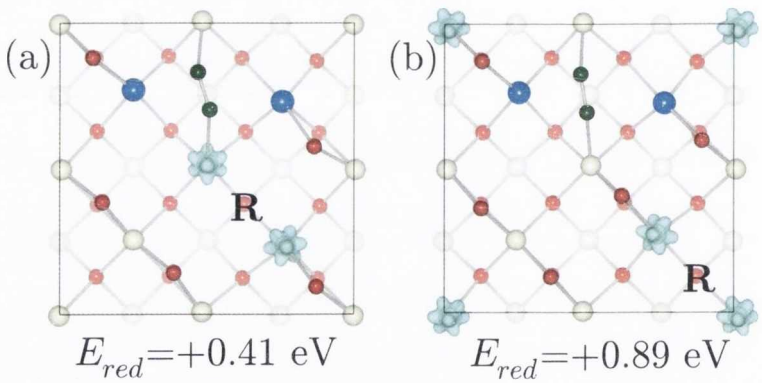

Figure 8.7: The position and formation energy for O vacancies on the La–doped (100) surface of CeO_2 that has been charge compensated with a peroxide ion. The position of the reduction vacancy is denoted by the letter R. The formation energies are given relative the vacancy formation on the pure (100) surface, 0.75 eV. The isosurfaces, shown in light blue, represent the spin density of the excess electrons on the Ce(III) ions and are set to 0.05 e/Å^3

Three different vacancy positions were tested for the peroxide–containing La–doped

(110) surface. Since vacancies on the pure (110) surface have several different configurations of the vacancy and the Ce(III) ions that are very close in energy (<0.05 eV), [202,291] several configurations were tested to which was more stable on a surface containing La(III) ions. The structures and reduction energies relative to the pure surface are shown in Figure 8.8 in order of increasing energy. The most stable vacancy position and Ce(III) configuration is shown in Figure 8.8 (a), with alternate Ce(III) configurations shown in Figures 8.8 (b) and (c). The average peroxide–Ce(III) distances are 4.81 Å, 5.02 Å and 6.38 Å for Figures 8.8 (a), (b) and (c) respectively. For the second vacancy position, Figure 8.8 (d) and (e), the average peroxide–Ce(III) distances are 4.87 Å and 6.36 Å respectively. This matches the results of the (100) surface, where the most stable vacancies on the doped surfaces are found for structures with low peroxide–Ce(III) distances. The third vacancy position, Figure 8.8 (f) and (g), appears to be in contrast with the previously observed trends as the reduction energy is significantly higher than the other vacancies, in spite of them having average peroxide–Ce(III) distances of 3.45 Å and 4.28 Å, respectively. These distances are lower than for all the other vacancies, which would suggest that these should have the lowest reduction energies, but instead they have the highest. The reason for this is probably the lack of the split–vacancy. When the vacancy is formed, the nearest neighbour O ion is part of the peroxide ion, and hence can not occupy the bridging position between the Ce(III) and La(III) ions. In Figures 8.8 (a) and (d), where there are O ions bridging a Ce(III) and a La(III) ion, the distances between these neighbouring cations are 4.14Å and 4.15Å respectively. In contrast, in Figures 8.8 (f) and 8.8 (g), where there is no bridging O ion, the Ce(III)–La(III) distance is now 4.35 Å and 4.39 Å respectively. Therefore, without the presence of the bridging O ion the Ce(III) and La(III) ions repel each other to a greater degree, increasing the lattice distortion and raising the reduction energy.

The reduction energies on the peroxide containing surfaces are summarised in Table 8.8. From the (100) and (110) surfaces, the general conclusion is that when a peroxide ion is present the most stable defects are when the Ce(III) ions are close to the peroxide. Both La(III) and Ce(III) ions are larger than Ce(IV) ions (1.17 Å and 1.14 Å compared

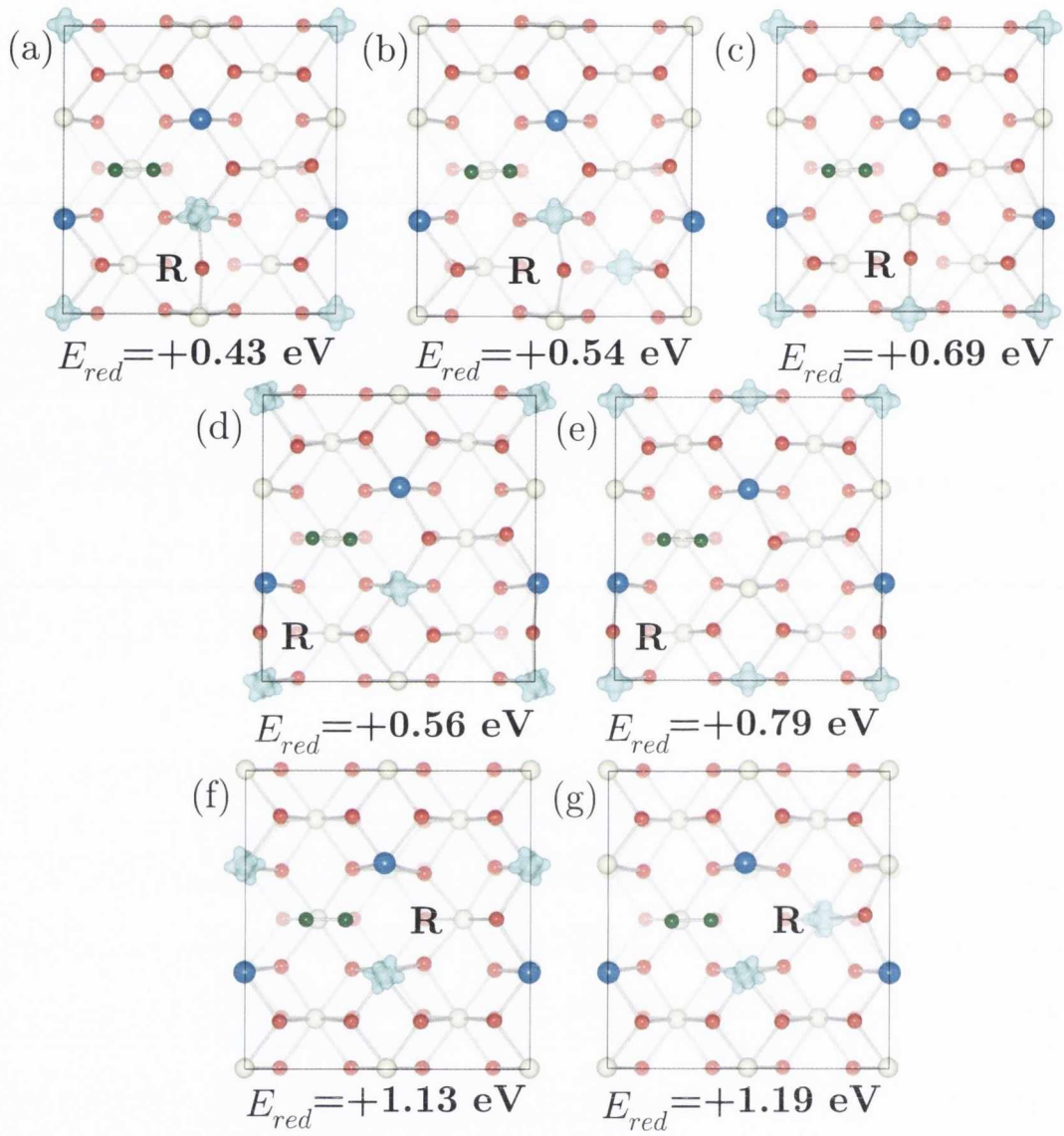

Figure 8.8: The positions, with spin density plots and formation energy for O vacancies on the La–doped (110) surface of CeO_2 charge compensated with a peroxide ion. The position of the reduction vacancy is represented by the letter R. The formation energies are given relative the vacancy formation on the pure (110) surface, 0.52 eV. The spin of the electrons on the Ce(III) ions are shown with the isosurfaces, coloured light blue, and are set to 0.05 e/Å^3

to 0.97 Å) and hence when they occupy a Ce(IV) site, they will cause expansion of the lattice through steric effects. On the other hand, the O vacancy is an area of effective positive charge, which attracts neighbouring O ions leading to lattice contraction. Since the peroxide ion replaces two O ions, it can also be considered as an area of effective

Surface	Average distance (Å)			E_{red} (eV)	
	$(O_2)_i''$–Vac(R)	$(O_2)_i''$–Ce(III)	La(III)–Ce(III)	O–poor	O–rich
100	4.34	4.52	4.65	-0.48	1.16
	5.81	5.99	4.65	0.00	1.64
110	4.57	4.81	4.20	-0.69	0.95
	4.57	5.02	4.20	-0.58	1.06
	4.57	6.38	4.46	-0.43	1.21
	4.71	4.87	4.44	-0.56	1.08
	4.71	6.36	4.66	-0.33	1.31
	3.77	3.45	4.51	0.01	1.65
	3.64	4.28	4.34	0.07	1.71

Table 8.8: The distance between important defect features and the chemical potential dependent reduction for the La–doped low index surfaces of CeO_2 that have been charge compensated with a peroxide ion. All distances are given in Å and all energies are given in eV.

positive charge. Therefore, by reducing the distance between the species which cause expansion and those that cause contraction, overall strain in the lattice is reduced. This is why the reduction energy of the vacancy seen in Figure 8.8(c) is higher than the vacancy seen in Figure 8.8(d). In the former, none of the Ce(III) ions neighbour the peroxide and hence its high reduction energy. Furthermore, the peroxide ion occupies an interstitial site, which means there is more space to accommodate the large Ce(III) ions. Due to the size of the surfaces used in this study, the La(III)–Ce(III) distances did not vary much, and hence their effect on the reduction energy could not be determine. However, in all cases the energy to form a vacancy is increased with respect to the pure surfaces.

8.7.2 Reduction of surfaces with a vacancy charge compensation mechanism

Relaxed structures of the reduction vacancies, created on the (100) surface with the vacancy charge compensation, along with their reduction energies relative to the pure surface, are shown in Figure 8.9. From these results it is once again apparent that the presence of the La(III) ions increases the reduction energy compared to pure CeO_2. The vacancy positions shown in Figures 8.9 (a), (b) and (c) have CCV–vacancy distances of 5.48 Å (Figure 8.9 (a)), 3.87 Å (Figure 8.9 (b)) and 7.75 Å (Figure 8.9 (c)), while the La(III)–Ce(III) distances were 3.87 Å, 3.97 Å and 3.54 Å, again respectively. These results indicate that it is easier to form a vacancy away from the CCV, however, short La(III)–Ce(III) distance can raise the energy significantly. The vacancy shown in Figure 8.9 (c) has a larger CCV–vacancy distance than Figure 8.9 (a), but its shorter La(III)–Ce(III) distance makes it the least stable reduction vacancy on this surface.

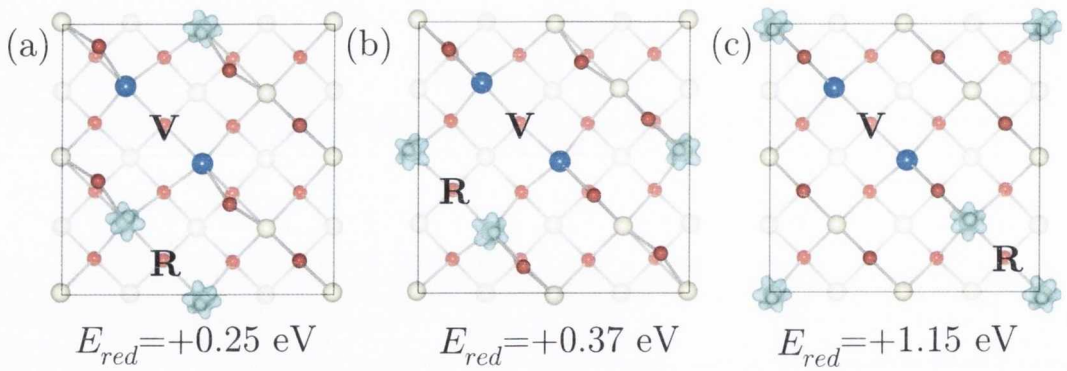

Figure 8.9: The position and formation energy for O vacancies on the La–doped (100) surface of CeO_2 where the charge is compensated through a vacancy. The letter V and R show the position of the CCV and the reduction vacancy respectively. The formation energies are given relative the vacancy formation on the pure (100) surface, 0.75 eV. The isosurfaces, representing plots of the spin density of the Ce(III) ions, are shown in light blue and are set to 0.05 e/Å^3

For the (110) surface with the vacancy compensation mechanism, different localisations for the Ce(III) ions were tested for reduction vacancies formed on the (110)

surface due to the small energy differences between some Ce(III) configurations on the pure (110) surface.[202,291] Figures 8.10 (a)–(d) displays the vacancies on the doped (110) surface where the localisation of the electrons matches the reduction vacancies on the pure surfaces, i.e. the electrons localise on nearest neighbour and next–nearest neighbour Ce ions, while a neighbouring O ion moves to a bridging position between a Ce(IV) and a Ce(III) ion (cf. Figure 8.4 (b)). For these four configurations, the CCV–vacancy distances were greater in Figures 8.10 (a) and (b) (6.76 Å) than in Figures 8.10 (c) and (d) (4.14 Å), which show that, similar to the (100) surface, larger CCV–vacancy distance are favoured. While the CCV–vacancy distance is important in determining the reduction energy, it is once again not the only factor. In Figure 8.10 (a), the average CCV–Ce(III) distance is 5.77 Å, whereas for Figure 8.10 (b) this distance is 4.97 Å, 0.80 Å shorter. This suggests it is easier to form a vacancy when the average CCV–Ce(III) distance is larger, thus decreasing the interaction between the positive charge of the ions and the effective positive charge of the vacancy. Similarly, in Figures 8.10 (c) and (d) the average CCV–Ce(III) distances are 5.77 Å and 4.97 Å, respectively, making the former vacancy position slightly more stable. For the configuration in Figures 8.10 (a)–(d), there was little variation in the average La(III)–Ce(III) distance, and therefore the influence of this factor on the reduction energy can not be determined.

Figure 8.10 (e)–(h) displays electron localisations that differ from from that which is seen for a vacancy on the pure (110) surface. In all cases, the formation energy is higher than for the surfaces displayed in Figure 8.10 (a)–(d), indicating that the arrangement of the Ce(III) ions relative to the reduction vacancy is the most important factor in determining the stability of the reduced (110) surface. For example, Figure 8.10 (d) has an average CCV–Ce(III) distance of 4.97 Å and an average La(III)–Ce(III) of 4.24 Å whereas in Figure 8.10 (e) these values are 5.32 Å and 5.27 Å respectively. From previous results, it might be expected for the vacancy position in Figure 8.10(e) would be more stable than Figure 8.10 (d). Instead, the favourable electron localisation displayed in Figure 8.10(d) means it has the lower reduction energy.

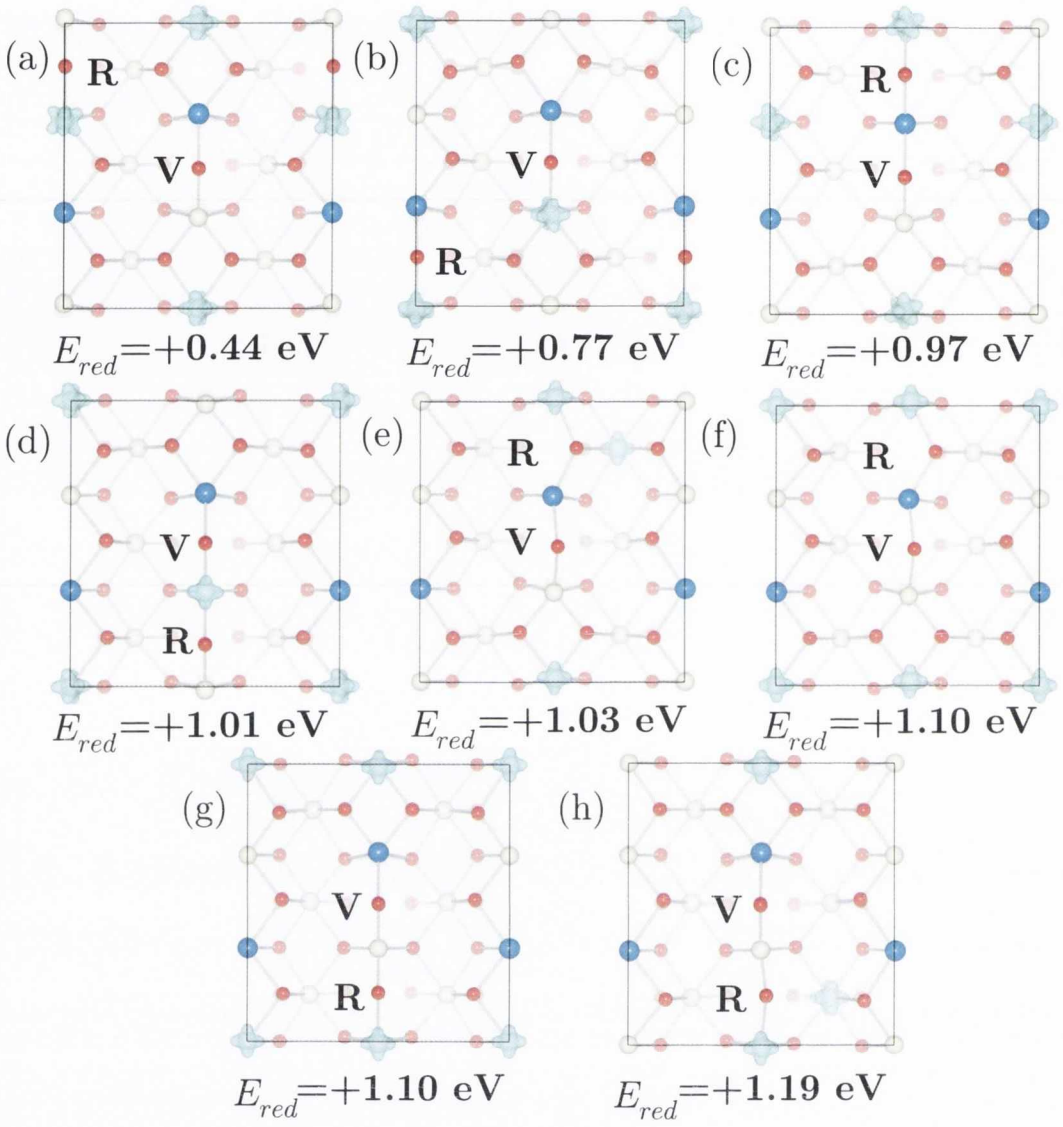

Figure 8.10: The position with spin density plots and formation energy for O vacancies on the (110) surface of CeO_2 with the O vacancy compensation scheme. V represents the site of the CCV, and R the site of the reduction vacancy. The formation energies are given relative the vacancy formation on the pure (110) surface, 0.52 eV. The isosurfaces, representing the excess spin on the Ce(III) ions, are shown in light blue and are set to 0.05 e/Å^3

For the La–doped (111) surface, vacancies were calculated at three different sites, and the position of the excess electrons were tested on all Ce(IV) ions next–nearest neighbour to the vacancy. The relaxed structures, with their reduction energies relative to the pure surface, are shown in order of increasing reduction energy in Figure 8.11.

As with the other two low index surfaces, the reduction energy is higher than on the pure surface. The first two vacancy positions have a CCV–vacancy distance of 6.71 Å (Figure 8.11(a)-(e)) whereas at the third vacancy site (Figure 8.11(f)–(h)) the distance is only 3.87 Å. Another factor that affects E_{red} is the average distance between the La(III) and Ce(III) ions. For Figures 8.11 (a) and (b) the La(III)–Ce(III) distance is 6.71 Å whereas Figures 8.11 (c), (d) and (e) have a La(III)–Ce(III) distance of 3.92 Å.

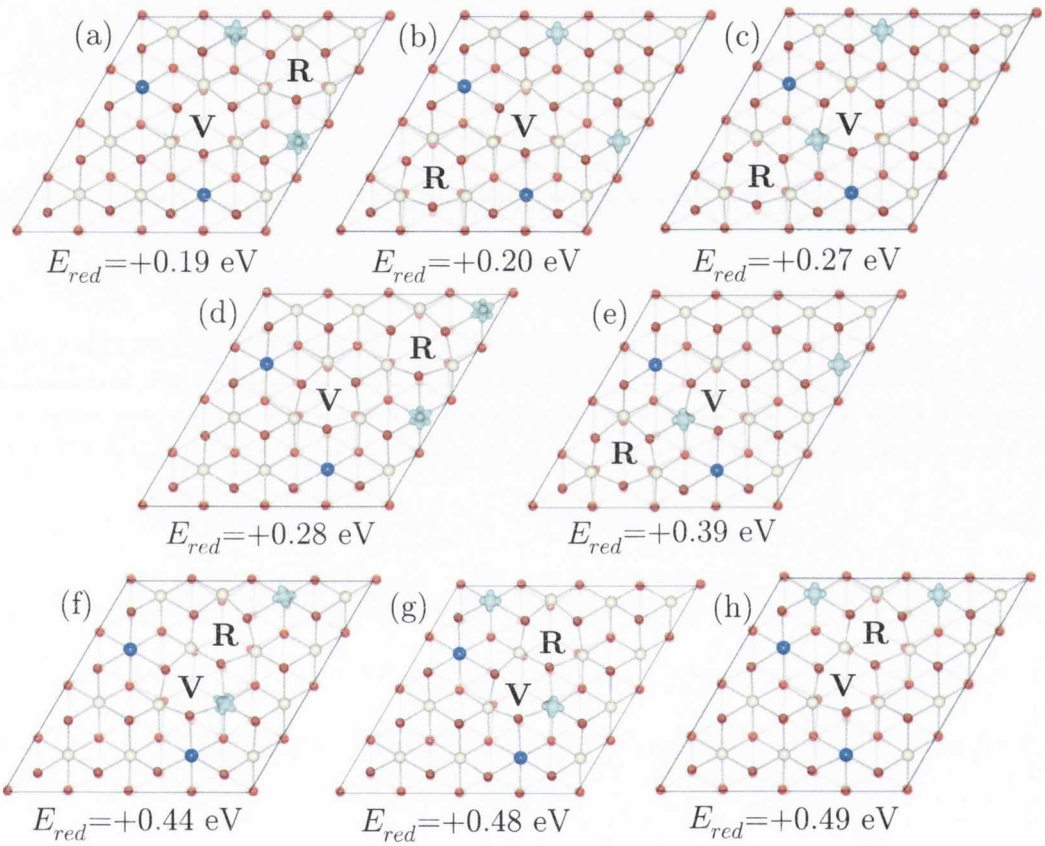

Figure 8.11: The position and formation energy for O vacancies on the (111) surface of CeO_2 with the vacancy charge compensation mechanism. The formation energies are given relative the vacancy formation on the pure (111) surface, 1.04 eV. The letter V denotes the position of the CCV, and R the site of the reduction vacancy. Plots of the spin density of the Ce(III) ions are represented by the light blue isosurfaces and are set to 0.05 e/Å^3

The reduction energies and structural features for the La–doped surfaces with the vacancy compensation are shown in Table 8.9. The results indicate that it is easier

to form a vacancy on the La–doped surface when the CCV–vacancy distance is larger. This is because both the CCV and vacancy are areas of effective positive charge, which attracts nearby O anions and serves to cause contraction in the lattice. Therefore, it is more stable to keep these two features apart to minimise strain within the lattice. The distance between the La(III) and Ce(III) ions also affects the reduction energy, with larger La(III)–Ce(III) distances being favoured when reducing the doped surfaces, as they are large positive ions, which cause expansion in the lattice around them. Similar to keeping the CCV and vacancy apart, larger La(III)–Ce(III) distances ensure less strain in the lattice. Overall, however, creating vacancies on the La–doped surfaces remains unfavourable, with the energy increasing with respect to the pure surfaces.

8.8 Alternate reduction mechanism: peroxide–vacancy switching

CeO_2 is often employed in the catalytic conversion of CO and NO_x, where CO and NO_2/NO are simultaneously converted to CO_2 and NO/N_2. In Kröger–Vink notation, these reactions are:

$$O_O^x + 2Ce_{Ce}^x + CO \rightarrow V_O^{\bullet\bullet} + 2Ce_{Ce}' + CO_2, \tag{8.4}$$

$$V_O^{\bullet\bullet} + 2Ce_{Ce}' + NO_2 \rightarrow O_O^x + 2Ce_{Ce}^x + NO, \tag{8.5}$$

$$V_O^{\bullet\bullet} + 2Ce_{Ce}' + NO \rightarrow O_O^x + 2Ce_{Ce}^x + \frac{1}{2}N_2. \tag{8.6}$$

In Equation 8.4, the surface is reduced, releasing oxygen which oxidises CO. In Equations 8.5 and 8.6, the surface is re–oxidised, reducing NO_2 and NO. So far, the effect of the dopant ions has only considered the charge compensation defect to be a spectator in the subsequent reductions, but these defects could play an active role in a redox mechanism. If the La–doped surfaces were able to switch between the peroxide and vacancy compensation mechanisms, they could play an active part in catalysis. In this proposed scheme, one of the oxygen atoms forming the peroxide is removed from the surface, reducing the oxygen of the peroxide to a O ion, O_O^x, leaving behind a vacancy,

Surface	Average distance (Å)			E_{red} (eV)	
	CCV–Vac(R)	CCV–Ce(III)	La(III)–Ce(III)	O–poor	O–rich
100	5.48	4.34	3.87	-0.64	1.00
	3.87	4.67	3.97	-0.52	1.12
	7.75	5.78	3.54	0.26	1.90
110	6.86	5.78	4.16	-0.68	0.96
	6.66	4.97	4.54	-0.35	1.29
	3.78	5.76	4.33	-0.15	1.49
	3.78	4.97	4.34	-0.11	1.53
	4.02	5.31	5.27	-0.09	1.55
	4.02	6.80	4.58	-0.02	1.62
	3.78	6.80	4.58	-0.02	1.62
	3.78	5.40	5.25	0.07	1.71
111	6.71	6.18	6.71	-0.41	1.23
	6.71	6.18	6.71	-0.40	1.24
	6.71	5.21	3.92	-0.33	1.31
	6.71	7.10	3.89	-0.32	1.32
	6.71	5.15	3.91	-0.21	1.43
	3.87	5.31	3.89	-0.16	1.48
	3.87	4.29	3.88	-0.12	1.52
	3.87	7.01	3.89	-0.11	1.53

Table 8.9: The distance between important defect features and the chemical potential dependent reduction energy for the La–doped low index surfaces of CeO_2 with the vacancy compensation mechanism. All distances are given in Å and all energies are given in eV.

providing oxygen to oxidise a molecule. During the re–oxidation of the surface, an adsorbed oxygen–containing molecule would occupy the vacancy site before reforming the peroxide ion. If this process were followed, Equations 8.4–8.6 would become:

$$(O_2)_i'' + 2V_O^{\bullet\bullet} + 2Ce_{Ce}^x + CO \rightarrow O_O^x + V_O^{\bullet\bullet} + 2Ce_{Ce}' + CO_2, \tag{8.7}$$

$$O_O^x + V_O^{\bullet\bullet} + 2Ce_{Ce}' + NO_2 \rightarrow (O_2)_i'' + 2V_O^{\bullet\bullet} + 2Ce_{Ce}^x + NO, \tag{8.8}$$

$$O_O^x + V_O^{\bullet\bullet} + 2Ce_{Ce}' + NO \rightarrow (O_2)_i'' + 2V_O^{\bullet\bullet} + 2Ce_{Ce}^x + \frac{1}{2}N_2. \tag{8.9}$$

Essentially, this scheme would be switching between the peroxide and vacancy charge compensation mechanisms, i.e. with the redox occurring by a change in the oxidation state of the O ions forming the peroxide rather than changes in the general oxidation state. However, as previously seen in Figures 8.5 (d) and (e), the optimal position of La(III) ions differs between the charge compensations schemes on the (100) and (111) surfaces. Therefore, the energy of this redox reaction can not be measured between the most stable defect structures. However, configurations for the peroxide/vacancy based on the most stable vacancy/peroxide structure may be sufficiently stable to make the scheme viable. alternatives to the optimal structures: the position of the La(III) match either the arrangement seen for the lowest energy vacancy structure (Figure 8.12 (a)) or the structure of the lowest energy peroxide defect (Figure 8.12 (b)). Since the position for the La(III) ions is the same for both defects on the (110) surface, there is no Figure 8.12 (b)[II]. The results in Figure 8.12 are only for O–rich limit.

The reduction energies for both the O–rich and O–poor limit are included in Table 8.10. In all cases, the reduction energy for the peroxide containing surfaces is far lower than for both the pure surfaces and reductions on the La–doped surfaces with the vacancy charge compensation mechanism, which suggest that the presence of La(III) on the CeO_2 surfaces can enhance the reducibility of the surfaces of CeO_2 by switching between the peroxide and vacancy charge compensation mechanisms. For the (100) and (111) surfaces reduction energy is lower for structure (a), where the La(III) configuration is based on the structure of the most stable vacancy defect, than structure (b), where the La(III) configuration is based on the most stable peroxide defect. This

	E_{red}					
	(O–poor)			(O–rich)		
	100	110	111	100	110	111
Pure surface	-0.89	-1.12	-0.60	0.75	0.52	1.04
La–Doped (vacancy)	-0.64	-0.68	-0.41	1.00	0.96	1.23
La–Doped (peroxide) – Structure (a)	-1.70	-1.58	-1.86	-0.06	0.06	-0.22
La–Doped (peroxide) – Structure (b)	-1.14	-1.58	-1.48	0.50	0.06	0.16

Table 8.10: The chemical potential dependent values of the reduction energy of the pure surfaces and the La–doped surfaces with the vacancy and peroxide charge compensation scheme. Structure (a) refers to the configuration of La(III) ions that matches the lowest vacancy compensation scheme, while structure (b) represents the the La(III) configuration that matches the lowest energy peroxide compensation mechanism for that surface. All values are given in eV.

is to be expected, as in structure (a), there is a driving force for the reduction, as the vacancy defect is the most stable structure for that arrangement of dopant ions, and vice–versa for structure (b). The (100) surface with structure (a) and the (110) surface both have a particularly low reduction energy, and therefore La–doped CeO_2 materials that expose this surface would be very effective for redox catalysis. The (111) surface is known to be the most stable, and therefore the most commonly expressed, surface, and far less effective than the other two for catalytic oxidation reactions.[99] However, the energy to move from the peroxide to the vacancy compensation schemes is far lower than the reduction energy of the pure (111) surface. This would suggest that La–doping is an effective method for increasing the oxidation on the (111) surface.

To test whether La–doped CeO_2 would be effective for catalysing oxidation/reduction reactions, first principle energetics were used to determine the energy required to oxidise CO to CO_2 and reduce NO_2/NO to NO/N_2 over the pure and doped surfaces, the La–doped surface with vacancy compensation, and the La–doped surfaces switching between the peroxide and vacancy compensation mechanisms. The results are shown

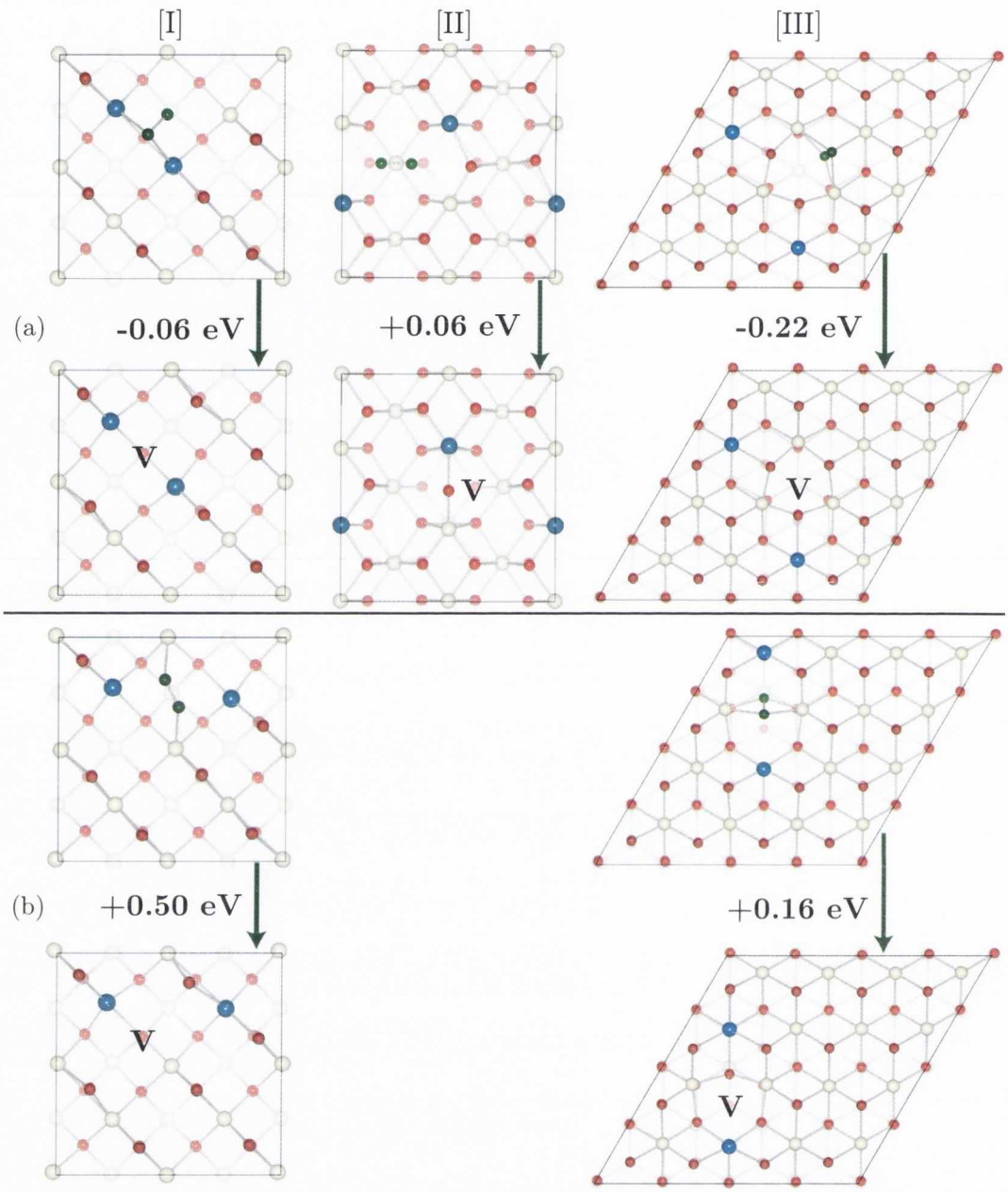

Figure 8.12: The structures and reduction peroxide/vacancy reduction scheme when the La(III) are positioned according to the lowest energy structure of the (a) vacancy compensation and (b) peroxide compensation for the [I] (100), [II] (110) and [III] (111) surfaces. The letter V shows the position of the CCV

in Table 8.11, from which it can be qualitatively determined whether the dopants can enhance oxidation or reduction reactions on CeO_2. For all cases, the addition of dopants increased the energy to create extra vacancies on the surface, which make the surfaces less effective at CO oxidation, but more effective at NO_2/NO reduction.

However, if the surfaces switch between peroxide and vacancy compensation, then the energy to oxidise CO decreases, whereas the energy to reduce NO_2/NO increases. This is a result of the low reduction energy associated with switching between the peroxide and vacancy compensation schemes: it is easy to remove an O ion from the surfaces to aid in oxidisation, but this makes the subsequent re–oxidisation of the surface more difficult.

In terms of CO oxidation between the doped surfaces, the (111) surface with structure (a) is the most effective at CO oxidation (ΔE = -3.05 eV), and the worst for the reduction of NO_2/NO (ΔE = 0.97/-1.44 eV). This an interesting result, as a previous studies on the pure surface found that (111) surface is the worst in terms of CO oxidation.[303] The reason for this enhanced oxidation is probably because the vacancy compensation mechanism is far more favourable on the (111) surface, and therefore there is a high driving to reduce the peroxide ion. The (111) surface with structure (b) is not as good for CO oxidation (ΔE = -2.67 eV), but performs better at NO_2/NO reduction (ΔE = 0.59/-1.82 eV) as this structure is based on the lowest energy peroxide and hence it is easier to oxidise the surface. However, the vacancy compensation mechanism is always the most stable on the (111), and hence, a redox cycle based on structure (b) is unlikely to occur. The (100) surface with structure (a) and the (110) are both very good at CO oxidation (ΔE = -2.89 eV and -2.77 eV respectively), as suggested by the low reduction energy of the surfaces and from previous experimental results.[99] As with the (111) surface with structure (a), they are not as good as subsequently reducing NO_2/N_2, but are better than the former surface. The (100) surface with structure (b) perhaps displays the best balance of energies between the oxidation and reduction energies. As such, enhanced redox properties could be obtained for La–doped CeO_2 if they expressed the (100) surface with a defect structure based on the most stable peroxide ion compensation mechanism. However, the addition of La(III), when it forms a peroxide ion, could enhance oxidation reactions on CeO_2.

Despite the increased reducibility observed through the La(III) doping of CeO_2, there is one notable drawback. The enhanced reactivity is only observed for the facile

Reduction	(100)		(110)	(111)	
	(a)ΔE	(b)ΔE	ΔE	(a)ΔE	(b)ΔE
Pure Surface	0.75		0.52	1.04	
La–Doped (Vacancy)	1.00		0.96	1.23	
La–Doped (Peroxide)	-0.06	0.50	0.06	-0.22	0.16
CO Oxidation					
Pure Surface	-2.08		-2.31	-1.79	
La–Doped (Vacancy)	-1.83		-1.87	-1.60	
La–Doped (Peroxide)	-2.89	-2.33	-2.77	-3.05	-2.67
NO_2 Reduction					
Pure Surface	0.01		0.24	-0.29	
La–Doped (Vacancy)	-0.25		-0.21	-0.47	
La–Doped (Peroxide)	0.81	0.26	0.69	0.97	0.59
NO Reduction					
Pure Surface	-2.41		-2.17	-2.70	
La–Doped (Vacancy)	-2.66		-2.62	-2.88	
La–Doped (Peroxide)	-1.60	-2.16	-1.71	-1.44	-1.82

Table 8.11: The energies for reduction and for the concurrent conversion of CO, NO_2 and NO on the pure surfaces and the La–doped surfaces with the vacancy and peroxide compensation mechanisms. The reduction of the La–doped (vacancy) surfaces are based on the lowest energy reduction vacancy. Two different structures are tested for the La–doped (100) and (111) surface with the peroxide compensation mechanism, where (a) the position of the La(III) ions match the lowest energy vacancy compensation structure and (b) the position of the La(III) ions match the lowest energy peroxide compensation structure. Since the position of the La(III) ions is the same for both defects, only one energy is given for the (110) surface. All energies are given in eV.

switching between the peroxide and the vacancy charge compensation mechanisms. Therefore, the effectiveness of La–doped CeO_2 catalysts will be highly dependent on the level of doping: at low doping levels, the increase in the reducibility introduced by the peroxide/vacancy compensation mechanisms will be countered by the increased reduction energy of all other surface O anions. This is in agreement with a previous experimental study that found La–doped CeO_2 more effective for methane oxidation then pure CeO_2, especially at higher levels of doping.[108] Another drawback of La–doping is that it makes it harder to reduce NO_2 and NO, which may affect the utility of CeO_2–based materials for three–way–catalysts. However, the results presented so far are pure thermodynamic data, and do not take into account kinetic factors. Previous theoretical work has demonstrated that for CO oxidation and NO_2/NO reduction, there is an intermediate step where the molecules adsorb on the surfaces.[103] To be able to definitively state whether La–doped CeO_2 is more, or less, effective for these catalytic processes, the interaction between the adsorbing molecules and these surfaces would need to be investigated. Ultimately, for the purposes of oxidation, or providing oxygen to assist other catalytic oxidisers, the results presented here suggest the addition of La(III) is an effective method for enhancing CeO_2 for these reactions.

8.9 Conclusions

Two intrinsic defects on the low index surfaces of CeO_2, O vacancies and peroxide ions, were investigated through PBE+U calculations. It was found that under O–poor conditions, the O vacancy was the most stable defects on all surfaces. However, O–rich conditions can stabilise an intrinsic peroxide defect, which is more stable than than the O vacancy by 0.40 eV on the (100) surface and 0.22 eV on the (110) surface.

A series of charge compensation mechanisms for the La–doped surfaces of CeO_2 were examined. Under O–poor conditions, the vacancy compensation mechanism is far more stable than alternative schemes, being more stable by 0.50 eV, 0.76 eV and 1.00 eV than the next most stable defect on the (100), (110) and (111) surfaces respectively.

However, O–rich conditions are able to stabilise a novel compensation scheme, where a peroxide ion compensates the charge of the La(III) ions. On the (100) and (110) surfaces, the peroxide is now more stable than vacancy compensation, by 0.40 eV and 0.06 eV, respectively, however, vacancy compensation is still favoured on the (111) surface.

The energy required to form a O vacancy on the doped CeO_2 surfaces was investigated in order to describe the effect of the dopants on the reducibility of CeO_2. It was found that the energy required to form new reduction vacancies on the surfaces increased in all cases, which would suggest that the catalytic performance of La–doped CeO_2 would be reduced.

However, the presence of the peroxide ion on the low index surfaces could play a direct role in catalysis. It was discovered that by switching between the peroxide and the vacancy compensation schemes the ability of CeO_2 to catalytically oxidise CO is enhanced, reducing the energy by 0.81/0.25 eV , 0.46 eV and 1.26/0.88 eV over the pure (100), (110) and (111) surfaces, respectively. The enhancement of the (111) surface towards oxidation reactions is particularly interesting: the (111) surface is the most stable, and therefore most commonly expressed surface, however, it performs worse than the other surfaces at CO oxidation.[85] The addition of La(III) could be an easy an effective method for enhancing oxidation reactions of CeO_2 based catalysts.

Chapter 9

Conclusions

9.1 Conclusions

In this thesis, a wide range of intrinsic and extrinsic defects were explored in CeO_2, in order to gain a better understanding of CeO_2 based materials. The ultimate goal was to assess whether the properties of CeO_2 are influenced by these defects, and assess possible methods for optimising CeO_2–based catalysts, fuel cells and MOSFETs. The first major result presented in this work was the application of an *ab initio* fitting procedure, based on Koopmans' theorem, for determining a U–value for the O $2p$ states in CeO_2. This method found that a value of $U = 5.5\,\text{eV}$ would be sufficient to account for the SIE associated with these states, which subsequently allowed for the accurate description of p–type defects in CeO_2 without employing costly hybrid DFT techniques. Furthermore, by demonstrating the effectiveness of this technique, future research will be able to apply it to a wide range of materials, improving the accuracy of DFT+U calculations.

In Chapter 4, a range of intrinsic defects in CeO_2 were investigated. The results concluded that the most common defect in CeO_2 would be the O vacancy under O–poor conditions, and an interstitial peroxide ion under O–rich conditions. A temperature and pressure dependence analysis found that in the range of 300–1200 K, the abundance of O vacancies is far higher than any other defect. This is in agreement with experimental

studies of the OSC of CeO_2, which has demonstrated that CeO_2 is capable of releasing high concentrations of oxygen to aid in oxidation reactions.[93–97] These results also have significant implications for SOFC applications. Firstly, Frenkel defects and not stable in CeO_2 compared to O vacancies, and hence will not contribute to ionic conductivity. This is in contrast with most fluorite materials, where Frenkel defect play a significant role.[224,310] Secondly, the abundance of O vacancies is highly problematic for SOFC electrolytes. The presence of the O vacancy can create electronic conductivity in CeO_2 and short circuit the operation of the SOFC.[125] Therefore, great care must be taken in the construction of CeO_2 based electrolytes in order to suppress the formation of O vacancies. In addition to these results, the magnetic moments of the intrinsic defects to determine whether they could account for the apparent ferromagnetism that had been observed in CeO_2. In all cases, it was found that none of the defects studied could account this property at the dilute limit. It was found that there was either no preference for the ferromagnetic or antiferromagnetic configurations, or the formation energy of the defect was prohibitively high, and therefore unlikely to ever form.

In Chapters 5 a series of trivalent dopants were tested in CeO_2 in order to determine which were most suitable for SOFC applications. It was found the the ionic radius of the dopant ions will dictate the structure they adopt in CeO_2, with the exception of Bi(III), where electronic factors also play a role. The relative attraction between the dopant cations and the CCV was also studied: this is an important factor for choosing dopants for SOFC electrolytes applications, as dopants with a high level of association would trap the CCV, hindering ionic conductivity. Finally, the exploration of the effect the dopants have on the reducibility revealed the reduction energy is not affected directly by the dopant's radius, instead the most important factor is the structure the dopants adopt in CeO_2. The analysis of doped CeO_2 concluded that Dy(III), Gd(III), Nd(III) and Pr(III) are possibly the optimal dopants for SOFC electrolytes, as they are readily soluble in CeO_2 and are unlikely to trap CCVs, which would hinder conductivity. Furthermore, the presence of Dy(III) and Gd(III) had little effect on the reducibility of CeO_2, while Nd(III) and Pr(III) actually make the formation of intrinsic

O vacancies more difficult. This is a highly important factor for avoiding unwanted electronic conductivity in CeO_2.

Chapter 6 explored the dynamic nature of O diffusion in doped CeO_2 through the use of *ab initio* MD. It was found that ionic conductivity in CeO_2 occurred through a hopping mechanism, where O ions neighbouring a vacancy in the $\langle 100 \rangle$ direction would hop to fill the vacancy site. There was some evidence of Frenkel defects affecting conductivity, but these were only observed for higher temperatures and possibly represent the initial stages of the CeO_2 structure melting. The position of the dopant cations was also found to play a significant role: when the dopants neighbour each other, stable dopant–CCV–dopant clusters can form, trapping the CCV and reducing conductivity. Therefore, a dispersed configuration of the dopants lessens the attraction of the CCV for the dopants, and lower activation energies were observed for these systems. One interesting result of the MD calculations was the In(III), which was found to have a high association energy between the dopants and the CCV, displays good ionic conductivity. Currently, there is nothing significant concerning In–doped CeO_2 in the literature, but the results presented here indicate it may be worthy of attention.

The calculations performed in Chapter 6 also provided good supporting information for the results of Chapter 5. The calculated activation energies for ionic diffusion matched well with the association energies from Chapter 5, with the exception of In–doped CeO_2, which despite have a higher association energy, displayed ionic conductivity which was on a par, or better, with Y–doped CeO_2. These result indicate that static PBE+U calculations can still provide valuable insight into dynamical processes, such as ionic diffusion, and when combined with results of MD simulations, becomes a highly effective method for screening potential dopants.

Chapter 7 explored another application of CeO_2, as a replacement for SiO_2 in MOSFETs. CeO_2 is a suitable material for high–κ applications, such as MOSFETs, due to its high dielectric constant, moderate band gap, small equivalent oxide thickness and low lattice mismatch with Si substrates. Unfortunately, CeO_2 MOSFETs will sometimes dispaly high leakage currents, affecting their operations. The results of an

analysis of the transition levels of CeO_2 found that the cause of these leakage currents were a result of intrinsic O vacancies leading to electronic conductivity. It was proposed that synthesising CeO_2 based MOSFETs in O–rich conditions could help limit leakage currents, a suggestion which is backed up by experimental observations.[261] To further enhance CeO_2 MOSFETs, a series of dopants were tested to see if they help prevent further leakage currents. It was found that both Y(III) and La(III) were both suitable for such applications, with La(III) being particularly attractive, as it presence increases the lattice constant of CeO_2, further reducing the mismatch with Si substrates.

In Chapter 8, the low index surface of pure and La–doped CeO_2 were explored, and their significance for catalysis was discussed. Investigations of the pure surfaces discovered an intrinsic peroxide vacancy, which has only been observed previously in the bulk. Under O–rich conditions, the surface peroxide is more stable than the traditional, and commonly discussed surface O vacancy. The presence of this defect provides new possibilities for research, as it may point to new reaction mechanism, leading to a fuller description of heterogeneous catalysis on CeO_2 surfaces. For La–doped surfaces, the peroxide defect was found once again to be stable under O–rich conditions, where it balanced the charge associated with the dopant ion, in contrast to the traditional charge compensation through the formation of a CCV. When the reducibility of La–doped CeO_2 surfaces were investigated, it was found that the presence of the dopants made it harder to introduce further reduction vacancies to the surface, regardless of whether the charge was compensated with a vacancy or a peroxide. However, the presence of the two competing compensation mechanisms raises the possibility of a new reaction pathway: the energy to reduce the peroxide ion, i.e. switching between the peroxide and vacancy charge compensation schemes, was found to be significantly lower than the energy required to reduce the pure surfaces. Therefore, doping La–doping of CeO_2 could be an effective method for enhancing the performance of CeO_2 for oxidation reactions, allowing it to provide, or absorb, oxygen to help catalyse reactions. The effectiveness of La–doped CeO_2 as a catalyst was also explored through first–principle thermodynamics. It was found that La–doped CeO_2 may be highly effective at the

oxidation of CO, and therefore La–doped CeO_2 catalysts tailored for oxidation reactions could proved to be extremely important for reducing atmospheric pollutants.

In conclusion, the work presented in this thesis has explored the usefulness of CeO_2 for a wide array of applications, and has demonstrated how defects control the important properties of CeO_2. Through the use of theoretical calculations, it was possible to gain a greater understanding of the formation of these defects, what external factors influence them, and how they determine the chemistry of CeO_2. Furthermore, through computational modelling it was also possible to predict new properties, which will aid future research of new, environmentally friendly technologies.

9.2 Future Work

Although the calculations presented in this thesis have provided valuable information on the properties of CeO_2–based electrolytes and catalysts, they remain preliminary steps, with many possible avenues available for future research. For enhancing the properties of CeO_2 electolytes, there are two major directions that this research could proceed. The first involves long time scale force–field MD calculations which can give a better description of how doped CeO_2 behaves over time. Furthermore, without the limit of the high computational cost of *ab initio* MD, larger systems can be utilised, and therefore better statistical data can be collected. The other path would be collaboration with experimental studies based on the most promising candidates from the theoretical results. Alternatively, the methods employed in this study can be applied to new potential electrolyte materials, such as perovskites[77] or apatites.[81] Materials with these crystal structures have shown promise, but suffer from similar problems to CeO_2, such as poor intrinsic conductivity or susceptibility to reduction. Once again a combination of static calculations combined with MD could help screen potential new materials, and determine methods for optimising them for the next generation of fuel cell electrolytes.

The presence of the novel peroxide defects on the low index surfaces raises interesting new avenues for research. The interaction of adsorbing species could be influence

by its presence, influencing catalytic reactions. A full theoretical study exploring such situations would aid in the understanding of catalytic reactions, and open up new methods for optimising catalyst materials. The presence of the charge compensation peroxide ion on La–doped CeO_2 is also worthy of further investigation. Preliminary calculations have suggested that it could be highly effective for the oxidation of CO, but without a description of how CO interacts with the peroxide, it can not be definitively stated. Additionally, the peroxide defect may also be a preferred compensation mechanism for other dopants in CeO_2. It may also be the case that the stability of the peroxide is dependent on the dopant present, and therefore careful selection of the dopants may be effective for enhancing certain catalytic processes.

Bibliography

[1] C. J. Bradley and A. P. Cracknell. *Mathematical Theory of Symmetry in Solids.* Oxford University Press, Oxford, UK, (1972).

[2] H. Goosse, E. Crespin, A. de Montety, M. E. Mann, H. Renssen and A. Timmermann. *J. Geophys. Res.*, **115**, D09108 (2010).

[3] E. J. Jansen, J. C. Overpeck, K. R. Briffa, F. Duplessy, V. Joos, D. Masson-Delmotte, B. Olago, W. R. Otto-Bliesner, S. Peltier, R. Rahmstorf, D. Ramesh, D. Raynaud, O. Rind, R. Solmina, R. Villalba and D. Zhang. Paleoclimate. In S. Solomon, D. Qin, M. Manning, Z. Chen, M. Marquis, K. B. Averyt, M. Tignor and H. L. Miller, editors, *Climate Change 2007: The Physical Science Basis. Contribution of Working Group I to the Fourth Assessment Report of the Intergovernmental Panel on Climate Change.* Cambridge University Press, Cambridge, United Kingdom and New York, NY, USA, (2007).

[4] Reconciling Observation of Global Temperature Change (2000), National Research Council of the National Academy of Sciences, Washington, DC.

[5] S. Levitus, J. I. Antonov, T. P. Boyer and C. Stephens. *Science*, **287**, 2225–2229 (2000).

[6] T. J. Zhou, F. F. Song and X. L. Chen. *Adv. Atmos. Sci.*, **30**, 638–657 (2013).

[7] J. I. Steinfeld. *Fuel Process. Technol.*, **71**, 121–129 (2001).

[8] P. Tans. *Oceanography*, **22**, 26–35 (2009).

[9] B. Wuethrich. *Science*, **287**, 793–795 (2000).

[10] C. Rosenzweig and D. Hillel. *Climate Change and the Global Harvest: Potential Impacts of the Green House Affect on Agriculture*. Oxford University Press, New York, NY, USA, (1998).

[11] G. Endfield, D. B. Ryves, K. Mills and L. Berrang-Ford. *Geogr. J.*, **175**, 181–195 (2009).

[12] A. Pardhan-Ali, J. Wilson, V. L. Edge, C. Furgal, R. Reid-Smith, M. Santos and S. A. McEwen. *BMJ Open*, **2**, e000732 (2012).

[13] M. Maione, U. Giostra, J. Arduini, F. Furlani, F. Graziosi, E. Lo Vullo and P. Bonasoni. *Sci. Total Environ.*, **445**, 155–164 (2013).

[14] M. J. Molina, L. T. Molina and C. E. Kolb. *Phys. Chem.*, **47**, 327–367 (1996).

[15] X. D. de Madron, C. Guieu, R. Sempr, P. Conan, D. Cossa, F. D. Ortenzio, C. Estournel, F. Gazeau, C. Rabouille, L. Stemmann, S. Bonnet, F. Diaz, P. Koubbi, O. Radakovitch, M. Babin, M. Baklouti, C. Bancon-Montigny, S. Belviso, N. Bensoussan, B. Bonsang, I. Bouloubassi, C. Brunet, J.-F. Cadiou, F. Carlotti, M. Chami, S. Charmasson, B. Charrire, J. Dachs, D. Doxaran, J.-C. Dutay, F. Elbaz-Poulichet, M. Elaume, F. Eyrolles, C. Fernandez, S. Fowler, P. Francour, J. Gaertner, R. Galzin, S. Gasparini, J.-F. Ghiglione, J.-L. Gonzalez, C. Goyet, L. Guidi, K. Guizien, L.-E. Heimbrger, S. Jacquet, W. Jeffrey, F. Joux, P. L. Hir, K. Leblanc, D. Lefvre, C. Lejeusne, R. Lem, M.-D. Loe-Pilot, M. Mallet, L. Mjanelle, F. Mlin, C. Mellon, B. Mrigot, P.-L. Merle, C. Migon, W. Miller, L. Mortier, B. Mostajir, L. Mousseau, T. Moutin, J. Para, T. Prez, A. Petrenko, J.-C. Poggiale, L. Prieur, M. Pujo-Pay, Pulido-Villena, P. Raimbault, A. Rees, C. Ridame, J.-F. Rontani, D. R. Pino, M. Sicre, V. Taillandier, C. Tamburini, T. Tanaka, I. Taupier-Letage, M. Tedetti, P. Testor, H. Thbault, B. Thouvenin, F. Touratier, J. Tronczynski, C. Ulses, F. V. Wambeke, V. Vantrepotte, S. Vaz and R. Verney. *Prog. Oceanogr.*, **91**, 97 – 166 (2011).

[16] D. M. Alongi. *Carbon Manage.*, **3**, 323–322 (2012).

[17] J. E. Lovelock and C. G. Rapley. *Nature*, **449**, 403 (2007).

[18] A. Spolaor, P. Vallelonga, G. Cozzi, J. Gabreili, C. Varin, N. Kehrwald, P. Zennaro, C. Boutron and C. Barbante. *Geophys. Res. Lett.*, **40**, 1618–1623 (2013).

[19] F. Larachi, O. Lacroix and B. P. A. Grandjean. *Chem. Eng. Sci.*, **73**, 99–115 (2012).

[20] N. Liu, G. M. Bond, A. Abel, B. J. McPherson and J. Stringer. *Fuel Cell Process. Technol.*, **86**, 1615–1625 (2005).

[21] M. C. Álvarez Galván, V. A. de la Peña O'Shea, J. L. G. Fierro and P. L. Arias. *Catal. Commun.*, **4**, 223–228 (2003).

[22] C. Douvris and O. V. Ozerov. *Science*, **29**, 1188–1190 (2008).

[23] S. J. Yang, C. Z. Wang, L. Ma, Y. Peng, Z. Qu, N. G. Yan, J. H. Chen, H. Z. Chang and J. H. Li. *Catal. Sci. Technol.*, **3**, 161–168 (2013).

[24] J. R. Khusnutdinova, N. P. Rath and L. M. Mirica. *J. Am. Chem. Soc.*, **132**, 7303–7305 (2010).

[25] G. Centi, S. Perathoner and Z. S. Rak. *Appl. Catal. B*, **41**, 143–155 (2003).

[26] S. Y. Christou and A. M. Efstathiou. *Top. Catal.*, **42–43**, 415–419 (2007).

[27] I. S. Nashawi, A. Malallah and M. Al-bisharah. *Energy Fuels*, **24**, 1788–1800 (2010).

[28] Renewable 2013 Global status Report. *http://www.ren21.net/REN21Activities/GlobalStatusReport.aspx*, (Acessed on 25th September 2013).

[29] Irish Wind Energy Association. *http:http://www.iwea.com*, (Accessed 3rd July 2013).

[30] S. B. Roy and J. J. Traiteur. *Proc. Natl. Acad. Sci. U.S.A.*, **107**, 17899–17904 (2010).

[31] World Watch Institute. *http://vitalsigns.worldwatch.org/vs-trend/global-hydropower-installed-capacity-and-use-increase test*, (Accessed 3rd July 2013).

[32] International Renewable Energy Agency. *http://www.irena.org/DocumentDownloads/Publications/RE_Technologies_Cost_Analysis-CSP.pdf*, (June 2012).

[33] A. Ahmed. *Energ. Environ.*, **22**, 1105–1113 (2011).

[34] Volvo Cars of North America. *https://www.media.volvocars.com/us/enhanced/en-us/Media/Preview.aspx?mediaid=48800*, (Accessed 30th July 2013).

[35] Tesla Motors. *http://www.teslamotors.com/supercharger*, (Acessed 30th July 2013).

[36] L. Reijnders. *Energy Policy*, **34**, 863–876 (2006).

[37] OECD 2011–12 Factbook. *http://www.oecd-ilibrary.org/sites/factbook-2011-en/06/01/04/index.html?contentType=&itemId=/content/chapter/factbook-2011-49-en&containerItemId=/content/serial/18147364&accessItemIds=&mimeType=text/h*, (Accessed on 23rd September 2013).

[38] D. Mitchell. *The World Bank Development Prospects Group*, **4682**, 1–20 (2008).

[39] R. Righelato and D. V. Spracklen. *Science*, **317**, 902–906 (2007).

[40] M. Park, S. J., Y. Lee, Y. H. Im and Y. W. Cho. *J. Alloys Compd.*, **575**, 393–398 (2013).

[41] Z. Gao, Y. Luo, R. Li, Z. Lin and L. Kang. *J. Pow. Sour.*, **241**, 509–516 (2013).

[42] P. Desclaux, M. Rzepka, U. Stimming and R. Hempelmann. *Phys. Chem. Chem. Phys.*, **227**, 627–649 (2013).

[43] S. P. S. Badwal and K. Foger. *Ceram. Int.*, **22**, 257–265 (1996).

[44] L. Blum, W. A. Merlenberg, H. Nabielek and R. Steinberger-Wilckens. *Int. J. Appl. Ceram. Technol.*, **2**, 482–492 (2005).

[45] D. J. L. Brett, A. Atkinson, N. P. Brandon and S. J. Skinner. *Chem. Soc. Rev.*, **37**, 1568–1578 (2008).

[46] J. B. Goodenough. *Annu. Rev. Mater. Res.*, **33**, 91–128 (2003).

[47] K. Nikooyeh, R. Clemmer, V. Alzate-Restreppo and J. M. Hill. *Appl. Catal. A*, **347**, 106–111 (2008).

[48] S. P. Jiang. *J. Mater. Sci.*, **43**, 6799–6833 (2008).

[49] Z. Li, M. Behruzi, L. Fuerst and D. Stover. *SOFC-IV.* The Electrochemical Society, Inc., Pennington, (1993).

[50] S. Otoshi, H. Sasaki, H. Ohnishi, M. Hase, K. Ishimaru, M. Ippommatsu, T. Higuchi, M. Miyayama and H. Yanagida. *J. Electrochem. Soc.*, **138**, 1519–1523 (1991).

[51] A. Hammouche, E. J. L. Schouler and M. Henault. *Solid State Ionics*, **28**, 1205–1207 (1988).

[52] M. Mori, Y. Hiei, N. M. Sammes and G. A. Tompsett. *SOFC-VI.* The Electrochemical Society, Inc., (1999).

[53] S. P. Jiang and W. Wang. *Solid State Ionics*, **176**, 1185–1191 (2005).

[54] X. Guo and R. Waser. *Prog. Mater. Sci.*, **51**, 151–210 (2006).

[55] J. Molenda, K. Swierczek and W. Zajac. *J. Power Sources*, **173**, 657–670 (2007).

[56] A. J. Jacobson. *Chem. Mater.*, **22**, 660–674 (2010).

[57] J. Mizuasaki, H. Yonemuram, Y. Kamata, K. Ohyama, N. Mori, H. Takai, H. Tagawa, M. Dokiya, K. Naraya, T. Sasamoto, H. Inaba and T. Hashimoto. *Solid State Ionics*, **132**, 167–180 (2000).

[58] A. S. Nesaraj. *J. Sci. Ind. Res.*, **69**, 169–176 (2010).

[59] T. Iwata. *J. Electrochem. Soc.*, **143**, 1521–1531 (1996).

[60] M. Cassidy, G. Lindsay and K. Kendall. *J. Power Sources*, **61**, 189–192 (1996).

[61] O. Yamamoto. *Electrochim. Acta*, **45**, 2423–2435 (2000).

[62] J. Mizusaki, J. Tabuchi, T. Matsuura, S. Yamamuchi and K. Fueki. *J Electrochem. Soc.*, **136**, 2082–2088 (1989).

[63] J. Li, W. S., R. Liu, Z. Wang and J. Q. Qian. *Solid Sate Ionics*, **179**, 1597–1601 (2008).

[64] L. Qiu, T. Ichikawa, A. Hirano, N. Imanishi and Y. Takeda. *Solid State Ionics*, **158**, 55–65 (2003).

[65] H. Zhang, H. Liu, Y. Cong and W. Yang. *J. Power. Sources*, **185**, 129–135 (2008).

[66] D. B. Ingram and S. Linic. *J. Electrochem. Soc.*, **156**, B1457–B1456 (2009).

[67] Z. Wang, W. Weng, K. Cheng, P. Du, G. Shen and G. Han. *J. Power Sources*, **179**, 541–546 (2008).

[68] F. Wang, G. Jung, A. Su, S. Chan, X. Hao and Y. Chiang. *J Power Sources*, **185**, 862–866 (2008).

[69] W. Bao, H. Guan and J. Cheng. *J. Power. Sources*, **176**, 232–237 (2008).

[70] J. Rossmeisl and W. G. Bessler. *Solid State Ionics*, **178**, 1694–1700 (2008).

[71] Q. Su, D. Yoon, A. P. Chen, F. Khatkhatay, A. Manthiram and H. Y. Wang. *J. Power Sources*, **242**, 455–463 (2013).

[72] R. Devanathan, S. Thevuthasan and J. D. Gale. *Phys. Chem. Chem. Phys.*, **11**, 5506–5511 (2009).

[73] B. C. H. Steele. *J. Mater. Sci.*, **36**, 1053–1068 (2001).

[74] M. J. Verkerk and A. J. Burggraaf. *J. Electrochem. Soc.*, **128**, 75–82 (1981).

[75] T. Takahshi, H. Iwahara and T. Arao. *J. Appl. Electrochem.*, **5**, 187–195 (1975).

[76] T. Takeyama, N. Takahashi, T. Nakamura and S. Itoh. *Surf. Coat. Technol.*, **200**, 16–17 (2006).

[77] P. Huang and A. Petric. *J. Electrochem. Soc.*, **143**, 1644–1648 (1996).

[78] K. Yamaji, T. Horita, M. Ishikawa, M. Sakai, N. Sakai and H. Yokokawa. *Solid State Ionics*, **121**, 217–224 (1999).

[79] J. W. Stevenson, T. R. Armstrong, L. R. Pederson, J. Li, C. A. Lewinsohn and S. Baskaran. *Solid Sate Ionics*, **113–115**, 571–583 (1998).

[80] K. N. Kim, B. K. Kim, J. W. Son, J. Kim, H.-W. Lee, J.-H. Lee and J. Moon. *Solid State Ionics*, **177**, 2155–2158 (2006).

[81] E. Kendrick, M. S. Islam and P. R. Slater. *J. Mater. Chem.*, **17**, 3104–3111 (2007).

[82] J. X. Guo, S. H. Yuan, M. C. Gong, L. Zhang, J. Zhang, L, M. Zhao and Y. Q. Chen. *Acta Chimica Sinica*, **65**, 937–942 (2007).

[83] K. Krishna, A. Bueno-Lopez, M. Makkee and J. A. Moulijn. *Top. Catal.*, **42–43**, 221–228 (2007).

[84] J. G. Nunan, M. J. Cohn and J. T. Dormer. *Catal. Today*, **14**, 277–291 (1992).

[85] K. Zhou, X. Wang, X. Sun, Q. Peng and Y. Li. *J. Catal.*, **229**, 206–212 (2005).

[86] W. L. Deng, C. Carpenter, N. Yi and M. Flytzani-Stephanopoulos. *Top. Catal.*, **44**, 199–208 (2007).

[87] R. Si and M. Flytsani-Stephanopoulos. *Angew. Chem., Int. Ed.*, **47**, 2884–2887 (2008).

[88] P. Panagiotopoulou, J. Papavasiliou, G. Avgouropoulos and T. Ioannides. *Chem. Eng. J.*, **134**, 16–22 (2007).

[89] M. F. Camellone and S. Fabris. *J. Am. Chem. Soc.*, **131**, 10473–10483 (2009).

[90] M. V. Ganduglia-Pirovano, C. Popa, J. Sauer, H. Abbott, A. Uhl, M. Baron, D. Stacchiola, O. Bondarchuk, S. Shaikhutdinov and H.-J. Freund. *J. Am. Chem. Soc.*, **132**, 2345–2349 (2010).

[91] T. J. Huang and J. F. Li. *J. Power Sources*, **181**, 62–68 (2008).

[92] T. J. Huang and C. H. Wang. *Chem. Eng. J.*, **132**, 97–103 (2007).

[93] M. A. Henderson, C. L. Perkins, M. H. Engelhard, S. Thevuthasan and P. C. H. F. *Surf. Sci.*, **526**, 1–18 (2003).

[94] Z. X. Yang, T. K. Woo, M. Baudin and K. Hermansson. *J. Chem. Phys.*, **120**, 7741–7749 (2004).

[95] D. A. Andersson, S. I. Simak, N. V. Skorodumova, I. A. Abrikosov and B. A. Johansson. *Appl. Phys. Lett.*, **90**, 031909 (2007).

[96] E. B. Lavik, I. Kosacki, H. L. Tuller, Y. M. Chiang and J. Y. Ying. *J. Electroceram.*, **1**, 7–14 (1997).

[97] M. Nolan, J. E. Fearon and G. W. Watson. *Solid State Ionics*, **177**, 3069–3074 (2006).

[98] C. Li, Y. Sakata, T. Arai, K. Domen, K. Maruya and T. Onishi. *J. Chem. Soc., Faraday Trans. 1*, **85**, 929–943 (1989).

[99] Z. L. Wu, M. J. Li, J. Howe, H. M. Meyer and S. H. Overbury. *Langmuir*, **26**, 16595–16606 (2010).

[100] J. A. Rodriguez, T. Jirsak, S. Sambasivan, D. Fisher and A. Maiti. *J. Chem. Phys.*, **112**, 9929–9939 (2000).

[101] Y. Namai, K. Fukui and Y. Iwasawa. *Nanotechnology*, **15**, S49–S54 (2004).

[102] S. H. Overbury, D. R. Mullins, D. R. Huntely and L. Kundakovic. *J. Catal.*, **186**, 296–306 (1999).

[103] D. O. Scanlon, N. M. Galea, B. J. Morgan and G. W. Watson. *J. Phys. Chem. C*, **113**, 11095–11103 (2009).

[104] Z. X. Yang, B. L. He, Z. S. Lu and K. Hermansson. *J. Phys. Chem. C*, **114**, 4486–4494 (2010).

[105] Z. X. Yang, T. K. Woo and K. Hermansson. *Surf. Sci.*, **600**, 4953–4960 (2006).

[106] M. Nolan, S. Grigoleit, D. C. Sayle, S. C. Parker and G. W. Watson. *Surf. Sci.*, **576**, 217–229 (2005).

[107] S. Fabris, G. Vicario, G. Balducci, S. de Gironcoli and S. Baroni. *J. Phys. Chem. B*, **109**, 22860–22867 (2005).

[108] B. Zhang, D. Li and X. Wang. *Catal. Today*, (2010).

[109] S. Zhao and R. J. Gorte. *Appl. Catal. A-Gen*, **277**, 129–136 (2004).

[110] J. Beckers, A. F. Lee and G. Rothenberg. *Adv. Synth. Catal.*, **351**, 1557–1566 (2009).

[111] R. J. Gorte. *AIChE J.*, **56**, 1120–1396 (2010).

[112] M. S. Hegde, G. Madras and K. C. Patil. *Acc. Chem. Res.*, **42**, 704–712 (2009).

[113] A. B. Kehoe, D. O. Scanlon and G. W. Watson. *Chem. Mater.*, **23**, 4464–4468 (2011).

[114] S. Patil, S. Seal, Y. Guo and J. Norwood. *Appl. Phys. Lett.*, **88**, 243110 (2006).

[115] H. Hayashi, R. Sagawa, R. Inaba and K. Kawamura. *Solid State Ionics*, **131**, 281–290 (2000).

[116] D. A. Andersson, S. I. Simak, N. V. Skorodumova, I. A. Abrikosov and B. Johansson. *Proc. Natl. Acad. Sci. U.S.A.*, **103**, 3518–3521 (2006).

[117] D. O. Scanlon, A. Walsh, B. J. Morgan and G. W. Watson. *e-J. Surf. Sci. Nanotech.*, **7**, 395–404 (2009).

[118] I. Yeriskin and M. Nolan. *J. Phys.: Condens. Matter*, **22**, 135004 (2010).

[119] I. Yeriskin and M. Nolan. *J. Chem. Phys.*, **131**, 244701 (2009).

[120] M. Nolan. *Chem. Phys. Lett.*, **492**, 115–118 (2010).

[121] V. Thangadurai and W. Weppner. *Ionics*, **12**, 81–92 (2006).

[122] F. Tietz, H. P. Buckremer and D. Stover. *J. Electroceram.*, **17**, 701–707 (2006).

[123] M. Yano, A. Tomita, M. Sano and T. Hibino. *Solid State Ionics*, **177**, 3351–3359 (2007).

[124] S. Basu, D. Sujatha and H. S. Maiti. *Mater. Res. Soc.*, **19**, 3162–3171 (2004).

[125] M. Mogensen, N. M. Sammes and G. A. Tompsett. *Solid State Ionics*, **129**, 63–94 (2000).

[126] Y. P. Fu, C. W. Tseng and P. C. Peng. *J. Eur. Ceram. Soc.*, **28**, 85–90 (2008).

[127] Y.-P. Fu, S.-H. Chen and J.-J. Huang. *Int. J. Hydrogen Energy*, **35**, 745–752 (2010).

[128] V. Esposito, M. Zunic and E. Traversa. *Solid State Ionics*, **180**, 1069–1075 (2009).

[129] S. Kuharuangrong. *J. Power Sources*, **171**, 506–510 (2007).

[130] B. Rambabu, S. Ghosh and J. Hrudananda. *J. Mater. Sci.*, **41**, 7530–7536 (2006).

[131] S. Sen, H. J. Avila-Paredes and S. Kim. *J. Mater. Chem.*, **18**, 3915–3917 (2008).

[132] B. Zhu, X. Liu, Z. Zhu and R. Ljungberg. *Int. J. Hydrogen Energy*, **33**, 3385–3392 (2008).

[133] S. Zha, C. Xia and G. Meng. *J. Power Sources*, **115**, 44–48 (2002).

[134] X. Sha, Z. Lu, X. Huang, J. Miao, Z. Ding, X. Xin and W. Su. *J. Alloys Compd.*, **428**, 59–64 (2007).

[135] X. Guan, H. Zhou, Z. Liu, Y. Wang and J. Zhang. *Mater. Res. Bull.*, **43**, 1046–1054 (2008).

[136] M. Balaguer, C. Solis and J. M. Serra. *J. Phys. Chem. C*, **116**, 7975–7982 (2012).

[137] S. A. Acharya. *J. Power Sources*, **198**, 105–111 (2012).

[138] D. J. Kim. *J. Am. Ceram. Soc.*, **72**, 1415–1421 (2005).

[139] D. Marrocchelli, S. R. Bishop, H. L. Tuller and B. Yildiz. *Adv. Funct. Mater.*, **22**, 1958–1965 (2012).

[140] L. Xu and G. Henkelman. *J. Chem. Phys.*, **129**, 114104 (2008).

[141] P. P. Dholabhai, S. Anwar, J. B. Adams, P. Crozier and R. Sharma. *J. Solid State Chem.*, **184**, 811–817 (2011).

[142] M. Burbano, D. Marrocchelli, B. Yildiz, H. L. Tuller, S. T. Norberg, S. Hull, P. A. Madden and G. W. Watson. *J. Phys.: Condens. Matter*, **23**, 255402 (2011).

[143] A. Gotte, D. Spångberg, K. Hermansson and M. Baudin. *Solid State Ionics*, **178**, 1421–1427 (2007).

[144] A. Guglielmetti, A. Chartier, L. van Brutzel, J.-P. Crocombette, K. Yasuda, C. Meis and S. Matsumura. *Nucl. Instrum. Methods Phys. Res., Sect. B*, **266**, 5120–5125 (2008).

[145] H. Inaba, R. Sagawa, H. Hayashi and K. Kawamura. *Solid State Ionics*, **122**, 95–103 (1999).

[146] M. Burbano, N. S. T., S. Hull, S. G. Eriksson, D. Morrocchelli, P. A. Madden and G. W. Watson. *Chem. Mater.*, **24**, 222–229 (2012).

[147] E. Y. Pikalova, V. G. Bamburov, A. A. Murashkina, A. D. Neuimin, A. K. Demin and S. V. Plaksin. *Russ. J. Electrochem.*, **47**, 738–744 (2011).

[148] A. V. Virkar. *J. Electrochem. Soc.*, **138**, 1481–1487 (1991).

[149] C. E. Hatchwell, N. M. Sammes, G. A. Tampsett and I. W. M. Brown. *J. Eur. Ceram. Soc.*, **19**, 1697–1703 (1999).

[150] G. Kresse and J. Furthmüller. *Comput. Mater. Sci.*, **6**, 12–50 (1996).

[151] G. Kresse and J. Furthmüller. *Phys. Rev. B*, **54**, 11169–11186 (1996).

[152] G. Kresse and J. Hafner. *Phys. Rev. B*, **49**, 14251–14269 (1994).

[153] E. Schrödinger. *Phys. Rev.*, **28**, 1049–1070 (1926).

[154] V. Fock. *Z. Phys. A: Hadrons Nucl.*, **62**, 795–805 (1930).

[155] A. R. Leach. *Molecular Modelling. Principles and Applications.* Prentice Hall, New Jersey, USA, (2001).

[156] P.-O. Löwdin. *Phys. Rev.*, **97**, 1509–1520 (1955).

[157] W. Kohn and L. J. Sham. *Phys. Rev.*, **140**, A1133–A1138 (1965).

[158] F. Bloch. *Z. Phys. A: Hadrons Nucl.*, **57**, 545–555 (1929).

[159] P. A. M. Dirac. *Math. Proc. Cambridge Phil. Soc.*, **26**, 376–375 (1930).

[160] D. M. Ceperley and B. J. Alder. *Phys. Rev. Lett.*, **45**, 566–569 (1980).

[161] S. H. Vosko, L. Wilk and M. Nusair. *Can. J. Phys.*, **58**, 1200–1211 (1980).

[162] B. J. Morgan and G. W. Watson. *J. Phys. Chem. C*, **114**, 2321–2328 (2010).

[163] D. O. Scanlon, A. Walsh, B. J. Morgan and G. W. Watson. *J. Phys. Chem. C*, **112**, 9903–9911 (2008).

[164] C. T. Lee, W. T. Yang and R. G. Parr. *Phys. Rev. B*, **37**, 785–789 (1988).

[165] A. D. Becke. *Phys. Rev. A*, **38**, 3098–3100 (1988).

[166] J. P. Perdew and W. Yue. *Phys. Rev. B*, **33**, 8800–9902 (1986).

[167] J. P. Perdew, K. Burke and M. Ernserhof. *Phys. Rev. Lett.*, **77**, 3865–3868 (1996).

[168] D. O. Scanlon, A. Walsh, B. J. Morgan, M. Nolan, J. Fearon and G. W. Watson. *J. Phys. Chem. C*, **111**, 7971–7979 (2007).

[169] B. J. Morgan, D. O. Scanlon and G. Watson. *J. Mater. Chem.*, **19**, 5175–5178 (2009).

[170] S. L. Dudarev, G. A. Botton, S. Y. Savrasov, C. J. Humphreys and A. P. Sutton. *Phys. Rev. B*, **57**, 1505–1509 (1998).

[171] Y. Z. Zhu, G. D. Chen, H. Ye, A. Walsh, C. Y. Moon and S.-H. Wei. *Phys. Rev. B*, **77**, 245209 (2008).

[172] S. Laubach, P. C. Schmidt, F. J. Thißen, Fernandez-Madrigal, Q. H. Wu, W. Jaegermann, M. Klemm and S. Horn. *Phys. Chem. Chem. Phys.*, **9**, 2564–2576 (2007).

[173] P. H. Dederichs, S. Blügel, R. Zeller and H. Akai. *Phys. Rev. Lett.*, **53**, 2512–2513 (1984).

[174] S. Lany and A. Zunger. *Phys. Rev. B*, **80**, 085202 (2009).

[175] E. Wimmer, A. J. Freeman, M. Weinert, H. Krakauer, J. R. Hiskes and A. M. Karo. *Phys. Rev. Lett.*, **48**, 1128–1131 (1982).

[176] P. E. Blöchl. *Phys. Rev. B*, **50**, 17953–17979 (1994).

[177] A. Baldereschi. *Phys. Rev. B*, **7**, 5212–5215 (1973).

[178] H. J. Monkhorst and J. D. Pack. *Phys. Rev. B*, **13**, 5188–5192 (1976).

[179] E. R. Davidson. *J. Comput. Phys.*, **17**, 87–94 (1975).

[180] R. P. Feynman. *Phys. Rev.*, **56**, 340–343 (1939).

[181] P. Pulay. *Mol. Phys.*, **17**, 179–204 (1969).

[182] E. Polak. *Computational Methods in Optimization.* Academic Press, New York, NY, USA, (1971).

[183] L. Verlet. *Phys. Rev.*, **159**, 98–1.03 (1967).

[184] S. Nosé. *J. Chem. Phys.*, **81**, 511–519 (1984).

[185] F. D. Murnaghan. *Proc. Natl. Acad. Sci. U.S.A.*, **30**, 244–247 (1944).

[186] K. Reuter and M. Scheffler. *Phys. Rev. B*, **65**, 035406 (2001).

[187] C. Freysoldt, J. Neugebauer and C. G. Van de Walle. *Phys. Rev. Lett.*, **102**, 016402 (2009).

[188] F. Zhang, Q. Jun and S. W. Chan. *J. Appl. Phys.*, **95**, 4319–4326 (2004).

[189] A. Janotti and C. G. Van de Walle. *Phys. Rev. B*, **76**, 165202 (2007).

[190] V. Fernandes, J. O. Mossanek, P. Schio, J. J. Klein, A. J. A. de Oliveira, W. A. Ortiz, N. Mattoso, J. Varalda, W. H. Schreiner, M. Abbate and D. H. Mosca. *Phys. Rev. B*, **80**, 035202 (2009).

[191] B. J. Morgan and G. W. Watson. *Phys. Rev. B*, **80**, 233102 (2009).

[192] M. Nolan and G. W. Watson. *J. Chem. Phys.*, **125**, 144701 (2006).

[193] T. G. Kuznetsova and V. A. Sadykov. *Kinet. Catal.*, **49**, 840–858 (2008).

[194] K. Yasunaga, K. Yasuda, S. Matsumura and T. Sonoda. *Nucl. Instrum. Methods Phys. Res., Sect. B*, **250**, 114–118 (2006).

[195] K. Yasunaga, K. Yasuda, S. Matsumura and T. Sonoda. *Nucl. Instrum. Methods Phys. Res., Sect. B*, **266**, 2877–2881 (2008).

[196] M. Venkatesan, C. B. Fitzgerald and J. M. D. Coey. *Nature*, **630**, 630 (2004).

[197] D. W. Abraham, M. M. Frank and S. Guha. *Appl. Phys. Lett.*, **87**, 252502 (2005).

[198] A. Sundaresan, R. Bhargavi, N. Rangarajan, U. Siddesh and C. N. R. Rao. *Phys. Rev. B*, **74**, 161306 (2006).

[199] A. B. Schick, W. E. Pickett and A. I. Liechtenstein. *J. Electron. Spectrosc.*, **114**, 753–758 (2001).

[200] J. L. Gavartin, P. V. Sushko and A. L. Shluger. *Phys. Rev. B*, **67**, 035108 (2003).

[201] C. W. M. Castleton, J. Kullgren and K. Hermansson. *J. Chem. Phys.*, **127**, 244704 (2007).

[202] N. M. Galea, D. O. Scanlon, B. J. Morgan and G. W. Watson. *Mol. Simul.*, **35**, 577–583 (2009).

[203] D. A. Andersson, S. I. Simak, B. Johansson, I. A. Abrikosov and N. V. Skorodumova. *Phys. Rev. B*, **75**, 035109 (2007).

[204] C. Zhang, A. Michaelides, D. A. King and S. J. Jenkins. *J. Chem. Phys.*, **129**, 194708 (2008).

[205] J. L. F. Da Silva, M. V. Ganduglia-Pirovano, J. Sauer, V. Bayer and G. Kresse. *Phys. Rev. B*, **75**, 045121 (2007).

[206] M. V. Ganduglia-Pirovano, J. L. F. Da Silva and J. Sauer. *Phys. Rev. Lett.*, **102**, 026101 (2009).

[207] J. P. Perdew, A. Ruzsinsky, G. I. Csonka, O. A. Vydrov, G. E. Scuseria, V. N. Staroverov and J. Tao. *Phys. Rev. A*, **76**, 040501(R) (2007).

[208] E. A. Kümmerle and G. Heger. *J. Solid State Chem.*, **147**, 485–500 (1999).

[209] Z. Wu, J. Zhang, X. Chen, Z. Chen, M. Sun, Z. Wu and L. Guo. *Phys. Scr.*, **T115**, 902–806 (2005).

[210] G. Magesh, B. Viswanathan, R. P. Viswanath and T. K. V. Varadarajan. *Indian J. Chem., Sec. A*, **46A**, 480–488 (2009).

[211] S. Sathyamurthy, K. J. Leonard, R. Davestani and M. P. Paranthaman. *Nanotechnology*, **16**, 1960–1964 (2005).

[212] S. Debnath, M. R. Islam and M. S. R. Khan. *Bull. Mater. Sci.*, **30**, 315–319 (2007).

[213] D. R. Mullins, P. V. Radulovic and S. H. Overbury. *Surf. Sci.*, **429**, 186–198 (1999).

[214] D. R. Mullins, S. H. Overbury and D. R. Huntley. *Surf. Sci.*, **409**, 307–319 (1998).

[215] M. Nolan, S. C. Parker and G. W. Watson. *Surf. Sci.*, **595**, 223–232 (2005).

[216] C. J. Zhang, A. Michaelides, D. A. King and S. J. Jenkins. *Phys. Rev. B*, **79**, 075433 (2009).

[217] A. F. Holleman, E. Wiber and N. Wiberg. *Inorganic Chemistry*. Academic Press, San Diego, CA, USA, (2001).

[218] A. A. Sokol, A. Walsh and C. R. A. Catlow. *Chem. Phys. Lett.*, **492**, 44–48 (2010).

[219] K. G. Godinho, A. Walsh and G. W. Watson. *J. Phys. Chem. C*, **113**, 439–448 (2009).

[220] S. Na-Phattalung, M. F. Smith, K. Kim, M.-H. Du, S.-H. Wei, S. B. Zhang and S. Limpijumnong. *Phys. Rev. B*, **73**, 125205 (2006).

[221] C. R. A. Catlow, S. A. French, A. A. Sokol, A. A. Al-Sunaidi and S. M. Woodley. *J. Comput. Chem.*, **29**, 2234–2249 (2008).

[222] M. K. Nowotny, L. R. Sheppard, T. Bak and J. Nowotny. *J. Phys. Chem. C*, **112**, 5275–5300 (2008).

[223] E. Mamontov and T. Egami. *J. Phys. Chem. Solids*, **61**, 1345–1356 (2000).

[224] C. R. A. Catlow and M. J. Norgett. *J. Phys-Paris*, **34**, C9–C45 (1973).

[225] C. H. Cheng, S. F. Lee and C. W. Hong. *J. Electrochem. Soc.*, **154**, E158–E163 (2007).

[226] M. Nakayama and M. Martin. *Phys. Chem. Chem. Phys.*, **11**, 3241–3249 (2009).

[227] W. Zając and J. Molenda. *Solid State Ionics*, **192**, 163–167 (2011).

[228] H. Yahiro, K. Eguchi and H. Arai. *Solid State Ionics*, **36**, 71–75 (1989).

[229] D. O. Scanlon, B. J. Morgan and G. W. Watson. *Phys. Chem. Chem. Phys.*, **13**, 4279–4282 (2011).

[230] J. Åhman, G. Scensson and J. Albertsson. *Acta. Cryst. C*, **52**, 1336–1338 (1996).

[231] P. R. L. Keating, D. O. Scanlon, B. J. Morgan, N. M. Galea and G. W. Watson. *J. Phys. Chem. C*, **116**, 2443–2452 (2012).

[232] A. Walsh, G. W. Watson, D. J. Payne, R. G. Edgell, J. Guo, P.-A. Glans, T. Learmonth and K. E. Smith. *Phys. Rev. B*, **73**, 235104 (2006).

[233] A. Walsh, D. J. Payne, R. G. Egdell and G. W. Watson. *Chem. Soc. Rev.*, **40**(9), 4455–4463 (2011).

[234] H. J. Avila-Paredes, K. Choi, C.-T. Chen and S. Kim. *J. Mater. Chem.*, **19**, 4837–4842 (2009).

[235] H. Inaba and H. Tagawa. *Solid State Ionics*, **83**, 1–16 (1996).

[236] H. Huang, T. M. Gur, Y. Saito and F. Prinz. *Appl. Phys. Lett.*, **89**, 143107 (2006).

[237] Q. Dong, S. Yin, C. Guo and T. Sato. *Nanoscale Res. Lett.*, **7**, 542 (2012).

[238] S. Collins, G. Finos, R. Alcántara, E. del Rio, S. Bernal and A. Bonivardi. *Appl. Catal. A*, **388**, 202–210 (2010).

[239] G. Li, Y. Mao, L. Li, S. Feng, M. Wang and X. Yao. *Chem. Mater.*, **11**, 1259–1266 (1999).

[240] H. J. Avila-Paredes, P. Jain, S. Sen and S. Kim. *Chem. Mater.*, **22**, 893–897 (2010).

[241] S. Omar, E. D. Wachsman, J. L. Jones and J. C. Nino. *J. Am. Ceram. Soc.*, **92**, 2674–2681 (2009).

[242] J. T. S. Irvine, J. W. L. Dobson, T. Politova, S. García Martín and A. Shenouda. *Faraday Discuss.*, **134**, 41–49 (2007).

[243] V. Parvulescu, S. Coman, V. I. Parvulescu, P. Grange and G. Poncelet. *J. Catal.*, **180**, 66–84 (1998).

[244] Y. Zheng, M. Zhou, L. Ge, S. Li, H. Chen and L. Guo. *J. Alloys Compd.*, **509**, 1244–1248 (2011).

[245] R. D. Shannon. *Acta. Cryst. A*, **32**, 751–767 (1976).

[246] J. Hafner. *J. Comput. Chem.*, **29**, 2044–2078 (2008).

[247] A. A. Skelton, P. Fenter, J. D. Kubicki, D. J. Wesolowski and P. T. Cummings. *J. Phys. Chem. C*, **115**, 2076–2088 (2011).

[248] K. Leung, S. B. Rempe and O. A. von Lilienfeld. *J Chem. Phys.*, **130**, 204507 (2009).

[249] S. Sameshima, T. Ichikawa, M. Kawaminami and Y. Hirata. *Mater. Chem. Phys.*, **61**, 31–35 (1999).

[250] S. V. Chavan, M. D. Mathews and A. K. Tyagi. *J. Am. Ceram. Soc.*, **87**, 1977–1980 (2004).

[251] S. S. Bhella, S. P. Shafi, F. Trobec, M. Bieringer and V. Thangadurai. *Inorg. Chem.*, **49**, 1699–1704 (2010).

[252] P. Praydot. *Handbook of Inorganic Chemicals.* McGraw–Hill, New York, USA, (2003).

[253] J. Van herle, T. Horita, T. Kawada, N. Sakai, H. Yokokawa and M. Dokiya. *J. Eur. Ceram. Soc.*, **16**, 961–973 (1996).

[254] D. R. Ou, T. Mori, F. Ye, M. Takahashi, J. Zou and J. Drennan. *Acta Materiala*, **54**, 3737–3746 (2006).

[255] X. Guo, W. Sigle and J. Maier. *J. Am. Ceram. Soc.*, **86**, 77–87 (2003).

[256] Y. Zheng, Y. Shi, H. Gu, L. Gao, H. Chen and L. Guo. *Mater. Res. Bull.*, **44**, 1717–1721 (2009).

[257] H. Yoshida, H. Deguchi, K. Miura, M. Horiuchi and T. Inagaki. *Solid State Ionics*, **140**, 191–199 (2001).

[258] T. Boutard, B. Rousseau, C. Couteau, C. Tomasoni, C. Simonnard, C. Jacquot, L. J. M. Coiffard, K. Konstantinov, T. Devers and C. Roussakis. *Mater. Lett.*, **108**, 13–16 (2013).

[259] R. A. Madero-Visbal, B. E. Alvarado, J. F. Colon, C. H. Baker, M. S. Wason, S. Isley, B. adn Seal and C. M. Lee. *Nanomed–nanotechnol*, **8**, 1223–1231 (2012).

[260] F.-C. Chiu, S.-Y. Chen, C.-H. Chen, F.-W. Chen, H.-S. Huang and H.-L. Hwang. *Jpn. J. Appl. Phys.*, **48**, 04C014–1–4 (2009).

[261] Y. Nishikawa, T. Yamaguchi, M. Yoshiki, H. Satake and N. Fukushima. *Appl. Phys. Lett.*, **81**, 4386–4388 (2002).

[262] C.-H. Chen, I. Y.-K. Chang, J. Y.-M. Lee and F.-C. Chiu. *Appl. Phys. Lett.*, **92**, 043507 (2008).

[263] W.-H. Kim, M.-K. Kim, W. J. Maeng, J. Gaineau, V. Pallem, C. Dussarrat, A. Noori, D. Thompson, S. Chu and H. Kim. *J. Electrochem. Soc.*, **158**, G169–G172 (2011).

[264] M. H. Tang, Y. C. Zhou, X. J. Zheng, Q. P. Wei, C. P. Cheng, Z. Ye and Z. S. Hu. *Trans. Nonferrous Met. Soc. China*, **17**, S741–S746 (2007).

[265] F.-C. Chiu and C.-M. Lai. *J. Phys. D: Appl. Phys.*, **43**, 075104 (2010).

[266] F.-C. Chiu. *Electrochem. Solid-State Lett.*, **11**, H135–H137 (2008).

[267] Y. Zhao. *Materials*, **5**, 1413–1438 (2012).

[268] E. J. Kim, M. Shandalov, K. C. Saraswat and P. C. McIntyre. *Appl. Phys. Lett.*, **98**, 032108 (2011).

[269] J. Y. Dai, P. F. Lee, K. H. Wong, H. L. W. Chan and C. L. Choy. *J. Appl. Phys.*, **94**, 912–915 (2003).

[270] D. W. McNeill, S. Bhattacharya, H. Wadsworth, F. H. Ruddel, S. J. Mitchell, B. M. Armstrong and H. S. Gamble. *J. Mater. Sci.: Mater. Electron.*, **19**, 119–123 (2008).

[271] Y. Aoki, T. Kunitake and A. Nakao. *Chem. Mater.*, **17**, 450–458 (2005).

[272] G. D. Wilk, R. M. Wallace and J. M. Anthony. *J. Appl. Phys.*, **89**, 5243–5275 (2001).

[273] J. Wang, H. P. Li and R. Stevens. *J. Mater. Sci.*, **27**, 5397–5430 (1992).

[274] N. V. Skorodumova, R. Ahuja, S. I. Simak, I. A. Abrikosov, B. Johansson and B. I. Lundqvist. *Phys. Rev. B*, **64**, 115108 (2001).

[275] Y. Nishikawa, N. Fukushima, N. Yasuda, K. Nakayama and S. Ikegawa. *Jpn. J. Appl. Phys., Part 1*, **41**, 2480–2483 (2002).

[276] T. Yamamoto, H. Momida, T. Hamada, T. Uda and T. Ohno. *Thin Solid Films*, **486**, 136–140 (2005).

[277] J. B. Varley, A. Janotti and C. G. Van de Walle. *Phys. Rev. B*, **81**, 245216 (2010).

[278] C. R. A. Catlow, A. A. Sokol and A. Walsh. *Chem. Comm.*, **47**, 3386–3388 (2011).

[279] S. Lany and A. Zunger. *Phys. Rev. B*, **78**, 235104 (2008).

[280] F. Oba, A. Togo, I. Tanaka, J. Paier and G. Kresse. *Phys. Rev. B*, **77**(24), 245202 (2008).

[281] S. Lany and A. Zunger. *Phys. Rev. B*, **81**, 205209 (2010).

[282] A. K. Singh, A. Janotti, M. Scheffler and C. G. Van de Walle. *Phys. Rev. Lett.*, **101**, 055502–4 (2008).

[283] J. B. Varley, J. R. Weber, A. Janotti and C. G. V. de Walle. *Appl. Phys. Lett.*, **97**, 142106 (2010).

[284] P. Agoston, K. Albe, R. M. Nieminen and M. J. Piska. *Phys. Rev. Lett.*, **103**, 245501 (2009).

[285] S. Limpijumnong, P. Reunchan, A. Janotti and C. G. Van de Walle. *Phys. Rev. B*, **80**, 193202 (2009).

[286] P. R. L. Keating, D. O. Scanlon and G. W. Watson. *J. Phys.: Condens. Matter*, **21**, 405502 (2009).

[287] O. F. Schirmer. *J. Phys.: Condens. Matter*, **18**, R667–R704 (2006).

[288] M. Yashima, S. Kobayashi and T. Yasui. *Solid State Ionics*, **177**, 211–215 (2006).

[289] A. Kohno, N. Aomine, Y. Soejima and A. Okazaki. *Jpn. J. Appl. Phys.*, **33**, 5073–5077 (1994).

[290] E. Aneggi, C. de Leitenburg, G. Dolcetti and A. Trovarelli. *Catal. Today*, **114**, 40–47 (2006).

[291] J. Kullgren, K. Hermansson and C. Castleton. *J. Chem. Phys.*, **137**, 044705 (2012).

[292] J. F. Jerratsch, X. Shao, N. Nilius, H. J. Freund, C. Popa, M. V. Ganduglia-Pirovano, A. M. Burow and J. Sauer. *Phys. Rev. Lett.*, **106**, 246801 (2011).

[293] F. Esch, S. Fabris, L. Zhou, T. Montini, C. Africh, P. Fornasiero, G. Comelli and R. Rosei. *Science*, **309**, 752–755 (2005).

[294] H. Y. Li, H. F. Wang, X. Q. Gong, Y. L. Guo, Y. Guo, G. Lu and P. Hu. *Phys. Rev. B*, **79**, 193401 (2009).

[295] V. V. Pushkarev, V. I. Kovalchuk and J. L. d'Itri. *J. Phys. Chem. B*, **108**, 5341–5348 (2004).

[296] S. Bernal, G. Blanco, G. Cifredo, J. A. Pérez-Omil and Rodrìguez-Izquierdo. *J. Alloys Compd.*, **250**, 449–454 (1997).

[297] G. W. Watson, E. T. Kelsey, N. H. de Leeuw, D. J. Harris and S. C. Parker. *J. Chem. Soc., Faraday Transactions*, **92**, 433–438 (1996).

[298] J. P. Allen and G. W. Watson. *In Preparation*,

[299] N. V. Skorodumova, M. Baudin and K. Hermansson. *Phys. Rev. B*, **69**, 075401 (2004).

[300] D. Marrocchelli and B. Yildiz. *J. Phys. Chem. C*, **116**, 2411–2424 (2012).

[301] J. Paier, C. Penschke and J. Sauer. *Chem. Rev.*, **113**, 3949–3985 (2013).

[302] H. F. Wang, H. Y. Li, X. Q. Gong, Y. L. Guo, G. Z. Lu and P. Hu. *Phys. Chem. Chem. Phys.*, **14**, 16521–16535 (2012).

[303] M. Nolan, S. C. Parker and G. W. Watson. *Phys. Chem. Chem. Phys.*, **8**, 216–218 (2006).

[304] N. Shehata, K. Meehan, M. Hudait and N. Jain. *J. Nanopart. Res.*, **14**, 1173 (2012).

[305] X. N. Wu, X. L. Ding, S. M. Bai, B. Xu, S. G. He and Q. Shi. *J. Phys. Chem. C*, **115**, 13329–13337 (2011).

[306] M. Huang and S. Fabris. *Phys. Rev. B*, **75**, 081404 (2007).

[307] S. Babu, R. Thanneeru, T. Inerbaev, R. Day, A. E. Masunov, A. Schulte and S. Seal. *Nanotechnology*, **20**, 085713 (2009).

[308] A. Kossov, A. I. Frenkel, Q. Wang, E. Wachtel and I. Lubomirsky. *Adv. Mater.*, **22**, 1659–1662 (2009).

[309] P. Fleming, S. Ramirz, J. D. Holmes and M. A. Morris. *Chem. Phys. Lett.*, **501**, 51–57 (2011).

[310] V. M. Zainullina and V. P. Zhukov. *Phys. Solid State*, **43**, 1686–1699 (2001).